

FORMATION AND EVOLUTION OF INCLUSIONS IN CALCIUM-TREATED  
LIQUID STEEL

FORMATION AND EVOLUTION OF INCLUSIONS IN CALCIUM-TREATED  
LIQUID STEEL

By  
KEYAN MIAO, B.Eng, M.A.Sc

A Thesis Submitted to the Graduate Studies in Partial Fulfilment of the Requirements  
for the Degree Doctor of Philosophy

McMaster University  
© Copyright by Keyan Miao, September 2022

DOCTOR OF PHILOSOPHY (2022)

McMaster University

(Materials Science and Engineering)

Hamilton, Ontario

TITLE:

Formation and Evolution of Inclusions in  
Calcium-Treated Liquid Steel

AUTHOR:

Keyan Miao, B.Eng., M.A.Sc (McMaster  
University, Canada)

SUPERVISOR:

Dr. Neslihan Dogan  
Dr. Stanley Sun

NUMBER OF PAGES:

xviii, 166

## Abstract

The cleanliness of steel impacts the success of steel production and the physical and chemical properties of the final product. Improving the cleanliness of steel, therefore, becomes a necessity in the present time, with an ever-increasing demand for high-quality steel products. The cleanliness can be improved by removing the harmful inclusions through flotation or by modifying their composition and morphology to less detrimental forms. The present study focuses on better understanding the second approach, a specific modification method commonly known as the calcium (Ca) treatment in advanced high strength steel (AHSS) production.

The chemical and morphological evolutions of  $\text{Al}_2\text{O}_3$  inclusions under experimental and industrial conditions, as well as the formation of CaS and MnS inclusions, were studied in this work. Six laboratory experiments with different combinations of calcium and sulfur contents of liquid steel were conducted. Samples were taken at different time durations after calcium addition. The inclusions on the sample cross-sections were analyzed using an automated SEM-EDS system to obtain their chemical, size distribution, population, and morphological information. Similar steps were taken in the analysis of industrial samples. The findings obtained based on the automated SEM-EDS analyses were further supported and validated against other analysis results such as manual SEM analysis, thermodynamics, and kinetics calculations.

The modification mechanism for  $\text{Al}_2\text{O}_3$  inclusions was established in the first part of the study. After adding 10 ppm, 20 ppm, and 35 ppm Ca, small-sized calcium aluminates  $\text{CA}_x$  (C and A denote CaO and  $\text{Al}_2\text{O}_3$ , respectively) inclusions become the primary oxygen bearer instead of  $\text{Al}_2\text{O}_3$  inclusions. The modification extent of the  $\text{CA}_x$  inclusions depends on the Ca content. CaS inclusions also form at the early stage of calcium treatment. In the later stage, CaS inclusions act as the Ca source to modify the remaining  $\text{Al}_2\text{O}_3$  inclusions to  $\text{CA}_x$  inclusions and simultaneously modify the existing  $\text{CA}_x$  inclusions until equilibrium is reached. CaO inclusions only form in steel containing 20 ppm S and 35 ppm Ca; the primary oxygen bearer will change from  $\text{Al}_2\text{O}_3$  to CaO, followed by a transformation from CaO to CaS. In other S and Ca contents, CaO inclusions do not form. This finding clarified that modification of  $\text{Al}_2\text{O}_3$  inclusions is mainly driven by dissolved Ca and CaS inclusions, with CaO showing a minor direct impact. Moreover, the experimental studies showed that total area fractions of liquid and semi-liquid inclusions, which are inclusions that are partially liquid and partially solid, are correlated with the thermodynamic stability of CaS inclusions. The fraction of liquid inclusions decreases after the area fraction of CaS inclusions drastically increases when steel chemistries allow stable CaS inclusions to precipitate.

The correlation between the steel chemistries and inclusions was improved by

incorporating more data from industrial heats. Three modification indexes were proposed to estimate the control of  $CA_x$ , CaS, and MnS inclusions. The fraction of  $CA_x$  inclusions with more than 50 pct liquid, and the area fraction of CaS and MnS inclusions in tundish samples were correlated with the Ca, Al, Mn, and S contents of liquid steel. Later, these modification indexes were incorporated to evaluate the effectiveness of calcium treatment quantitatively. This makes the present study the first to discuss the correlations between Ca, Al, Mn, and S contents and the number of inclusions in the open literature. The correlations were validated against industrial data, they may be used in industry to determine the optimum Ca content for inclusion control and modification.

Based on the experimental and industrial data, the coarsening of CaS inclusions was initially governed by mass transport, then shifted to collision-related mechanisms. When agitation is absent, Brownian motion shows the most significant impact on the growth of CaS inclusions, while turbulent flow is the critical cause of collision and coagulation when the melt is stirred, such as in industrial conditions. It has been found that  $CA_x$  inclusion growth mainly occurs in the early stage after Ca addition. The potential reason is that the lack of attraction prevents coagulation after  $CA_x$  inclusions are modified to liquid and semi-liquid.

## **Acknowledgments**

I would like to thank my supervisor, Dr. Neslihan Dogan and Dr. Stanley Sun for providing useful and in-time suggestions and guidance throughout my 5-year Ph.D. program. Dr. Dogan was able to hold research meetings regularly to help me on the right track of researching. Without her help, the research will most likely prolong even further. I am also grateful to Dr. Stanley Sun, who was able to help coordinate ASPEX usage at the ArcelorMittal Hamilton lab and give suggestions on journal writing and research progress from the industrial point of view. I would also like to thank Dr. Kenneth Coley, who always gave valuable suggestions in a discussion. The help from these three members of the supervisor committee improved the quality of the work.

I would also like to thank the other members of the Materials Science and Engineering department. Especially, Dr. Muhammad Nabeel and the lab technicians. I received help from Dr. Muhammad Nabeel from the first till the last day of this program. I got his help on almost every part of this project, from conducting experiments to analysis and journal as well as thesis writing. As for the lab technicians, I would like to thank Dr. Xiaogang Li, Doug Culley, and Ed McCaffery for their help and training on various lab equipment. Without their support, the preparation and analysis in the lab would not be as smooth. I also want to thank Mary-Anne Bechamp for the administration work and other paperwork. I am also thankful to John Thompson for organizing the Steel Research Centre meetings and allowing me to share my findings and receive feedback on my work from an industrial perspective.

My friends and co-workers were all beneficial when I needed them. Thanks to Dr. Mukesh Sharma for explaining the basics of inclusions in the early days of my study and Dr. Michel Alba for sharing the struggles dealing with inclusion analysis. Dr. Kezhuan Gu and Dr. Wangzhong Mu both tirelessly gave suggestions on the detail of my research and invited me to various activities during the weekends and holidays. Dr. Ameya Kadrolkar, Dr. Aliyeh Rafiei, Dr. Jayasree Biswas, Dr. Yousef Tabatabaei, and Dr. Brian Jamieson were all good friends and willing to give me a hand, both on research and other things when needed.

Finally, I would like to extend my gratitude to my family, who continually support and understand whatever I do throughout my life.

## Table of Contents

<b>Abstract</b>	<b>iii</b>
<b>Acknowledgments</b>	<b>v</b>
<b>Table of Contents</b>	<b>vi</b>
<b>List of Figures</b>	<b>ix</b>
<b>List of Tables</b>	<b>xiv</b>
<b>List of Abbreviations and Symbols</b>	<b>xv</b>
<b>Declaration of Academic Achievement</b>	<b>xviii</b>
<b>Chapter 1 Introduction</b>	<b>1</b>
1.1 Research Background	1
1.2 Research Objectives	2
1.3 Thesis Outline	2
<b>Chapter 2 Literature Review</b>	<b>4</b>
2.1 Secondary Steelmaking	4
2.1.1 Deoxidation	5
2.1.2 Desulfurization	6
2.2 Inclusion Control during the Refining Process	7
2.2.1 Inclusion Removal	7
2.2.2 Calcium Addition Method	9
2.2.3 Modification of Oxide Inclusions by Ca Treatment	11
2.2.4 Formation of CaS by Ca Treatment	14
2.2.5 Modification of MnS Inclusions by Ca Treatment	17
2.2.6 Inclusion Modification by Slag	19
2.2.7 Inclusions Modification by Rare Earth Elements	21
2.3 Effects of Inclusions and Modification on Steel Properties	22
2.4 Evolution of Inclusion Sizes during the Refining Process	24
2.4.1 Mechanisms Affecting the Inclusion Size Changes	25
2.4.2 Mathematical Models for Particle Coarsening Kinetics	27
2.5 Inclusion Characterization Techniques	30
2.5.1 Optical Emission Spectrometry - Pulse Discrimination Analysis (OES-PDA)	30
2.5.2 Mannesmann Inclusion Detection by Analyzing Surfboards (MIDAS)	31
2.5.3 Infrared Absorption Spectroscopy (IR)	32
2.5.4 Scanning Electron Microscopy - Energy Dispersive Spectrometry (SEM-EDS)	33
2.6 Knowledge Gaps	37
<b>Chapter 3 Experimental Study of Inclusion Modification by Ca in AHSS</b>	<b>40</b>

3.1	Introduction .....	41
3.2	Experimental Methodology .....	43
3.3	Experimental results .....	45
3.3.1	Steel chemistries.....	45
3.3.2	Inclusion compositions and quantities.....	48
3.4	Experimental results .....	51
3.4.1	Effect of Ca and S contents on inclusion stabilities.....	51
3.4.2	Effect of Ca and S contents on inclusion stabilities.....	53
3.4.2.1	Mechanism involving CaO inclusions.....	53
3.4.2.2	Mechanism in the absence of CaO inclusion.....	55
3.5	Comparison of modification results.....	58
3.5	Conclusion.....	63
3.6	Acknowledgement .....	64
3.7	Appendix: Simplification of dimensionless Ca calculation .....	64
3.8	References .....	67
<b>Chapter 4 Evaluation of Ca Treatment on Oxide and Sulfide Inclusions through Modification Indexes.....</b>		<b>70</b>
4.1	Introduction .....	71
4.2	Industrial trial.....	74
4.3	Results and Discussion .....	75
4.3.1	Effect of Ca, S and Al on calcium aluminate inclusions.....	77
4.3.2	Effect of Ca, S and Al on CaS containing inclusions .....	81
4.3.3	Effects of steel chemistries on MnS inclusions .....	84
4.3.4	Evaluation of calcium treatment in industrial heats.....	92
4.4	Summary.....	96
4.5	Acknowledgement .....	97
4.6	Reference .....	97
<b>Chapter 5 Coarsening Mechanisms of CaS Inclusions in Ca-treated Steels .</b>		<b>100</b>
5.1	Introduction .....	101
5.2	Experimental Methodology .....	104
5.3	Methods of Calculating Coarsening of CaS Inclusions .....	107
5.3.1	Determination of the Rate-Controlling Component .....	107
5.3.2	Coarsening Due to Ostwald Ripening .....	109
5.3.3	Coarsening Due to Ca Diffusion .....	110
5.3.4	Coarsening Due to Brownian Motion.....	112
5.3.5	Coarsening Due to Ascending Velocity Difference .....	112
5.3.6	Coarsening Due to Melt Flow .....	113
5.3.6	Coarsening Due to the Multiple Mechanisms Predicted by Population	

Balance Equation (PBE).....	113
5.4 Results .....	114
5.4.1 CaS Growth in Experimental Conditions .....	114
5.4.2 CaS Growth in Industrial Conditions .....	120
5.5 Discussion.....	121
5.5.1 Coarsening Mechanisms of CaS Inclusions under Experimental Conditions .....	122
5.5.2 Cause of Change in Coarsening Mechanisms .....	124
5.5.3 Coarsening Mechanisms of CaS Inclusions under Industrial Conditions.....	127
5.6 Conclusions .....	131
5.7 Acknowledgement .....	131
5.8 References .....	132
<b>Chapter 6 Coarsening Mechanisms of Calcium Aluminates in Ca-treated Steels .....</b>	<b>137</b>
6.1 Introduction .....	137
6.2 Experimental Methodology .....	138
6.3 Results .....	139
6.3.1 CA <sub>x</sub> Growth in Experimental Conditions.....	139
6.3.2 CA <sub>x</sub> Growth in Industrial Conditions .....	144
6.4 Discussion.....	146
6.4.1 Coarsening Mechanisms of CA <sub>x</sub> under Experimental Conditions .....	146
6.4.2 Coarsening Mechanisms of CA <sub>x</sub> under industrial conditions .....	148
6.4 Conclusion.....	152
<b>Chapter 7 Concluding Remarks.....</b>	<b>154</b>
7.1 Key Findings and Contributions .....	154
7.1.1 General Overview .....	154
7.1.2 Specific Findings.....	155
7.2 Future Works.....	156
<b>Reference .....</b>	<b>158</b>

## List of Figures

<b>Chapter 1</b>	<b>Introduction .....</b>	<b>1</b>
<b>Chapter 2</b>	<b>Literature Review.....</b>	<b>4</b>
	Figure 2.1 Schematic diagram of the general steelmaking flow.....	4
	Figure 2.2 Ellingham diagram.....	6
	Figure 2.3 Schematic diagram of the Thyssen-Niederrhein (TN) powder injection method (a) lifter (b) pressure vessel (for powder delivery) (c) swingarm (d) control panel (e) Ar panel (f) 120 t ladle.....	10
	Figure 2.4 Schematic diagram of the cored wire injection method .....	11
	Figure 2.5 CaO-Al <sub>2</sub> O <sub>3</sub> phase diagram .....	12
	Figure 2.6 Schematic diagram of a layered inclusion.....	13
	Figure 2.7 Calculated coverage of steel-gas interface by O and S in liquid steel containing 3 ppm [O] and different S levels.....	15
	Figure 2.8 Schematic diagrams of the CaS containing complexes inclusion morphology .....	17
	Figure 2.9 Inclusion evolutions in liquid steel.....	25
	Figure 2.10 (a) Schematic diagram of OES-PDA results and (b) reassignment of PDA histogram for soluble and insoluble components .....	31
	Figure 2.11 Differences between ultrasonic indications (A) and ultrasonic defects (F) in the MIDAS test .....	32
	Figure 2.12 Schematic diagram of the electrolytic extraction setup.....	34
	Figure 2.13 Schematic drawing of the bisected chord method and sizing.....	36
<b>Chapter 3</b>	<b>Experimental Study of Inclusion Modification by Ca in AHSS .....</b>	<b>40</b>
	Figure 3.1 Schematic diagram of the experimental setup.....	43
	Figure 3.2 Flow chart of a typical inclusion modification experiment.....	44
	Figure 3.3 Inclusion distribution represented on a ternary diagram from Exp. 3020 at 20 minutes after Ca addition. A solid line illustrates 50 pct liquid region. ....	45
	Figure 3.4 A typical SEM backscatter image of the Al <sub>2</sub> O <sub>3</sub> crucible (a) before and (b) after an experiment.....	48
	Figure 3.5 Inclusions quantity evolution from six experiments studied in the form of (a) area fraction (AF) change and (b) number (N <sub>A</sub> ) change .....	49
	Figure 3.6 Evolution of inclusion area fraction (AF) in (a) Exp. 2035, (b) Exp. 2020, (c) Exp. 2010, (d) Exp. 3035, (e) Exp. 3020 and (f) Exp. 3010.....	50
	Figure 3.7 Inclusion stability diagram constructed using FactSage for experimental steel containing (a) 20 ppm S and (b) 30 ppm S and constant 0.06 wt pct C, 0.25 wt pct Si, 1 wt pct Mn and 20 ppm T.O.....	52
	Figure 3.8 CaO, Al <sub>2</sub> O <sub>3</sub> and CaS mass fractions of Ca-rich and CaS inclusions in Exp.	

2035 at 1 minute (b) 5 minutes (c) 10 minutes and (d) 20 minutes after Ca addition...	54
Figure 3.9 SEM-EDS elemental maps of CaO-CaS dual-phase inclusions from Exp. 2035 samples (a) and (b) both taken at 3 minutes after Ca addition.....	55
Figure 3.10 SEM-EDS elemental maps of typical oxysulfide inclusions observed in the sample taken at (a-b) 3 minutes after Ca addition (c-d) 20 minutes after Ca addition in Exp. 2020 .....	56
Figure 3.11 Change of CaS-other average compositions (a) CaO + Al <sub>2</sub> O <sub>3</sub> (b) CaS in Exp. 2020, Exp. 2010, Exp. 3035, Exp. 3020 and Exp. 3010.....	57
Figure 3.12 Normalized AF of (a) all inclusions and (b) CA <sub>x</sub> inclusions in six experiments at 20 minutes after Ca addition .....	59
Figure 3.13 The percentage of liquid CA <sub>x</sub> dependency on dimensionless Ca in laboratory results .....	61
Figure 3.14 The AF of inclusions industrial heats (a) Heat 1 (b) Heat 2 (L and T represent ladle and tundish, respectively).....	61
Figure 3.15 The relative AF of inclusions with respect to dimensionless Ca for industrial heats (a) Heat 1 (b) Heat 2.....	63
Figure 3.A1 The upper limit and lower limit T.Ca of the liquid window were calculated in FactSage assuming 20 ppm T.O and experimental temperature of 1873K.....	63
Figure 3.A2 The dependency of parameter B on T.S.....	63
<b>Chapter 4 Evaluation of Ca Treatment on Oxide and Sulfide Inclusions through Modification Indexes.....</b>	<b>70</b>
Figure 4.1 Schematic diagram of industrial sample. ....	74
Figure 4.2 AF of all inclusion types in tundish samples from (a) Series 1, (b) Series 2, and (c) Series 3 heats. Heats were categorized into Series 1, 2, 3 based on their average Mn contents 0.55, 0.96, and 1.13 wt pct, respectively.....	76
Figure 4.3 Change of area fraction (AF) of total inclusion as a function of total Ca (T. Ca) content in steel samples in Series 1, 2, and 3 heats.....	77
Figure 4.4 Examples of CA <sub>x</sub> , CaS, and CaS-other inclusion composition distribution on a CaO-Al <sub>2</sub> O <sub>3</sub> -CaS ternary diagram at 1833K from (a) a heat with modified CTI = -1.8 and (b) a heat with modified CTI = 1.7 .....	78
Figure 4.5 Change of average CaO/Al <sub>2</sub> O <sub>3</sub> ratio of CA <sub>x</sub> with steel chemistry in tundish samples.....	79
Figure 4.6 Inclusion stability diagram obtained using FactSage for steel containing 20 ppm S, 0.06 wt pct C, 0.25 wt pct Si, 1 wt pct Mn and 20 ppm T.O at 1833 K.....	80
Figure 4.7 Relationship between average CaO/Al <sub>2</sub> O <sub>3</sub> ratio in CA <sub>x</sub> type inclusions and dimensionless Ca at 1833 K in industrial samples .....	81
Figure 4.8 Change of estimated CaS amount in (a) all types, (b) CaS type, (c) CaS-other type, and (d) CA <sub>x</sub> inclusions with dimensionless Ca at 1833 K in industrial	

samples.....	82
Figure 4.9 Relation between estimated AF of CaS phase and AF of CaO phase in (a) CaS-other, (b) CA <sub>x</sub> , and (c) CaS inclusions.....	83
Figure 4.10 The AF of MnS in all types of inclusions in (a) Series 1, (b) Series 2 and (c) Series 3.....	85
Figure 4.11 Change of MnS AF with <i>T.Ca/T.S</i> ratio in (a) Series 1 and Series 3 and (b) Series 2.....	86
Figure 4.12 Effect of Mn content in steel on <i>T.Ca/T.S</i> ratio to form a low amount of MnS inclusions.....	87
Figure 4.13 (a) Correlation between the fraction of S in MnS calculated using Equation (4.9) and Equation (4.10). (b) Correlation between the observed MnS AF and the S content in MnS inclusions predicted by SPC in Series 2.....	88
Figure 4.14 Comparison of estimated steel temperature and calculated local transformation temperature change during solidification in industrial heats.....	91
Figure 4.15 Schematic diagram for evaluation the overall effectiveness of CaS, MnS and CA <sub>x</sub> inclusion control.....	94
Figure 4.16 (a) Dependency of <i>d</i> value on <i>T.Ca</i> content for Heat A with <i>x</i> = 23.7, <i>y</i> = 23.4, and <i>z</i> = 16.2 and varying weighing coefficients and (b) AF of all inclusion types in Heat A tundish sample.....	95
Figure 4.17 Comparison of (a) the measured <i>T.Ca</i> content and the estimated optimum <i>T.Ca</i> and (b) AF of all inclusion types in tundish sample in Heat B, Heat C and Heat D.....	96
<b>Chapter 5 Coarsening Mechanisms of CaS Inclusions in Ca-treated Steels . 100</b>	
Figure 5.1 Schematic diagram of the experimental setup.....	104
Figure 5.2 Schematic diagram of the lollipop sample.....	105
Figure 5.3 Evolution of area fraction (AF) of inclusions in (a) Exp. 2035, (b) Exp. 3035, and (c) Exp. 2025.....	115
Figure 5.4 SEM-EDS elemental maps of CaS inclusion in (a) 1-min sample of Exp. 2035, (b) 3-min sample of Exp. 2035 and (c) 20-min sample of Exp. 3035.....	115
Figure 5.5 Average diameters and compositions of CaS type inclusions in (a) Exp. 2035, (b) Exp. 3035, and (c) Exp. 2025.....	116
Figure 5.6 The particle size distribution of CaS type inclusions in (a,b) Exp. 2035, (c,d) Exp. 3035, and (e,f) Exp. 2025.....	119
Figure 5.7 Evolution of the average diameters of CaS type inclusions in samples taken from (a) Heats 1 and 3–30 ppm S and 35 ppm T.Ca and (b) Heats 4 and 5–20 ppm S and 35 ppm T.Ca.....	120
Figure 5.8 The evolution of particle size distribution for CaS type inclusions in Heat 1 including inclusions with <i>d</i> <sub>max</sub> > 0.5 μm (a) ladle samples and (b) tundish samples.....	121

Figure 5.9 Comparison of the average diameters of CaS type inclusions in samples taken in (a) Exp. 2035, (b) Exp. 3035, and (c) Exp. 2025, and predicted using different coarsening mechanisms .....	122
Figure 5.10 Comparison of the average diameters of CaS type inclusions in samples taken from (a) Exp. 2035, (b) Exp. 3035, and (c) Exp. 2025, and predicted based on diffusion-controlled growth followed by Brownian motion .....	124
Figure 5.11 Change of driving force for Ca diffusion in Exp. 2035, Exp 3035, and Exp. 2025 .....	125
Figure 5.12 Variation in the volume fraction of CaS inclusions over time in Exp. 2035, Exp. 3035, and Exp. 2025 .....	125
Figure 5.13 Comparison of collision frequency function of Brownian motion and Stokes motion for an inclusion of diameter $d_i$ (a) 0.5 $\mu\text{m}$ , (b) 1 $\mu\text{m}$ , (c) 2 $\mu\text{m}$ , (d) 3 $\mu\text{m}$ and varied $d_j$ .....	126
Figure 5.14 Comparison of the observed rate of change of CaS population density and the calculated rate of change of population density due to collision in the ladle at (a) 1 min and 2 min, (b) 3 min, and (c) 4 min after Ca addition, and (d) in tundish at 33 min after Ca addition.....	128
Figure 5.15 Comparison of collision frequency function for Brownian motion, Stokes motion, and laminar and turbulent flow for an inclusion with a diameter $d_i$ of (a) 2 $\mu\text{m}$ , (b) 3 $\mu\text{m}$ , (c) 4 $\mu\text{m}$ and varied $d_j$ .....	130
<b>Chapter 6 Coarsening Mechanisms of Calcium Aluminates in Ca-treated Steels</b> .....	<b>137</b>
Figure 6.1 Schematic diagram of the lollipop sample .....	139
Figure 6.2 Area fraction of $\text{CA}_x$ type inclusions in (a) Exp. 2035, (b) Exp. 3035, (c) Exp. 2025 (d) Exp. 2020, (e) Exp. 3020, (f) Exp. 2010, (g) Exp. 3010.....	141
Figure 6.3 Average diameters of $\text{CA}_x$ type inclusions in (a) Exp. 2035, (b) Exp. 3035, (c) Exp. 2025 (d) Exp. 2020, (e) Exp. 3020, (f) Exp. 2010, (g) Exp. 3010 .....	143
Figure 6.4 Area fraction of $\text{CA}_x$ type inclusions in (a) Heat 1, (b) Heat 2, (c) Heat 3, (d) Heat 4 and (e) Heat 5 .....	144
Figure 6.5 Evolution of the average diameter of $\text{CA}_x$ type inclusions from industrial heats (a) Heat 1, (b) Heat 2, (c) Heat 3, (d) Heat 4 and (e) Heat 5 .....	146
Figure 6.6 Comparison of the average diameters of $\text{CA}_x$ inclusions in samples taken in Exp. 3035 and the theoretical coarsening rate .....	147
Figure 6.7 The evolution of particle size distribution for liquid $\text{CA}_x$ type inclusions in Heat 1 including inclusions with $d_{\text{max}} > 0.5 \mu\text{m}$ (a) (b) ladle samples (c) tundish samples. (d) (e) (f) Size distribution including inclusions with $d_{\text{max}} > 2 \mu\text{m}$ .....	150
Figure 6.8 The evolution of liquid $\text{CA}_x$ type inclusion particle size distribution in Heat 2 including inclusions with $d_{\text{max}} > 2 \mu\text{m}$ (a) ladle samples (b) tundish samples.....	151

Figure 6.9 The evolution of liquid CA <sub>x</sub> type inclusion particle size distribution in (a) Heat 3, (b) Heat 4 and (c) Heat 5 including inclusions with d <sub>max</sub> > 2 μm.....	152
<b>Chapter 7 Concluding Remarks.....</b>	<b>154</b>
<b>Reference .....</b>	<b>158</b>

## List of Tables

<b>Chapter 1</b>	<b>Introduction .....</b>	<b>1</b>
<b>Chapter 2</b>	<b>Literature Review .....</b>	<b>4</b>
<b>Chapter 3</b>	<b>Experimental Study of Inclusion Modification by Ca in AHSS .....</b>	<b>40</b>
	Table 3.1 The composition of experimental steels after Ca addition .....	47
	Table 3.2 Detailed sampling time of both industrial heats.....	62
<b>Chapter 4</b>	<b>Evaluation of Ca Treatment on Oxide and Sulfide Inclusions through Modification Indexes.....</b>	<b>70</b>
	Table 4.1 The composition ranges of industrial heats in Series 1, 2, and 3 .....	75
	Table 4.2 Physical properties used for calculation of concentration change due to segregation .....	90
<b>Chapter 5</b>	<b>Coarsening Mechanisms of CaS Inclusions in Ca-treated Steels 100100</b>	
	Table 5.1 Chemical composition of experimental and industrial samples (wt. pct.) ....	106
	Table 5.2 The comparison of calculated coarsening rate ( $m^3/s$ ) of different $CA_x$ and CaS to determine the rate-controlling component, namely, Ca, Al, O, and S.....	109
<b>Chapter 6</b>	<b>Coarsening Mechanisms of Calcium Aluminates in Ca-treated Steels .....</b>	<b>137</b>
	Table 6.1 Chemical composition of laboratory and industrial tundish samples (wt pct) .....	139
<b>Chapter 7</b>	<b>Concluding Remarks.....</b>	<b>154</b>
<b>Reference</b>	<b>.....</b>	<b>158</b>

## List of Abbreviations and Symbols

$A$	Surface area of steel in contact with Ar gas in a crucible ( $m^2$ )
AF	Area fraction (ppm)
$AF_i$	AF of $i$ phase in an inclusion (ppm)
$A_{inclusion}$	Area of inclusions analyzed by ASPEX ( $m^2$ )
$A_{steel}$	Area of steel analyzed by ASPEX ( $m^2$ )
$C_e$	Equilibrium concentration ( $kg/m^3$ )
$C_i$	Interfacial concentration ( $kg/m^3$ )
$C^{(i)}$	Concentration of component $i$ in inclusion ( $kg/m^3$ )
$C_{[i]}$	Average concentration of component $i$ in steel ( $kg/m^3$ )
$C_{[i],0}$	Initial average concentration of component $i$ in steel ( $kg/m^3$ )
$C_{[i],b}$	Concentration of component $i$ in bulk steel ( $kg/m^3$ )
$C_{[i],eq}$	Equilibrium concentration of component $i$ ( $kg/m^3$ )
$C_{[j],i}$	Concentration of component $j$ at steel-inclusion interface ( $kg/m^3$ )
CTI	Calcium treatment index
$D_i$	Diffusion coefficient of component $i$ ( $m^2/s$ )
$Dim. Ca_{1833K}$	Dimensionless Ca at 1833K
$\Delta G$	Molar Gibbs free energy of formation (J/mol)
$\Delta G^\circ$	Standard molar Gibbs free energy of formation (J/mol)
$K_{eq}$	Equilibrium constant
$K_{sp,\gamma}$	Solubility product constant in $\gamma$ -Fe
$K_{sp,\delta}$	Solubility product constant in $\delta$ -Fe
$Me$	Generalized metallic elements
$MV_i$	Molar volume of component $i$ ( $cm^3/mol$ )
$N_A$	Planar number density of inclusion ( $mm^{-2}$ )
$N_{V,i}$	Volumetric number density of inclusion with size $i$ ( $mm^{-2}$ )
$R$	Gas constant ( $J \cdot K^{-1} \cdot mol^{-1}$ )
$Sh$	Sherwood number
SPC	Sulfur partition coefficient
$T$	Temperature (K)
$T_{Ar4}$	$\delta$ -Fe to $\gamma$ -Fe transformation temperature (K)
$T_{liq}$	Liquidus temperature (K)
$T_{sol}$	Solidus temperature (K)
T. $AF_i$	Sum of AF of $i$ phase in all inclusions (ppm)
T. $AF_i(j)$	Sum of AF of $i$ phase in all type $j$ inclusions (ppm)
T. $i$	Total content of component $i$ (ppm)
$(T. Ca)_{measured}$	Measured T.Ca content (ppm)

$(T.Ca)_{CA_2 sat.}$	The T.Ca content for $CA_2$ formation (ppm)
$(T.Ca)_{CaS sat.}$	The T.Ca content for CaS formation (ppm)
$V$	Volume of steel in a crucible ( $m^3$ )
$X_{[i],b}$	Molar concentration of component $i$ in the bulk of steel ( $kg/m^3$ )
$X_{[j],i}$	Molar concentration of component $j$ at steel-inclusion interface ( $kg/m^3$ )
$a_i$	Activity of component $i$
$a, b, c$	Weighing coefficients when calculating the values of $d$
$d$	Deviation of measured T.Ca from optimum T.Ca
$d$	Diameter of inclusion ( $\mu m$ )
$d_{avg}$	Average diameter of multiple inclusions ( $\mu m$ )
$d_i$	Diameter of inclusion with size $i$ ( $\mu m$ )
$d_{max}$	Maximum diameter of an inclusion ( $\mu m$ )
$d_{min}$	Minimum diameter of an inclusion ( $\mu m$ )
$e_j^i$	Interaction coefficients, the effect of component $i$ on $j$
$f$	Volume fraction of inclusions
$f_0$	Initial volume fraction of inclusions
$f_i$	Henrian activity coefficient of component $i$
$f_s$	Solid fraction (pct)
$g$	Acceleration of gravity ( $m/s^2$ )
$h_i$	Henrian activity of component $i$
$(i)$	Concentration of component $i$ in inclusion (wt pct)
$[i]$	Concentration of component $i$ in steel (wt pct)
$k_B$	Boltzmann constant ( $m^2 \cdot kg/s^2 K$ )
$k_i^j$	Equilibrium partition coefficient of component $i$ between liquid steel and solid steel phase $j$
$k_{m,i}$	Mass transfer coefficient of component $i$ in steel (m/s)
$m_i$	Effects of component $i$ on $T_{liq}$ (K/wt pct)
$n_i$	Quantity of component $i$ (mol)
$n_i$	Effects of component $i$ on $T_{Ar4}$ (K/wt pct)
$r$	Inclusion radius ( $\mu m$ )
$r_0$	Initial inclusion radius ( $\mu m$ )
$r_i$	Radius of inclusion with size $i$ ( $\mu m$ )
$t$	Time (sec)
$t_f$	Solidification time (sec)
$u$	Velocity (m/s)
$\frac{du}{dy}$	Velocity gradient in the laminar shear zone (1/s)
$w_{[j],i}$	Weight fraction of component $j$ at steel-inclusion interface (wt pct)

$x_i$	Molar fraction of component $i$ (pct)
$\alpha$	Turbulent coagulation coefficient
$\beta^B$	Collision frequency functions of Brownian collisions ( $m^3/s$ )
$\beta_{ij}^C$	Sum of collision frequency functions ( $m^3/s$ )
$\beta^G$	Collision frequency functions of gradient collisions in the laminar shear zone ( $m^3/s$ )
$\beta^S$	Collision frequency functions of Stokes collisions ( $m^3/s$ )
$\beta^T$	Collision frequency functions of turbulent collisions ( $m^3/s$ )
$\beta_i$	Back diffusion parameter
$\gamma$	Liquid-solid interfacial tension (mN/m)
$\gamma_i$	Liquid-solid interfacial tension of component $i$ (mN/m)
$\varepsilon$	Turbulence energy dissipation rate ( $m^2/s^3$ )
$\theta$	Liquid-solid phase contact angle ( $^\circ$ )
$\theta_S$	Sulfur surface coverage (pct)
$\theta_O$	Oxygen surface coverage (pct)
$\lambda_{SDAS}$	Secondary dendrite arm spacing ( $\mu m$ )
$\mu$	Dynamic viscosity ( $kg/m \cdot s$ )
$\rho_{steel}$	Steel density ( $kg/m^3$ )
$\rho_P$	Inclusion density ( $kg/m^3$ )
$\sigma_{LV}$	Liquid-surface tension (mN/m)
$\sigma_{SV}$	Solid surface tension (mN/m)

## **Declaration of Academic Achievement**

The enclosed work is an effort to better understand the specific requirements to modify inclusions to desired extents by calcium treatment. Discrepancies exist in the literature regarding the modification mechanism of  $\text{Al}_2\text{O}_3$  inclusions, especially on the role of CaO in the process and their formation conditions. The present study clarifies the discrepancies. With respect to the correlations between steel chemistries and the amount of CaS and MnS inclusions in industrial conditions, the discussions in previous studies were limited. Determining Based on these findings, a method to quantitatively estimate the level of success in inclusions control and determine the optimum Ca content was established. These findings will serve as helpful guidelines for making adjustments to improve the effectiveness of the calcium treatment process. The present study also investigated the coarsening mechanism of CaS and calcium aluminate inclusions. The evolution of CaS inclusion size was never systematically discussed in previous studies; hence, this work presents important new additions to the field in terms of collected data and coarsening mechanisms. The present work should support future research and implementation of process improvements to produce advanced high strength steel.

## Chapter 1 Introduction

### 1.1 Research Background

Primary steelmaking processes introduce a significant amount of oxygen into liquid steel. <sup>[1]</sup> Due to the high affinity of many metallic elements to oxygen, micro-particle formation is inevitable. These particles are named inclusions. Most of the inclusions are solid because their melting points are higher than the typical steelmaking temperatures. The micrometer-sized inclusions negatively affect steel production and quality; hence, they are said to make the steel “dirty” if not adequately controlled. Steel is “cleaned” in the secondary refinement processes usually by two approaches: modification of the composition and/or morphology of the inclusions or removal of inclusions to the slag phase. The remaining inclusions within the steel strongly influence the properties of the finished product, such as strength, formability, corrosion resistance, and surface quality.

Calcium treatment by powder injection or wire feeding is a common approach used in steel refining to modify the composition of solid oxide inclusions and control the shape of sulfide inclusions. <sup>[2]</sup> A typical example is the modification of alumina ( $Al_2O_3$ ) inclusions into liquid or partially liquid calcium aluminates ( $CA_x$ ) inclusions, which are less likely to attach to the refractory lining when molten steel passes through a submerged entry nozzle (SEN) during continuous casting. <sup>[3]</sup> In addition, modified inclusions are spherical, which helps avoid anisotropic steel properties if the shape is maintained after fabricating. Meanwhile, calcium also reacts with dissolved sulfur and forms CaS inclusions.

Previous studies <sup>[4–12]</sup> focused on determining the sequence of reactions between inclusions and calcium, minimizing the mass of calcium addition while promoting the formation of calcium aluminate inclusions and controlling the formation of CaS inclusions. However, the preferential order of reactions is still unclear, let alone how the current practice can be improved. Some researchers <sup>[5,13–15]</sup> also focused on the kinetics of transformation between inclusion phases. Several studies <sup>[10,11,16–21]</sup> focused mainly on correlating steel compositions with the inclusions’ compositions and proposed modification indexes to predict inclusion modification. The quantities of inclusions were usually not discussed. In addition, to the best of the author’s knowledge, no study has been able to incorporate multiple modification indexes to give a comprehensive and quantitative evaluation of the modification results. Apart from composition and quantity, the size of inclusions also influences the quality of steel products. No study exists on the growth and coarsening of CaS inclusions in the literature. Some studies <sup>[22–24]</sup> on the coarsening behavior of  $CA_x$  inclusions were conducted, but none included any industrial data in the analysis. The objective of this study is to fill the gap in these areas of knowledge.

## 1.2 Research Objectives

The objective of this study is to develop an understanding of the formation and evolution of inclusions in calcium-treated liquid steel. It involves the following three sub-objectives:

1. Obtain experimental data for inclusion characteristics, including, size distribution, number, and composition of inclusions as a function of calcium addition and sulfur content of liquid steel, and propose modification mechanisms of  $\text{Al}_2\text{O}_3$  inclusions by calcium treatment.
2. Propose modification indexes for  $\text{CA}_x$ ,  $\text{CaS}$ , and  $\text{MnS}$  inclusion control under industrial conditions and develop a method of incorporating the modification indexes to study the overall effectiveness of Ca treatment.
3. Investigate the evolution of  $\text{CaS}$  and  $\text{CA}_x$  inclusions size distribution by Ca treatment and propose growth mechanisms of inclusions.

## 1.3 Thesis Outline

The research background, the motivation of the study, and the thesis outline are introduced in Chapter 1. Chapter 2 reviews the effect of calcium treatment on inclusion composition, population, and morphology reported in the literature and the information related to inclusion analysis techniques.

Chapter 3, entitled “Experimental study of inclusion modification by Ca in AHSS,” provides the experimental data on inclusion evolution in three calcium levels and two sulfur levels. The two modification mechanisms by Ca treatment are proposed. By comparing the fraction of liquid inclusions with the thermodynamics calculation of inclusion stability, the conditions for preventing excessive  $\text{CaS}$  inclusion formation in experiments are clarified in this chapter. This chapter is published in the *Metallurgical and Materials Transactions B* (DOI: 10.1007/s11663-021-02243-1).

Chapter 4, “Evaluation of calcium treatment on oxide and sulfide inclusions through modification indexes,” reports the inclusion types in tundish of thirty-seven industrial heats separated into three series of distinct C and Mn contents of liquid steel. This chapter introduces three modification indexes using the steel chemistries to define the level of success in  $\text{CA}_x$ ,  $\text{CaS}$ , and  $\text{MnS}$  inclusions control. The modification indexes for  $\text{CA}_x$  and  $\text{CaS}$  inclusions are universally applicable in all three series. The index on  $\text{MnS}$  inclusion control is applicable in predicting the modification results in 0.06C-0.5Mn (Series 1) and 0.18C-0.9Mn (Series 2) containing heats. The discrepancy in 0.06C-1Mn (Series 3) containing heats is explained with different  $\text{MnS}$  formation mechanisms using a segregation model. The overall modification results are quantified based on the deviation

from the ideal Ca content. This chapter is published in Metallurgical and Materials Transactions B (DOI: 10.1007/s11663-022-02573-8).

Chapter 5 discusses the coarsening of CaS inclusions under experimental and industrial conditions. The coarsening mechanisms of CaS inclusions are determined by comparing the observed and the theoretical coarsening rates calculated for various coarsening mechanisms depending on the availability of data on small-sized inclusions. This chapter is published in Metals (DOI: 10.3390/met12050707). Chapter 6 applies the similar analysis techniques used in Chapter 5 to study the coarsening of  $CA_x$  inclusions under experimental and industrial conditions.

Chapter 7 concludes this project by highlighting the key findings of each chapter and suggests potential future works that can be done based on the findings established so far.

## Chapter 2 Literature Review

### 2.1 Secondary Steelmaking

Basic oxygen furnaces (BOF) and electric arc furnaces (EAF) and their derivations are the most common methods of producing liquid steel. The schematic diagram of the flow of the BOF and EAF steelmaking process is illustrated in Figure 2.1. [25] The BOF and EAF are referred to as the primary steelmaking process, which are the first steps of converting the source material to liquid steel. The primary purpose of BOF and EAF is to remove carbon by reacting with the oxygen injected. [1] This inevitably increases the oxygen content in liquid steel.

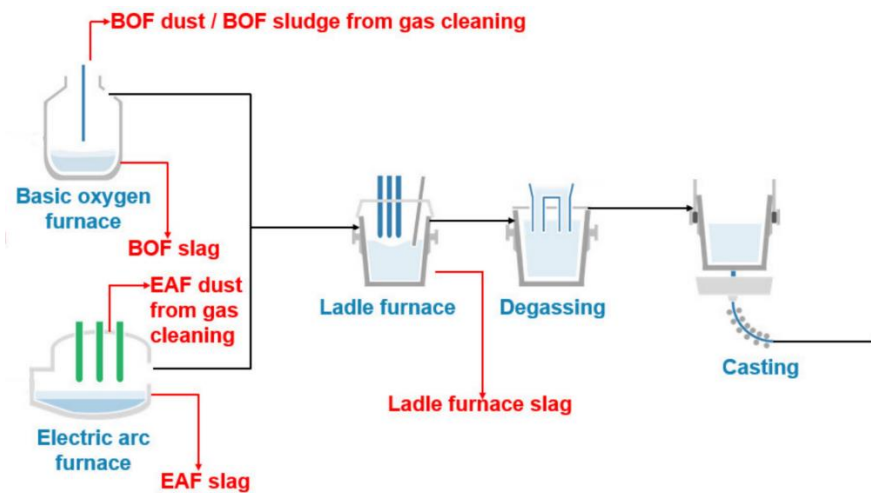


Figure 2.1 Schematic diagram of the general steelmaking flow [25] (Reprinted with permission)

The term “secondary steelmaking” refers to the refining processes between the primary steelmaking and the casting processes shown in Figure 2.1. One of its purposes is to further adjust the compositions of steel after the primary steelmaking processes to meet its specifications. In addition, secondary steelmaking objectives include homogenizing steel composition, improving steel cleanliness, and adjusting the temperature. [26] The secondary steelmaking metallurgy usually involves deoxidizing, desulphurizing, degassing, and inclusion removal. They are achieved by combinations of slag refining, vacuuming, stirring, heating, etc. [27] Many of these aforementioned processes can be carried out in a ladle furnace shown in Figure 2.1; hence, the term “secondary steelmaking” and “ladle metallurgy” are sometimes used interchangeably. The degassing process in Figure 2.1 is sometimes used with a ladle mainly to enhance the removal of gaseous elements such as hydrogen and nitrogen using a vacuum chamber. In this study, the non-metallic inclusions related to the deoxidation and techniques of preventing the

inclusions from causing problems during production and in final products are of particular interest.

### 2.1.1 Deoxidation

Steel deoxidation refers to reducing the oxygen content of liquid steel and is a necessary step in steel production. During primary steelmaking, oxygen reacts with liquid iron and the impurities such as carbon, manganese, and silicon. At the end of this process, the melt contains excessive oxygen content, which can be high as 800 ppm. <sup>[28]</sup> Oxygen can form an oxide with many alloying elements added during the secondary steelmaking process. This decreases the efficiency of alloying, and the oxides formed degrade the steel properties. <sup>[28]</sup> In addition to that, gas bubbles can be trapped in the steel and cause the formation of cracks in the final products. <sup>[29]</sup>

The deoxidation practice is performed by the addition of deoxidant, which reacts with dissolved oxygen in liquid steel. The general representation of such a reaction is provided in Equation (2.1). <sup>[28,30]</sup>  $Me$  and  $[O]$  denote the deoxidant and dissolved oxygen, respectively.  $MeO_x$  is the deoxidation product, also known as the non-metallic inclusions. The potential deoxidants have different deoxidation strengths, which can be shown graphically with the Ellingham diagram in Figure 2.2. <sup>[31]</sup> The lower the deoxidant in Figure 2.2, the stronger the strength. The typical deoxidants include Mn, Si, and Al, <sup>[30]</sup> listed in the order of increasing strength. Mn and Si can decrease the dissolved oxygen content to approximately 50 ppm  $[O]$ . <sup>[3]</sup> Alternatively, Al and Mg can reduce dissolved oxygen concentration to low as 2 ppm. <sup>[3]</sup> Less common deoxidizers like Ca and Ti are also used for particular purposes. <sup>[32,33]</sup> Ca gives the lowest oxygen level among all elements listed in Figure 2.2, but it is rarely used for that purpose because of its volatile nature and cost. <sup>[7]</sup>



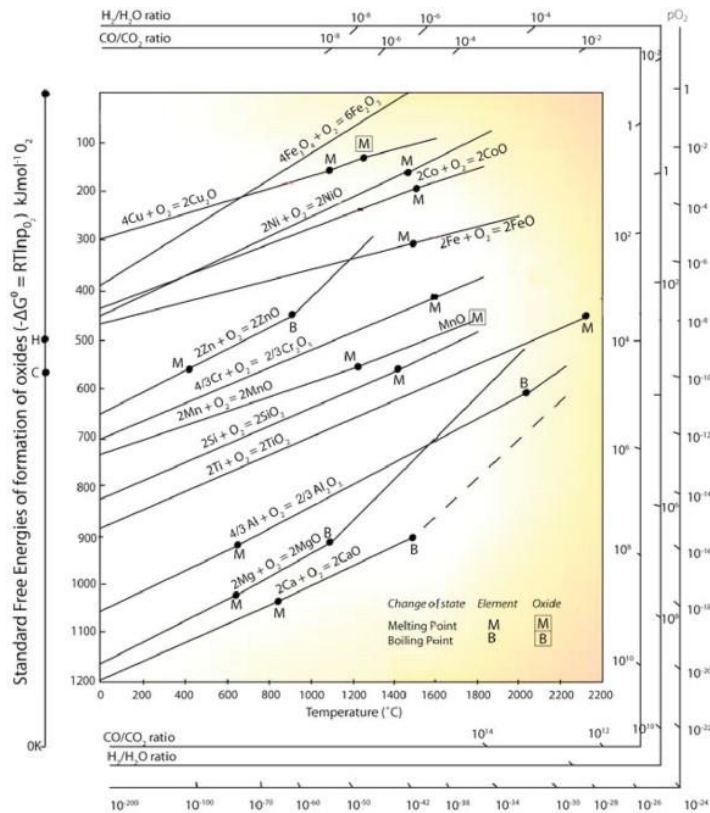


Figure 2.2 Ellingham diagram <sup>[31]</sup> (Reprinted with permission)

### 2.1.2 Desulfurization

Just like oxygen, excessive sulfur is also detrimental to steel. Therefore, reducing the sulfur content (desulfurization) is necessary for many steel grades. Sulfur in steel comes from various sources, including impurities in liquid iron, scrap, and slag materials. Without proper desulfurization, sulfides, including FeS and MnS, may form during solidification, which is known for inducing cracks. <sup>[28]</sup> In the continuous production of steel grades other than the free-cutting steel, the sulfur content can be high as approximately 200 ppm without special treatment. <sup>[34]</sup> The S content should be low as 10 ppm in special plates requiring ultra-low sulfur content, such as line pipes. <sup>[34]</sup> The purpose is to achieve high resistance to hydrogen-induced cracking (HIC). The details about relationships between the properties of steel and the inclusions are discussed in a later section.

During secondary steelmaking processes, desulfurization is mainly achieved through a slag-steel reaction. <sup>[1]</sup> Based on the ionic theory of slags, sulfur in slag presents mainly as S<sup>2-</sup> or SO<sub>4</sub><sup>2-</sup> depending on the partial pressure of oxygen. When the partial pressure of oxygen is lower than 1e-6 atm, which can be achieved even with Mn and Si deoxidation according to Figure 2.2, S<sup>2-</sup> is the dominant form. <sup>[35]</sup> Therefore, in Al deoxidized steel, the current project is interested in, desulfurization being achieved through Reaction (2.2).

The round and square brackets denote species in slag and steel, respectively.



Therefore, the final [S] largely depends on slag composition. CaO in slag (source of  $(\text{O}^{2-})$  in Reaction (2.2)) can react with [S] to form CaS and [O], so basic slags usually result in lowering [S].<sup>[36]</sup> Other than increasing  $(\text{O}^{2-})$ , Reaction (2.2) also suggests the desulfurization can be enhanced when [O] is decreased. Therefore, it is a conventional understanding that low FeO contents in the slag are critical for desulfurization.<sup>[26,28,34,37]</sup> Due to the same reason, the deoxidation of steel also contributes to the desulfurization process.<sup>[34]</sup> The partition of sulfur between slag and steel increases as the FeO content decreases from 1 wt pct.<sup>[26]</sup> In addition, because Reaction (2.2) is an endothermic reaction,<sup>[34]</sup> increasing the temperature pushes Reaction (2.2) towards the products' side, which leads to deeper desulfurization. Desulfurization can also be achieved with gas stirring, and injection of desulfurization agents such as CaSi or rare earth elements,<sup>[34]</sup> but they will not be discussed in further detail here as desulfurization is not the focus of this study.

## 2.2 Inclusion Control during the Refining Process

Many of the non-metallic inclusions are the reaction products of deoxidation and desulfurization. After the initial stage of nucleation, precipitation, and growth, inclusions may react with alloying elements; hence, leading to the formation of new compounds. The inclusions also coagulate and agglomerate, which leads to their sizes increasing with time. These large size inclusions cause problems if not controlled or removed. In the case of  $\text{Al}_2\text{O}_3$  inclusions, this project is interested in; they were found to have a strong tendency to agglomerate with each other, as well as deposit and accumulate on refractory walls due to their low wettability to typical steelmaking slag.<sup>[38-40]</sup> There are generally two methods to prevent damages from inclusions: removal and modification.

### 2.2.1 Inclusion Removal

This project focus on the second method, but general knowledge about the removal process is provided in this section. The removal of inclusions generally involves two steps: floatation and separation.

Many of the inclusions are removed from steel to the slag-steel interface and absorbed by slag with the help of gentle stirring close to the end of the ladle metallurgy process. Other than floatation by buoyancy, Ar bubbles can also carry inclusions to the slag/steel interface.<sup>[41]</sup> Bubble-aided floatation involves four steps.<sup>[41]</sup> The first step is that an inclusion approaches a bubble either by random movement, shear flow collision, or their

buoyancy force. <sup>[42]</sup> Upon contact, a liquid film forms between the bubble and inclusion. Inclusions may oscillate or slide on the bubble surface. When inclusion is in contact with a bubble, the liquid film drains and forms three-phase contact. After a short time, the system is stabilized, and the bubble can carry the inclusion up to the steel-slag interface. <sup>[41]</sup> Inclusion removal by floatation is affected by many factors such as conditions of the flow, inclusions and steel densities, inclusion size, slag, and steel surface, interfacial tensions, etc. <sup>[41]</sup> This is a brief description of the overall phenomena, and the process was modeled in several studies, <sup>[42-44]</sup> but is not the focus of the present one. The floated inclusions can also be trapped on refractory walls, but this only accounts for a small fraction of the removal compared to the inclusion removed due to their buoyancy and bubble-inclusion buoyancy collision. <sup>[42]</sup> Also, there are studies on using ceramic filters to remove inclusion. <sup>[45,46]</sup> This is a very special treatment, and will not be discussed here.

It was suggested that the floatation does not necessarily guarantee the permanent removal of inclusions, as they might return to steel if the slag phase doesn't have good wettability on the inclusions. <sup>[47-49]</sup> To the best of the authors' knowledge, there have been limited studies on the wettability of inclusions formed during Ca treatment, but studies on Al<sub>2</sub>O<sub>3</sub> inclusions have been conducted. Choi and Lee <sup>[50]</sup> studied the wettability of CaO-Al<sub>2</sub>O<sub>3</sub>-SiO<sub>2</sub> slag droplets on the Al<sub>2</sub>O<sub>3</sub> substrate using a sessile drop technique at 1873 K by recording the change of contact angle in 30 seconds. The authors proposed a contact angle model. However, Abdeyazdan et al. <sup>[51,52]</sup> raised a concern that experimental data might be over-fitted. Choi and Lee <sup>[50]</sup> did not comment on the two variables used in their model. Whether they have physical meanings or just fitting parameters, was not explained. In the study by Abdeyazdan et al., <sup>[51]</sup> the interaction between MgAl<sub>2</sub>O<sub>4</sub> spinel and CaO-Al<sub>2</sub>O<sub>3</sub>-SiO<sub>2</sub>-MgO slag was studied. They found changing spinel substrate porosity from 1.9 pct to 6.7 pct increased slag penetration depth. This suggests that porous inclusions have higher removability because of the stronger slag-inclusion bond associated with a higher contact angle. The same research group in recent years studied a more extensive range of slag compositions and substrates. In addition to the three ladle type slags on spinel, Monaghan et al. <sup>[52]</sup> investigated three more tundish type slags (lower basicities) and two other substrates, Al<sub>2</sub>O<sub>3</sub>, and CA. They found that the same type of inclusion will be more strongly bonded to a ladle slag than to a tundish slag. Within the same slag type, the work of adhesion was similar for all inclusion types, but contact angle was the highest for Al<sub>2</sub>O<sub>3</sub> and lowest for CA. Abdeyazdan et al. <sup>[53]</sup> correlated wettability with different slag structures to explain this phenomenon. From the viscosity perspective, with less SiO<sub>4</sub><sup>4-</sup> former SiO<sub>2</sub> and more chain breaker CaO available in more basic slags, slag viscosity generally decreases, which means less retarding force for wetting. Therefore, the contact angle is likely going to decrease, as well. From the surface tension perspective, with SiO<sub>2</sub> being surface-active to the CaO-Al<sub>2</sub>O<sub>3</sub> system, basic slag will exhibit higher surface tension,  $\sigma_{SV}$ . Then according to Young's equation in Equation (2.3), the interfacial tension,  $\gamma$ , must decrease to satisfy the higher  $\sigma_{LV}$  and  $\cos \theta$  associated with basic slags for any constant  $\sigma_{SV}$  (same

substrate). This proposed mechanism was summarized by showing  $\sigma_{LS}$  decreases linearly as optical basicity,  $\Lambda$ , increases (acidic to basic transformation).

$$\cos \theta = \frac{\sigma_{SV} - \gamma}{\sigma_{LV}} \quad (2.3)$$

The inclusions with low wettability are not impossible to remove from the liquid steel if they are dissolved in the slag within a rather limited contact time. The dissolution of common oxide inclusions such as  $\text{Al}_2\text{O}_3$  [54–58] and  $\text{CaO}$  [59–62] inclusions has been studied extensively in the literature through laboratory experiments. However, there are only two studies focused on  $\text{CA}_x$  particles to the best of the author’s knowledge. Coletti et al. [63] reported that the  $30\text{CaO}-70\text{Al}_2\text{O}_3$  inclusions did not dissolve in a  $46.5\text{Al}_2\text{O}_3-0.1\text{SiO}_2-53.3\text{CaO}$  slag. The compositions of inclusions and slag are both in wt pct. The authors suggested that a solid reaction layer at the inclusion/slag interface prevented the direct dissolution of inclusions, but they did not provide further support for such an explanation. However, the dissolution of  $\text{CA}_2$  particles was observed in the work of Miao et al. [64] This work confirmed that  $\text{CA}_2$  inclusions with approximately 100  $\mu\text{m}$  require approximately 2 minutes to dissolve in  $31\text{CaO}-23\text{Al}_2\text{O}_3-46\text{SiO}_2$  and  $56\text{CaO}-39\text{Al}_2\text{O}_3-5\text{SiO}_2$  slag at 1823K and 1873K. The dissolution was found to be controlled by the mass transfer in slag and the dissolution kinetics was affected by slag viscosity and concentration difference at the slag/inclusion interface as the driving force. Considering  $\text{CA}_x$  inclusions larger than 100  $\mu\text{m}$  are rare in industrial conditions,  $\text{CA}_x$  inclusions are likely to be successfully dissolved after reaching the slag/steel interface. Unfortunately, there has been no study on the dissolution of  $\text{CaS}$  inclusions in similar conditions, so the criteria for the successful removal of  $\text{CaS}$  inclusions remain unclear.

### 2.2.2 Calcium Addition Method

The remaining inclusions in liquid steel can be controlled with the second method, by modifying them from solid to liquid or semi-liquid calcium aluminates by calcium (Ca) treatment [34]. Ca is very commonly used to modify  $\text{Al}_2\text{O}_3$  inclusions in the present steelmaking practice. It has a boiling point of approximately 1763 K, [1] so it immediately evaporates once it is introduced into the liquid steel. This results in a generally very low yield, which varies from 5 pct to 35 pct between facilities, but usually is around 12 pct. [7,65–67] Various methods of introducing Ca were developed in the past, [68] but nowadays it is mainly added in the form of powder or wire.

Thyssen-Niederrhein company developed a secondary steelmaking process for desulfurization and inclusion shape control. This process is known as the TN method. It is a typical powder injection method. A schematic diagram is shown in Figure 2.3. [69] The system places a lance to the bottom of the ladle and injects Ar gas which carries metallic powder needed for the refining. [69] Adding Ca to the bottom of the ladle has two

characteristics: longer Ca bubble travel and larger ferrostatic pressure. A longer traveling distance for the Ca bubbles to reach the surface naturally gives Ca a longer time to dissolve in steel. Larger ferrostatic pressure prevents Ca from boiling as the critical vaporization pressure is positively related to the ferrostatic pressure. <sup>[65,68]</sup> Also, larger pressure exerted on the Ca gas bubble increases the solubility of Ca; hence, increases the dissolution kinetics of calcium. Both phenomena increase the yield of Ca. The yield can be further increased by using Ca alloy instead of pure Ca. The activity of Ca is reduced when in the form of alloy, so the vaporization of Ca, expressed in Reaction (2.4), can be suppressed because Ca pressure decreases.



Other powder injection methods were also invented, such as the Capped Argon Bubbling (CAB) and the SL system by Scandinavian Lancer, <sup>[26,68]</sup> but they all share the same working principle and have similar positive effects on Ca yield.

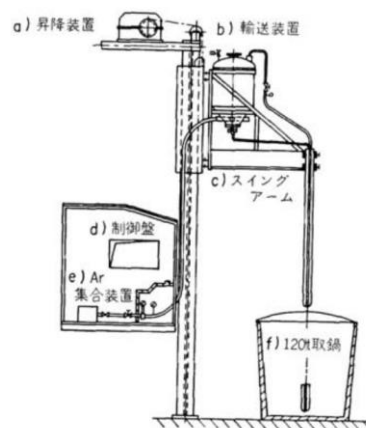


Figure 2.3 Schematic diagram of the Thyssen-Niederrhein (TN) powder injection method (a) lifter (b) pressure vessel (for powder delivery) (c) swingarm (d) control panel (e) Ar panel (f) 120 t ladle <sup>[69]</sup> (Reprinted with permission)

The Ca wire feeding introduces Ca into the steel in the form of wire. A schematic diagram of the process is shown in Figure 2.4. Injecting wire deep into the ladle using a ceramic tube has similar advantages to the powder injection method. The yield can be further increased by using cored or alloyed Ca wire. The advantage of cored wire is that Ca starts to dissolve after leaving the lance outlet. The dissolution of Ca therefore is not affected by the purging gas and is simultaneously injected through the lance. Apart from Ca, the wire feeding technique has also been used for the addition of other alloying and refining elements. <sup>[26]</sup>

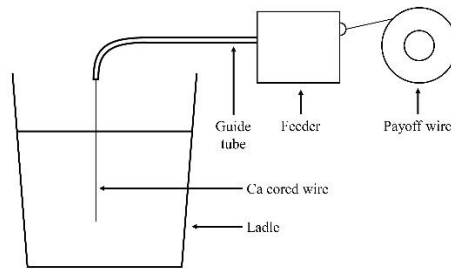


Figure 2.4 Schematic diagram of the cored wire injection method

### 2.2.3 Modification of Oxide Inclusions by Ca Treatment

Calcium reacts with  $\text{Al}_2\text{O}_3$  inclusions to form calcium aluminates,  $\text{CA}_x$  inclusions, where C and A denote CaO and  $\text{Al}_2\text{O}_3$ , respectively. There are five thermodynamically stable stoichiometric combinations of calcium aluminates:  $\text{CA}_6$ ,  $\text{CA}_2$ , CA,  $\text{C}_{12}\text{A}_7$ , and  $\text{C}_3\text{A}$ , as shown in Figure 2.5. The melting points of  $\text{C}_3\text{A}$ ,  $\text{C}_{12}\text{A}_7$ , and CA phases are below or close to the typical steelmaking temperatures; hence are more likely to be fully liquid or semi-liquid. <sup>[2]</sup>  $\text{CA}_2$  and  $\text{CA}_6$  phases remain solid phases, and they are reported as detrimental since they cause nozzle clogging. <sup>[66,70]</sup> It can be difficult to modify every  $\text{Al}_2\text{O}_3$  inclusion to fully liquid  $\text{CA}_x$  inclusions due to several reasons such as short reaction time, slow Ca mass transfer in the melt or inclusions, or Ca loss due to evaporation, reactions with refractories, and entrapped slag. <sup>[13]</sup> Fortunately, from the production perspective, the purpose of Ca treatment, which is to improve castability, can be fulfilled without fully modified inclusions. <sup>[68,71]</sup> A liquid surface significantly increase the inclusion wettability to molten steel and reduces the attraction force between inclusions. <sup>[71-73]</sup> As a result, SEN clogging can be avoided considerably. For example, Faulring et al. <sup>[74]</sup> studied the effect of the Ca/Al weight fraction ratio in liquid steel in tundish on the amount of steel passing through the nozzle. They reported that the Ca/Al ratio higher than 0.15 allowed the formation of CA and  $\text{CA}_2$  inclusions and eliminated  $\text{CA}_6$  inclusions. <sup>[74]</sup> This Ca/Al ratio drastically increased the mass of liquid steel that can be cast before nozzle clogging from approximately 20 kg to approximately 150 kg in pilot-scale tests. <sup>[74]</sup>

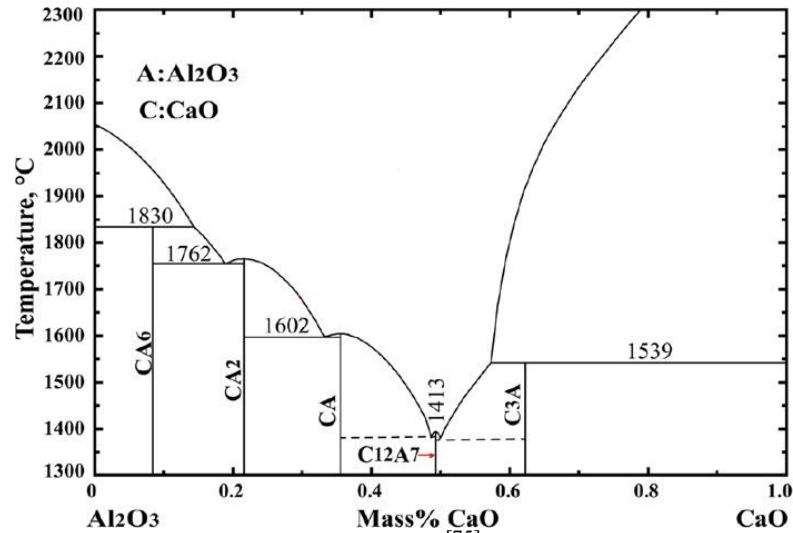
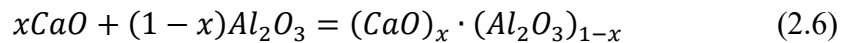
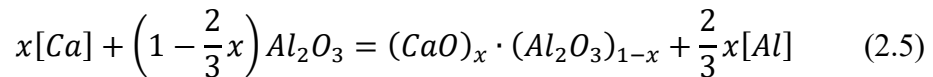


Figure 2.5 CaO-Al<sub>2</sub>O<sub>3</sub> phase diagram <sup>[75]</sup> (Reprinted with permission)

Both Reaction (2.5) and Reaction (2.6) had been proposed to be the modification mechanism of Al<sub>2</sub>O<sub>3</sub> inclusions. <sup>[7,76,77]</sup> Reaction (2.5) describes the scenario of Ca gas dissolving in liquid steel and then modifying Al<sub>2</sub>O<sub>3</sub> inclusions, whereas Reaction (2.6) considers Al<sub>2</sub>O<sub>3</sub> inclusions agglomerate with CaO inclusions. <sup>[8]</sup> Reaction (2.5) has been referenced extensively as part of the modification mechanism or used in specific calculations. <sup>[9,11,15,66,78-82]</sup> Some researchers also included Reaction (2.6) as part of the mechanism when S contents were lower than 7 ppm, <sup>[8,83]</sup> or when the Ca contents were significantly higher than the Al contents. <sup>[10,84]</sup> Square and round brackets refer to contents dissolved in liquid steel and forms of inclusions, respectively.



The relative significance of the two reactions is not discussed in any publications to the best of the author's knowledge. The noticeably less mentioned Reaction (2.6) compared to Reaction (2.5) may be coming from rarely observed CaO inclusions. Only a few researchers attempted to explain the source of CaO in Reaction (2.6). <sup>[20,83]</sup> Verma et al. <sup>[83]</sup> studied the modification of Al<sub>2</sub>O<sub>3</sub> inclusions as a function of S content in the melt (7, 40, 45, and 100 ppm S). This is one of the few publications which showed the preference Reaction (2.6) to Reaction (2.5) as the modification mechanism when the S content is 7 ppm. It was reported that experiments involved little or no direct reaction between [Ca] and Al<sub>2</sub>O<sub>3</sub> inclusions. Instead, Al<sub>2</sub>O<sub>3</sub> inclusions reacted with the intermediate phases: CaO inclusions in low S steel and CaS inclusions in 40-100 ppm S steel. <sup>[83]</sup> Verma et al. <sup>[83]</sup> argued that CaS could only account for a maximum of 9 ppm Ca in the case of a melt containing 7 ppm S. The Ca solubility in steel is low, yet the total Ca (T.Ca) was about

29 ppm at 2 min after Ca addition. The only possible explanation for the 20 ppm Ca content difference ( $29 - 9 = 20$  ppm) is that most Ca reacted with O and formed CaO inclusions, which makes Reaction (2.6) possible.

In the work of Liu et al.,<sup>[8]</sup> agglomeration of CaO and Al<sub>2</sub>O<sub>3</sub> particles was suggested to be one of the mechanisms of CA<sub>x</sub> formation. A similar mechanism was proposed by Gollapalli et al.<sup>[10]</sup> However, unlike Verma et al.,<sup>[83]</sup> neither of these two works provided support for Reaction (2.6) being an essential part of the modification mechanism. Ren et al.<sup>[84]</sup> based on a kinetic model of the ladle suggested the formation of CaO inclusions, as well as its reaction with Al<sub>2</sub>O<sub>3</sub> inclusions to form CA<sub>x</sub> inclusions is possible, but only in the Ca-rich region.

Those who believed Equation (2.5) as the main mechanism of Al<sub>2</sub>O<sub>3</sub> modification often also considered that inclusions have a multilayer structure during Ca treatment created by the reaction products between Ca and Al<sub>2</sub>O<sub>3</sub>.<sup>[9,14,15,82]</sup> The presence of the reaction products within the inclusions was detected in ladle steel samples after Ca additions.<sup>[85]</sup> The formation of multi-layer CA<sub>x</sub> inclusions was attributed to the slow Ca diffusion inside Al<sub>2</sub>O<sub>3</sub> inclusions.<sup>[5,14]</sup> As a result, the outer layers would consist of high Ca content modified CA<sub>x</sub> with low liquidus temperature, whereas inner layers are unmodified Al<sub>2</sub>O<sub>3</sub> or partially modified CA<sub>2</sub> and CA<sub>6</sub>, as shown by the schematic diagram in Figure 2.6. This theory was well accepted in Al<sub>2</sub>O<sub>3</sub> modification-related studies and has also been adapted to explain the modification of spinel inclusions.<sup>[5,85–87]</sup> But this theory was not able to explain the absence of some CA<sub>x</sub> phases in a multilayer inclusion as pointed out by some researchers.<sup>[4,13]</sup>

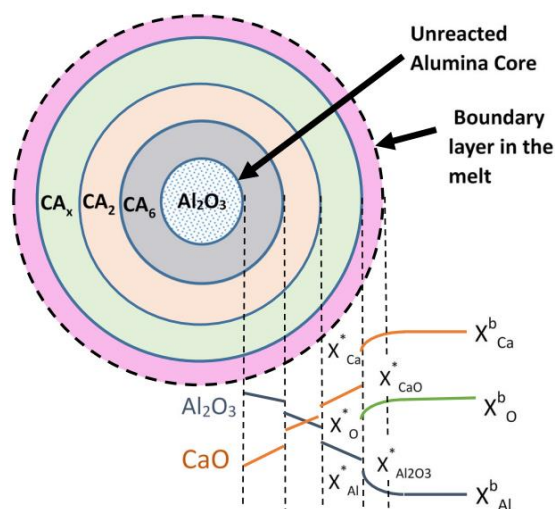


Figure 2.6 Schematic diagram of a layered inclusion<sup>[13]</sup> (Reprinted with permission)

Tabatabaei et al.<sup>[13]</sup> modified the existing diffusion-controlled solid-state reactions of spherical particles in multi-phase binary systems to calculate the required time for Al<sub>2</sub>O<sub>3</sub>

inclusion modification. They found that by decreasing the mass transfer coefficient in liquid steel by one order of magnitude, the modification time increases from 22 sec (calculated using published data) to 160 sec. While changing other parameters such as the diffusion coefficient of Ca in solid by the same order of magnitude only increased the modification time by 1.4 times. <sup>[13]</sup> Therefore, they concluded that the mass transport through the inclusion-steel boundary layer mainly determines the modification rate because the transformation time is the most sensitive to the change in mass transfer rate inside the boundary layer. With solid-state processes faster than mass transfer in the boundary layer, a multi-layer inclusion not necessarily has to consist of every CA<sub>x</sub> phase formed. Such theory helps explain the absence of some CA<sub>x</sub> phases in inclusions seen in modification practice.

In general, it is conventional that increased Ca content in steel will increase the CaO/Al<sub>2</sub>O<sub>3</sub> ratio in CA<sub>x</sub> inclusions; hence, leading to a higher fraction of liquid phase in CA<sub>x</sub> inclusions. <sup>[2,34]</sup> There are two modification mechanisms of Al<sub>2</sub>O<sub>3</sub> inclusions proposed in the literature, and the criteria for Reaction (2.5) or Reaction (2.6) being the more dominant mechanism has not been specified.

#### 2.2.4 Formation of CaS by Ca Treatment

Calcium can also form the sulfide inclusions in liquid steel after Ca injection even if the steel has been desulfurized by slag. <sup>[81]</sup> CaS inclusions were proposed to play a significant role in the modification of Al<sub>2</sub>O<sub>3</sub> inclusions, especially in the melt with high S or Ca content. <sup>[11,66]</sup> Abdelaziz et al. <sup>[66]</sup> studied 17 heats produced by Ezz Flat Steel at 1893 K. Based on the EDS analysis of inclusions at different times, they concluded that CaS and CA<sub>x</sub> inclusions were formed simultaneously. A similar conclusion was reached with laboratory experiments conducted by Xu et al. <sup>[11]</sup> Abdelaziz et al. <sup>[66]</sup> reported that the transformation from Al<sub>2</sub>O<sub>3</sub> inclusions to CA<sub>x</sub> inclusions in a heat containing S content between 10 ppm and 100 ppm follows Reaction (2.7), with CaS being a transient phase.



Abdelaziz et al. <sup>[66]</sup> also suggested that Ca content is a more important factor than S content for CaS concentration in inclusions, and by extension, in CaS inclusion formation. This conclusion was reached through sensitivity analysis. In the case of 0.06 kg/ton steel Ca addition, the CaS concentration in inclusions ranged from 0.77 pct to 4.5 pct when S concentration lies in the range of 17 – 69 ppm. On the other hand, CaS concentration drastically increased from 4.21 pct to 41.02 pct when the amount of Ca added increased from 0.06 kg/ton (Average T.Ca = 23.1 ppm, T.S = 18 ppm in ladle) to 0.095 kg/ton steel (T.Ca = 31.5 ppm, T.S = 24 ppm in ladle).

A similar study but with higher S contents was also performed by Verma et al. <sup>[83]</sup> Steels

containing 40, 45, and 100 ppm S were studied at 1873 K, each with T.Ca of 21 ppm, 20 ppm, and < 20 ppm at 2 min after Ca addition, respectively. Most Ca were found to be in the form of CaS inclusions in 2 min after Ca addition regardless of experimental conditions. CaS concentration reduced afterward and mostly disappeared in 4 min after Ca addition. The Ca/Al weight ratio in the inclusions was increased accordingly. A similar phenomenon was also observed by these authors in the industrial heat, which contained 50 ppm S. Verma et al. [83] hence concluded that CaS inclusions played a crucial role in the higher S content experiments in Ca treatment (Reaction (2.7)). Based on the drastic inclusion evolution trend change from low S to high S steel, Verma et al. proposed that the preferential formation of CaO or CaS inclusions can be related to different nucleation behavior of CaO and CaS determined by S and O surface coverage on the liquid steel-Ca vapor interface. [83] O and S segregation constants in the N<sub>2</sub>-steel reaction were used to calculate O and S surface coverage ratio shown in Figure 2.7.  $\theta_S$  and  $\theta_O$  are surface coverage of S and O, respectively. The transition from O to S being the dominating species occurs at about 7 ppm S, which means CaS will have a higher probability to nucleate than CaO in a melt containing S content more than 7 ppm. The prediction shown in Figure 2.7 was in good agreement with experimental observations. A similar theoretical result was reached by Liu et al. [8] However, they claimed that the S surface coverage calculated based on the inclusion analysis is slightly lower than the predictions based on segregation constants. The difference was explained with the dissociation of CaS inclusions after reacting with O.

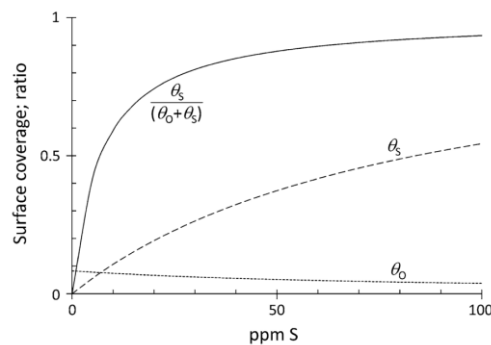
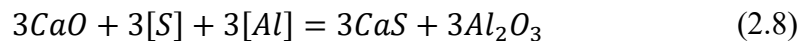


Figure 2.7 Calculated coverage of steel-gas interface by O and S in liquid steel containing 3 ppm [O] and different S levels [83] (Reprinted with permission)

The effect of S content on the modification mechanism of Al<sub>2</sub>O<sub>3</sub> inclusions was experimentally studied by Ren et al. [9] at 1873 K. The S levels were 30 ppm and 310 ppm, whereas the Ca level was 13 ppm at 30 min after Ca addition. Their results and conclusions agreed with the study of Verma et al. [83] They described the evolution trajectory of inclusions in 30 ppm S steel as Al<sub>2</sub>O<sub>3</sub> to Al<sub>2</sub>O<sub>3</sub>-CaS, to Al<sub>2</sub>O<sub>3</sub>-CaS(-CaO), to Al<sub>2</sub>O<sub>3</sub>-CaO(-CaS) to Al<sub>2</sub>O<sub>3</sub>-CaO, [9] the round bracket here denotes relatively minor constituents. On the other hand, the inclusions evolution in 310 ppm S steel will follow Al<sub>2</sub>O<sub>3</sub> to Al<sub>2</sub>O<sub>3</sub>-CaS, to Al<sub>2</sub>O<sub>3</sub>-CaS(-CaO), and finally to Al<sub>2</sub>O<sub>3</sub>-CaO(-CaS). There was always a small amount of CaS presented as part of the inclusions due to the stability of

CaS in high S heats, whereas the formation of CaS in 30 ppm S steel is due to locally high Ca content a short time after Ca dissolution. Hence, the latter will dissociate as the system approaches equilibrium. Similar experimental results were obtained by Lind and Holappa, <sup>[14]</sup> who studied industrial samples taken at Ovako Bar Imatra Steelworks after Ca treatment. The samples contained 300 ppm S and 21 ppm Ca before casting. Inclusions were found to contain 25 pct CaS (instead of 15 pct at 30 min).

In the above studies, CaS inclusions were usually found to co-exist with other inclusions generally in three forms. CaS can either form a ring around other inclusions (Type 1A), evenly distribute inside other inclusions (Type 1B) or attach to another inclusion (Type 2). <sup>[9,66,83,85]</sup> The schematic diagram of each type is shown in Figure 2.8. CaS ring (Type 1A) is probably the most common form reported. <sup>[66,78,88-90]</sup> As Yang et al. <sup>[85]</sup> explained, the formation of Type 1A CaS inclusions follows Reaction (2.8), which is Reaction (2.7) in the opposite direction. CaO in over-modified CA<sub>x</sub> inclusions may react with high [S] and [Al], then reverse back to CaS. A different explanation by Abdelaziz et al. is that CaS rings are products of cooling. <sup>[66]</sup> A liquid CA<sub>x</sub> inclusion is essentially a CaO-Al<sub>2</sub>O<sub>3</sub> slag droplet; then, it must have a corresponding S capacity. If the cooling rate is not fast enough to lock S inside CA<sub>x</sub> inclusions, S may segregate and precipitate a superficial CaS layer by reacting with Ca on the outer surface of CA<sub>x</sub> inclusions. <sup>[66,85]</sup> Another explanation can be that the Al<sub>2</sub>O<sub>3</sub>-steel interface is the preferential CaS nucleation site, as proposed by Verma et al. <sup>[83]</sup> Yang et al. <sup>[85]</sup> suggested Type 1B inclusions, which have CaS uniformly precipitated in CA<sub>x</sub> inclusions during cooling. Kang et al. <sup>[22]</sup> explained that the attached CaS (Type 2) inclusions result from inclusion agglomeration or collision.



In the reviewed literature, S shows the following effects during Ca treatment. 1. CaS usually form in S-containing steel, but depending on steel chemistries, CaS inclusions can be a stable or transient phase. Both types of CaS inclusions can participate in the modification of oxide inclusions and serve as a Ca source. 2. CaS inclusion formation means there exists a competition between O and S to react with Ca. The partition of Ca between CaS and CaO may depend on the surface coverage of O and S on the Ca bubble. 3. Three types of oxide-sulfide morphologies have been observed, and they all have different formation mechanisms.

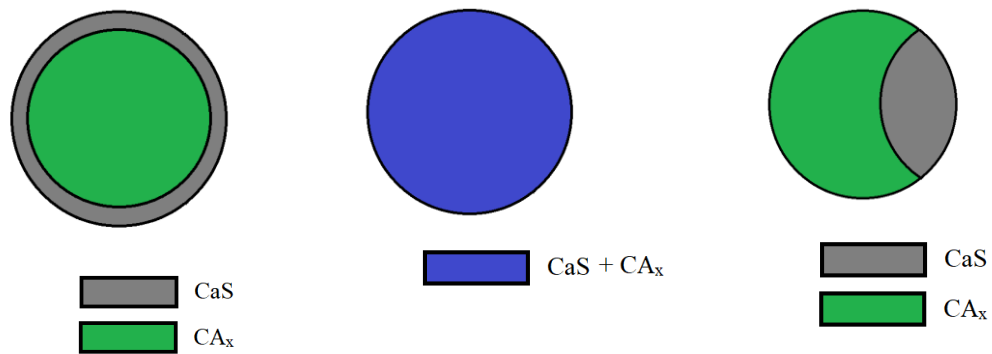


Figure 2.8 Schematic diagrams of the CaS containing complexes inclusion morphology

### 2.2.5 Modification of MnS Inclusions by Ca Treatment

When the dissolved sulfur concentration is high and steel contains Mn, MnS inclusions likely form during solidification. The characteristics of MnS inclusions have been studied for several reasons. <sup>[91-94]</sup> Anisotropic properties of Al-killed steel are usually attributed to MnS inclusions, which may have a non-unity aspect ratio after fabrication or even right after casting if MnS inclusions are segregated at grain boundaries. <sup>[91,92]</sup> The non-spherical MnS inclusions are believed to introduce directionality to the products. Also, it is suggested that MnS inclusions exceeding critical sizes have adverse effects on product qualities. <sup>[93,94]</sup> For example, fatigue crack in rolled carbon steel can be initiated by MnS inclusions with a diameter larger than 1 micrometer. More details about the effect of MnS inclusions on steel properties are included in a later section. Therefore, it is essential to promote the formation of less detrimental sulfides by the addition of elements such as Ti, Ca, Mg, and rare earth elements. <sup>[91]</sup> This section will highlight research related to controlling the morphology and number of MnS inclusions using Ca treatment.

The number of MnS inclusions can be minimized by the formation of CaS inclusions, but as stated previously, CaS inclusions are almost as undesirable as MnS inclusions. Hence, steelmakers always encounter a trade-off between CaS and MnS inclusions. An experimental study by Tomita <sup>[95]</sup> showed that the stringy MnS inclusions were transformed to dominantly CaO-CaS inclusions by introducing about 60 ppm Ca in 0.4C-Cr-Mo-Ni steel containing 20 ppm S. However, they didn't provide any discussion of this finding. Shi et al. <sup>[96]</sup> studied the effects of rare earth elements and Ca addition on inclusion shape control in steel with compositions similar to AISI 1020 grade in industrial-scale operations. The experimental results showed that introducing 57 ppm to 65 ppm Ca into steel with about 77 ppm S did not reach the desired extent of MnS control. A significant number of MnS stringers was observed in a rolled sample. This study also reported that effective inclusion shape control can be achieved with the addition of 0.03

wt. pct rare earth element (element specified), but will not be discussed further here. The results by Tomita <sup>[95]</sup> and Shi et al. <sup>[96]</sup> suggest the effects of Ca on sulfide inclusion control most probably vary with experimental conditions.

The dilemma in sulfide control is sourced from two contradictory targets. <sup>[1,97,98]</sup> On the one hand, adding Ca forms a sufficient amount of CaS inclusions can reduce [S] concentration, then MnS inclusions precipitation during steel solidification is restricted. Alternatively, most MnS are transformed into CaS-MnS complex inclusions so that even the soft MnS part is deformed; the hard CaS inclusions will retain their relatively spherical shape to suppress directionality. On the other hand, the amount of CaS inclusions formed needs to be small so that they do not induce nozzle clogging, the majority of Ca added is consumed in the modification of CA<sub>x</sub> inclusions to reach a high fraction of the liquid phase. The aforementioned sulfide inclusion control targets suggest that the CaS and MnS control are interconnected. CaS and MnS inclusions are commonly encountered during ladle metallurgy and casting, which are not usually discussed at the same time.

Based on published thermodynamics data and equilibrium experiments at 1673 K and 1773 K, Piao et al. <sup>[99]</sup> developed the expression for calculating the excess Gibbs free energy of formation of CaS-MnS complexes. This study allows calculating not only CaS-MnS equilibrium more accurately but also the activities of solution components, which the latter may be particularly crucial for better understanding sulfide inclusion compositions in steel. Piao et al. <sup>[99]</sup> claimed that the proposed model provides more accurate predictions than that suggested by previous studies. Gatellier et al. <sup>[100]</sup> reported the activity coefficients extrapolated from CaS-MnS-FeS ternary system. And regular solution parameters reported by Lu et al. <sup>[101]</sup> did not consider asymmetric characteristics of the CaS-MnS miscibility gap.

The aforementioned activity models had been incorporated into several experimental works. <sup>[78,98]</sup> The finding from Piao et al. <sup>[99]</sup> was supported by Guo et al., <sup>[98]</sup> who found a good agreement between the inclusions types observed in modification experiments and predicted complex compositions after introducing excess Gibbs energy into thermodynamic calculations. Choudhary and Ghosh <sup>[78]</sup> applied the model suggested by Lu et al. <sup>[101]</sup> for their theoretical predictions, which agreed with inclusion types observed in industrial samples from Tata Steel. Both models can be applied to predict the stable inclusion phases relevant to steelmaking conditions.

In the experimental study by Imagumbai and Takeda, <sup>[16]</sup> volume fractions, and to some extent, the size of MnS inclusions in the residual melt was calculated using continuous casting slab chemistries. Based on mass balance and a dendrite model, Imagumbai and Takeda <sup>[16]</sup> established the quantitative correlations between steel composition (Ca, S, O) and the Ca partition between CaS and CaO, as well as the relationship between steel

compositions and S partition between CaS and MnS. Building upon that, the expression of MnS volume fraction was achieved, and the sizes of MnS inclusions were expressed in the form of the mean diameter of the cylindrical dendritic branch. Their predictions were successfully validated with industrial samples containing 19 – 29 ppm sulfur content, 24 – 34 ppm total oxygen content, 0 – 50 ppm Ca, and 0.02 – 0.034 wt pct Al content. In this study, the discussion focused on inclusion composition and size, and morphology related topics were not included. The limitation of this study is that it assumes steady-state solidification; the temperature gradient on the dendrite tip was not considered. <sup>[102]</sup> In addition, Ca and S partition in inclusions may change with the solidification rate.

In summary, the challenge of sulfide inclusion control mainly comes from the fact that both MnS and CaS show negative influences. Their amount, size, and morphology all contribute to how detrimental they are. However, except for the work by Imagumbai and Takeda <sup>[16]</sup>, hitherto sulfide control-related research paid attention more to thermodynamics and chemistries. The relationship between steel chemistries and sizes of sulfide complex, however, was discussed rarely.

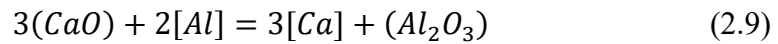
### **2.2.6 Inclusion Modification by Slag**

Suito and Inoue <sup>[103]</sup> suggested that controlling inclusion compositions with slag is possible from a thermodynamics perspective. They predicted that the number of Al<sub>2</sub>O<sub>3</sub> inclusions is lower when slags are used instead of Al as the deoxidizer after Mn and Si because local enrichment of Al will not occur in liquid steel. <sup>[103]</sup> For the same reason, the compositions of inclusions were expected to be more uniform and closer to equilibrium. <sup>[103]</sup> If Al<sub>2</sub>O<sub>3</sub> in slag can be the source of Al for further deoxidation, most probably some CaO in slag will also reduce to Ca and enter liquid steel.

The study of slag deoxidation had inspired other researchers to assess the feasibility of modifying inclusions using Ca in the top slag. <sup>[104]</sup> CaO is an important component of the refining slag. Because equilibrium can be reached at the steel-slag interface, Ca<sup>2+</sup> from CaO in slag should enter liquid steel if the steel has low Ca activity. Therefore, in theory, slag with high CaO contents is capable of modifying inclusions to some extent. But on the other hand, Suito and Inoue <sup>[103]</sup> did not discuss the kinetics of slag treatment. It was later understood that one of the main challenges of the slag treatment is the slow slag-metal reaction. <sup>[105]</sup>

Yang et al. <sup>[104]</sup> compared the efficiency of Ca transfer to the melt via CaSi additions and refining slags in industrial heats. In the Ca-treated steels, T.Ca was 31 ppm at 20 min after Ca addition in vacuum degasser, while T.Ca was 6 ppm in steels treated with CaO-containing slag. As a result, pure CaO and CaS were the dominating inclusions in the Ca-treated steel, and the existence of such inclusions is an indication of over-

modification. On the other hand, most of the inclusions were low melting point  $CA_x$  in slag-refined steel. The slag treatment yielded a better result than the 31 ppm Ca treatment from a production perspective. The researchers proposed that (CaO) in the slag was reduced by [Al] (Reaction (2.9)), and inclusion modification was possible with high basicity high  $Al_2O_3$  refining slags in steel with lower than 16 ppm T.O. <sup>[104]</sup> Even though the authors emphasized the importance of high  $Al_2O_3$  concentrations in slags, they didn't provide any reason for it in this work. If (CaO) to [Ca] transformation occurs through Reaction (2.9) as the authors suggested, high ( $Al_2O_3$ ) activity should reduce the equilibrium [Ca]; hence, suppressing the extent of modification of  $Al_2O_3$  inclusions. Another limitation of this work is that there is no discussion on how the slag composition affects the inclusion modification.



The slag also contains MgO to protect the refractory. They also affect the composition of inclusions after reacting with slag. Liu et al. <sup>[79]</sup> investigated the effect of Al content in molten steel on the modification of inclusions via CaO and MgO saturated slag (55CaO-15MgO-30 $Al_2O_3$  in wt pct) at 1873 K. Al contents were 0.25 wt pct, 0.75 wt pct, and 2.5 wt pct Ca concentration increase was reported, but the highest Ca level was only about 3 ppm in the 2.5 wt pct Al experiment, and lower than 1 ppm in the other two experiments. During the slag treatment for the low Al steel, inclusions were found to follow the route of  $Al_2O_3$  to MgO- $Al_2O_3$  spinel, then to MgO. In mid and high Al steels, CaO concentration in inclusions increased after the  $Al_2O_3$  to MgO transformation. After 120 min of slag-metal reaction, most inclusions were  $CA_x$ -containing inclusions with a small fraction of MgO. Liu et al. <sup>[79]</sup> suggested the inclusion evolution route follows Reaction (2.5) and Reaction (2.10). In the study by Mu et al., <sup>[106]</sup> the inclusion evolution route again generally follows  $Al_2O_3$  to spinel then MgO, and finally CaO- $Al_2O_3$ -MgO. This transformation of inclusion compositions only occurred in steel with higher than 2 wt pct Al. The slag composition was 51CaO-39 $Al_2O_3$ -10MgO, which is saturated with CaO and MgO. CaO contents in inclusions did not increase until 30 minutes after the reaction started. When using slag with 57CaO-43 $Al_2O_3$ , the CaO content increase started slightly earlier at 15 minutes after experiments started, and close to pure MgO was not observed. Shin and Park <sup>[107]</sup> studied five MgO saturated slag compositions with CaO/ $Al_2O_3$  ratios ranging from 0.9 to 3.3 in MgO crucibles. All spinel inclusions were well modified to liquid inclusions when the CaO/ $Al_2O_3$  ratios were 1.8 and 2.3 within 30 minutes of experimental time. However, at a higher CaO/ $Al_2O_3$  ratio of 3.3, combination of liquid and MgO inclusions were observed. Shin and Park <sup>[107]</sup> attributed unsuccessful inclusion modification at high CaO/ $Al_2O_3$  ratio to low  $Al_2O_3$  activity in slag and suggested CaO/ $Al_2O_3$  ratio from 1.5 to 2.5 is the preferential.



The existing studies revealed some characteristics of inclusion modifications by slag. First, inclusion modification took a long time to achieve. For example, in the industrial trial-based work by Chen et al.,<sup>[108]</sup> 60 min were spent before most inclusions had compositions in the liquid region of a phase diagram. It took a shorter time when laboratory-scale studies were conducted, such as 30 min in the work of Shin and Park<sup>[107]</sup> and Mu et al.<sup>[106]</sup> Normally, agitation in the industrial ladle is expected to accelerate the reaction kinetics; the reason for different modification times is not clear. Secondly, the formation of spinel should be expected in most cases. Even if MgO activities are not high in the initial slag composition, CaO and Al<sub>2</sub>O<sub>3</sub> in slag can react with the MgO crucible, which is a typical refractory material, to introduce Mg into liquid slag and initiate spinel formation. Therefore, the inclusion transformation route usually follows Al<sub>2</sub>O<sub>3</sub> to Al<sub>2</sub>O<sub>3</sub>-MgO to CaO-Al<sub>2</sub>O<sub>3</sub>-MgO when inclusions are only modified by slag.

### 2.2.7 Inclusions Modification by Rare Earth Elements

Rare earth elements (RE) are a group of 17 elements from the lanthanum group plus Sc and Y,<sup>[109]</sup> some have been used in the steelmaking industry to modify inclusions. Cerium (Ce) has been studied by several researchers.<sup>[110–112]</sup> Generally positive results were achieved. Wang et al.<sup>[110]</sup> studied the modification of spinel inclusions by Ce experimentally. Six levels of Ce ranging from 0 wt pct to 0.1 wt pct were added. The authors found when Ce contents were lower than 0.02 wt pct, a superficial Ce layer was formed around the spinel core and the shapes were described as rectangular. Increasing Ce content created globular and smaller inclusions. The evolution route based on the SEM results was suggested to be MgAl<sub>2</sub>O<sub>4</sub> to Ce<sub>2</sub>O<sub>3</sub>-MgAl<sub>2</sub>O<sub>4</sub> or Ce<sub>2</sub>O<sub>3</sub>S-MgAl<sub>2</sub>O<sub>4</sub> and eventually Ce<sub>2</sub>O<sub>3</sub> and Ce<sub>2</sub>O<sub>3</sub>S. A similar evolution trend was reported by Li et al.<sup>[111]</sup> who studied the evolution of Al<sub>2</sub>O<sub>3</sub> inclusions in low C high Mn steel. In this study, the Ce content varied between 0 wt pct to 0.034 wt pct. Again, with Ce content lower than 0.018 wt pct, Al<sub>2</sub>O<sub>3</sub> inclusions were surrounded by a ring of Ce<sub>2</sub>O<sub>3</sub>S-Al<sub>2</sub>O<sub>3</sub> were observed. Starting with 0.026 wt pct Ce, the inclusions were fully modified to Ce oxysulfides with globular shapes. The authors also reported some large inclusions with irregular shapes formed at the highest Ce content. As a result, the fraction of small inclusions was the highest when inclusions were modified with 0.026 wt pct Ce, which was the second-highest Ce content. Similar effects on Al<sub>2</sub>O<sub>3</sub> inclusion modification were also reported by Wang et al.<sup>[112]</sup>

Sulfides can also be modified by RE treatment. Shi et al.<sup>[96]</sup> conducted industrial trials on 16 Mn steel to compare the shape of inclusion modified with RE and with and without Ca addition. Unfortunately, the RE used was not specified. They suggested that the RE/S ratio can be used to quantify the combined effects of RE and Ca treatment. The RE/S ratio of 3 is the appropriate value for sulfide shape control. This was supported by the experimental results of having no elongated MnS after the effective RE/S ratio exceeded 3. However, the size of the inclusions increased and distributed in a chain pattern at a

high RE/S ratio, which the authors believed to be not beneficial to mechanical properties. Shi et al. <sup>[96]</sup> conducted two more follow-up studies about the effects of RE treatment on fracture, electrochemical properties, and microstructure. <sup>[113,114]</sup> Improvements in steel qualities were reported.

Another RE element, La, was also studied before. <sup>[115,116]</sup> Overall, RE were found to be capable of controlling the shape of inclusions and negative effects were rarely reported. <sup>[113]</sup> Unfortunately, it seems there is no comparison of Ca treatment and RE treatment in the literature except Shi et al., <sup>[96]</sup> so it was not clear how beneficial using RE and Ca treatment simultaneously in a wide range of steel chemistries is.

### 2.3 Effects of Inclusions and Modification on Steel Properties

Apart from the well-known effects on the castability of steel discussed in a previous section, inclusions also have significant effects on both the physical and chemical properties of solid steel products. This includes the resistance to fatigue, ductility, machinability, resistance to corrosion, etc. <sup>[2]</sup> It was suggested that brittle inclusions are more detrimental to the strength and fatigue resistance of steel than ductile inclusions. <sup>[117]</sup> That is because voids can emerge close to inclusions and act as stress raisers then initiate cracks. <sup>[118]</sup> Voids and micro-crack formation around Al<sub>2</sub>O<sub>3</sub> inclusions were frequently reported in the literature. <sup>[119–121]</sup> Such micro-voids are also suggested to be traps for hydrogen and can be the cause of hydrogen-induced cracking (HIC). <sup>[122]</sup> As Ca treatment had become a very common inclusion engineering approach, there have been several designated studies for understanding the relationship between various steel properties and inclusions in calcium-treated steel. <sup>[123–128]</sup>

It had been reported that Ca treatment had positive effects on the fatigue life of 60Si2MnA spring steel produced at the industrial scale level. <sup>[123]</sup> By increasing the Ca content from 8 ppm to 23 ppm, the fatigue life increased from 3.5e4 cycles to 9.8e4 cycles. Hu et al. <sup>[123]</sup> suggested that Ca treatment or using slag with higher basicity, increasing CaO/SiO<sub>2</sub> ratio from 3.4 to 5 in their study, decreased T.O hence the population and size of inclusions also decreased, which reduced the formation of voids. Because steel fracture occurs by growth and coalescence of voids, <sup>[129]</sup> fewer inclusions naturally suppress this phenomenon. Another reason was that Ca treatment and using appropriate slag change the composition of solid angular inclusions to liquid or partially liquid globular inclusions. By maintaining a globular shape during solidification and rolling processes, the voids between inclusions and steel matrix can be reduced largely and therefore improve the fatigue resistance. The correlation between inclusion shape and fracture was also confirmed in recent work by Rahman et al., <sup>[130]</sup> who also reported that very few cracks started from globular inclusions and most cracks initiated from spinal or rectangular inclusions in X70 grade steel when studying the role of inclusions in HIC.

Another advantage of having  $CA_x$  inclusions with globular shapes is to maintain isotropy. Tervo et al. [124] studied the ductility and roughness of experimental samples, which were rolled ultra-high-strength steel with two T.Ca/T.S ratios, 0.8 and 3.1. In the high T.Ca/T.S ratio sample, the dominant inclusion types were reported to be  $CA_x$ . The fracture was suspected to start from the round dimples surrounding calcium aluminates in standardized transverse tensile tests, and the fracture surfaces of the rod-shaped tensile samples were circular. In the low T.Ca/T.S ratio sample, the main inclusions were MnS and TiN, and the sample showed an elongated fracture surface after the tensile test. This finding suggested anisotropy of the ductility in the latter case. Further analysis with a confocal scanning laser microscope by Tervo et al. [124] showed the elongated dimples around the deformed MnS inclusions were likely the cause of fracture. MnS inclusions can easily deform therefore deteriorating the transverse tensile properties and introducing anisotropy to the steel properties. [117]

Ca treatment modifies MnS inclusions to CaS-MnS complexes or CaS inclusions which tend to have spherical or spindle morphologies. [3,131,132] This modification improves the mechanical properties of steel. Tomita [125] reported when T.Ca was 57 ppm in commercial 4340 steel containing 20 ppm S, CaS inclusions were observed instead of MnS inclusions, which were found in the low sulfur 4340 steel without Ca addition. The fracture toughness determined using ASTM E399-72 specification showed improvement from 52.3  $Mpa \cdot m^{1/2}$  to 74.5  $Mpa \cdot m^{1/2}$  and 40.9  $Mpa \cdot m^{1/2}$  to 68.7  $Mpa \cdot m^{1/2}$  in the longitudinal and transverse direction, respectively. The author also found with commercial 4340 steel that had approximately 160 ppm T.S, CaS-MnS inclusions were formed when adding 32 ppm T.Ca. The fracture toughness increase was less significant, the longitudinal and transverse direction fracture toughness only increased from 50.3  $Mpa \cdot m^{1/2}$  to 55.1  $Mpa \cdot m^{1/2}$  and from 38.9  $Mpa \cdot m^{1/2}$  to 42.3  $Mpa \cdot m^{1/2}$ , respectively. Tomita [125] suggested that the change of fracture mode from brittle lamellate fracture to fibrous fracture after Ca addition was the reason for an increase in fracture toughness after Ca addition. Mechanical property improvement by Ca treatment was also reported by Li et al. [127] SEM imaging showed treating 30MnVS steel with 27 ppm Ca in an industrial practice replaced the long strip of MnS inclusions with short rod-shaped CaS-MnS inclusions while keeping Mn and S contents at 1.5 wt pct and 65 ppm, respectively. It led to the increase of impact toughness (method of measurement not reported) from 60 J to 81 J. Modifying MnS inclusions with Ca also increases the resistance to HIC. Elongated MnS is normally susceptible to HIC, but CaS or CaS-MnS inclusions with proper shape control disperse the hydrogen ion, and stress around spherical CaS or CaS-MnS inclusions instead at the edge of MnS inclusions increases the resistance to HIC. [126] Moon et al. [126] reported that experimental steel with Ca/S ratio higher than 1.25 prevented HIC from occurring for API pipeline steel with 1 – 1.6 wt pct Mn and 8 to 26 ppm S. A similar ratio of 1.5 for steel with S content higher than 10 ppm was summarized in the review by Ghosh et al. [128]

It is important to remember all the characteristics: population, size, shape, thermal properties, elastic properties, etc. together to determine if inclusions are detrimental to the properties of the steel. <sup>[133]</sup> Further, modifying inclusion can cause trade-offs between different properties. For example, the presence of  $CA_x$  inclusions in the steel matrix prevents anisotropy and increases ductility and toughness, but also decreases the machinability because cutting force and power consumption are high. <sup>[134]</sup>

Determining the exact relationship between the steel properties and inclusions is not the focus of this study therefore will not be discussed in further detail. But overall, the aforementioned studies all suggested modifying  $Al_2O_3$  and  $MnS$  inclusions with Ca improved the properties of steel, <sup>[123–128]</sup> as Ca addition can prevent anisotropy, and increase the fatigue resistance, fracture toughness, and corrosion resistance.

## **2.4 Evolution of Inclusion Sizes during the Refining Process**

The previous sections mainly discussed the composition change of inclusions during the refining process. But apart from that, other phenomena such as size changes also occur during the refining process. Figure 2.9 shows a summary of the important phenomena inclusions experience during the refining process. <sup>[135]</sup> After the addition of deoxidizer, inclusions nucleate, precipitate and grow. Inclusions will continue to grow after the addition of Ca and simultaneously be removed from the liquid steel. All these phenomena contribute to the size change of inclusions at any stage. The present study focuses on the coarsening of inclusions during Ca treatment, and the mechanisms will be discussed in this section. The separation and removal of inclusions are not the focus of this study although do affect the size of inclusions.

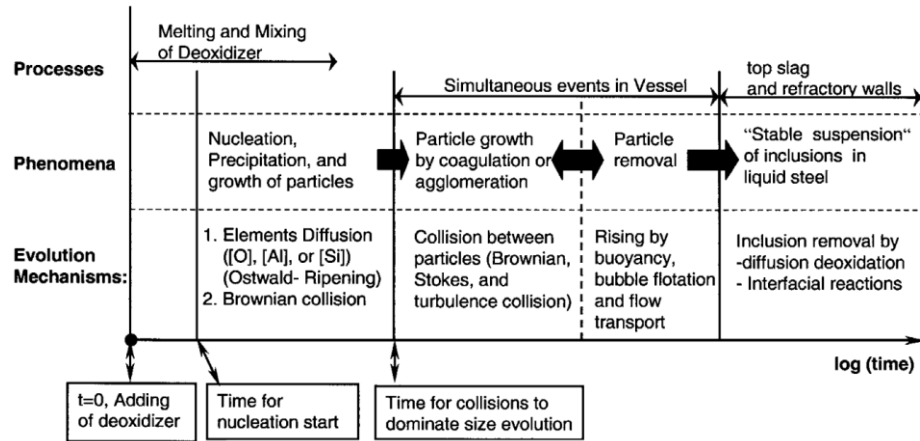


Figure 2.9 Inclusion evolutions in liquid steel <sup>[135]</sup> (reprinted with permission)

### 2.4.1 Mechanisms Affecting the Inclusion Size Changes

The coarsening mechanisms can be generally separated into two types: those that depend on mass transport, and those that depend on collisions. The mass transport-related mechanisms studied in the literature include basic mass transport-controlled growth and Ostwald ripening. <sup>[24,136–140]</sup> Ostwald ripening refers to the unique mechanism that is driven by the difference in solubility due to inclusion size. They are referred to as “mass transport-controlled growth” and “Ostwald ripening”, respectively in the following text to avoid confusion. Coarsening by coagulation is achieved by combinations of Brownian collision, Stokes collision, and collision in a laminar or turbulent flow.

Mass transport-controlled growth describes a scenario where species forming the inclusion diffuse from the steel to the inclusion-steel interface. The reaction product between these components, which is assumed to form fast, precipitates on the inclusion as a new layer and promotes an increase in inclusion size.

Ostwald ripening refers to the phenomenon of dissolution of small inclusions followed by the redeposition of the dissolved species on the surface of larger inclusions. <sup>[141]</sup> Due to the Gibbs-Thomson effect, the interfacial concentration,  $C_i$ , increases from the equilibrium value,  $C_e$ , as inclusion radius,  $r$ , decreases and this relationship is provided in Equation (2.11). <sup>[142]</sup> Interfacial tension and molar volume are denoted with  $\gamma$  and  $MV$ . Therefore, the solvent may diffuse from the surface of small inclusions to steel and then from steel to the surface of large inclusions.

$$C_i = C_e \exp\left(\frac{2\gamma MV}{rRT}\right) \quad (2.11)$$

The common collision-related coarsening mechanisms usually considered in previous

studies include Brownian collision, Stokes collision, and the collision caused by turbulent and laminar flow. [23,42,137,139,143,144] The relative motion between two inclusions can be created by the bombardment of molecules in steel. Then growth may occur due to the tendency to minimize the surface area. [145] This mechanism of inclusion coarsening is referred to as Brownian coagulation. The collision frequency between two inclusions  $I$  and  $j$  due to Brownian motion,  $\beta_{ij}^B$ , was derived by Smoluchowski [146] and given in Equation (2.12).

$$\beta_{ij}^B = \frac{2 k_B T}{3 \mu} (r_i + r_j) \left( \frac{1}{r_i} + \frac{1}{r_j} \right) \quad (2.12)$$

The relative motion between inclusions also exists because of their size differences. The floatation velocity,  $u$ , obtained by balancing the buoyancy force and the drag force is shown in Equation (2.13).  $\rho_{steel}$  and  $\rho_P$  are steel and inclusion density.  $\mu$  and  $r$  are viscosity and inclusion radius, respectively. The floatation velocity is proportional to  $r^2$ , meaning larger inclusions travel faster than the smaller ones. Therefore, two inclusions may collide during floatation if their distance is sufficiently small. Coagulation due to this mechanism is referred to as Stokes coagulation and the collision frequency due to the Stokes coagulation is provided in Equation (2.14).

$$u = \frac{2(\rho_{steel} - \rho_P)}{9\mu} gr^2 \quad (2.13)$$

$$\beta_{ij}^S = \frac{2 \pi g (\rho_{steel} - \rho_{Cas})}{9 \mu} |r_i - r_j| (r_i + r_j)^3 \quad (2.14)$$

In reality, the steel is rarely stagnant, and the steel flow can also cause collision between inclusions which leads to inclusion size change. Saffman and Turner [147] conducted a theoretical study on the collision of drops in turbulent clouds, and their findings were used extensively in the study of inclusion coagulation. [136,148–150] Saffman and Turner [147] explained the turbulent flow gives drops different velocities; hence, causes collision regardless of the size of the inclusions. This coarsening mechanism is referred to as the turbulent shear collision. [42,137] The collision frequency between two inclusions  $I$  and  $j$  due to turbulent flow,  $\beta_{ij}^T$ , was derived by Saffman and Turner [147] but modified by Higashitani et al. [151] as shown in Equation (2.15). The coagulation coefficient,  $\alpha$ , was introduced to factor in the complicated trajectory of inclusions colliding and shown in Equation (2.16).

$$\beta_{ij}^T = 1.3\pi^{0.5}\alpha \sqrt{\frac{\varepsilon\rho_{steel}}{\mu}} (r_i + r_j)^3 \quad (2.15)$$

$$\beta_{ij}^G = \frac{4}{3}(r_i + r_j)^3 \left| \frac{du}{dy} \right| \quad (2.16)$$

Although the removal of inclusions does not directly affect the size of individual inclusions, it will affect the overall size distribution of inclusions. The removal of inclusions was considered to be achieved through several mechanisms. <sup>[42–44,152]</sup> One of these mechanisms is the removal to refractory. Inclusions may adhere to the refractory surface when affected by the turbulent fluctuation; hence leaving the liquid steel. <sup>[42]</sup> The second one is the removal due to the buoyancy of inclusion. Many common inclusions like Al<sub>2</sub>O<sub>3</sub> have lower densities than liquid steel, so these inclusions travel to the top slag due to the buoyancy force. <sup>[42]</sup> Gas stirring is a very common application in industrial practice, and the presence of gas bubbles also promotes the removal of the inclusions. A bubble collides with inclusions when moving in the flow or when ascending, so the inclusions can be carried to the top slag by the bubbles and removed from the liquid steel. <sup>[42]</sup> An additional effect of the bubble on inclusion removal is that inclusions may be trapped in the wake and taken to the top slag. <sup>[42]</sup> A previous study by Lou and Zhu <sup>[42]</sup> compared the inclusion removal rate due to different mechanisms. They reported that with a gas flow rate of 10 NL/min the removal rates of inclusions due to the ascending of gas bubbles were between 0.001 kg/m<sup>3</sup>s<sup>-1</sup> to 0.002 kg/m<sup>3</sup>s<sup>-1</sup> while the removal rates of other mechanisms were close to 0 kg/m<sup>3</sup>s<sup>-1</sup> in the first 600 seconds after gas stirring starts. After that, the removal rates due to inclusions' buoyancy and collision with bubbles in turbulent flow gradually increased to 0.004 kg/m<sup>3</sup>s<sup>-1</sup> and 0.002 kg/m<sup>3</sup>s<sup>-1</sup>, respectively, at 1800 seconds. The other removal mechanism remained insignificant. At higher gas flow rates, 50 NL/min, 100 NL/min, and 200 NL/min, the increase of removal rate due to inclusions' buoyancy and collision with bubbles in turbulent flow started at around 200 seconds after gas stirring starts and were always the two most significant removal mechanisms starting approximately 600 seconds after the stirring starts.

## 2.4.2 Mathematical Models for Particle Coarsening Kinetics

Previous research on inclusion size change focused on Al<sub>2</sub>O<sub>3</sub>, MgO, ZrO<sub>2</sub>, SiO<sub>2</sub>, and CA<sub>x</sub> inclusions. <sup>[23,136,137,143,144,153–155]</sup> Many of them used the population balance model or its simplifications to interpret the experimental and industrial results or predict the inclusion size change. The population balance model has been used extensively in various fields of study including crystallization, dissolution, polymerization, and cell growth. <sup>[156]</sup> Depending on the factors included, the form of the population balance equation (PBE) varies significantly. The expression for collision and coagulation of inclusions usually takes the general form of Equation (2.17). <sup>[157,158]</sup> It expresses the rate of number density

change of size  $k$  inclusions  $\frac{dN_{V,k}}{dt}$  to be the sum of the frequency inclusions with size  $I$  and  $j$  collide (the first term) and the the frequency inclusions with size  $k$  leave the current size group after colliding with another inclusion (second term).  $\beta_{ij}^C$  and  $\beta_{ik}^C$  are the collision frequency function.

$$\frac{dN_{V,k}}{dt} = \frac{1}{2} \sum_{i=1, i+j=k}^k \beta_{ij}^C N_{V,i} N_{V,j} - \sum_{i=1}^k \beta_{ik}^C N_{V,i} N_{V,k} \quad (2.17)$$

Zhang and Lee <sup>[137]</sup> predicted the Al<sub>2</sub>O<sub>3</sub> inclusions size change using PBE. The effect of mass transport, Brownian collision, Stokes collision, and collision due to laminar and turbulent shear were considered. The authors found that mass transport was the controlling mechanism only within 1e-6 seconds after Al deoxidation started. Then Brownian collision became significant until 3 seconds after the start, followed by collision in turbulent flow when assuming an average stirring power of 0.01 m<sup>2</sup>s<sup>-3</sup>. A similar technique had been used by Zhang and Pluschkell, <sup>[143]</sup> who studied pseudo-inclusions, and by Lei et al., <sup>[159]</sup> who studied calculated the PSD evolution of ZrO<sub>2</sub> and Al<sub>2</sub>O<sub>3</sub> inclusions. A similar conclusion was reached. Ostwald ripening and mass transport-controlled growth were believed to be the significant growth mechanism only for small inclusions, and as the size of inclusion increases, Brownian collision then turbulent collision are the main collision modes.

Zhang and Lee <sup>[137]</sup> compared the predicted PSD of Al<sub>2</sub>O<sub>3</sub> inclusions against the PSD of Al<sub>2</sub>O<sub>3</sub> inclusions measured from an industrial practice and good agreements between the two were observed. Lei et al. <sup>[159]</sup> also compared their results with the experimentally measured PSD of ZrO<sub>2</sub> and Al<sub>2</sub>O<sub>3</sub> inclusions at 60 seconds, 180 seconds, 600 seconds, and 1800 seconds after the addition. However, significant differences were found between the observed and the calculated PSD. The authors suggested the possible sources of error include not considering the difference between agglomerated clusters and inclusions and coarse mesh when simplifying the calculation of PBE with a numerical method. Also, average stirring power was assumed while the actual value fluctuated with time. Similarly, in the work of He et al., <sup>[160]</sup> disagreement was again reported when comparing the calculated and observed PSD of MgO inclusions. Similar reasons as Lei et al. <sup>[159]</sup> were given. One may argue that another reason for the disagreement between observation and PBE predictions is that the removal of inclusions was not included in the PBE calculation at the time. That was unlikely the main reason as most of the inclusions they studied had diameters lower than 3 μm, and Equation (2.13) signifies that the larger inclusions were more likely to be removed. Also, as the PSD were measured from experiments without bubble stirring, inclusions cannot be effectively removed by attaching to the floating gas bubbles. Besides, the calculated number densities were lower than the observed number densities. Including the effect of

removal in PBE calculation will reduce the number densities and deviates further from the experimental data. In the case of Zhang and Lee, <sup>[137]</sup> on the other hand, the aforementioned sources of error, particularly effects of forming Al<sub>2</sub>O<sub>3</sub> cluster on PSD and the varying stirring power were most likely not apparent within 1 second after Al addition. Therefore, close agreement between observed and calculated PSD can be observed in that work.

In some studies, <sup>[23,144,161,162]</sup> instead of calculating the actual PSD, only the frequency function  $\beta$  were calculated. Although one cannot predict the evolution of PSD through this method, it makes quantitative comparison of the relative significance of different growth mechanisms possible. Similar finding was reached based on the  $\beta$  values in the previous studies. Generally, as the inclusion size increases, the dominant coarsening mechanism evolves from Brownian collision to Stokes collision or turbulent collision, depending on the stirring power. The collision due to laminar shear was usually not considered, potentially because the laminar shear layers in reality usually arises limited regions near the walls. <sup>[137]</sup>

PBE as a fundamental approach is capable of calculating the evolution of PSD of inclusions. It can incorporate multiple coarsening mechanisms but at the same time, increases the complexity; hence, can be difficult to use. As suggested by Lei et al. <sup>[159]</sup> and He et al. <sup>[160]</sup> that the inaccuracy can be caused by the presence of non-spherical inclusions and coarse mesh size when solving PBE with numerical methods. Also, the accuracy of PBE prediction depends significantly on the accuracy of initial PSD, which may not always be available as inclusion analysis including all the small inclusions can take a significant amount of time. Therefore, PBE had been simplified to provide analytical solutions of inclusion average radius change as functions of time, steel, and inclusion properties when not all details of the experimental conditions and information on inclusions are available. <sup>[147,163]</sup>

This approach was used to calculate the average size change of SiO<sub>2</sub> inclusions in the work of Suzuki et al. <sup>[136]</sup> In this study, samples were taken during the solidification of AISI 304. The average diameter change was calculated using due to Brownian collision and Stokes collision, as well as mass transport-controlled growth using the model proposed by Ueshima et al. <sup>[164]</sup> and Ostwald ripening based on the LSW (Lifshitz, Slyozov, and Wagner) theory. <sup>[142]</sup> The rate of mass transport-controlled growth was essentially calculated using the finite element method. The theoretical growth by Ostwald ripening gave the best agreement with the observations, so it was believed to control the growth of SiO<sub>2</sub> inclusion during solidification. Suzuki et al. <sup>[136]</sup> noticed that the mass transport-controlled growth, Brownian collision, and Stokes collision underpredicted the size change. The reason was not explained. Wang et al. <sup>[24]</sup> studied the CA<sub>x</sub> inclusion size change when steel was deoxidized with different combinations of Al and CaSi. It was found that when the steel was deoxidized with 0.05 pct Al and 0.25

pct Ca, 0.05 pct Al and 0.78 pct Ca and 0.25 pct Al and 0.78 pct Ca, the calculated coarsening rate by Ostwald ripening matched the experimental coarsening rate of CA<sub>x</sub> inclusions in three experiments within the first 360 seconds after addition. Some agreement can still be observed till 600 seconds but in the later samples. The observed coarsening rates were significantly higher than the calculated values. Wang et al. [24] therefore concluded that the Ostwald ripening is the predominant mechanism for CA<sub>x</sub> inclusions during the first 600 seconds.

It can be summarized that comparing the measured average size change with predicted size change using LSW theory and simplified PBE still provides some insights into the growth mechanisms and kinetics. Certainly, details of the PSD evolution cannot be obtained just based on the average size change and needs to rely on PBE.

## **2.5 Inclusion Characterization Techniques**

In the past few decades, several research tools have been applied to characterize inclusions and assess steel cleanliness. Many of these approaches have been summarized by Kaushik et al. [165] For Al-deoxidized steel grades, suggested inclusion characterization techniques include OES-PDA spectrometer, MIDAS, automated SEM, and Infrared Absorption Spectroscopy. A summary of the principle and applications of these analysis techniques are provided below.

### **2.5.1 Optical Emission Spectrometry – Pulse Discrimination Analysis (OES-PDA)**

Optical emission spectroscopy pulse discrimination analysis (OES-PDA), sometimes referred to as the spark analysis, is widely applied to measure steel composition rapidly. [166,167] OES-PDA generates numerous electrical discharge sparks between the sample and a counter electrode. The wavelength and intensity of light emitted can be associated with elements and their status, whether dissolved in steel or in the form of inclusions. OES-PDA results are usually presented as the distribution of emission intensity. A graphical representation for an arbitrary element is given in Figure 2.10 (a). The normal distribution portion has modes that are proportional to the total content. [166] The low and high intensities correspond to emissions from the steel matrix and inclusions, respectively. Therefore, reporting the dissolved (in steel) and undissolved (in inclusions) content for any element makes OES-PDA a convenient online analysis tool. [165,168] This technique, in theory, allows the rapid estimation of the amount of oxide, sulfides, and nitrides, but OES-PDA does not provide information about the location of the inclusions just like other common chemical analysis techniques.

The determination of inclusion size distribution (PSD) using OES data is currently possible with advanced mathematical methods.<sup>[167]</sup> However, there is a limitation related to the OES-PDA technique.<sup>[166]</sup> The calculated dissolved and undissolved contents might be overestimated and underestimated, respectively. The intense selective spark discharge on inclusions creates a large number of finely dispersed particles. Performing OES-PDA on finely dispersed particles forms low-intensity sparks, which contribute to the left side of the intensity distribution. Therefore, the soluble contents calculated by the conventional model is the sum of soluble contents and insoluble contents from fine particles. The graphical representation of this phenomenon is shown as Figure 2.10 (b). For the same reason, there will also be an error when estimating inclusion size distribution using the same OES-PDA data. Finally, repetition of inclusion analysis within the same area would be challenging due to OES analysis being destructive to some extent.

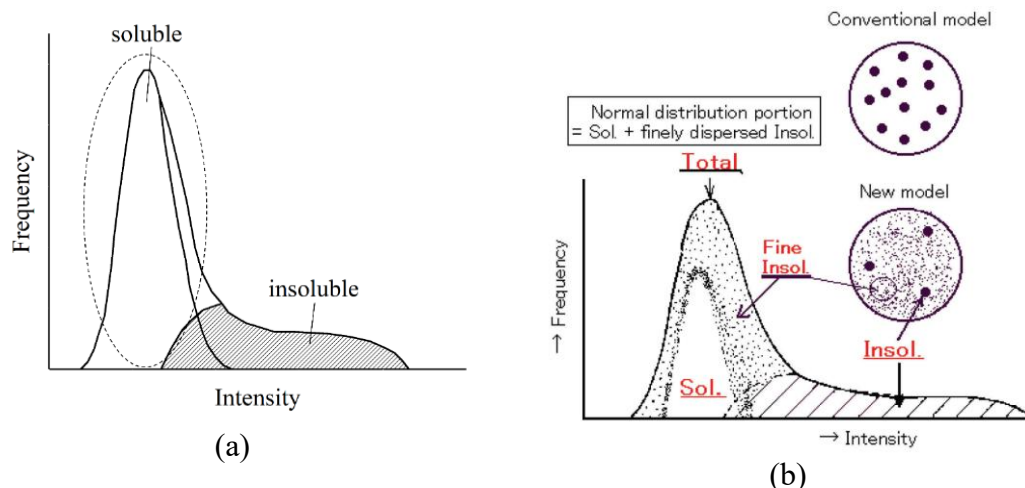


Figure 2.10 (a) Schematic diagram of OES-PDA results and (b) reassignment of PDA histogram for soluble and insoluble components<sup>[166]</sup> (reprinted with permission)

## 2.5.2 Mannesmann Inclusion Detection by Analyzing Surfboards (MIDAS)

Another broadly applied inclusion characterization tool is ultrasonic detection. There exist tests that require rolling the sample to a thin surfboard shape such as the Mannesmann inclusion detection (MIDAS),<sup>[169]</sup> as well as examinations that require no special preparation like the c-scan imaging and more.<sup>[170]</sup> Although details may vary, the same general concept is applied to different ultrasonic detection approaches. Inclusion is expected to readily reflect the ultrasonic beam with specific amplitudes depending on their sizes and depth. It has been proven that with suitable amplitude-threshold configuration, ultrasonic counts are closely associated with T.O.<sup>[170]</sup> The ability to provide volumetric information as opposed to planer information from typical microscopic and spectroscopic methods is probably the most significant advantage of

ultrasonic characterization techniques, although some researchers might consider the “depth of field” is shallow. A study has shown that equipment with a 10 MHz transducer is only sensitive to echo from 2 mm to 6 mm underneath the steel surface. <sup>[169]</sup> Probably the most significant disadvantage is the lack of inclusion chemistry information. Besides, because echo amplitudes may either come from inclusion or internal defects, it is somewhat empirical to conclude the source of echo, based on amplitudes and the presence of echo from adjacent locations. <sup>[170]</sup>

By setting different threshold FSH, the number of inclusions may vary. An example of amplitude-based decision-making is shown in Figure 2.11. At positions 12 mm, 13 mm 14 mm, amplitudes were higher than 80 pct FSH. Setting the threshold to 80 pct FSH leads to the conclusion that there is one inclusion between 12 mm and 14 mm. In practice, the scanning interval ( $\Delta x$  in Figure 2.11) should be much smaller. Using the same data set shown in Figure 2.11 and placing the threshold to be 50 pct FSH, there are three groups of adjacent ultrasonic indications at 5 mm, 10 mm to 15 mm, and 18 mm to 20 mm, hence 3 defects. In practice, ultrasonic is usually used to search for macro inclusions ( $d = 10\sim 50 \mu\text{m}$ ), <sup>[170]</sup> which are very unlikely to be detected in experimental melts as most of the inclusions are small inclusions.

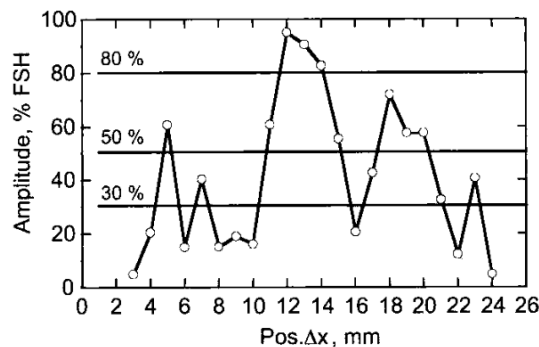


Figure 2.11 Differences between ultrasonic indications (A) and ultrasonic defects (F) in the MIDAS test <sup>[169]</sup> (Reprinted with permission)

### 2.5.3 Infrared Absorption Spectroscopy (IR)

Different molecules absorb different wavelengths of electromagnetic radiation, so infrared absorption spectroscopy (IR) can be a useful tool for the measurement of molecule concentrations. <sup>[171]</sup> In the field of steelmaking, this technique was frequently used to measure the total oxygen, sulfur, and carbon contents. Combusting a steel sample in a ceramic crucible with the help of purified oxygen and catalyst can transform all C and S into  $\text{CO}_2$  and  $\text{SO}_2$ . Because  $\text{CO}_2$  and  $\text{SO}_2$  absorb infrared energy at specific wavelengths, by comparing the infrared spectrum of samples with that of the standards, the concentration of  $\text{CO}_2$  and  $\text{SO}_2$  in the carrying gas can be determined and back-calculate the C and S contents in the original sample. <sup>[172]</sup> The working principle is the

same for measuring the total O content, except graphite crucibles are used to produce CO<sub>2</sub> gas.

The T.O and T.S contents are particularly important in many of the studies on inclusions. A proper deoxidation process can allow most of the oxygen in steel in the form of pure oxide or oxide-containing complexes. Therefore, T.O is indirect, but a very reasonable measure of the total amount of oxides. <sup>[168]</sup> But one should remember the size of inclusions does affect the T.O. As suggested by Zhang and Thomas, <sup>[168]</sup> the number of large inclusions is typically small, so they may be not in all the IR analysis samples, which are usually less than 20 g. As a result, when a sample containing a large inclusion gives an unusually high reading in T.O, the results may be omitted as an error; hence, potentially underestimates the T.O in the steel. Therefore, T.O should be considered as the measure of only the small oxide inclusions instead of the entire inclusion population. Nevertheless, T.O has been used extensively in previous research as a semi-quantitative measurement of the oxide inclusions. <sup>[7,173,174]</sup>

Total S, T.S, was used as a measurement of sulfide in steel. <sup>[8,19,175]</sup> However, one should remember that the dissolved S concentration can be higher than a few ppm except in some ultra-low sulfur grades. This means T.S is not necessarily a close estimation of the S content in inclusions. This logic also holds for T.O, but as most of the steel grades focused in the present work were Al deoxidized and further treated with Ca, the T.O can be considered to be approximately equal to the O content in inclusions.

#### **2.5.4 Scanning Electron Microscopy – Energy Dispersive Spectrometry (SEM-EDS)**

Scanning electron microscopy (SEM) typically requires more care for the preparation of the analyzed surface compared to spark and ultrasonic analysis reviewed in the previous section. The two common preparation techniques are remelted button and electrolytic extraction.

The remelt button is usually listed together with other inclusion characterization techniques. However, it is more of a preparation method than a characterization tool. The principle of this technique is to melt a small pin sample so that the inclusions can float up to the surface and be further studied in later processes. <sup>[173,176]</sup> In the case where the levitation melting technique is used, floatation of about one  $\mu\text{m}$  diameter inclusions under the influence of electromagnetic force takes about 300 s. During the floatation time, the possibility of these inclusions to agglomerate was calculated to be only one time, and the chance will reduce with inclusion size increase. After inclusions are exposed on the surface, they can be easily extracted or directly observed. The advantage of preparing inclusions using the remelt button method is to study the morphology of

inclusions more accurately compared to studying a sectioned surface. The disadvantage is that without a flat and clean surface, obtaining statistical data such as inclusion quantities and size distributions must be done manually. The inclusion electrolytic extraction technique shares the same principle, except the inclusions are acquired by electrochemically removed from the steel matrix.

Inclusions have distinct electrochemical properties compared to that of the steel matrix. Therefore, it is possible to selectively dissolve the steel matrix while keeping the inclusions in their original composition and morphology. This technique has been used in several studies focusing on different inclusions types such as calcium aluminates. [5,9,177–182] A schematic diagram of the setup is shown in Figure 2.12. 10 pct AA solution (1 pct weight/volume tetramethylammonium chloride–10 pct volume/volume acetyl-acetone–methanol) is a commonly used electrolyte. [177–182] Other non-aqueous such as 4 pct MS (4 pct volume/volume methylsalicylate-1 pct weight/volume tetramethylammonium chloride-methanol) are also used. In the work of Inoue et al. [177], it was mentioned a large number of modified  $CA_x$  inclusions could be extracted by decreasing the moisture in the 4 pct MS and 10 pct AA electrolytes. In the research conducted by Ren et al. [9], a solution of 89 pct methanol + 5 pct glycerine + 5 pct triethanolamine + 1 pct tetramethyl ammonium chloride was used to fully expose embedded  $CA_x$  inclusions. Compared to the selection of electrolytes, the power supply has not been well documented and likely varies with experimental conditions. The biggest challenge most probably comes from adjusting the power supply. The voltage, current, electric charge, and extraction time all have to be adjusted for the steel chemistries studied and can only be learned from carrying out trials. After dissolution, inclusions suspended in the electrolyte can be filtered out and collected for further analysis. Extraction was found to be particularly useful for manual SEM as it allows a researcher to skip the time-consuming process of searching for inclusions.

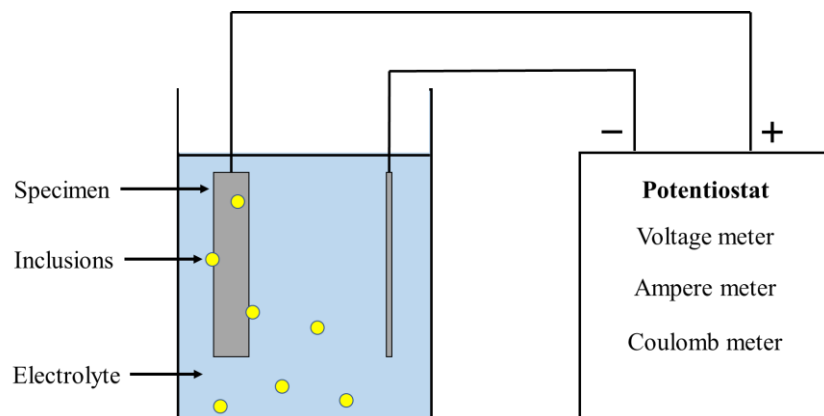


Figure 2.12 Schematic diagram of the electrolytic extraction setup

After the initial preparation, the inclusions can be observed under the microscope. For research of inclusions, usually scanning electron microscopes (SEM) were used. SEM is

a very common analysis technique, the basics are available elsewhere <sup>[183]</sup> and will not be discussed here. In the present study, a unique form of SEM: SEM with an automated EDS analysis function was used. Common commercialized automated SEM/EDS available on the market includes ASPEX, INCA, and Automated Steel Cleanliness Analysis Tool (ASCAT). <sup>[165,176,184]</sup> The purpose of these techniques is to automatically find inclusions and obtain morphological and compositional information about inclusions, and reduce analysis time significantly.

The method that is available for the author is ASPEX; hence, it will be the focus here. Before the ASPEX analysis, metallography preparation of steel samples is still required to obtain good and consistent results. This conventionally includes grinding and polishing of the steel surface exposed. In common applications, water is used as the lubricant and for cleaning between polishing steps. For the analysis of inclusions, ethanol is sometimes used instead of water to avoid the loss or compositional change of inclusions on the exposed surface due to reactions with water. <sup>[14,66,185]</sup> The final polishing step can be finished with a 1  $\mu\text{m}$  water-free diamond suspension. <sup>[165]</sup>

The working principles of ASPEX have been explained in detail by their producers. <sup>[186]</sup> The sample area is first subdivided into many smaller regions, referred to as “mag fields.” ASPEX scans mag fields with pre-defined steps based on the grade casting, so it acts like a sieve that filtrates most of the undersized particles, which are believed to have insignificant adverse effects on the processing and product quality. <sup>[186]</sup> ASPEX responds only to a sudden change in brightness, as that is the indicator of a feature at the scanned point, to start characterizing the corresponding feature. This technique can scan numerous particles promptly. This explains the high efficiency of ASPEX compared to human operators.

The first step of dynamic sizing is to find the geometric center of a particle. That is when the beam detects a particle; it moves horizontally to both sides to find the edge, then draws a vertical line intersecting the midpoint of the first horizontal line. The second horizontal line is drawn with the same method. By repeating these two steps, the intersection points are going to converge to the geometric center of the particle gradually. A schematic drawing of such a process is shown in Figure 2.13. After the center is found, 16 chords with the same included angles in between are going to extend from the center till reaching the edge. The longest and the shortest among them are the maximum diameter ( $d_{\text{max}}$ ) and minimum diameter ( $d_{\text{min}}$ ), respectively. The average length of the 16 chords is the average diameter ( $d_{\text{avg}}$ ) of an inclusion. By measuring different lengths and angles, ASPEX can measure the size of most of the particles, except those with complex shapes such as rings. A much more complicated “complex feature” algorithm needs to be used to handle the form of arbitrary complexity, by spending a long time.

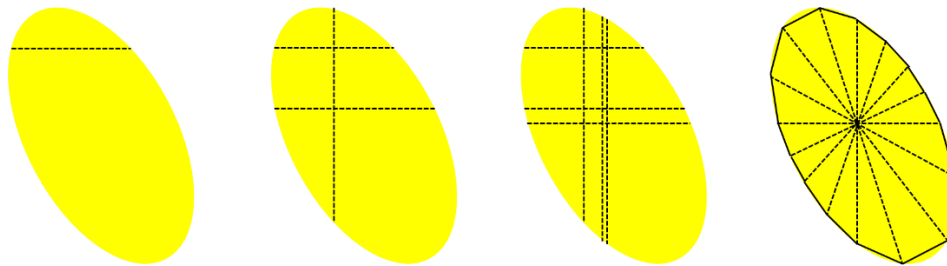


Figure 2.13 Schematic drawing of the bisected chord method and sizing

In the area of inclusion, as identified by ASPEX, the average weight fraction of predefined elements is calculated based on the EDS results. Then the inclusions are classified concerning their compositions. ASPEX also provides information about the image (shape), average, min and max diameters, cross-section area, and spatial location of each inclusion. ASPEX inclusion analysis also has several weaknesses. Firstly, ASPEX sometimes misclassifies features that are not inclusions. ASPEX identifies features as inclusions based on the contrast in SEM, so contaminations and tiny cracks may also be treated as inclusions. The solution is to check all the images manually and exclude suspicious features. Secondly, which should be a general challenge in all inclusion characterizing techniques discussed in this section is to recognize complex inclusions. Inclusion classification is based on the overall inclusion composition of the entire cross-section, so these techniques cannot distinguish calcium aluminates and alumina combined with calcium oxide. Manual inclusion characteristics with SEM are therefore conducted to obtain more detailed information on inclusion chemistries and morphology.

Another commercialized automated inclusion analysis technique: INCA shares similar working principles as ASPEX. One of the differences is that the inclusion analysis with INCA requires a preset resolution to accommodate the smallest inclusion size while ASPEX automatically divides a field of view multiple times into smaller more manageable fields and then searches for inclusions. <sup>[187]</sup> It was suggested that ASPEX, as a system that integrated both software and hardware, traded some abilities of accurately detecting and measuring (morphology and composition) very small inclusions for the analyzing speed and reliability; hence, is more suitable for production environments. <sup>[187]</sup> While INCA is only software, is capable of being used in combination with more powerful SEM of users' choice, and shows more potential in research environments. <sup>[187]</sup> The tasks INCA and ASPEX perform are the same, so the author believes the use of ASPEX is equally appropriate.

The principle of detecting inclusions of ASCAT is not available in the open literature to the best of the author's knowledge. INCA and ASPEX classify inclusions as recognized metallurgical species by comparing the EDS results of inclusions to a set of user-defined criteria. <sup>[185,186,188]</sup> For example, an inclusion is classified as  $\text{Al}_2\text{O}_3$  if Al and O counts exceed preset thresholds. ASCAT on the other hand, adopts the same approach, the

criteria are generated by neural networks and some adjustment with expert oversight is required. <sup>[188]</sup>

Abdulsalam et al. <sup>[189]</sup> suggested the analysis speed of automated SEM/EDS systems is still insufficient for monitoring production online. The potential of detecting and classifying inclusions in BSE SEM images through machine learning was investigated by Abdulsalam et al. <sup>[189,190]</sup> and Gao et al. <sup>[191]</sup> Using the random forest (RF) and convolutional neural networks (CNN), inclusions can be differentiated from other features with approximately 90 pct accuracy. <sup>[189]</sup> However, the accuracy decreased to 75 pct and 78 pct, respectively, when RF and CNN were tasked to identify oxides, sulfides, oxysulfides, and non-inclusions separately. <sup>[189]</sup> And the accuracy decreased to 60 pct when trying to distinguish Al<sub>2</sub>O<sub>3</sub>, CA, oxysulfides, CaS, and CaS-MnS inclusions. It had been shown that a neural network can also correctly measure the dimensions of defects with complex shapes, <sup>[192]</sup> so it may be used to identify complex-shaped inclusions such as a ring or having branches, and this is an ability that ASPEX lacks. <sup>[186]</sup> However, the authors admitted the computational time and related cost of the training process are high. Also, extracting the criteria of inclusion classification can be difficult. In the author's opinion, classifying inclusions through machine learning certainly has great potential, however, requires further improvement before can be used in practice with confidence.

In this study, the automated SEM, ASPEX, manual SEM at CCEM, and electrolytic extraction techniques are applied. This decision was made based on comparing the pros and cons of several conventional characterization techniques in addition to the availability of different approaches.

## 2.6 Knowledge Gaps

The modification of oxide inclusions by Ca treatment has been studied extensively in previous studies. Despite a wide range of steel conditions that have been considered, there are still a few unclarified points in the existing modification mechanism of Al<sub>2</sub>O<sub>3</sub> inclusions. For example, the criteria for the formation of CaO inclusions were not specified when included as part of the modification mechanism. Also, while transient CaS inclusions were reported to be another Ca source for modification, conditions of its appearance were not clarified in the literature hence one cannot confidently conclude whether the CaS inclusions formed will react in a later stage of the modification, or will remain permanently as part of the final product. That is probably due to the complex nature of the multi-component system, uncertainties of high temperature, and limited analysis of inclusion characterization. With the help of the automated SEM-EDS technique employed, comparable inclusion analysis results with reduced uncertainties and incorporating manual analysis can be obtained. As a result, the remaining gap of knowledge in the modification mechanism in the low S, Al killed steels of the author's interest is expected to be closed in the present study.

In previous studies, the average composition changes were frequently correlated with steel compositions, but they did not provide specific suggestions about means of improving the process or product control based on these findings. For example, Yang and Wang<sup>[20]</sup> reported the average Al<sub>2</sub>O<sub>3</sub> content in inclusions to decrease linearly as the T.Ca/T.O ratio increases from 1 to 3, and a positive linear relationship exists between CaS/CaO in inclusions and the T.S/T.O in steel. A similar suggestion was also provided by Xu et al.<sup>[11]</sup> However, the desirable Ca content or similar information was not drawn in either study. The challenge in drawing such conclusions probably lies in the fact that the quantities of inclusions, which is equally important as their compositions, was rarely considered for such kind of correlations. After all, excess number of inclusions, even if well-modified, can still be problematic in the final product. Also, as demonstrated in this chapter, the Ca treatment have multiple purposes, so the optimum Ca content therefore varies for different types of conditions. Therefore, the second potential reason for not being able to provide suggestions in the literature is that while the modification results of multiple types of inclusions need to be considered. No method of incorporating multiple steel-inclusion correlations does exist.

The characteristics of inclusions are determined together by their composition, population, and size. The effect of Ca treatment on oxide and sulfide inclusions composition was investigated extensively in the previous studies<sup>[10,66,83,193]</sup> and effects on the amount of oxide and sulfide inclusions had also been reported.<sup>[17,194]</sup> The size change of inclusions related to Ca treatment was studied recently by Wang et al.<sup>[24,195]</sup> and by Ferreira et al.,<sup>[23]</sup> who focused on CA<sub>x</sub> inclusions. There has been no study on the growth of CaS inclusions during Ca treatment even though they are undoubtedly a crucial part of Ca treatment, for both process control and product quality.

The present work studied systematically the evolution of oxide and sulfide inclusions during Ca treatment in both experimental and industrial conditions. The aforementioned gaps of knowledge were closed with the help of automated SEM-EDS and other inclusion analysis techniques. The uncertainties in the modification mechanism were investigated under different Ca and S levels. Under these conditions, a series of modification indexes inspired by those reported in previous studies were established. The effects of Al, Ca, and S contents on the composition of CA<sub>x</sub> inclusions, and the amount of CaS and MnS inclusions were incorporated. The method of incorporating multiple modification indexes allows one to evaluate the overall modification results from the perspective of multiple inclusion types and potentially determines the optimum Ca content. And lastly, the size change of CaS and CA<sub>x</sub> inclusions in experimental and industrial conditions were investigated and the coarsening mechanisms were determined.

The author believes that the present study from the academic perspective closes the knowledge. From the industrial point of view, the present study provides useful insight

to improve the inclusion modification process in the future. This would ultimately contribute to the reduction of production cost and improve steel cleanliness and quality through more precise Ca injection.

## Chapter 3 Experimental Study of Inclusion Modification by Ca in

### AHSS

This chapter is a pre-publication version of the article published in Metallurgical and Materials Transactions B, 2021, Volume 52, DOI: 10.1007/s11663-021-02243-1. Due to the complexity of the multiple-component system, some uncertainties remain in the modification mechanisms of inclusions during calcium treatment. This chapter aims to clarify the reaction mechanisms. This chapter studies mainly the evolution of inclusion compositions in six experimental steels containing around 20 ppm and 30 ppm S being modified by 35 ppm, 20 ppm, and 10 ppm Ca. The samples taken at different times after calcium additions were analyzed using an automated SEM-EDS system equipped ASPEX inclusion analysis feature. The criteria for inclusion classification were defined by ArcelorMittal Dofasco. The evolution trend allows the author to propose modification mechanisms for different conditions. When CaO inclusion formation is possible, the modification starts with CaO inclusions formation, then CaO to CaS inclusions transformation, and eventually CaS inclusions modify  $Al_2O_3$  inclusions to calcium aluminates. CaO has an insignificant impact on the modification of  $Al_2O_3$  inclusions directly. In other cases, the modification of  $Al_2O_3$  inclusions is achieved by dissolved Ca and later using CaS inclusions as the main calcium source. By conducting manual SEM-EDS analysis for these samples, typical inclusions supporting the proposed modification mechanisms were found. The hypothesis on modification mechanisms was also validated using the detailed composition change of intermediate inclusions.

This chapter also investigates the development of an accessible index for the prevention of over-modification of oxide inclusions. The fraction of liquid inclusions as the indicator of over-modification in all experiments at 20 minutes after Ca addition were compared with their position on a stability diagram. It was found that the fractions of liquid inclusions were high when the stabilities of CaS were low. The correlation between the two was further validated against the modification results in two industrial heats and a similar trend was observed. A new modification index, dimensionless Ca, was introduced based on this finding.

All the experiments and inclusion and metal chemistry analyses were completed by the primary author. Dr. Muhammad Nabeel assisted with the experiments. The industrial samples and associated inclusion analysis were completed by ArcelorMittal Dofasco and shared with the author by Dr. Stanley Sun. Dr. Li Sun from ArcelorMittal Dofasco provided training for using automated SEM and ASPEX for inclusion analysis. The manuscript was drafted by the primary author. The contributions of all co-authors, Dr. Muhammad Nabeel, Dr. Neslihan Dogan, and Dr. Stanley Sun include providing suggestions and revising the manuscript.

## **Experimental Study of Inclusion Modification by Ca in AHSS**

Keyan Miao\*, Muhammad Nabeel, Neslihan Dogan, Stanley Sun

Keyan Miao, Ph.D Student, [miaok@mcmaster.ca](mailto:miaok@mcmaster.ca)

Department of Materials Science and Engineering, McMaster University, 1280 Main Steet West, Hamilton, Ontario, L8S4L8, Canada

Muhammad Nabeel, Postdoctoral Fellow,

Department of Materials Science and Engineering, McMaster University, 1280 Main Steet West, Hamilton, Ontario, L8S4L8, Canada

Neslihan Dogan, Associate Professor

Department of Materials Science and Engineering, McMaster University, 1280 Main Steet West, Hamilton, Ontario, L8S4L8, Canada

Stanley Sun, Principal Researcher,

ArcelorMittal Global R&D – Hamilton, 1390 Burlington Street East, Hamilton, Ontario, Canada, L8H 3N8

### **Abstract**

The effects of different Ca and S contents of steel on the modification of endogenous  $Al_2O_3$  inclusions were studied in the laboratory. Three Ca levels (35 ppm, 20 ppm, 10 ppm) and two S levels (30 ppm, 20 ppm) were studied. An automated SEM-EDS system was used for the characterization of inclusions. It was found that the quantity of inclusions in steel increases in the amount of Ca and S contents in the melt. The mechanism of inclusion modification has been discussed based upon the obtained results and thermodynamics. Furthermore, a parameter named ‘dimensionless Ca’ was introduced, which can be used to estimate the extent of modification of inclusions based upon the Ca content of the steel. This parameter was validated against industrial heats.

### **3.1 Introduction**

Deoxidation in the ladle is commonly achieved by adding Al in molten steel, but the inevitable formation of  $Al_2O_3$  and  $MgAl_2O_4$  spinel inclusions as the deoxidation product is not favourable. These inclusions are not wetted by liquid steel, so they tend to deposit and accumulate inside submerged entry nozzles (SEN) or on a tundish stopper [1]. This triggers nozzle clogging and slows down or even stops the production process. One of the solutions is to modify these inclusions to less detrimental forms. Calcium treatment by powder injection or wire feeding is a common approach used in steel refining to alter the solid  $Al_2O_3$  and  $MgAl_2O_4$  inclusions. They react with Ca to form liquid or partially

liquid CaO-MgO-Al<sub>2</sub>O<sub>3</sub> inclusions [2-7], so they are less likely to attach onto the refractory lining and stopper when molten steel passes through the nozzle. In addition, modified inclusions are spherical, which helps to avoid steel properties being anisotropic if the shape is maintained after fabricating. Meanwhile, Ca also reacts with dissolved S and forms solid CaS inclusions. This lowers the concentration of dissolved S in steel and minimizes the formation of MnS inclusions. The present study aims to study the fundamentals of Ca interaction with a single oxide, hence focus only on Al<sub>2</sub>O<sub>3</sub>.

Total calcium (T.Ca) and total oxygen (T.O) have a significant influence on the type of calcium aluminates that formed in liquid steel [8]. For example, Yang et al. [9] reported that the Al<sub>2</sub>O<sub>3</sub> content decreases drastically when the T.Ca/T.O ratio increases and CaS/CaO ratio in inclusions is linearly related to T.S/T.O. Similarly, Xu et al. [10] reported that CaO content decreases when T.S/T.O increases, and CaS/Al<sub>2</sub>O<sub>3</sub> ratio increases with T.Ca/T.O. Based on their calculation, Deng and Zhu [11] proposed that inclusions tend to be C<sub>12</sub>A<sub>7</sub> and C<sub>3</sub>A when T.Ca/T.O ratios are between 0.91 and 1.25. The ratio between Ca and Al was also used to evaluate the calcium treatment results. Sun et al. [1] found the area fraction of Al<sub>2</sub>O<sub>3</sub> and CA<sub>6</sub> inclusions and the occurrence of nozzle clogging decreases sharply with T.Ca/ΔAl, where ΔAl = total Al – dissolved Al (T.Al – [Al]). It has also been reported that the amount of steel passing through the tundish nozzle decreases starting when Ca/Al is higher than 0.006 and then increases drastically when Ca/Al is higher than 0.1 when CA forms [12].

It is suggested that Al<sub>2</sub>O<sub>3</sub> is indirectly or directly modified by [Ca] or CaO, and also using transient CaS as the Ca source for modification. Direct modification by [Ca] is believed to be mainly controlled by the transfer of [Ca] in solid Al<sub>2</sub>O<sub>3</sub> inclusions [13-16]. Still, a recent study has shown that the mass transport of [Ca] in liquid steel may be the actual primary rate-limiting step [17,18]. Lind and Holappa [19] found that a 5.2 mm CaO cylinder can adequately react with a 3.3 mm Al<sub>2</sub>O<sub>3</sub> cylinder within 3 minutes at 1873K, indicating that the kinetics is fast and modification of micron-sized inclusions will most probably be completed within seconds. The amount of CaO and CaS available for modification was suggested to be dependent on [O] and [S] concentrations, which determine the probability of them occupying a CaO or CaS nucleation site on the Ca gas-liquid surface [20,21]. Previous studies [10,20,22-28] focused on determining the sequence of reactions between inclusions and calcium, minimizing the mass of calcium addition while promoting the formation of calcium aluminate inclusions, and controlling the formation of CaS inclusions. Some researchers [17,19,23,29] also focused on the kinetics of transformation between inclusion phases. However, due to the nature of a complex multi-component system and vigorous reactions at high temperatures, a significant amount of uncertainties occur during the experiments and industrial practices. Therefore, despite a wide range of steel conditions that have been considered, there is no established reaction mechanism to explain the modification of inclusions. In addition, despite findings and theories related to the Ca treatment process have been reported, an accessible indicator

of proper calcium treatment for industrial practice is still absent in the literature.

The present research aims to understand the effect of Ca addition on the modification of inclusions in liquid steel. Based on the results of laboratory experiments, an inclusion modification mechanism is proposed to explain the details of inclusion evolution. Thermodynamic calculations, Ca addition experiments, and SEM-EDS analysis are used for this purpose. By the end, the amount of Ca addition to the specific steel chemistries has been suggested.

### 3.2 Experimental Methodology

Inclusion modification experiments were conducted in a vertical tube furnace at 1873 K. A schematic diagram of the experimental setup is shown in Figure 3.1. To prepare the synthetic melt, about 6.5 g Mn (from Alfa Aesar), 0.3 g graphite rod (from McMaster-Carr), and 0.027 g or 0.04 g FeS (from Fisher Scientific) were initially added to the electrolytic iron (from North American Höganäs). The total mass of the synthetic melt was 500 g. The composition of steel will be discussed in a later section. All base materials held within an Al<sub>2</sub>O<sub>3</sub> crucible (inner diameter 5.6 cm, height 10.4 cm) was placed in the hot zone of the furnace and heated to 1873K. The composition of steel will be discussed in a later section. Al<sub>2</sub>O<sub>3</sub> crucibles were used instead of MgO or CaO. The purpose was to prevent the formation of spinel inclusions due to reaction with MgO crucible and the effect of CaO crucible on Ca content of the steel. Ar gas with 99.999 pct purity was fed continuously into the furnace at a rate of 0.5 L/min after passing through Ti turnings at 973K to maintain a protective atmosphere. The oxygen was continuously measured by an oxygen sensor connected to the gas outlet of the furnace. The partial pressure of oxygen was measured to be about 10<sup>-16</sup> atm during the experiment.

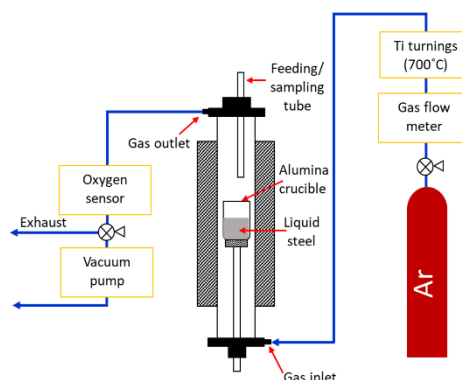


Figure 3.1 Schematic diagram of the experimental setup

The course of a representative modification experiment is shown in Figure 3.2. The crucible was heated from room temperature to the experimental temperature of 1873 K

at a rate of 10 K/min, then held for 30 minutes to homogenise the liquid steel. Thereafter, Al and Si were added simultaneously through the feeding/sampling tube to achieve 0.03 pct and 0.25 pct content in steel, respectively. After 15 minutes, Ca was added to the molten steel. This is considered as the time-zero of all modification experiments. Pin shaped samples (5 mm diameter, 10 cm length) were then taken at different holding times before and after Ca addition. In all experiments, Al and Si were introduced in the form of small lumps, while Ca was wrapped in steel foils together with some electrolytic Fe. The use of a small pin sample instead of the ASTM cleanliness evaluation standard is that a smaller sample preserves more high temperature inclusions due to its relatively faster cooling rate <sup>[30]</sup>. Assuming that a pin sample is a lumped system, the estimated cooling rate of pin samples in the air is about 2.5 K/s.

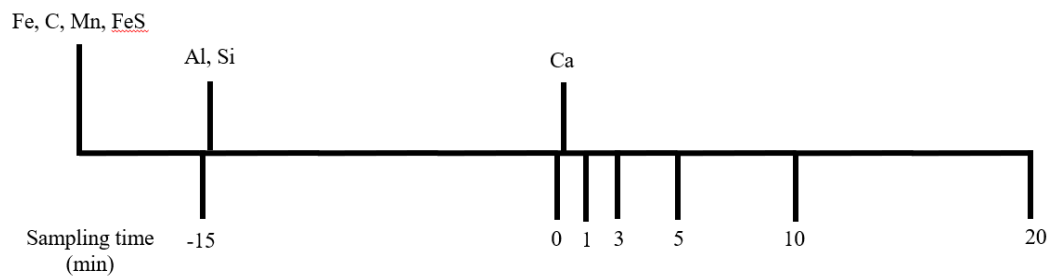


Figure 3.2 Flow chart of a typical inclusion modification experiment

Steel samples were used to analyse steel chemistry and the characteristics of inclusions. Both ends of a pin sample were removed before chemical analysis. After that, the oxide scale on the pin sample surface was removed to avoid its influence on the chemical analysis. The chemistry of the steel samples was determined using inductively coupled plasma optical emission spectrometry (ICP-OES) and LECO<sup>TM</sup> CS744 carbon/sulfur analyzer. LECO<sup>TM</sup> ON736 oxygen/nitrogen analyzer was used to measure the total oxygen (T.O) content for some samples. Accuracy of concentrations was also confirmed against results obtained through the spark OES-PDA (Pulse height Distribution Analysis) method. T.O was not measured in some experiments due to an insufficient amount of sample.

A section of the pin sample was cut along the longitudinal axis to expose the centre for inclusion analysis. The samples were first ground using SiC of 120 to 1200 grit. Ethanol was used as the lubricant during this process to avoid any potential reaction with Ca. Samples were then sequentially polished by using water-free diamond suspension containing 6  $\mu\text{m}$ , 3  $\mu\text{m}$ , and 1  $\mu\text{m}$  average particle size. An automated SEM-EDS system (ASPEX) was employed to observe and characterize inclusions on the polished cross-sections. The analysed cross-section area varied from 10 to 40  $\text{mm}^2$ . In the current study, the inclusions having a maximum diameter ( $D_{\text{max}}$ ) larger than 2  $\mu\text{m}$  were considered for analysis. Smaller inclusions were not considered because they are considered less detrimental. Moreover, inclusions with an average diameter larger than 5  $\mu\text{m}$  and features

with irregular shapes were also not considered in the analysis due to their negligible percentage.

ASPEX conducts an EDS analysis on every detected inclusion. Based on the results, the detected inclusions are classified into seven types: Ca-rich, liquid  $CA_x$ , solid  $CA_x$ , CaS, CaS-other, CaS-MnS, and MnS. Liquid  $CA_x$  includes  $C_3A$ ,  $C_{12}A_7$ , and CA inclusions, whereas solid  $CA_x$  includes  $CA_2$  and  $CA_6$  inclusions. Ca-rich inclusions are inclusions with higher CaO content than the liquid  $CA_x$ . CaS-other inclusions are those with compositions between CaS and  $CA_x$ . CaS-MnS inclusions have a significant fraction of both CaS and MnS; however, their fractions are not high enough to be considered as a single-phase CaS or MnS. Figure 3.3 shows the distribution of inclusion types detected in a sample from Exp. 3020 at 20 minutes after Ca addition as an example. The CaO- $Al_2O_3$ -CaS ternary diagram is represented based on weight fraction. The region bounded by a solid line represents the 50 pct liquid region at 1873K calculated using FactSage. As can be seen, the inclusion types cover corresponding areas of the diagram. Liquid and solid  $CA_x$  are inside and outside the 50 pct liquid region, respectively. CaS inclusions are close to the CaS corner, and CaS-other inclusions lie between CaS and  $CA_x$ . In some cases, the areas of two types overlap on the graph, but generally, the change of inclusion types between samples corresponds well with the shift in inclusion compositions. Therefore, inclusion types are used instead of detailed compositions in most of the following contexts for simplicity.

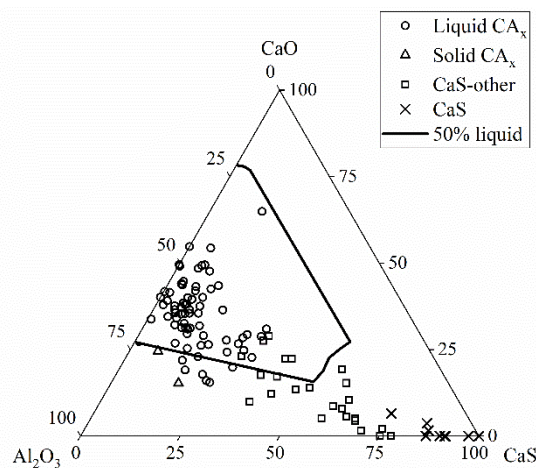


Figure 3.3 Inclusion distribution represented on a ternary diagram from Exp. 3020 at 20 minutes after Ca addition. A solid line illustrates 50 pct liquid region.

### 3.3 Experimental results

#### 3.3.1 Steel chemistries

In this study, six experiments were conducted, which can be divided into two sets. In the

first set, three different amounts of Ca (i.e., ~ 1.2, 0.8 and 0.4 g) were added in a 500 g experimental steel containing 20 ppm S. Whereas, in the second set a 30 ppm S containing steel was treated with Ca levels similar to that in the first set. The detailed composition of all experimental steels is shown in Table 3.1. The error of Ca and S contents are based on two standard deviations of repeated measurements to give 95 pct confidence. The experiments are denoted in the form of “[S content][Ca content]”. Here the Ca content of samples taken after 20 minutes of Ca addition is used. For example, Exp. 2035 represents the experimental condition with 20 ppm S and 35 ppm Ca. Deriving from this format, 2035-X is used to describe a sample obtained at X minutes after Ca addition in Exp. 2035.

For all experiments, Si and C contents didn't vary during an experiment and kept constant at about 0.25 wt pct and 0.06 wt pct, respectively. Similarly, the Mn content remained stable at close to 1 pct, except for Exp. 2020 where Mn content was measured to be about 0.75 wt pct.

In all experiments, the Al content was estimated to be 0.03 wt pct in the samples taken after adding Al and before Ca addition. During the experiment, the reaction between Ca and  $\text{Al}_2\text{O}_3$  crucible increased dissolved Al in the system (Reaction (1)). Due to this reason, the Al content increased within 1 minute after Ca addition, as indicated in Table 1, then remains constant throughout the experiment. The increments are in positive correlation with Ca content.

Total Ca concentration (T.Ca) generally decreased over time, especially in Exp. 2035 and Exp. 3020, which had about 20 ppm Ca drop. Whereas in Exp. 2010 and Exp. 3010, T.Ca remained nearly constant. The decrease in T.Ca is likely due to Ca evaporation and reaction with the crucible. The Ca-crucible reaction is indicated by the increased Al and O contents of steel after Ca addition, as well as the fact that calcium aluminates ( $\text{CA}_x$ , here C and A denote CaO and  $\text{Al}_2\text{O}_3$ , respectively) were found on the crucible inner wall. SEM image of the crucible inner surface before and after the experiment is shown in Figure 3.4. As shown in Figure 3.4 (a), the crucible generally had homogeneous  $\text{Al}_2\text{O}_3$ . After a modification experiment, multiple new phases appeared on the crucible inner surface (Figure 3.4 (b)). According to the EDS measurement, Ca concentration gradually decreases from about 15 wt pct at the inner surface ( $\text{CA}_x$  phase 1) to 9.5 wt pct in the middle ( $\text{CA}_x$  phase 2) then 4 pct in a layer adjacent to the crucible body ( $\text{CA}_x$  phase 3). The crucible body after the experiment now contains about 1 wt pct Ca.

Table 3.1 The composition of experimental steels after Ca addition

Exp. #	2035	2020	2010	3035	3020	3010
Time (min)	Ca (ppm)					
1	56 ± 3	29 ± 3	10 ± 3	42 ± 1	37 ± 1	15 ± 2
3	50 ± 2	20 ± 2	11 ± 3	41 ± 1	19 ± 2	14 ± 2
5	48 ± 2	17 ± 2	11 ± 3	40 ± 1	17 ± 2	14 ± 2
10	46 ± 4	20 ± 2	10 ± 3	39 ± 1	17 ± 2	N/A
20	37 ± 3	18 ± 3	9 ± 3	37 ± 1	17 ± 2	13 ± 2
	S (ppm)					
1	21	22	18	31	32	25
3	23	22	18	32	33	26
5	23	22	18	30	32	31
10	26	23	18	27	34	26
20	21	23	19	34	33	25
	Al (wt pct)					
1	0.1	0.039	0.037	0.059	0.055	0.041
3	0.090	0.042	0.034	0.062	0.056	0.041
5	0.093	0.041	0.041	0.061	0.055	0.042
10	0.096	0.042	0.036	0.062	0.052	N/A
20	0.090	0.051	0.036	0.062	0.056	0.043
	O (ppm)					
0	21	25	23	n/a	21	n/a
1	25	12	14	n/a	13.2	n/a
3	22	18	37	n/a	11	n/a
5	24	23	45	n/a	14	n/a
10	35	31	7	n/a	40	n/a
20	30	29	n/a	n/a	23	n/a

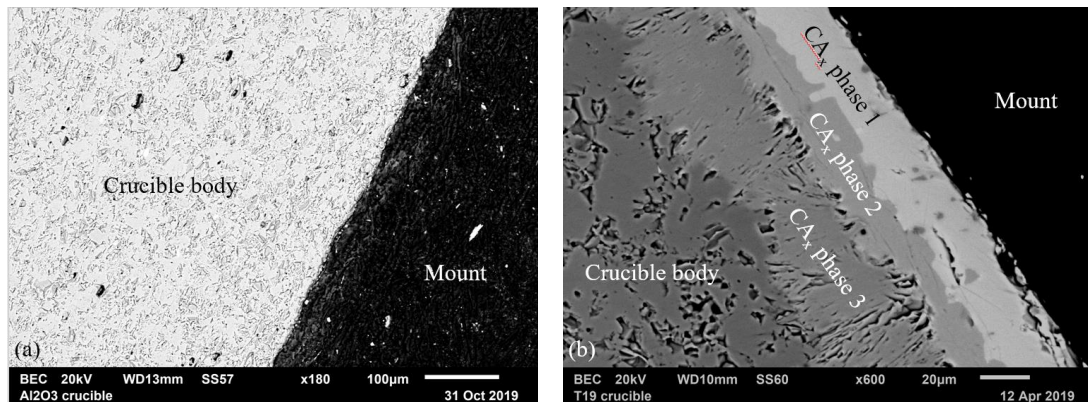


Figure 3.4 A typical SEM backscatter image of the  $\text{Al}_2\text{O}_3$  crucible (a) before and (b) after an experiment

### 3.3.2 Inclusion compositions and quantities

Figure 3.5 presents the variation in the area fraction (AF) and the number per unit area ( $N_A$ ) of all inclusions observed in each experiment. Area fraction is calculated as the area of inclusion divided by the area of steel matrix scanned in ASPEX. As can be seen in Figure 3.5 (a), for all the experiments, a similar value of total AF (about  $13\text{E-}6$ ) was found in the sample taken before Ca addition. Just after Ca addition, the AF value decreases and then gradually increases till the end of the experiment. It can also be seen that a higher T.Ca leads to a higher AF of inclusions. This tendency can be clearly seen by comparing the AF of inclusions in samples taken after 20 minutes of Ca addition. Exp. 2035 has almost  $\sim 13$  times higher AF than that of Exp. 2020. Similarly, for 30 ppm S set experiments, the AF of inclusions in 35 ppm Ca containing steel (Exp. 3035) is  $\sim 1.6$  and  $\sim 16$  times of the AF of inclusions in Exp. 3020 and Exp. 3010, respectively. The evolution of  $N_A$  is presented in Figure 3.5 (b), which exhibits similar trends to those of the AF change in Figure 3.5 (a). Hereafter, the AF of inclusions is used to present and discuss the results. According to Table 3.1, no significant T.O and T.S content changes were observed in any experimental heats other than Exp. 2010, in which the AF increase is negligible. Therefore, a significant AF growth seen in Figure 3.5 cannot be attributed to T.O or T.S change. The fact that AF increase is more apparent in high Ca experiments suggesting that undetected tiny CaS inclusions formed in early stages, their size increases with time, and they become detectable by ASPEX, either through particle coarsening or agglomeration.

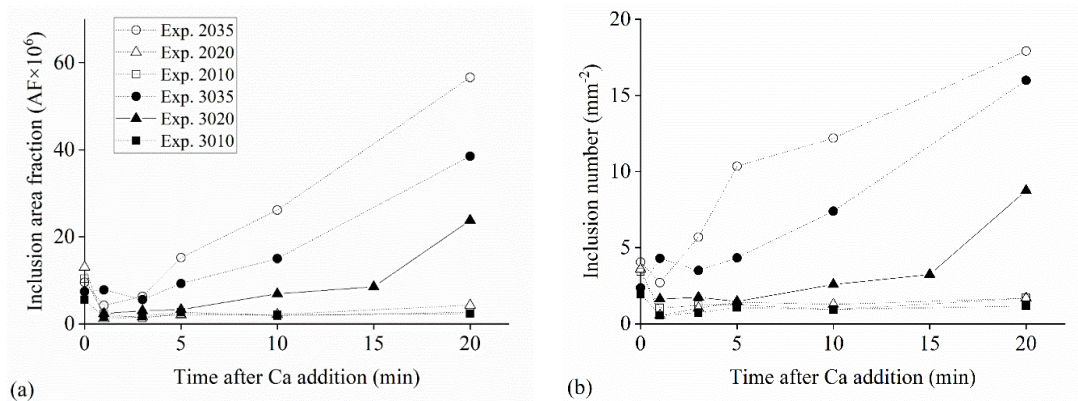


Figure 3.5 Inclusions quantity evolution from six experiments studied in the form of (a) area fraction (AF) change and (b) number ( $N_A$ ) change

Figure 3.6 presents the AF variation of the main types of inclusions observed in experimental steel. Apart from these types, a neglectable amount (<5 pct of total inclusions) of Ti and Mg containing inclusions was detected. Ca-rich inclusion class in Figure 3.6 represents inclusions that are mainly composed of CaO. CA,  $C_{12}A_7$  and  $C_3A$  are grouped in one category due to their relatively low melting points, and hereafter they are referred to as liquid  $CA_x$ . Whereas,  $CA_2$  and  $CA_6$ , having high melting points, are called solid  $CA_x$ . CaS-MnS inclusions contain both CaS and MnS. CaS-other inclusions can be a combination of CaS and  $CA_x$ , or CaS and  $Al_2O_3$ .

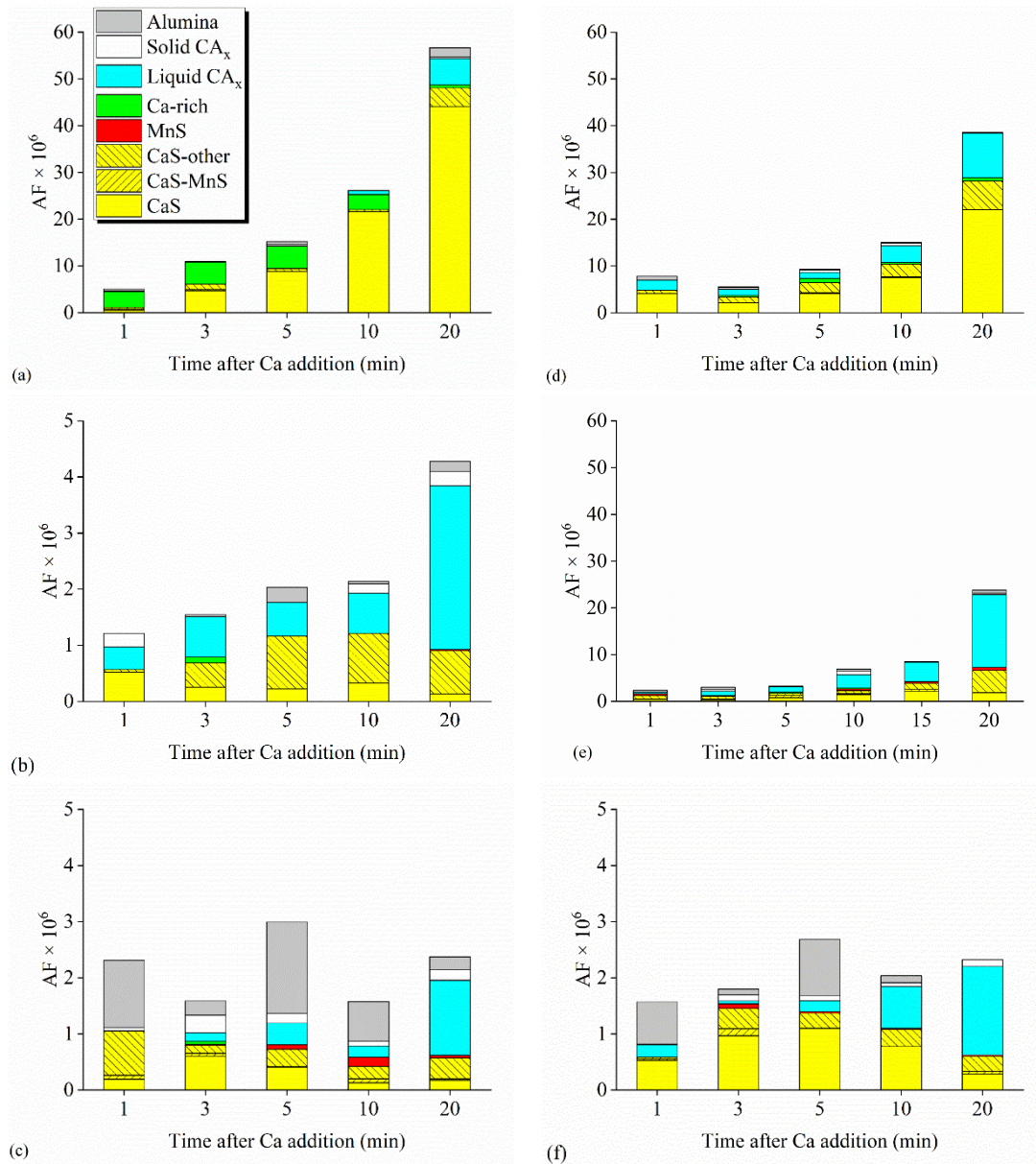


Figure 3.6 Evolution of inclusion area fraction (AF) in (a) Exp. 2035, (b) Exp. 2020, (c) Exp. 2010, (d) Exp. 3035, (e) Exp. 3020 and (f) Exp. 3010

In Exp. 2035 (Figure 3.6 (a)), Ca-rich inclusions appear just after Ca addition, and their AF remains almost constant (at about 4 ppm) until 10 minutes. CaS inclusions appear in the sample taken at 3 minutes after Ca addition, and the AF of these inclusion increases from 0.5 ppm to 44 ppm till 20 minutes. A tiny amount (0.8 ppm) of liquid  $CA_x$  appeared in 10 minutes sample, which substantially increased to 5.7 ppm in the sample taken after 20 minutes of Ca addition. CaS-other inclusions started to emerge from the beginning of this experiment; however, the AF only became significant in 20 minutes sample.

With a less Ca addition, Exp. 2020 (Figure 3.6 (b)) did not exhibit any considerable AF of Ca-rich inclusions. Instead, liquid  $CA_x$  and CaS appeared within 1 minute after Ca

addition. After that, the AF of liquid  $CA_x$  remained almost constant (at  $\sim 0.6$  ppm) in the first 10 minutes and then increased to 2.9 ppm in 20 minutes sample. In comparison, the AF of CaS decreased to a relatively low amount in 20 minutes. From 2020-1 to 2020-5, the AF of CaS-other inclusions increased from 0.05 ppm to 0.9 ppm, then slightly decreased to 0.8 ppm at 20 minutes.

As Ca addition further decreased, in Exp. 2010 (Figure 3.6 (c)), the retention of  $Al_2O_3$  inclusions shortly after Ca addition was observed. Another feature of the Exp. 2010 was the appearance of CaS-MnS and MnS. Although their AF is still incomparable to any other major inclusion types, their existence indicates the modification results are different from the other two experiments shown above.

Unlike 20 ppm S containing steel, a higher Ca addition in 30 ppm S containing steel (i.e. Exp. 3035) didn't produce Ca-rich inclusions (compare Figure 3.6 (a) and (d)). Instead, 2.3 ppm liquid  $CA_x$  and 4.1 ppm CaS inclusions were observed in Exp. 3035 just after Ca addition and the AF of liquid  $CA_x$  and CaS gradually increased to 9.4 ppm and 22.1 ppm during the experiment, respectively. However, by the end of 20 minutes, the inclusion characteristics of Exp. 3035 were very similar to those of Exp. 2035, except with less CaS relative to  $CA_x$  in Exp. 3035.

In Exp. 3020 (Figure 3.6 (e)) the AF of liquid  $CA_x$  and CaS inclusions increased with holding time. Between 1 minute and 20 minutes, the AF of liquid  $CA_x$  increased from 0.4 ppm to 15.5 ppm. Also, the AF of CaS-other and CaS inclusions gradually increased from 0.7 ppm to 4.8 ppm and 0.5 ppm to 1.9 ppm, respectively. Moreover, CaS-MnS and MnS inclusions were detected throughout the experiment with a small AF.

The inclusion characteristics in Exp. 3010 (Figure 3.6 (f)) were similar to those of Exp. 2010 (Figure 3.6 (c)). The similarity comes from two key characteristics. Firstly, the oscillating AF of  $Al_2O_3$ , which does these two experiments the only two cases with  $Al_2O_3$  being formed after Ca addition. The other feature is the increase in the AF of CaS inclusions from 0.5 to 1.1 ppm followed by decreasing to 0.4 ppm. Except for the AF of CaS in Exp. 3010 is generally higher than that in Exp. 2010.

### **3.4 Experimental results**

#### **3.4.1 Effect of Ca and S contents on inclusion stabilities**

Thermodynamic calculations were carried out by employing Factsage 7.2 to predict stable phases in molten steel at 1873K. The stability diagram of inclusions in experimental steel containing 20 ppm and 30 ppm S are shown in Figure 3.7 (a) and (b), respectively. Based upon the measured T.O values, a value of 20 ppm was used in these

calculations.

Figure 3.7 shows that CaO, CaS, liquid  $CA_x$ , and  $CA_2$  are in equilibrium with molten steel containing 5 to 60 ppm Ca and 0.03 to 0.1 pct Al. The inclusion stability mainly varies with Ca content. While liquid  $CA_x$  is always stable, decreasing Ca leads to the disappearance of thermodynamically stable CaO, then CaS, and finally the formation of  $CA_2$ . CaS stability is associated with S content. By increasing S content from 20 to 30 ppm, the CaS stable region expands by narrowing both liquid  $CA_x$  and CaO stable regions. However, the formation of liquid  $CA_x$  and  $CA_2$  does not depend on S content; hence, it appears identical in Figure 3.7 (a) and (b).

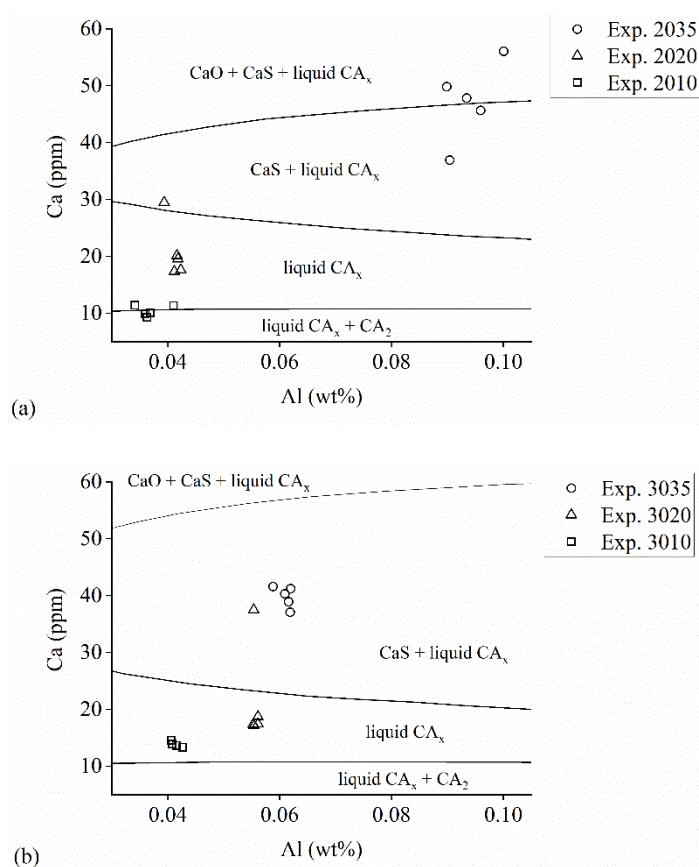


Figure 3.7 Inclusion stability diagram constructed using FactSage for experimental steel containing (a) 20 ppm S and (b) 30 ppm S and constant 0.06 wt pct C, 0.25 wt pct Si, 1 wt pct Mn and 20 ppm T.O

Hollow marks in Figure 3.7 represent the measured Ca and Al contents of samples taken after Ca addition. The sampling sequence has been shown in detail in Table 3.1. Inclusion stability diagrams show that regardless of S content, the sample from higher Ca addition experiments (Exp. 2035 and Exp. 3035) lie above the fully liquid region. Moreover, for Exp. 2035, the samples, taken within 10 minutes of Ca addition, are in the CaO stability region. This explains the presence of Ca-rich inclusions in Exp. 2035 and a substantial

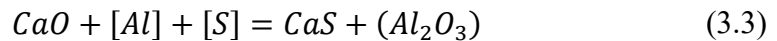
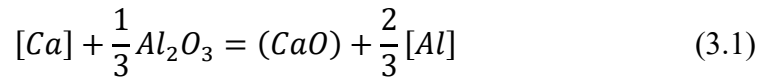
amount of CaS inclusions in both Exp. 2035 and Exp. 3035. Exp. 2020 and Exp. 3020 had initial compositions located in the region where CaS is stable, and as the Ca content stabilized, both experiments ended in the fully liquid region. The inclusion analysis also showed that the majority of the inclusions in these two experiments are liquid CA<sub>x</sub>. All the samples from Exp. 2010 lie close to the CA<sub>2</sub> saturation line. Whereas, those of Exp. 3010 are in the fully liquid region. As mentioned earlier, the equilibrium line between liquid CA<sub>x</sub> and CA<sub>2</sub> is independent of S content. The different locations of Exp. 2010 and Exp. 3010 are due to the slight variation in their Ca contents (see Table 3.1). This difference, to some extent, did reflect on the modification results.

### 3.4.2 Effect of Ca and S contents on inclusion stabilities

An occurrence of Ca-rich (mainly CaO) inclusions in Exp. 2035 (see Figure 3.6) suggests that the inclusions modification mechanism for this experiment is different than that of the other five experiments. The following discusses the possible inclusion modification mechanisms involved in all the experiments conducted in the current study.

#### 3.4.2.1 Mechanism involving CaO inclusions

When Ca is added to molten steel, due to its volatile nature, it can leave the system in the form of gas, and some of it can dissolve in molten steel as [Ca]. [Ca] is consumed in 3 ways: 1) reduction of the Al<sub>2</sub>O<sub>3</sub> inclusions in accordance with Reaction (3.1) (CaO in round brackets denotes CaO and Al<sub>2</sub>O<sub>3</sub> are miscible); 2) formation of CaS according to Reaction (3.2); and 3) reaction with Al<sub>2</sub>O<sub>3</sub> crucible. Reaction (3.1) is considered as a primary route of CaO formation since ASPEX did not detect visible AF of Al<sub>2</sub>O<sub>3</sub> inclusions in sample 2035-1, as seen in Figure 3.6 (a).



In addition to the formation of CaS by Reaction (3.2), Ca-rich inclusions transformed to CaS inclusions following Reaction (3.3). While the transformation of Ca-rich inclusions to CaS, [O] from CaO reacts with [Al] to form Al<sub>2</sub>O<sub>3</sub> as part of CA<sub>x</sub> (denoted using round brackets). This can be confirmed by their chemistry change. By using the method described by Lind and Holappa <sup>[19]</sup>, elemental compositions of inclusions obtained by EDS during ASPEX analysis can be converted to mass fractions of MnS, CaO, Al<sub>2</sub>O<sub>3</sub>, and CaS. The compositions of CaS and Ca-rich inclusions at different times in Exp. 2035

are plotted in Figure 3.8. MnS is not included as it is considered as a solidification product that did not exist at 1873K. Although these inclusions are classified as “CaS” and “Ca-rich” in the inclusion analysis, they are all CaO-CaS complexes. Before 10 minutes after Ca addition, the complexes were almost composed of only CaO and CaS (Figure 3.8 (a) to (c)). As the experiment proceeded, Ca-rich and CaS became richer in CaS, and at 20 min, the fraction of Al<sub>2</sub>O<sub>3</sub> increases. Therefore, the respective increase and decrease of CaS and Ca-rich AF shown in Figure 3.6 reflect a continuous CaO to CaS transformation in CaO-CaS complexes throughout the experiment according to Reaction (3.3). CaS can also be a solidification product due to its increased stability at lower temperature [20,31]. However, these inclusions most probably have sizes under the detection limit of ASPEX with the short solidification time in pin samples.

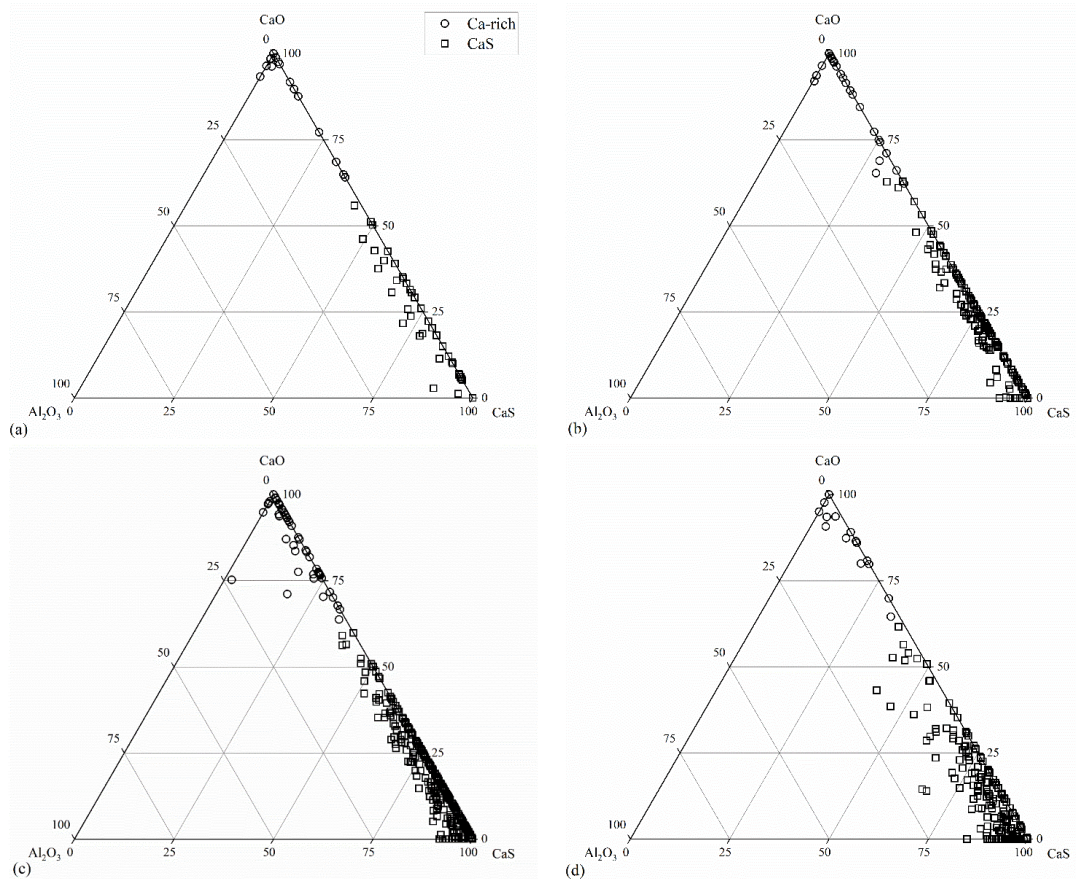


Figure 3.8 CaO, Al<sub>2</sub>O<sub>3</sub> and CaS mass fractions of Ca-rich and CaS inclusions in Exp. 2035 at 1 minute (b) 5 minutes (c) 10 minutes and (d) 20 minutes after Ca addition

EDS mappings on Ca-rich inclusions were also performed to verify the occurrence of early CaO to CaS transformation. Examples of two such inclusions are shown in Figure 3.9. The elemental map of Ca in both inclusions cover almost the entire inclusions surface, while the map of S misses some region as the upper part of the inclusions in Figure 3.9 (a) and Figure 3.9 (b). Even though the low contrast in O maps causes some difficulty to directly compare with S and Ca maps, both inclusions in Figure 3.9 are likely

CaO-CaS dual-phase inclusions.

After the CaO to CaS transformation, CaS became the main Ca bearer, hence is the major Ca source for oxide modification. These Al<sub>2</sub>O<sub>3</sub> inclusions were modified by CaS in accordance with Reaction (3.4). In this case, CaO is not the major Ca source for modification through Reaction (3.5) because the concentration of [Ca] and CaO were low after Reaction (3.3).

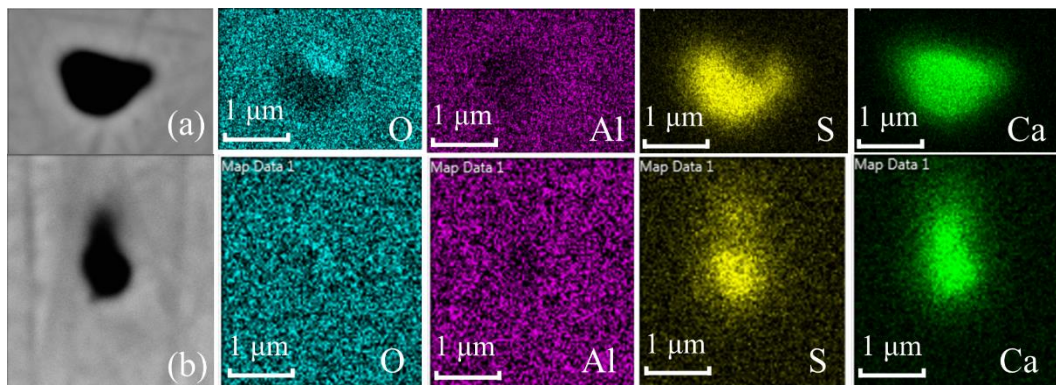
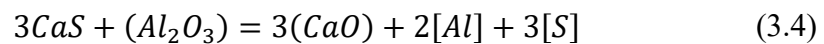


Figure 3.9 SEM-EDS elemental maps of CaO-CaS dual-phase inclusions from Exp. 2035 samples (a) and (b) both taken at 3 minutes after Ca addition

### 3.4.2.2 Mechanism in the absence of CaO inclusion

Similar to Exp. 2035, the added Ca in all the other experiments participated in reducing Al<sub>2</sub>O<sub>3</sub> inclusions, the formation of CaS, and reacting with Al<sub>2</sub>O<sub>3</sub> crucible. However, due to low Ca content and thermodynamic instability, CaO (Ca-rich inclusion) was not formed, but instead, Reaction (3.1) yielded in the formation of CA<sub>x</sub>. The occurrence of liquid CA<sub>x</sub> within 1 minute of Ca addition is in agreement with the suggestion of Tabatabaei *et al.* [17], i.e., the transformation of micron-sized Al<sub>2</sub>O<sub>3</sub> to liquid CA<sub>x</sub> can complete in a very short time. In all the experiments, CaS or CaS-other inclusions were formed immediately after Ca addition.

The [Ca] is consumed immediately after Ca addition resulting in the formation of liquid CA<sub>x</sub> and CaS containing inclusions. Any further modification will use CaS as the Ca source (Reaction (3.4)). Unlike the aforementioned [Ca]-Al<sub>2</sub>O<sub>3</sub> reaction, modification of Al<sub>2</sub>O<sub>3</sub> by CaS involves two solids, which is understandably slower than [Ca]-Al<sub>2</sub>O<sub>3</sub> modification reaction. Hence, a detectable amount of oxysulfide inclusions as reaction intermediates is likely to exist. CaS-other inclusions were defined in ASPEX inclusion

classification to be oxysulfide complexes compounded by a similar amount of CaS and  $\text{Al}_2\text{O}_3$  or  $\text{CA}_x$ . They may be the reaction intermediates of  $\text{Al}_2\text{O}_3$  or  $\text{CA}_x$  modified by CaS.

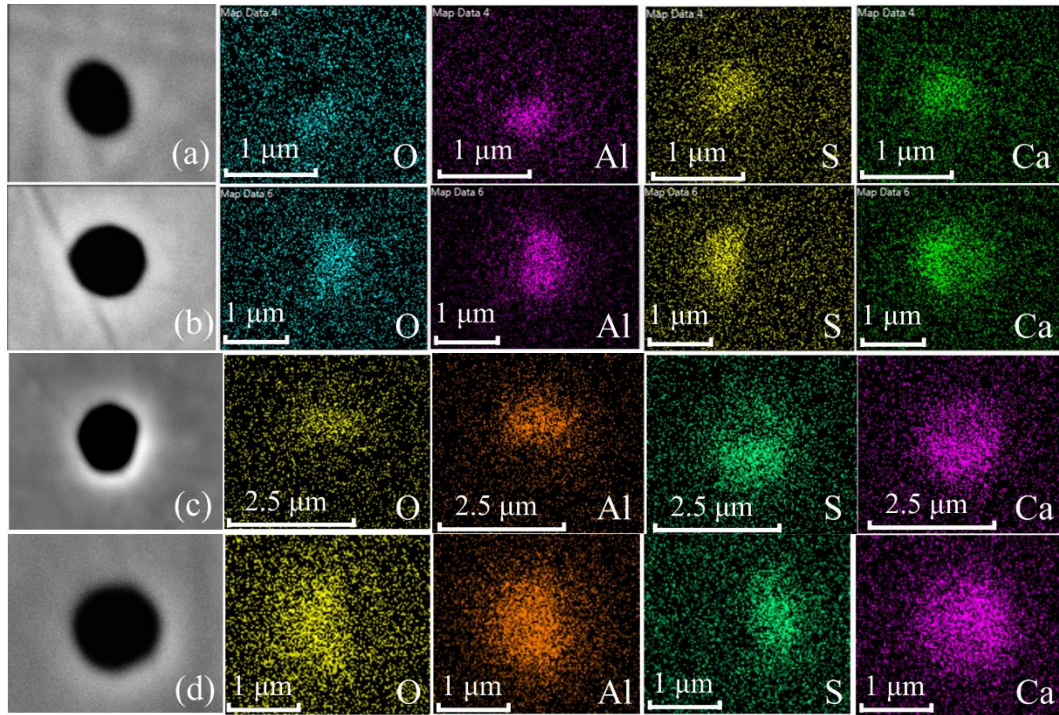


Figure 3.10 SEM-EDS elemental maps of typical oxysulfide inclusions observed in the sample taken at (a-b) 3 minutes after Ca addition (c-d) 20 minutes after Ca addition in Exp. 2020

The SEM-EDS elemental maps of some typical oxysulfide inclusions are shown in Figure 3.10. All four inclusions exhibit two separate phases. In Figure 3.10 (a) and (b), Ca, and S elemental maps overlap and correspond to the upper and left region of the inclusions, respectively. In Figure 3.10 (b), some Ca is also detected in the right part of the inclusion. Al and O maps cover the lower and right part of these inclusions. This implies that Figure 3.10 (a) likely shows a CaS- $\text{Al}_2\text{O}_3$  complex inclusion, whereas Figure 3.10 (b) is an CaS- $\text{CA}_x$  complex inclusion. Similar inclusions can also be found at 20 minutes after Ca addition as shown in Figure 3.10 (c) and (d).

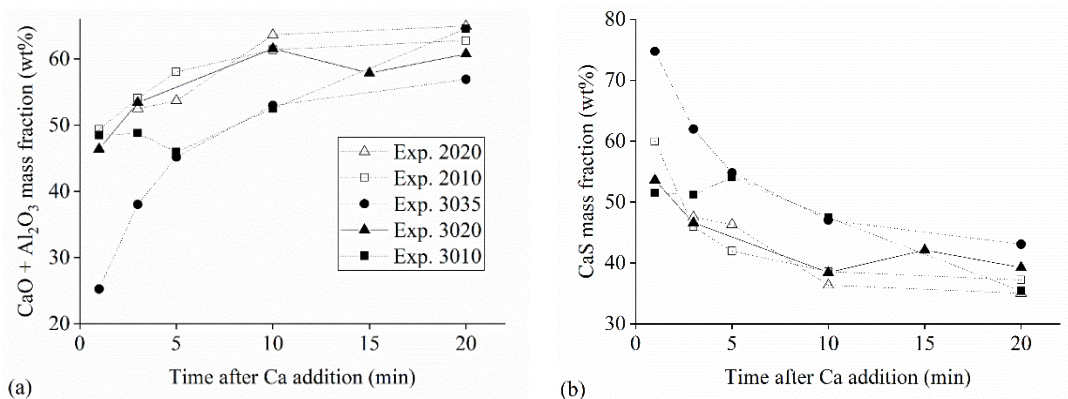


Figure 3.11 Change of CaS-other average compositions (a) CaO + Al<sub>2</sub>O<sub>3</sub> (b) CaS in Exp. 2020, Exp. 2010, Exp. 3035, Exp. 3020 and Exp. 3010

The variation in the composition of CaS-other inclusions with time is shown in Figure 3.11 for all the experiments except Exp. 2035. It can be seen that for all the experiments, the mass fraction of CaO + Al<sub>2</sub>O<sub>3</sub> increased from less than 50 wt pct to around 60 wt pct, while that of CaS decreased from more than 50 wt pct to approximately 40 pct. The EDS mapping presented in Figure 3.10 and the variation in the composition of CaS-other inclusions shown Figure 3.11 in support the suggested modification mechanism of inclusions modified by CaS.

In the present study, the amount of MnS inclusions formed is directly related to [S] because [Mn] levels are similar across experiments if sample cooling rates are assumed to be similar. The formation of MnS and CaS-MnS inclusions was observed in Exp. 2010, Exp. 3020 and Exp. 3010. Due to either the low Ca content or high S contents, these experiments still had sufficient [S] to precipitate MnS during solidification.

Based upon the discussion in the above section, the inclusion modification mechanism for the current experimental steel compositions can be summarized as below:

1. [Ca] in liquid steel reduces Al<sub>2</sub>O<sub>3</sub> and depending on the amount of added Ca, the reaction product could be CaO or different types of CA<sub>x</sub> (or remains Al<sub>2</sub>O<sub>3</sub> in the case of low Ca additions). At the same time, [Ca] desulfurizes liquid steel to produce CaS.
2. In the case where CaO is formed, CaO gradually reacts with [S] to produce CaS and [O]. The produced [O] reacts with [Al] to form Al<sub>2</sub>O<sub>3</sub>, which is modified to CA<sub>x</sub> by CaS.
3. With low Ca addition, the inclusions are CA<sub>x</sub> (and potentially some Al<sub>2</sub>O<sub>3</sub>) and CaS. CaS is now the only Ca source. Hence, CaS will further modify CA<sub>x</sub> to a higher modification extent.
4. If the conditions (mainly [S]) satisfy the criteria of MnS nucleation or precipitation, MnS and CaS-MnS inclusions will form during solidification.

### 3.5 Comparison of modification results

From the perspective of improving castability, liquid and semi-liquid inclusions are preferred. The samples taken at 20 minutes after Ca addition are selected to compare the extent of liquefaction achieved in each experiment. The AF of different types of inclusions at 20 minutes after Ca addition is normalized to 100 pct and shown in Figure 3.12 (a). The exact AF values are already shown in Figure 3.6. The three high CaS inclusion types, CaS, CaS-other and CaS-MnS are more than 70 pct of the overall inclusion AF in Exp. 2035 and Exp. 3035. In the other four experiments, the percentage is about 20 pct. The excessive CaS formation indicates over-modification in the two 35 ppm Ca experiments. The liquid  $CA_x$  percentages appear similar in 20 ppm and 10 ppm T.Ca experiments regardless of S content, but are in fact, very different as types of  $CA_x$  formed vary. Figure 3.12 (b) shows the relative area fraction of  $CA_x$  inclusions. The  $CA_x$  present in 20 minutes samples of Exp. 2035 and Exp. 3035 are highly modified as more than 80 pct of their AF contains  $C_3A$  and  $C_{12}A_7$ . However, since a significant amount of CaS (6 times more than AF of all  $CA_x$ ), these experiments are not considered to have superior modification results. The liquid  $CA_x$  ( $CA + C_{12}A_7 + C_3A$ ) has the highest percentage of AF (>60 pct) among all inclusion types in the other four experiments. However, according to Figure 3.12, the  $CA_x$  from Exp. 2010 is relatively less modified compared to those of Exp. 2020, Exp. 3020 and Exp. 3010. This is because about 68 pct of the  $CA_x$  in Exp. 2010 are CA, and the melting point of CA is very close to 1873K. If the same inclusion combination appears in the industrial heats at a lower temperature, the castability may still be negatively affected. The steel compositions of Exp. 2020, Exp. 3020 and Exp. 3010, with at least 28 pct  $CA_x$  being  $C_{12}A_7$  and limited CaS, exhibit preferred modification results. This agrees with the thermodynamic calculation presented in Figure 3.6, which shows that the endpoint Ca contents of these three experiments fall in the liquid  $CA_x$  region.

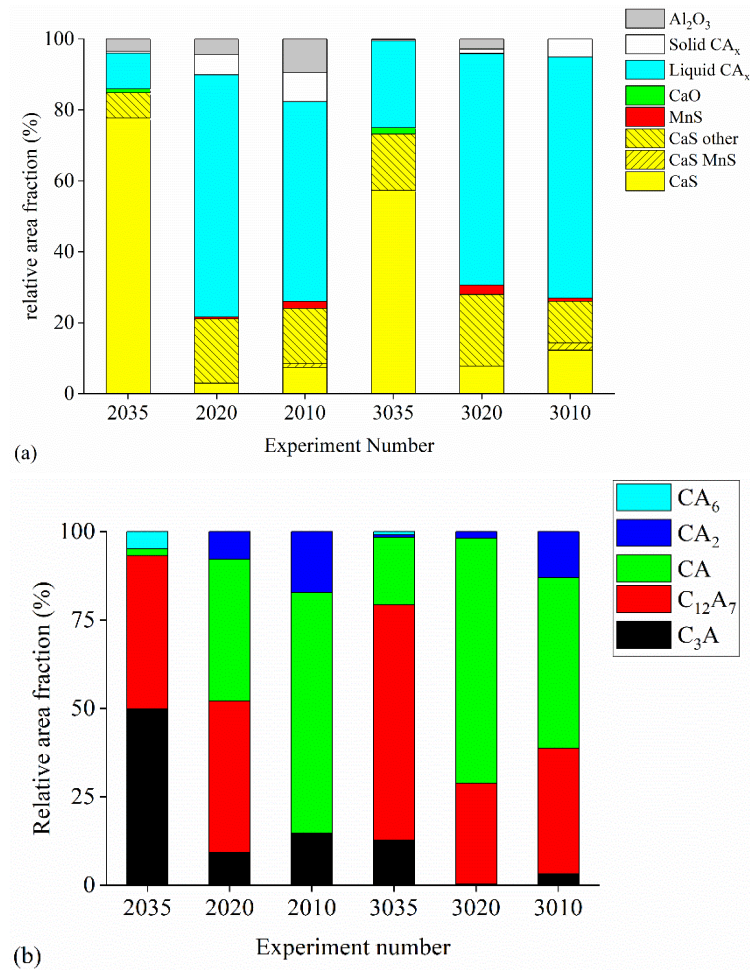


Figure 3.12 Normalized AF of (a) all inclusions and (b)  $CA_x$  inclusions in six experiments at 20 minutes after Ca addition

As inferred from Figure 3.12, a comparison of AF of  $CA_x$  inclusions can help determine a relative modification extend of specific steel chemistries as compared to that of others. However, the AF of CaS containing inclusions must also be considered when adopting the idea of Figure 3.12. Moreover, this idea of determining the extent of modification counts on inclusion analysis, which can't be conducted on-line during the production of a heat. Therefore, it is necessary to have a parameter that can be determined on-line and can also hint at the extent of modification of inclusions. For this purpose, Sun et al. [1] proposed a parameter called Ca treatment index. It is a ratio between Ca content of steel and the Al content present in the form of inclusions ( $Al_{inc}$ ). Hence, the authors propose a new parameter that can be used to estimate the extent of inclusion modification by correlating thermodynamics and measured Ca content of the steel. For this, the measured Ca content of steel and inclusion stability diagrams (given in Figure 3.7) are used to determine the location of measured Ca content in the liquid window (liquid  $CA_x$  region) of the stability diagram. The site is determined relative to the two boundaries ( $CA_2$  saturation line and CaS saturation line) of the liquid window for the steel composition of interest. This relative location measured Ca content on the stability diagram is named as

dimensionless Ca, and can be calculated using Equation (3.6). Where,  $(T.Ca)_{measured}$ ,  $(T.Ca)_{CA_2 sat.}$  And  $(T.Ca)_{CaS sat.}$  Are the measured T.Ca, T.Ca required for CA<sub>2</sub> saturation and T.Ca required for CaS saturation, respectively.  $(T.Ca)_{CA_2 sat.}$  And  $(T.Ca)_{CaS sat.}$  Are calculated by determining the functions of the CA<sub>2</sub> saturation line and CaS saturation line on the stability diagram of a given steel composition. If T.Ca falls in the liquid window, the value of dimensionless Ca would be between 0 and 1. Dimensionless Ca larger than unity and being negative indicates that the T.Ca falls in the CaS stability region and CA<sub>2</sub> stability region, respectively.

$$\text{dimensionless Ca} = \frac{(T.Ca)_{measured} - (T.Ca)_{CA_2 sat.}}{(T.Ca)_{CaS sat.} - (T.Ca)_{CA_2 sat.}} \quad (3.6)$$

$$\begin{aligned} \text{dimensionless Ca at 20 ppm T.O} \\ \approx \frac{T.Ca - 10.5}{1.128 \cdot T.S^{-0.406} \cdot T.Al^{-0.226} - 10.5} \end{aligned} \quad (3.7)$$

$(T.Ca)_{CA_2 sat.}$  And  $(T.Ca)_{CaS sat.}$  Values depend on T.O, T.S and T.Al contents of steel. These values for a value of T.O = 20 ppm are given in Equation (3.7). The developments of Equation (3.6) and Equation (3.7) are included in the appendix. The three variables: T.Ca, T.S and T.Al used to calculate Equation (3.7) can be obtained through typical online analysis, therefore it is potentially suitable for process control in industrial practice.

The proposed parameter in Equation (3.6) is validated against the obtained experimental results and industrial heats containing 20 ppm T.O. Figure 3.13 presents the calculated dimensionless Ca against the percentage of the AF of liquid CA<sub>x</sub> (CA + C<sub>12</sub>A<sub>7</sub> + C<sub>3</sub>A) present in the 20 minutes sample of all the six experiments. Having a dimensionless Ca between 0 and 1, Exp. 2020, Exp. 3020 and Exp. 3010 showed the highest inclusion liquefaction. A dimensionless Ca value slightly below 0 (Exp. 2010) led to an apparent drop in inclusion liquefaction. High dimensionless Ca values from Exp. 2035 and Exp. 3035 indicate that the measured Ca contents were in the CaS stability region and gave very low liquefaction due to the formation of CaS containing inclusions.

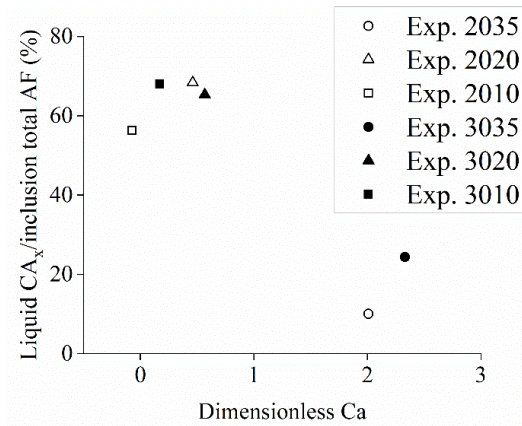


Figure 3.13 The percentage of liquid CA<sub>x</sub> dependency on dimensionless Ca in laboratory results

In addition to experimental steels, industrial heat data is also used to evaluate dimensionless Ca. Figure 3.14 (a) shows the inclusion AF change in ladle during Ca injection and AF change in the tundish samples. This heat contains 0.05C-1Mn-0.23Si-0.03Al-0.003S (values are in wt pct). Figure 3.14 (b) corresponds to a heat of 0.05C-1.2Mn-0.21Si-0.03Al-0.001S named Heat 2. The ladle samples were taken at different times after Ca injection was completed. The detailed sampling times as well as the temperatures are listed in Table 2. Both heats are about 165 t. As seen in Figure 3.14, in both heats, the percentages of liquid CA<sub>x</sub> are generally stable while CaS type inclusions increase over time. It is worth noticing that there is a sudden increase in the AF of CaS type inclusions at in L3 of Heat 1 and keep increasing in the rest of the ladle and tundish samples. Although a similar phenomenon also appears in Heat 2 starting L4, the increment in Heat 2 is no doubt much smaller.

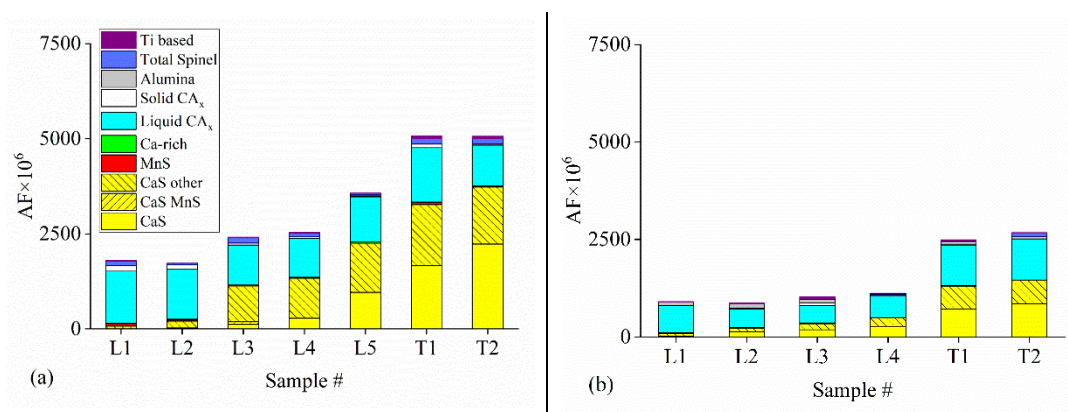


Figure 3.14 The AF of inclusions industrial heats (a) Heat 1 (b) Heat 2 (L and T represent ladle and tundish, respectively)

Table 3.2 Detailed sampling time of both industrial heats

Heat 1		Heat 2	
Sample No	Sampling time	Sample No	Sampling time
L1	1.2 minutes after Ca injection start	L1	Ca injection complete
L2	2.2 minutes after Ca injection start	L2	1.5 minutes after completion
L3	3.2 minutes after Ca injection start	L3	4.1 minutes after completion
L4	4.3 minutes after Ca injection start	L4	6.3 minutes after completion
L5	4.7 minutes after Ca injection start (Ca injection complete)		
T1	80 t cast in Tundish	T1	80 t cast in Tundish
T2	125 t cast in Tundish	T2	125 t cast in Tundish
Temperature			
Ladle		1848K	
Tundish		1833K	

By plotting the relative AF of liquid  $CA_x$  and that of solid  $CA_x$  and CaS type inclusions together against a change of dimensionless Ca, Figure 3.15 can be generated. Marks represent the relative AF, and solid lines show the evolution of dimensionless Ca. The dashed line indicates dimensionless Ca = 1 to improve visualization. During calcium addition in Heat 1, the dimensionless Ca increased from 0.32 to 2.16, and then decreased to 1.30 in the last tundish sample. It can be seen that, in the first two samples, when the dimensionless Ca was less than 1, the percentage of liquid  $CA_x$  is about 75 pct while the solid  $CA_x$  and CaS complexes are about 12 pct. MnS, spinel, and aluminate titanates also exist but are omitted because they are less than 8 pct of the total inclusion AF. As the dimensionless Ca exceeds unity, the percentage of CaS containing inclusions increased significantly, which is in line with what's shown in Figure 3.14. This results in a drastic reduction of inclusion liquefaction and agrees with the concept of introducing dimensionless Ca, as it correctly reflects the direction of inclusion liquefaction change. Although dimensionless Ca decreased in tundish samples, the steel composition would still be in the CaS stability region, the AF percentages of CaS complexes increase in the system. Similar trends were observed in the other heat shown in Figure 3.15 (b). The percentage of liquid inclusions was high as about 80 pct in sample L1 of Heat 2 while dimensionless Ca was less than 1. This phenomenon is in line with what has been observed in Heat 1. As dimensionless Ca increases to 1.76 in L2 of Heat 2, the expected decrease in liquid  $CA_x$  percentage and increase in solid inclusion percentage can be observed. After that, the fraction of liquid  $CA_x$  and CaS complexes maintain a low value. The less significant liquefaction and CaS change in Heat 2 are potentially due to low S content. Interestingly, even after dimensionless Ca decreases to less than 1 (starting at sample L4), there is no significant variation in the percentage of liquid and solid

inclusions.

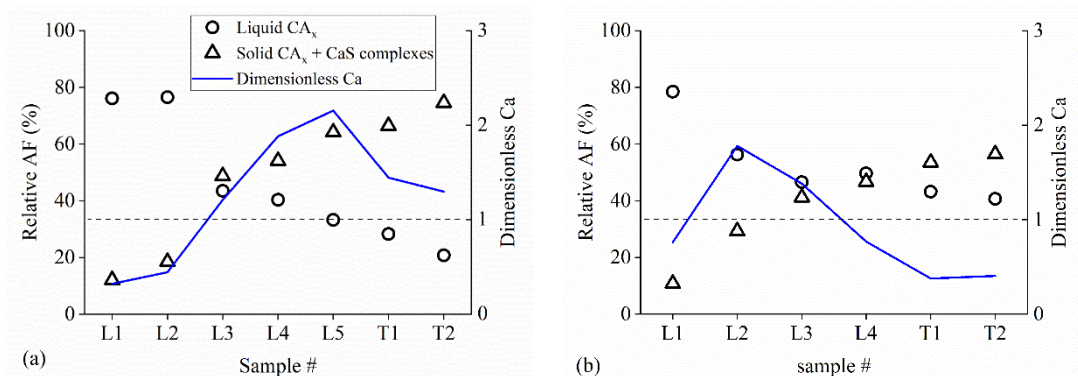


Figure 3.15 The relative AF of inclusions with respect to dimensionless Ca for industrial heats (a) Heat 1 (b) Heat 2

Results shown in Figure 3.13 to Figure 3.15 signify that there exists a strong correlation between the number of inclusions and dimensionless Ca. Hence, dimensionless Ca may be used to estimate the type of inclusions that will form if the evolution of the steel compositions is known. Moreover, due to the facile nature of Equation 6, dimensionless Ca can be applied on-line during the production process. More industrial heats will be studied in the future to confirm this finding.

The authors are aware that other means of estimating inclusion compositions, such as ratios of Ca/O and Ca/Al, have been proposed in the literature as reviewed in the introduction. The advantage of dimensionless Ca in comparison to previously proposed correlations is that the calculation of dimensionless Ca includes all of the important variables: Al, S and Ca, hence can be adapted in a wide range of compositions with no important parameter omitted in the prediction. Secondly, the direct correlation between dimensionless Ca and the fraction of liquid inclusions makes dimensionless Ca more intuitive and accessible for practical uses.

### 3.6 Conclusion

The effect of different amounts of Ca addition on the modification of inclusions was studied. The obtained results are summarized as follows:

1. The total amount of inclusions in steel depends on the amount of added Ca. In relatively high and low Ca conditions, the amount of CaS and liquid  $CA_x$  inclusions, which are respectively the thermodynamically stable inclusion types, increases with holding time.
2. Two inclusion modification mechanisms are observed in experiments. Firstly, when the Ca contents are high in the melt, CaO can be observed. Then as Ca content decreases, CaO transforms to CaS. Subsequently,  $Al_2O_3$  inclusions are modified by

CaS to CA<sub>x</sub>. The second mechanism is when the added Ca is insufficient to form CaO. In this case, Al<sub>2</sub>O<sub>3</sub> inclusions are initially modified by [Ca] then by CaS. In this case, CaS inclusions are the product of [Ca] and [S] reaction.

3. A new parameter, ‘dimensionless Ca’ is proposed in this study, which can be used to predict the extent of modification of inclusions based upon the measured Ca content of the steel. A value of dimensionless Ca between 0 and 1 suggests higher liquefaction of inclusions, whereas dimensionless Ca greater than one predicts liquefaction drop due to the increase in CaS containing inclusions. This is validated against industrial heat data.

### 3.7 Acknowledgement

The authors would like to thank the Natural Sciences and Engineering Research Council of Canada (NSERC CRDPJ=505545-16) for funding this research. The authors would also like to thank Dr. Li Sun from ArcelorMittal Dofasco for help with inclusion analysis.

### 3.8 Appendix: Simplification of dimensionless Ca calculation

Dimensionless Ca in theory can be calculated of any known chemistry. In practise, its value can be approximated for a fixed T.O. Figure 3.A1 shows the change of inclusion stability with respect to the steel chemistry. Similar graphs for different conditions can be found in the literature<sup>[78,89,196,197]</sup>. The region where steel chemistry falls in the “liquid CA<sub>x</sub>” region is referred to as the liquid window, and high inclusion liquefaction can be observed.

As shown in Figure 3.A1, the upper and lower T.Ca limits of the liquid window can be determined by the Equilibrium (3.A1) and (3.A2), respectively.



For Equilibrium (3.A1), there must exist equation (3.A3), which can be converted to equation (3.A4).

$$\Delta G = -RT \ln \left( \frac{1}{h_{Ca}^a h_{Al}^b h_S^c} \right) \quad (3.A3)$$

$$h_{Ca} = \exp\left(\frac{\Delta G}{aRT}\right) \cdot h_{Al}^{-\frac{b}{a}} h_S^{-\frac{c}{a}} \quad (3.A4)$$

C, Si, and Mn mostly dissolve in the liquid steel, so  $T.C \approx [C]$ ,  $T.Si \approx [Si]$ ,  $T.Mn \approx [Mn]$ . Taking steel with composition of 0.06C-0.25Si-1Mn (all in wt pct) as an example, the Al activity coefficient can be represented with equation (3.A5) where  $e_j^i$  and  $[i]$  are the interaction coefficient and mass fraction of component i. The interaction coefficients used can be found in the literature<sup>[11,198]</sup>. The [Ca] and [O] have low concentrations; hence they can be omitted in the calculation of the Al activity coefficient. If the steel contains 20 ppm T.O and all O exists in the form of  $Al_2O_3$ , this will only account for 23 ppm of Al, which is still about one order of magnitude lower than typical T.Al in Al-killed steels. Hence, it is considered  $T.Al \approx [Al]$  is a valid assumption in most of the cases. Taking the industrial heats from ArcelorMittal Dofasco as an example, the maximum T.Al = 0.082 wt pct. And at the upper limit of the liquid window, the amount of CaS formed will be very small, so  $T.S \approx [S]$ . Maximum T.S = 278 ppm in the industrial heats. Either using simultaneously the maximum T.Al and T.S or minimum T.Al and T.S give  $\log f_{Al}$  ranges from 0.026 to 0.03, which means always  $f_{Al} \approx 1$ . Therefore,  $h_{Al} \approx [Al] \approx T.Al$  in equation (3.A4). Following the same logic,  $h_S \approx [S] \approx T.S$ .

$$\log f_{Al} = \sum_i e_{Al}^i [i] = 0.026 + 0.045[Al] + 0.03[S] \quad (3.A5)$$

So far the author cannot find a simply correlated between Ca activity and T.Ca. It is therefore assumed:

$$h_{Ca} = k \cdot T.Ca \quad (3.A6)$$

where  $0 < k \ll 1$ . Substitute all activities to equation (3.A4), we have

$$T.Ca = \frac{1}{k} \exp\left(\frac{\Delta G}{aRT}\right) \cdot T.Al^{-\frac{b}{a}} \cdot T.S^{-\frac{c}{a}} \approx A \cdot T.S^{-j} \cdot T.Al^{-i} \quad (3.A7)$$

Assuming  $\frac{1}{k} \exp\left(\frac{\Delta G}{aRT}\right) = A$  is a constant (need to be improved in the future) and fit the upper limit T.Ca of the liquid windows at various S levels shown in Figure 3.A1 into a series of power function of T.Al, we get the equations listed in Table 3.A1. Comparing equations in Table 3.A1 and equation (3.A7), clearly the factor  $B$  satisfies  $B = A \cdot T.S^{-j}$ . Plotting  $B$  against S level in Figure 3.A2, gives a fitted function  $y = 1.128x^{-0.406}$ . Using the average of parameter I in Table 3.A1 for Equation 3.A7, we get:

$$T.Ca = 1.128 \cdot T.S^{-0.406} \cdot T.Al^{-0.226} \quad (3.A8)$$

Validating the fitted function (3.A8) against FactSage calculated upper limit T.Ca of the liquid window from 20 ppm to 80 ppm T.S, the error of T.Ca was  $\pm 4$  pct. This can be used to calculate dimensionless Ca using equation (3.A9). Constant 10.5 is the T.Ca lower limit of the liquid window, which has negligible dependence on S and Al contents. Equation (3.A8) does not incorporate the effect of other elements in steel because their effects on the liquid window are found to be insignificant within the interested steel composition ranges at 1873K.

The purpose of Equation 3.A9 is to provide a quick and more accessible approximation of dimensionless Ca for practical use, although it can only be applicable for a limited range of steel chemistries at the current stage of research.

$$\begin{aligned} & \text{dimensionless Ca at 20 ppm T.O} \\ & \frac{T.Ca - 10.5}{1.128 \cdot T.S^{-0.406} \cdot T.Al^{-0.226} - 10.5} \end{aligned} \quad (3.A9)$$

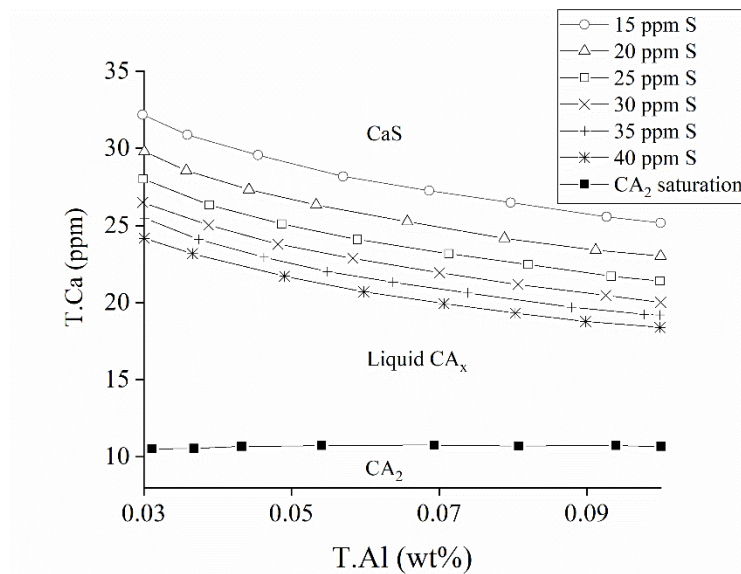


Figure 3.A1. The upper limit and lower limit T.Ca of the liquid window were calculated in FactSage assuming 20 ppm T.O and experimental temperature of 1873K

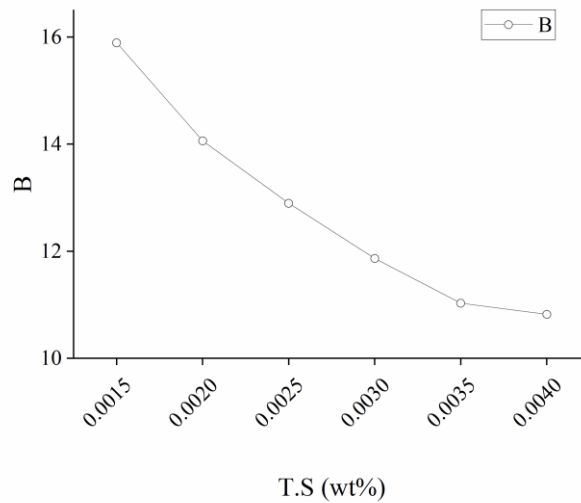


Figure 3.A2. The dependency of parameter B on T.S

Table 3.A1. Excel fitted power functions for the upper limit T.Ca of the liquid window

T.S (ppm)	Fitted function $T.Ca = B \cdot T.Al^{-i}$	R <sup>2</sup>
15	$T.Ca = 15.892 \cdot T.Al^{-0.201}$	0.9993
20	$T.Ca = 14.061 \cdot T.Al^{-0.214}$	0.9994
25	$T.Ca = 12.896 \cdot T.Al^{-0.221}$	0.9992
30	$T.Ca = 11.866 \cdot T.Al^{-0.230}$	0.9989
35	$T.Ca = 11.143 \cdot T.Al^{-0.235}$	0.9996
40	$T.Ca = 10.824 \cdot T.Al^{-0.230}$	0.9996

### 3.9 References

- 1 S. Sun, S. Waterfall, N. Strobl, D. Liao, and D. Holdridge: *Miner. Met. Mater. Ser.*, 2017, vol. Part F5, pp. 347–57.
- 2 E.T. Turkdogan: *Fundamentals of Steelmaking*, The Institute of Materials, London, 1996.
- 3 W. Yang, L.F. Zhang, X. Wang, Y. Ren, X. Liu, and Q. Shan: *ISIJ Int.*, 2013, vol. 53, pp. 1401–10.
- 4 N. Verma, P.C. Pistorius, R.J. Fruehan, M.S. Potter, H.G. Oltmann, and E.B. Pretorius: *Metall. Mater. Trans. B Process Metall. Mater. Process. Sci.*, 2012, vol. 43, pp. 830–40.
- 5 K. Yang, S., Zhang, L., Sun, L., Li, J., and Peaslee: *AISTech 2011 Proc.*
- 6 S.F. Yang, J.S. Li, Z.F. Wang, J. Li, and L. Lin: *Int. J. Miner. Metall. Mater.*, 2011, vol. 18, pp. 18–23.
- 7 D. Zhao, H. Li, C. Bao, and J. Yang: *ISIJ Int.*, 2015, vol. 55, pp. 2115–24.
- 8 S.K. Choudhary and A. Ghosh: *ISIJ Int.*, 2008, vol. 48, pp. 1552–9.

- 9 G. Yang and X. Wang: *ISIJ Int.*, 2015, vol. 55, pp. 126–33.
- 10 J. Xu, F. Huang, and X. Wang: *Metall. Mater. Trans. B*, 2016, vol. 47, pp. 1217–27.
- 11 Z. Deng and M. Zhu: *Steel Res. Int.*, 2013, vol. 84, pp. 519–25.
- 12 G.M. Faulring, J.W. Farrell, and D.C. Hilty: *Ironmak. Steelmak.*, 1980, vol. 7, pp. 14–20.
- 13 S. Yang, Q. Wang, L. Zhang, J. Li, and K. Peaslee: *Metall. Mater. Trans. B*, 2012, vol. 43, pp. 731–50.
- 14 J.H. Park, D.S. Kim, and S.B. Lee: *Metall. Mater. Trans. B Process Metall. Mater. Process. Sci.*, 2005, vol. 36, pp. 67–73.
- 15 D. Lu: PhD Thesis, McMaster University, 1992.
- 16 L. Holappa, M. Hämäläinen, M. Liukkonen, and M. Lind: *Ironmak. Steelmak.*, 2003, vol. 30, pp. 111–5.
- 17 Y. Tabatabaei, K.S. Coley, G.A. Irons, and S. Sun: *Metall. Mater. Trans. B Process Metall. Mater. Process. Sci.*, 2018, vol. 49, pp. 375–87.
- 18 Y. Tabatabaei, K.S. Coley, G.A. Irons, and S. Sun: *Metall. Mater. Trans. B Process Metall. Mater. Process. Sci.*, 2018, vol. 49, pp. 2022–37.
- 19 M. Lind and L. Holappa: *Metall. Mater. Trans. B Process Metall. Mater. Process. Sci.*, 2010, vol. 41, pp. 359–66.
- 20 N. Verma, P.C. Pistorius, R.J. Fruehan, M. Potter, M. Lind, and S.R. Story: *Metall. Mater. Trans. B Process Metall. Mater. Process. Sci.*, 2011, vol. 42, pp. 720–9.
- 21 Y. Liu, L. Zhang, Y. Zhang, H. Duan, Y. Ren, and W. Yang: *Metall. Mater. Trans. B Process Metall. Mater. Process. Sci.*, 2018, vol. 49, pp. 610–26.
- 22 Z.J. Han, L. Liu, M. Lind, and L. Holappa: *Acta Metall. Sin. (English Lett.)*, 2006, vol. 19, pp. 1–8.
- 23 Y. Ito, M. Suda, Y. Kato, H. Nakato, and K. Sorimachi: *ISIJ Int.*, 1996, vol. 36, pp. S148–50.
- 24 M.K. Sardar, S. Mukhopadhyay, U.K. Bandopadhyay, and S.K. Dhua: *Steel Res. Int.*, 2007, vol. 78, pp. 136–40.
- 25 J.M.A. Geldenhuis and P.C. Pistorius: *Ironmak. Steelmak.*, 2000, vol. 27, pp. 442–9.
- 26 Y. Ren, L.F. Zhang, and S. Li: *ISIJ Int.*, 2014, vol. 54, pp. 2772–9.
- 27 V. Gollapalli, M.B.V. Rao, P.S. Karamched, C.R. Borra, G.G. Roy, and P. Srirangam: *Ironmak. Steelmak.*, 2018, pp. 1–8.
- 28 X. Wang, X. Li, Q. Li, F. Huang, H. Li, and J. Yang: *Steel Res. Int.*, 2014, vol. 85, pp. 155–63.
- 29 Y. Higuchi, M. Numata, S. Fukagawa, and K. Shinme: *ISIJ Int.*, 1996, vol. 36, pp. S151–4.
- 30 N. Verma, P.C. Pistorius, R.J. Fruehan, M. Potter, M. Lind, and S. Story: *Metall. Mater. Trans. B Process Metall. Mater. Process. Sci.*, 2011, vol. 42, pp. 711–9.
- 31 S. Sun, L. Sun, S. Waterfall and D. Liao, ArcelorMittal Global R&D – Hamilton: in *Proceedings of 2018 China Symposium on Sustainable Steelmaking Technology*, vol. 2, Tianjing, 2018
- 32 S. Wang, J. Zhang, R. Cheng, and H. Ma: *Trans. Indian Inst. Met.*, 2018, vol. 71, pp.

2231–42.

33 W.V. Bielefeldt and A.C.F. Vilela: *Steel Res. Int.*, 2015, vol. 86, pp. 375–85.

34 Japan Society for the Promotion of Science: *Steelmaking Data Sourcebook*, Gordon and Breach Science Publishers, New York, 1988.

## **Chapter 4 Evaluation of Ca Treatment on Oxide and Sulfide Inclusions through Modification Indexes**

This chapter is a pre-publication version of the article published in Metallurgical and Materials Transactions B 2021, Volume 52, DOI: 10.1007/s11663-021-02243-1. This chapter was inspired by the qualitative dependency of the fraction of liquid inclusions on CaS stability discussed in Chapter 3. As the three major purposes of calcium treatment are  $CA_x$ , CaS, and MnS control, a modification index is proposed for each inclusion type in this chapter. Even though some modification indexes have already been proposed in the literature, they mainly focus on the composition of inclusions while omitting the quantity of inclusions. To fill this knowledge gap, the modification results of inclusions in thirty-seven tundish samples were used to establish the modification indexes. The success of  $CA_x$  type inclusion control can be related to the percentage of inclusions with higher than 50 pct liquefaction, as it prevents inclusion agglomeration. It was known that the fraction of the liquid phase increases with CaO content in  $CA_x$ , so the percentage of liquid  $CA_x$  inclusions was qualitatively correlated with the ratio of Ca content to Al content in steel, which is the first modification index. In Chapter 3, the amount of CaS inclusions was found to drastically increase after it becomes thermodynamically stable. The industrial data suggests as the area fraction of CaS inclusions on the sample surface analyzed increased linearly with dimensionless Ca. Therefore, dimensionless Ca, which is a function of Ca, Al, and S contents, was considered the second modification index to quantify the success of CaS inclusion control. The third modification index introduced in this chapter determines the Ca content to S content ratio needed to prevent the formation of MnS inclusions as well as correlates the distribution of S between CaS and MnS inclusions with the Ca content to S content ratio.

Moreover, the modification indexes proposed before were never considered together to provide an overall assessment of the modification results of multiple inclusion types. The method proposed in this chapter quantifies this overall success level of inclusion control by calculating the deviation of actual Ca content from the ideal Ca content calculated based on the three modification indexes introduced. This method was validated using industrial data. In addition, a method of predicting optimum Ca content was also established using the same knowledge basis.

The industrial samples and associated inclusion analysis were completed by ArcelorMittal Dofasco and shared with the author by Dr. Stanley Sun. The analysis based on these results and drafting of the manuscript were conducted by the primary author. The contributions of all co-authors, Dr. Muhammad Nabeel and Dr. Neslihan Dogan include providing suggestions and revising the manuscript. Dr. Stanley Sun also participated in the manuscript revision process.

## Coarsening Mechanisms of CaS Inclusion in Ca-Treated Steels

Keyan Miao\*, Muhammad Nabeel, Neslihan Dogan

Keyan Miao, Ph.D Student, [miaok@mcmaster.ca](mailto:miaok@mcmaster.ca)

Department of Materials Science and Engineering, McMaster University, 1280 Main Steet West, Hamilton, Ontario, L8S4L8, Canada

Muhammad Nabeel, Postdoctoral Fellow,

Department of Materials Science and Engineering, McMaster University, 1280 Main Steet West, Hamilton, Ontario, L8S4L8, Canada

Neslihan Dogan, Associate Professor

Department of Materials Science and Engineering, McMaster University, 1280 Main Steet West, Hamilton, Ontario, L8S4L8, Canada

### Abstract

In this work, 37 industrial trials were conducted to examine the effect of Ca treatment on inclusion formation and transformation. The samples were taken from tundish and separated into three series based on their compositions. Three correlations between the steel chemistries and the amount as well as the composition of inclusions were determined through inclusion analysis using an automated SEM-EDS system and with the help of a segregation model. Firstly, a modified Ca treatment index was introduced which correlated the composition of modified calcium aluminates to Ca, S, and Al content in the system. For modified Ca treatment index higher than 0.5, the calcium aluminates were found to contain more than 50 wt pct liquid phase. The second index was dimensionless Ca which signifies that the amount of CaS inclusions in a system depends on the thermodynamics stability of CaS. It was used to estimate the area fraction of CaS inclusions. The third index was related to the control of MnS inclusion formation using Ca treatment and it was found that the Ca, S and Mn contents can be used to predict the level of success of MnS inclusion control. Further, the phase of steel may also have an impact on MnS formation. A method of integrating the correlations between steel chemistries and calcium aluminate, CaS, and MnS inclusions to determine the overall success in inclusion control was proposed, which has the potential of predicting the optimum Ca content.

### 4.1 Introduction

Injecting Ca into liquid steel has been an effective method of modifying detrimental inclusions to desirable conditions <sup>[1-4]</sup>. For example, modification of Al<sub>2</sub>O<sub>3</sub> inclusions produces calcium aluminates, CA<sub>x</sub>, where C and A denote CaO and Al<sub>2</sub>O<sub>3</sub>, respectively.

At the same time, CaS may form because of the strong affinity of S to Ca <sup>[5-7]</sup>. Both improperly modified solid CA<sub>x</sub>, which are CA<sub>2</sub>, CA<sub>6</sub> and similar compositions, and excess CaS inclusions are detrimental to the production process due to their tendency to cause nozzle clogging <sup>[8,9]</sup>. Despite the presence of MnS inclusions improving the machinability of some steel grades <sup>[10,11]</sup>, MnS is considered another undesirable inclusion due to its adverse effects on the strength of steel and corrosion resistance <sup>[12-15]</sup>. From the perspective of MnS inclusion control, forming a moderate amount of CaS inclusions through Ca treatment is beneficial because Ca reacting with S reduces the content of dissolved S, [S], to react with Mn in the later process and overall reduces the amount of MnS inclusions. The square brackets, [i], denote the content of component I dissolved in steel. All compositions are in wt pct unless noted.

Many studies related to calcium treatment were based on laboratory experiments <sup>[3,16-21]</sup>, and agreements were found in numerous industrial data, many of which were obtained from the ladle <sup>[2,5,22-28]</sup>. There are also several studies on the characteristics of inclusions in tundish <sup>[29-32]</sup>. It has been suggested that the alumina inclusions are modified to calcium aluminates through a partly direct reaction with the calcium added and partly with CaS that usually formed as a transient phase in the early stage of the treatment. Based on those modification mechanisms, few steel chemistry-based parameters had been proposed in the literature as guidelines to help improve inclusion modification strategy. The suggested parameters varied from straightforward as total calcium, *T.Ca*, to total oxygen, *T.O*, ratio <sup>[16,17]</sup>, to more sophisticated ones like indexes derived based on thermodynamics and mass balance <sup>[33-36]</sup>. In the work of Story et al. <sup>[36]</sup>, a “modified Ca/Al ratio” was introduced and correlated with the clogging behavior of the submerged entry nozzles. The modified Ca/Al ratio equation is shown in Equation (4.1), which essentially describes CaO to Al<sub>2</sub>O<sub>3</sub> atomic concentration ratios in CA<sub>x</sub> inclusions. The values are calculated using the atomic percentage of Ca, S and Al in inclusions. The round brackets, (i), denote the content of component I in inclusions. Ca exists both as CaO and CaS in CA<sub>x</sub>, but CA<sub>x</sub> has around 2 at pct S solubility, hence the term “-(S) + 2” was included in the numerator. By comparing the modified Ca/Al ratio with the industrial data on clogging during the casting, Story et al. <sup>[36]</sup> reported stable casting when the ratio was between 0.4 and 0.8. Higher values led to ladle gate erosion. The correlation between the modified Ca/Al ratio, and modification results were also discussed in a few other studies <sup>[7,37,38]</sup>, and similar observations were reported. Stable casting was also reported when modified Ca/Al ratios were > 0.4. The limitation of the modified Ca/Al ratio is that it cannot be directly applicable to industrial operations. Equation (4.1) does not use the melt composition, thereby it does not provide information on how much Ca should be added for better inclusion control. The production is most likely finished by the time inclusion compositions are known. Ca treatment index shown as Equation (4.2) proposed by Sun et al. <sup>[35]</sup> used similar concept to predict the modification results. It was the ratio between total Ca content, *T.Ca*, and Al content in inclusions, (Al), expressed as the difference between the total Al content, *T.Al*, and Al

dissolved in liquid steel, [Al]. Sun et al. [35] reported that due to decrease in solid inclusions, the tendency of nozzle clogging was reduced when the Ca treatment index was higher than 0.6. However, the effect of S was not incorporated in Equation (4.2). On the other hand, an oxygen partition coefficient (OPC) was proposed by Imagumbai and Takeda [33] to describe the distribution of O content between CaO and alumina-silicate. The parameter was derived from the thermodynamic data. The OPC is a function of Ca, O, and S contents in the melt and was successfully validated against 16 samples from ingots. The samples had somewhat similar compositions; therefore, even though there was no doubt about the scientific significance of the finding, it was not clear whether OPC is widely applicable for predicting the inclusion compositions.

$$\text{Modified Ca/Al} = \frac{(\text{Ca}) - (\text{S}) + 2}{(\text{Al})} \quad (4.1)$$

$$\text{Ca treatment index} = \frac{T. \text{Ca}}{T. \text{Al} - [\text{Al}]} \quad (4.2)$$

The effects of calcium and rare earth element (RE) addition on MnS inclusions had been studied in the past [39–44]. Generally, consistent findings were reported in these studies. CaS was found to form compounds with MnS and remedied the physical and chemical properties of MnS inclusions. However, due to the metal chemistry differences between studies, different modification indexes were given. Tomita [43] reported that  $T.\text{Ca}/T.\text{S}$  ratio of 3 (wt pct / wt pct) drastically reduced the number of stringy type MnS inclusions in the steel sample containing around 0.4C-0.2Si-0.74Mn-0.03Al-0.002S-0.0012O (in wt pct).  $T.\text{S}$  is the total S content. While in the work of Blais et al. [42],  $T.\text{Ca}/T.\text{S} = 1$  (wt pct / wt pct) was suggested to be the optimum concentration for shape control but without reporting the steel chemistries. Shi et al. [44] observed the behavior of MnS inclusions with a range of rare earth elements, RE, and Ca combinations in ingots containing 0.19C-1.4Mn-0.41Si-0.023P (in wt pct) and suggested that effective inclusion modification requires  $[T.\text{RE}/T.\text{S}] + 1.875[T.\text{Ca}/T.\text{S}] = 3$  (in wt pct / wt pct). However, limitations exist for large-scale application because of the potential of forming oxides of RE and economic reasons [41]. In the study of Imagumbai and Takeda [33], a sulfur partition coefficient (SPC) was proposed, but this coefficient was validated against limited industrial data. Only samples with around 0.04C-0.3Si-1.5Mn-0.027Al-0.0025S-0.029O (all in wt pct) were examined.

The present study aims to study the effects of steel chemistry on the modification of oxide inclusions and formation of sulfide inclusions by calcium treatment and apply correlations using steel chemistry to propose optimum Ca additions in steel refining units. A number of industrial data were analyzed using an automated SEM-EDS analysis. The effectiveness of Ca addition was evaluated by thermodynamics and kinetics-based calculation. Based on the findings, correlations between the steel chemistries and

inclusion composition and amount were reported. Explanations were provided for insufficient MnS control in a series of heats using a segregation model.

## 4.2 Industrial trial

The industrial heats of high strength low alloyed (HSLA) steel were produced in a 165 t ladle, through the EAF-LF-CC processes. Al was introduced during the ladle refining to reduce dissolved oxygen, [O]. Close to the end of ladle treatment, Ca wire was added to modify the remaining inclusions. The amount of Ca added varied depending on the composition of corresponding heats.

A lollipop sample was taken from the tundish when about half of the heat had been cast. The temperature of the tundish was 1833 K. An image of a typical sample is shown in Figure 4.1. The lollipop samples were approximately 10 mm × 32 mm × 35 mm. Each sample was cut at around 17 mm from the lower end. The exposed surface was cleaned, polished, and analyzed using an automated SEM-EDS system, ASPEX. The inclusions in lollipop samples were mainly formed at 1833 K. Another piece of the sample was used to obtain the chemical compositions through the technique of spark OES-PDA (optical emission spectrometry pulse height distribution analysis).

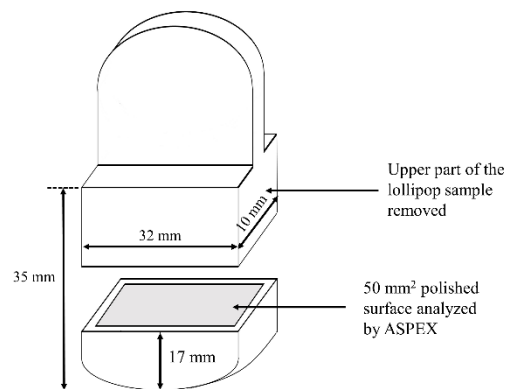


Figure 4.1 Schematic diagram of industrial sample.

The detailed working principle of ASPEX is described elsewhere <sup>[34]</sup>. Generally, the automated SEM identifies inclusions based on their contrast with the steel matrix. Then 16 evenly spaced chords pass through the geometric center to obtain morphological information. The present analysis included only inclusions with a maximum diameter (longest of the 16 chords) larger than 2  $\mu\text{m}$ . The smaller inclusions were considered to show less detrimental effects on product quality, and including those in the study drastically accelerates the processing time of ASPEX. In the end, the inclusions were classified into different types based on the average composition of the inclusion's exposed surface.

All heats are divided into three series based on their Mn and C contents. The composition range of major constituents is shown in Table 4.1. Series 1 had relatively low C and Mn contents, while Series 2 had higher C and Mn contents. In Series 3, the C contents were close to that of Series 1 heats, while Mn contents were close to that of Series 2 heats. The three series shared similar S, Al, and Ca ranges. These heats have S levels between 10 ppm and 40 ppm. Al contents varied from 0.03 wt pct to 0.06 wt pct, and Ca contents ranged from 20 ppm to 40 ppm. The Si contents were lower in Series 1, but that was expected to show an insignificant impact on inclusions. Since the samples were taken from tundish, which is a long time after deoxidation, they are considered to have a similar 20 ppm T.O as the number of samples measured in the past.

Table 4.1 The composition ranges of industrial heats in Series 1, 2, and 3

	C (wt pct)	Mn (wt pct)	S (ppm)	Si (wt pct)	Al (wt pct)	Ca (ppm)
Series 1	0.06	0.52–0.57	18–40	0.03–0.06	0.03–0.05	16–38
Series 2	0.18–0.21	0.87–1.04	10–41	0.21–0.26	0.03–0.05	13–37
Series 3	0.05–0.06	1.07–1.19	10–29	0.21–0.23	0.03–0.04	23–35

### 4.3 Results and Discussion

In this work, area fraction (AF) was used to quantify the amount of inclusions. It was calculated using Equation (4.3), where  $A_{inclusion}$  is the area of inclusions on a cross section of steel matrix analyzed by ASPEX, and  $A_{steel}$  is the area of the steel cross section analyzed by ASPEX. The AF was used instead of number density, as the trends exhibited using the latter were identical to those of AF. Figure 4.2 compares the AF of different types of inclusions classified by ASPEX in all analyzed heats. The method of inclusion classification by ASPEX was explained elsewhere [45], and the accuracy had been introduced in the authors' previous work [34]. The principle is that an inclusion is classified based on the average EDS results of the analyzed surface. For example, an inclusion with Al larger than x wt pct will be classified as  $Al_2O_3$ .

$$AF = \frac{A_{inclusion}}{A_{steel}} \quad (4.3)$$

Liquid  $CA_x$ , CaS, and CaS-other were typical inclusion types. Liquid  $CA_x$  inclusions includes CA,  $C_{12}A_7$ , and  $C_3A$ , and CaS-other inclusions with compositions between CaS and  $CA_x$ . The liquid  $CA_x$  inclusions were observed in every heat, and their values varied from 2 ppm to about 40 ppm. In most heats, AF of liquid  $CA_x$  was around 20 ppm to 30 ppm. On the contrary, solid  $CA_x$ ,  $CA_2$  and  $CA_6$ , were only slightly noticeable in Series 1, with only two heats having more than 9 ppm solid  $CA_x$  AF while the rest were lower than 7 ppm. In Series 1 and 2, all heats except one had CaS-other AF lower than 28 ppm,

while in Series 3, the minimum was 31 ppm when disregarding the 1<sup>st</sup> heat shown in Figure 4.2 (c). A similar trend was also observed for the AF of CaS type inclusions, which reached 30 ppm in Series 1 and 2 and ranged from 27 ppm to 51 ppm in Series 3 except one heat that also had low CaS-other AF. In series 2, a noticeable amount of MnS type inclusions was observed. Other inclusions also appeared, but their AF was not significant in almost all heats.

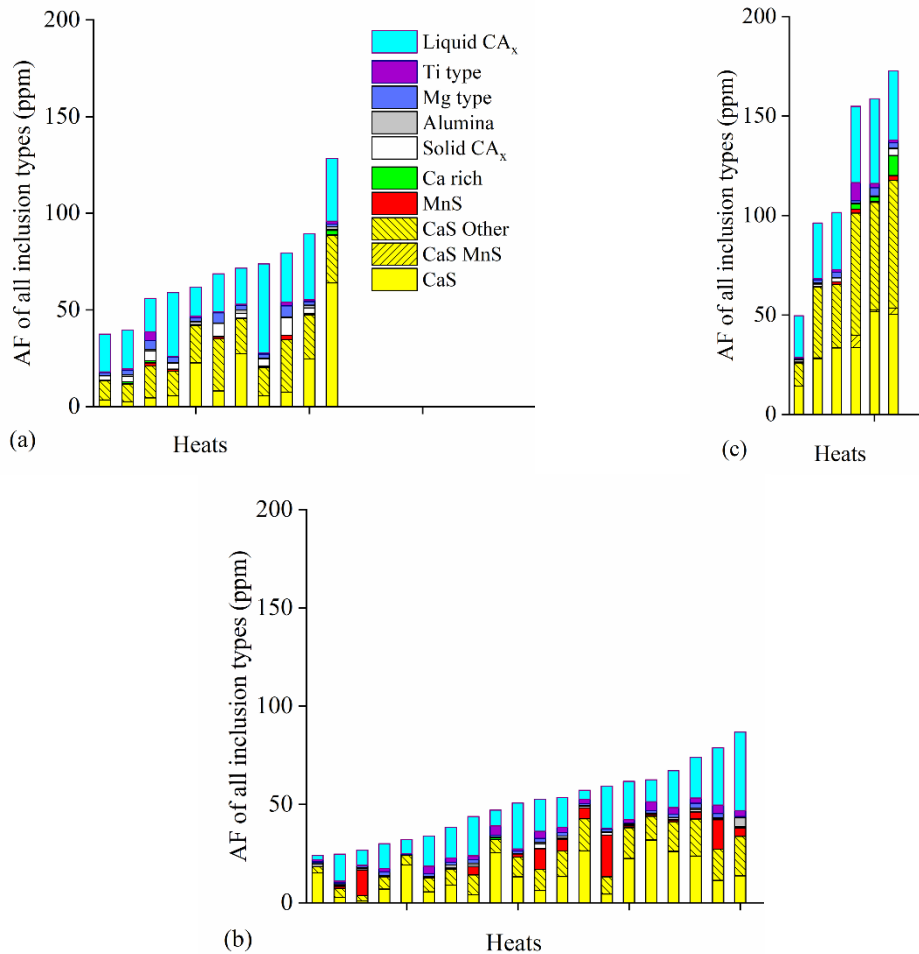


Figure 4.2 AF of all inclusion types in tundish samples from (a) Series 1, (b) Series 2, and (c) Series 3 heats. Heats were categorized into Series 1, 2, 3 based on their average Mn contents 0.55, 0.96, and 1.13 wt pct, respectively.

The authors intended to correlate modification extent of inclusions with the chemistry of liquid steel, which can be measured online (or at least within a very short time after samples are taken from ladle and tundish using the spark analysis) and provide suggestions on the Ca addition strategy. A higher  $CA_x$  modification extent can be achieved by increasing the amount of Ca addition. However, since excess Ca addition leads to over-modification and is not economical, suggesting an optimum Ca content would be necessary. So as a start, Figure 4.3 was generated to show the effects of Ca content on the AF of all inclusion types in each heat.

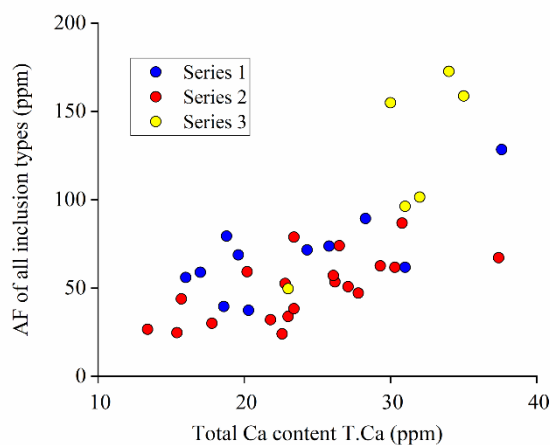


Figure 4.3 Change of area fraction (AF) of total inclusion as a function of total Ca (T. Ca) content in steel samples in Series 1, 2, and 3 heats.

Overall, an increasing trend can be observed in Figure 4.3. This should not be surprising as more CaS inclusions form with additional Ca available for reaction. When increasing *T.Ca* from 13 ppm to 38 ppm, the total AF increased from about 20 ppm to over 100 ppm. The AF was higher than 100 ppm in four heats. Among them, three were from Series 3, and the AF of those was close to 150 ppm. Those were significantly higher total inclusion AF than the two other Series 3 of similar *T.Ca* as well as heats from Series 1 and Series 2. So although the pattern in Figure 4.3 appeared to suggest a relationship between *T.Ca* and the area fraction of inclusions, the correlation needs to be further refined by considering the interplay with other steel constituents. In the following sections, the relationship between inclusion types and steel chemistries will be discussed.

#### 4.3.1 Effect of Ca, S and Al on calcium aluminate inclusions

Figure 4.2 shows the solid  $CA_x$  essentially only existed in Series 1 heats, and their AF values were usually much smaller than AF of liquid  $CA_x$  inclusions. This finding implied that the oxide modification had been successfully carried out in most heats. Nevertheless, it is still essential to understand what caused the different solid  $CA_x$  and liquid  $CA_x$  combinations. And once known, one should be able to find the optimum chemistry range to achieve a high modification extent. A number of parameters and indexes were suggested in the literature, and among them, the ‘modified Ca/Al ratio’ proposed by Story et al. <sup>[36]</sup> appeared to provide a reasonable explanation for the phenomenon observed in the present study. As shown in Equation (4.1), the modified Ca/Al ratio is a function of Ca, S, and Al concentrations in inclusions that can only be obtained after the production; hence it cannot be directly applied to optimize the Ca treatment strategy during steel refining. The Ca treatment index in Equation (4.2) by Sun et al. <sup>[35]</sup> used the steel concentration but did not consider the effects of S. In this study, modified Ca

treatment index (modified CTI) shown in Equation (4.4) was established based on the steel compositions. Similar to the modified Ca/Al ratio, the numerator of Equation (4.4) was also meant to quantify the Ca that forms CaO. The authors were aware that not all the S content participated in CaS formation, but  $T.S$  was nevertheless used as an estimation. The term  $T.Al-[Al]$  represented the amount of Al that forms  $Al_2O_3$ , where  $[Al]$  denoted dissolved Al concentration in steel. The dissolved and undissolved Al concentrations were measured using spark OES-PDA. A higher value of modified CTI would mean a high  $CaO/Al_2O_3$  ratio (wt pct/ wt pct), C/A ratio for short, in  $CA_x$ . To help visualize it, two extreme cases of  $CA_x$  inclusion composition distribution on the  $CaO-Al_2O_3-CaS$  diagram are given in Figure 4.4. The two other major inclusion types: CaS and CaS-other seen in Figure 4.2 are included to further explain these inclusion types' compositions. The dashed line represents the 50 wt pct liquid inclusion calculated using FactSage 8.0, and each circle represents a single inclusion. All five types of  $CA_x$  inclusions classified by ASPEX as  $C_3A$ ,  $C_{12}A_7$ , CA,  $CA_2$ , and  $CA_6$ , are included. In open literature, it is well established that partially liquid calcium aluminates can largely suppress the clogging of the nozzles. A few studies [3,30,46,47] proposed that achieving 50 wt pct liquid inclusion can be considered as the indication of successful modification. The authors used the same approach in the present work. When modified CTI was -1.8, most  $CA_x$  inclusions can be found outside the 50 wt pct liquid region in Figure 4.4 (a), and were classified as mainly  $CA_2$  and  $CA_6$  inclusions. In Figure 4.4 (b), when modified CTI was 1.7, other than four inclusions located adjacent to the  $Al_2O_3$ , all  $CA_x$  inclusions contained more than 50 wt pct liquid phase. These inclusions were  $C_3A$ ,  $C_{12}A_7$ , and a small fraction of CA with high  $CaO/Al_2O_3$  ratios.

$$\text{Modified Ca treatment index} = \frac{T.Ca - T.S}{T.Al - [Al]} \quad (4.4)$$

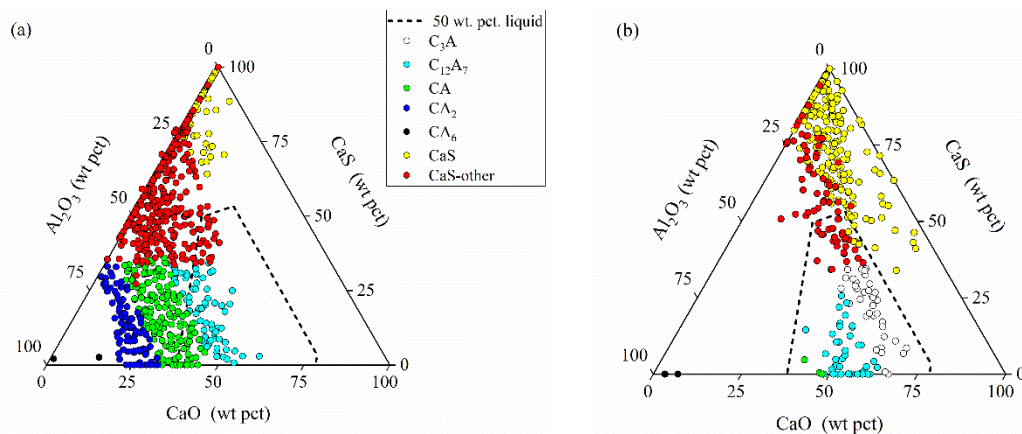


Figure 4.4 Examples of  $CA_x$ , CaS, and CaS-other inclusion composition distribution on a  $CaO-Al_2O_3-CaS$  ternary diagram at 1833K from (a) a heat with modified CTI = -1.8 and (b) a heat with modified CTI = 1.7.

Figure 4.5 shows the relationship between the average  $CaO/Al_2O_3$  ratio (wt pct/ wt pct)

of  $CA_x$  inclusions and the steel chemistries in all heats. As expected, a positive correlation can be observed. The upper and lower bars are 1.28 times of standard deviation, corresponding to about 80 pct composition coverage. When the modified CTI was -2, the average C/A ratios were around 0.5. As the modified CTI gradually increased, the average C/A ratio rose to about 1.3. The horizontal line represents C/A ratio equals 0.38, which is similar to the lower bound of the C/A ratio to achieve 50 wt pct liquid on a CaO-Al<sub>2</sub>O<sub>3</sub>-CaS ternary diagram at 1833K (close to tundish temperature). Comparing the 80 pct C/A ratio coverage with the dashed line in Figure 4.5 showed that when the modified CTI was between -2 and -0.5, almost every heat would have a noticeable amount of  $CA_x$  with a C/A ratio < 0.38. That means a significant fraction of the  $CA_x$  inclusions can be found outside the 50 wt pct liquid region, similar to Figure 4.4 (a). When modified CTI approached 0, more heats had a C/A ratio above the dashed line. When the modified CTI was higher than 0.5, the entire 80 pct C/A ratio coverage was consistently located above the 0.38 C/A ratio. In other words, around 90 pct of the  $CA_x$  can be found in the 50 wt pct liquid windows. It is therefore a logical inference that modified CTI > 0.5 would result in a good modification of  $CA_x$ .

The CaS-other inclusions are a combination of CaO-Al<sub>2</sub>O<sub>3</sub>-CaS. It has been established in a previous study [34] that they are intermediates for  $CA_x$  modified by CaS. The C/A ratios of CaS-other, although not shown but also exhibited a similar trend as Figure 4.5, but were mostly outside the 50 wt pct liquid region due to high CaS content in them.

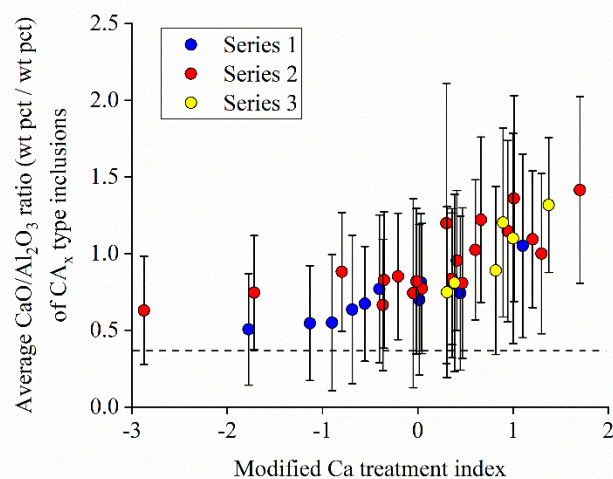


Figure 4.5 Change of average CaO/Al<sub>2</sub>O<sub>3</sub> ratio of  $CA_x$  with steel chemistry in tundish samples.

In the authors' previous study, the parameter "dimensionless Ca" was introduced [34]. The relationship between dimensionless Ca and steel compositions at 1873 K is shown in a previous publication [34], but can be adjusted to be used for the temperature of 1833 K related to tundish operations as shown in Equation (4.5). The concept can be best

explained with the aid of a stability diagram, as shown in Figure 4.6. The stable phases below “liquid CA<sub>x</sub> + CA<sub>2</sub>” were omitted. For the calculations, T.O was assumed to be 20 ppm, and the temperature was considered 1833 K. When Ca content increases, the stable phases change from CA<sub>2</sub> + liquid CA<sub>x</sub> to liquid CA<sub>x</sub>, then liquid CA<sub>x</sub> + CaS. In the liquid CA<sub>x</sub> only region, dimensionless Ca increases from 0 and reaches 1 when thermodynamically stable CaS starts to form. In the liquid CA<sub>x</sub> + CaS region, the Ca content is further away from the phase boundary where CaS becomes stable; more CaS inclusions are expected to form. Dimensionless Ca quantifies the relation between steel chemistry and the stability of CaS. A dimensionless Ca < 1 indicates that only the liquid CA<sub>x</sub> inclusions are in the stable region, while dimensionless Ca > 1 means that the CaS also becomes stable. In other words, dimensionless Ca can be directly connected to the amount of CaS. The fractions of liquid CA<sub>x</sub> and CaS containing inclusions were proven to drastically decrease and increase, respectively, when dimensionless Ca exceeded 1 [34].

$$\text{Dim. Ca}_{1833\text{K}} = \frac{T.\text{Ca} - 14.7}{1.671 \cdot T.\text{S}^{-0.315} \cdot T.\text{Al}^{-0.207} - 14.7} \quad (4.5)$$

It is important to note that the dimensionless Ca does not provide any insight into the compositions of CA<sub>x</sub> inclusions. That was simply because of the lack of connection between the physical meaning of dimensionless Ca and CA<sub>x</sub>. As visualized in Figure 4.7, the average C/A ratio exhibited no apparent relation with dimensionless Ca. Therefore, it became reasonable to correlate dimensionless Ca with the characteristics of CaS containing inclusions but not with CA<sub>x</sub> inclusions, which is discussed in the following section.

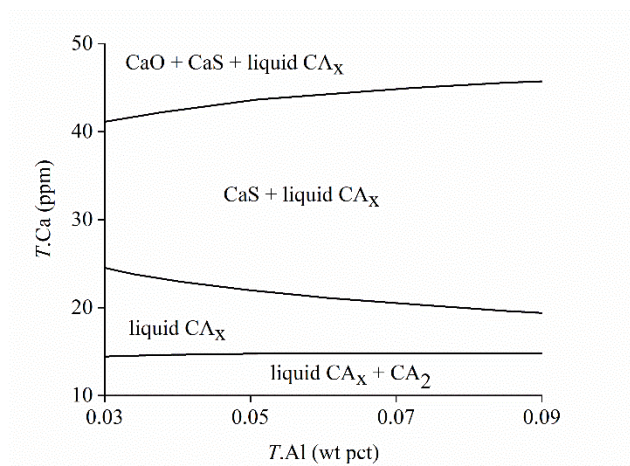


Figure 4.6 Inclusion stability diagram obtained using FactSage for steel containing 20 ppm S, 0.06 wt pct C, 0.25 wt pct Si, 1 wt pct Mn and 20 ppm T.O at 1833 K.

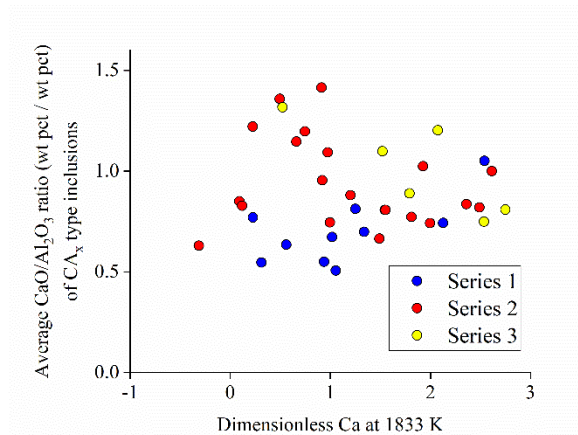


Figure 4.7 Relationship between average CaO/Al<sub>2</sub>O<sub>3</sub> ratio in CA<sub>x</sub> type inclusions and dimensionless Ca at 1833 K in industrial samples.

#### 4.3.2 Effect of Ca, S and Al on CaS containing inclusions

The sum of AF of CaS phase in all inclusions are plotted against the dimensionless Ca, and the results are shown in Figure 4.8. The AF of CaS phase in an inclusion, AF<sub>CaS</sub>, was obtained through first converting EDS results of the inclusion to a combination of CaO, Al<sub>2</sub>O<sub>3</sub>, CaS, MgO, MnS, and TiO<sub>2</sub>, then multiplying AF of that inclusion and the weight percentage of CaS in that inclusion. The sum of the AF<sub>CaS</sub> of all inclusions detected in a sample, T.AF<sub>CaS</sub> for short, is the y-axis of Figure 4.8 (a). The 1833 K dimensionless Ca were calculated using Equation (4.5).

Figure 4.8 (a) shows that the T.AF<sub>CaS</sub> increased linearly with dimensionless Ca. The maximum y-axis value was 80 ppm. In heats with dimensionless Ca range from 0 to 1, T.AF<sub>CaS</sub> were all lower than 25 ppm. In these heats, CaS inclusions were not thermodynamically stable. They are assumed to be formed during solidification; and did not exist in the tundish during the production. While CaS also precipitated during solidification of samples from heats with dimensionless Ca > 1, the additional stable CaS formed at high temperature caused higher T.AF<sub>CaS</sub>. However, this does not explain why the T.AF<sub>CaS</sub> in Series 1 and Series 2 heats was less than that of Series 3, in which the T.AF<sub>CaS</sub> increased much steeper with dimensionless Ca. To explain such phenomenon, the sum of AF of CaS phase in CaS type, CaS-other type, and CA<sub>x</sub> type inclusions were shown with respect to dimensionless Ca in Figure 4.8 (b), (c), and (d), respectively. The sum of AF of j phase in inclusion type I, is denoted by T.AF<sub>(j)i</sub>.

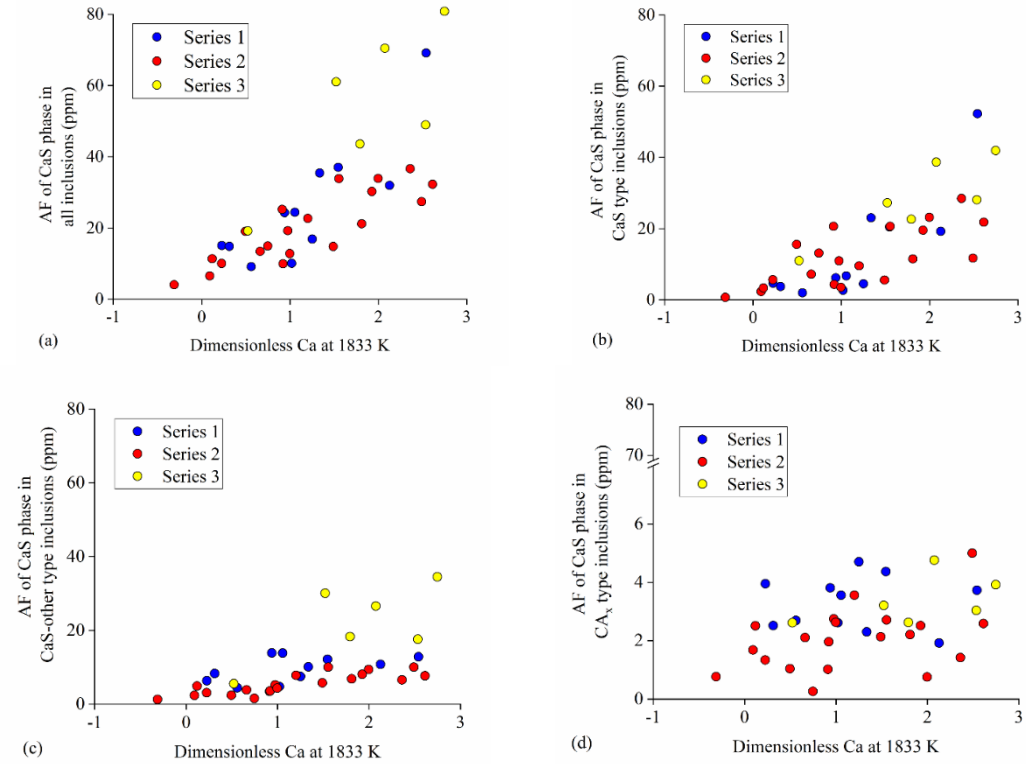


Figure 4.8 Change of estimated CaS amount in (a) all types, (b) CaS type, (c) CaS-other type, and (d)  $CA_x$  inclusions with dimensionless Ca at 1833 K in industrial samples.

The sum of AF of CaS phase in CaS type inclusions,  $T.AF_{CaS}(CaS)$ , increases with an increase in dimensionless Ca, as shown in Figure 4.8 (b).  $T.AF_{CaS}(CaS)$  varied from 0 ppm to 20 ppm in heats with dimensionless Ca < 1. When dimensionless Ca exceeded unity, the  $T.AF_{CaS}(CaS)$  ranged mainly between 20 ppm and 30 ppm (eleven out of eighteen heats). The  $T.AF_{CaS}(CaS)$  was higher than 40 ppm in three heats and lower than 20 ppm for four heats, mainly from Series 2.

The sum of AF of CaS in CaS-other type inclusions,  $T.AF_{CaS}(CaS\text{-other})$ , of Series 1 and Series 2 heats showed a similar trend (see Figure 4.8 (c)). The values increased slightly with dimensionless Ca. The maximum AF was 14 ppm. It was apparent that  $T.AF_{CaS}(CaS\text{-other})$  from Series 3 was about 5 ppm to 20 ppm higher than that of Series 1 and 2 when dimensionless Ca > 1. CaS-other inclusions had been established in the authors' previous study to be the combination of CaS and  $CA_x$ <sup>[34]</sup>. Liquid  $CA_x$  is known to have the ability to absorb S in liquid steel like a CaO- $Al_2O_3$  binary slag<sup>[22]</sup>. The slag desulfurization is achieved through Reaction (4.6). Since CaO in liquid  $CA_x$  provides ( $O^{2-}$ ) to react with [S], the amount of CaO determines the capacity of S absorption as CaS in liquid  $CA_x$  or other inclusions that contain a significant amount of liquid  $CA_x$  like CaS-other type. The same logic should also apply to CaS in  $CA_x$  type inclusions, which according to Figure 4.8 (d), exhibited no specific pattern when plotted against

dimensionless Ca. The sum of AF of CaS in  $CA_x$ ,  $T.AF_{CaS}(CA_x)$ , were even lower than that in CaS-other inclusions, with only a maximum AF of 5 ppm in one of the Series 2 heat.



Figure 4.9 (a) shows there is a linear correlation between change  $T.AF_{CaS}(CaS\text{-other})$  with  $T.AF_{CaO}(CaS\text{-other})$ . The  $T.AF_{CaS}(CaS\text{-other})$  increased from close to 0 ppm to 35 ppm while  $T.AF_{CaO}(CaS\text{-other})$  increased to 9 ppm. A similar trend can also be seen in the  $CA_x$  type. In Figure 4.9 (b), As the  $T.AF_{CaO}(CA_x)$  increased linearly from about 17 ppm accordingly, the  $T.AF_{CaS}(CA_x)$  increased to 5 ppm. In Figure 4.9 (c), no prominent increasing trend can be observed. Most of the heats had less than 1 ppm  $T.AF_{(CaO)CaS}$ , which was incomparable with the  $T.AF_{CaS}(CaS)$ . Therefore, only a negligible portion of the CaS in CaS type inclusions was retained through Reaction (4.6).

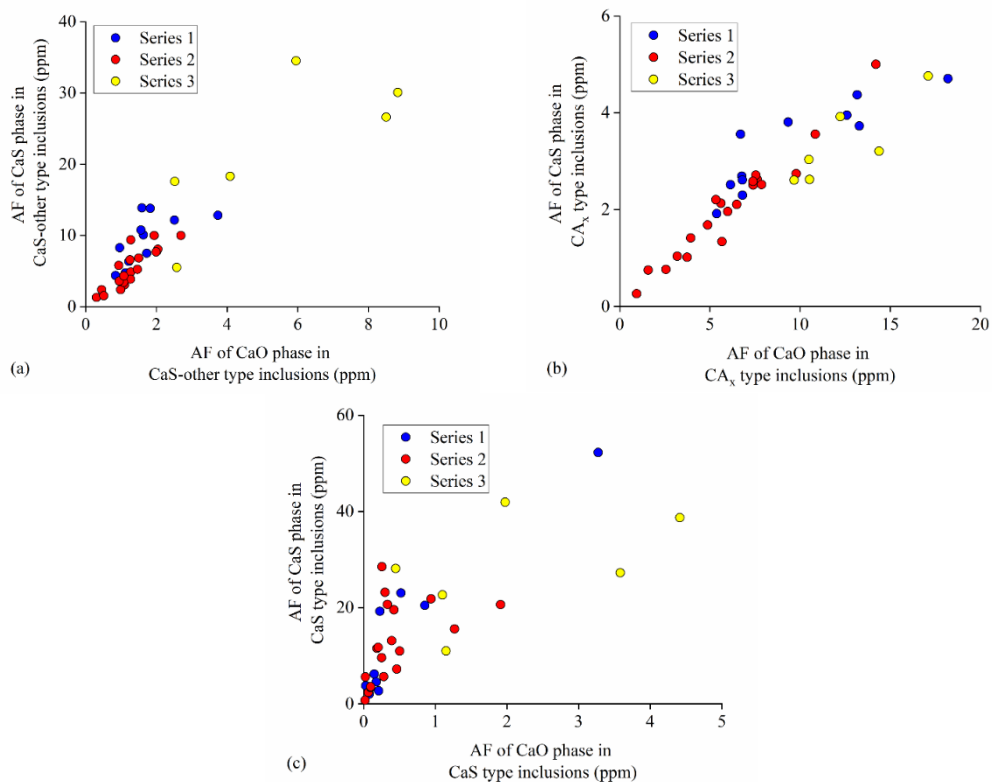


Figure 4.9 Relation between estimated AF of CaS phase and AF of CaO phase in (a) CaS-other, (b)  $CA_x$ , and (c) CaS inclusions.

Analyzing the distribution of CaS in different inclusion types through Figure 4.8 and Figure 4.9 suggested that the amount of CaS in a sample was affected by various factors in different inclusion types. The authors' previous study <sup>[34]</sup> showed that CaS type inclusions contain barely any  $CA_x$ , and the AF was almost solely controlled by the thermodynamic stability of the CaS phase; hence, it was related to dimensionless Ca.

Oppositely, analysis on  $CA_x$  type inclusions indicated the CaS in them were controlled by the ability of CaO to absorb S and almost independent of the stability of CaS quantified through dimensionless Ca. CaS-other being the complexes of CaS and  $CA_x$ , inherited characteristics of both types. The  $T.AF_{CaS}(CaS\text{-other})$  did generally increase as CaS became more stable, but at the same time, in some heats, the  $T.AF_{CaS}(CaS\text{-other})$  can be higher because of the higher amount of CaO in them.

### 4.3.3 Effects of steel chemistries on MnS inclusions

To assess the level of success of Ca treatment performed in industrial heats from the perspective of MnS control, the sum of AF of MnS phase in different inclusion types in heats from Series 1 to Series 3 is compared in Figure 4.10. Series 1 heats in Figure 4.10 (a) tend to have a much lower total AF of MnS phase in all inclusions,  $T.AF_{MnS}$ , than many Series 2 and Series 3 heats, with a maximum  $T.AF_{MnS}$  of about 3.75 ppm. In Figure 4.10 (b), the MnS type inclusions are the dominant MnS containing inclusions in Series 2 when  $T.AF_{MnS} > 1$  ppm, which includes 16 of the total 24 heats. While in Series 3 heats (Figure 4.10 (c)), MnS can be found in different inclusion types. At least 47 pct of the  $T.AF_{MnS}$  were found in CaS and CaS-other type. Also, the percentage of  $T.AF_{MnS}$  in liquid  $CA_x$  varied from 15 pct to 44 pct. And as already shown by Figure 4.2, Series 3 heats had a negligible amount of MnS type inclusions.

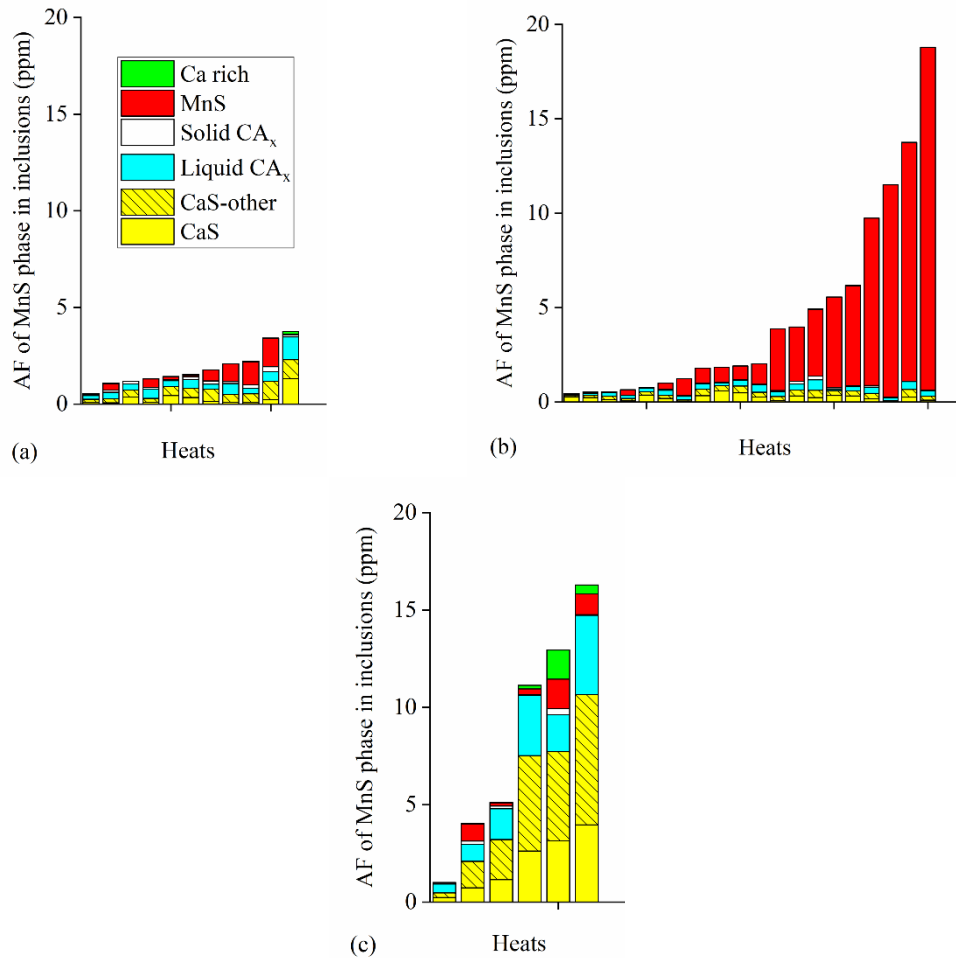


Figure 4.10 The AF of MnS in all types of inclusions in (a) Series 1, (b) Series 2 and (c) Series 3.

The  $T.AF_{MnS}$  differed between heats even from the same series containing similar Mn content. This variation could be related to the amount of Ca available to react with S to form CaS. To verify this, the  $T.Ca/T.S$  ratio of every heat is plotted against the AF of MnS type inclusions (MnS AF for short) in Figure 4.11 (a) and (b). MnS AF was used here instead of  $T.AF_{MnS}$  because MnS is considered to be more detrimental when close to pure substance than when forming complexes<sup>[48–50]</sup>. It can be seen that in Series 1 and 2 the MnS AF decreased with the  $T.Ca/T.S$  ratio. The MnS AF in Series 1 decreased from slightly over two ppm to 0 ppm, and this indicates that no inclusion was classified as MnS type inclusion by ASPEX when  $T.Ca/T.S$  approached 1. In Series 2 heats, shown in Figure 4.11 (b), the MnS AF was 20 ppm for  $T.Ca/T.S = 0.5$ . As  $T.Ca/T.S$  increased to higher than 1.5, the MnS AF decreased to almost 0 ppm. Because the MnS type inclusions were the primary MnS source in most Series 1 and 2 heats, the MnS AF in all inclusions exhibited a similar relationship with  $T.Ca/T.S$ . This phenomenon suggested a correlation between the MnS AF and the  $T.Ca/T.S$  ratio in these two series. As already reflected in Figure 4.2 and Figure 4.10, a significant portion of the MnS AF was found outside the MnS type inclusions in Series 3 heats. Therefore, despite total

MnS AF being higher than 4 ppm in five out of six heats from Series 3 (Figure 4.10 (c)), the MnS AF were all lower than 3 ppm (Figure 4.11 (a)), showing no apparent difference from that of Series 1 heats. The reason will be explained in a later section, but it was not clear what the desirable  $T.Ca/T.S$  ratio is.

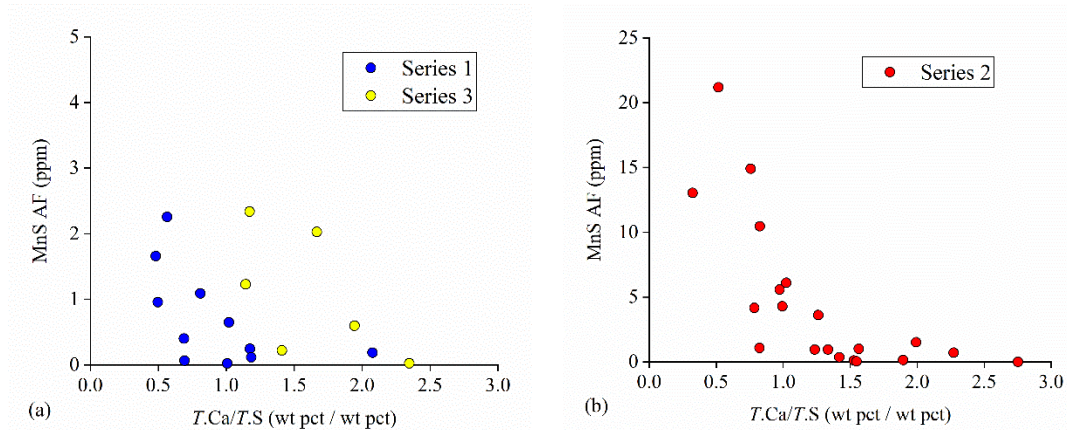


Figure 4.11 Change of MnS AF with  $T.Ca/T.S$  ratio in (a) Series 1 and Series 3 and (b) Series 2.

Imagumbai and Takeda <sup>[33]</sup> proposed a correlation named the Sulfur Partition Coefficient (SPC) to quantify the effects of Ca and S content on the formation of MnS inclusions. It was assumed that the concentration of S dissolved in steel is neglectable, and all S exists as either CaS or MnS. Imagumbai and Takeda <sup>[33]</sup> also claimed that  $T.Ca/T.S$  mass ratio is critical to the partitioning of S between CaS and MnS. The expression of SPC proposed by Imagumbai and Takeda <sup>[33]</sup> is shown as Equation (4.7). The term  $\frac{S_{as\ CaS}}{T.S}$ , expresses the mass fraction of S in CaS inclusions. They found SPC should be a second-order polynomial function of the  $T.Ca/T.S$  ratio. The coefficients were suggested to be dependent on the distribution coefficient of Ca, O, and S, but were obtained through fitting experimental data. Since the distribution coefficients change with steel compositions, it was expected that the same equation might not be directly applicable for the steel compositions studied by the authors. According to Equation (4.7), for all S in steel to exist as CaS, i.e.,  $SPC = 1$ , the value for  $T.Ca/T.S$  should be 2.5. As shown in Figure 4.11, the values for Series 1 and Series 2 were approximately 1 and 1.5, respectively. Some uncertainties exist for both series. The difference in  $T.Ca/T.S$  is related to the Mn content of steel. In the study of Imagumbai and Takeda <sup>[33]</sup>, the Mn content of 16 investigated samples ranged from 1.39 to 1.61 wt pct. Whereas, the Mn content in Series 1 was 0.5 wt pct and Series 2 was 1 wt pct. There appears to be a correlation between  $T.Ca/T.S$  needed to achieve low MnS amount and Mn content of steel, and it was plotted in Figure 4.12. For this figure, an average Mn content of 1.5 wt pct was used to represent data from Imagumbai and Takeda <sup>[33]</sup>. The standard deviation of four datapoints closest to  $T.Ca/T.S = 1$  was 0.2; hence, was used as the error in Figure 4.12. The same method was used to obtain error of Series 2. Linear fitting suggested that

Equation (4.8) gives the best fit.  $T.Mn$  denotes the total Mn content in liquid steel (wt pct). This correlation may need more validation for a wider range of Mn contents, but authors believed this simple and accessible correlation can be a helpful tool for determining the suitable Ca content range for MnS inclusion control in compositions similar to Series 1 and 2. Series 3 cannot be incorporated in Figure 4.12, and the reasons are discussed in a later part of this section.

$$\text{SPC for 1.5 wt pct Mn} = \frac{S_{as} CaS}{T.S} = 0.8 \frac{T.Ca}{T.S} - 0.16 \left( \frac{T.Ca}{T.S} \right)^2 \quad (4.7)$$

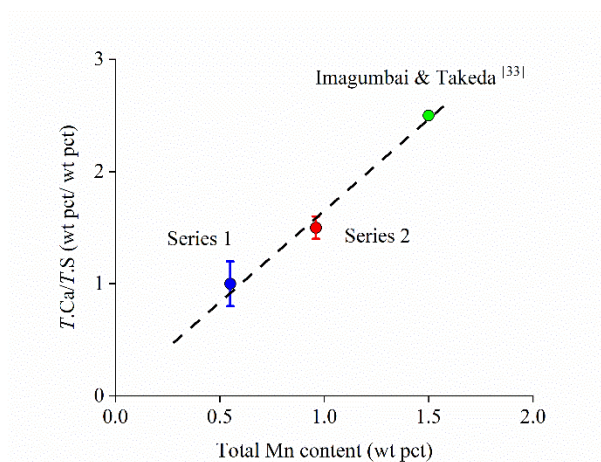


Figure 4.12 Effect of Mn content in steel on  $T.Ca/T.S$  ratio to form a low amount of MnS inclusions.

$$\frac{T.Ca}{T.S} = 1.65T.Mn \quad (4.8)$$

Equation (4.7) can be applied if Mn contents are close to 1.5 wt pct. When Mn content changes, the numerical values in Equation (4.7) have to change accordingly. A similar fitting approach described by Imagumbai and Takeda<sup>[33]</sup> had been adapted to generate Equation (4.9). The numerical values in Equation (4.9) were adjusted to achieve the highest fitting.

$$\text{SPC for 1 wt pct Mn} = 1.09 \frac{T.Ca}{T.S} - 0.28 \left( \frac{T.Ca}{T.S} \right)^2 \quad (4.9)$$

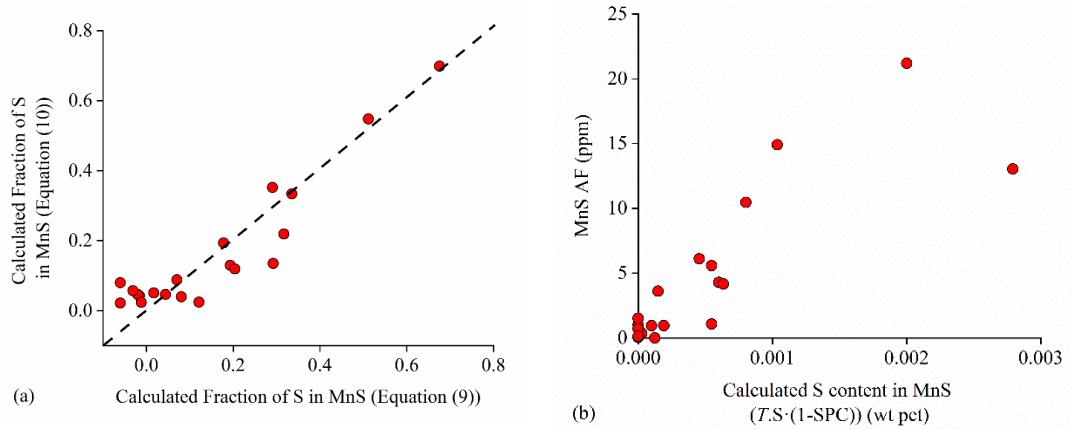


Figure 4.13 (a) Correlation between the fraction of S in MnS calculated using Equation (4.9) and Equation (4.10). (b) Correlation between the observed MnS AF and the S content in MnS inclusions predicted by SPC in Series 2.

The comparison of the fraction of S content in MnS inclusions estimated based on inclusion AF and calculated using Equation (4.9) is shown in Figure 4.13 (a). Figure 4.13 (a) includes only Series 2 heats data as the  $T.Mn$  content in heats from the other two series differed from 1 wt pct. The fraction of S content in MnS was estimated by first considering AF as the approximation of mass, then the y-axis values were obtained through Equation (4.10), where  $MW_i$  is the molar mass of component  $i$ . With constants in Equation (4.9) set to 1.09 and 0.28, the calculated fractions of S using two approaches show a good agreement. A comparison of the predicted S content ( $T.S*(1-SPC)$  (in wt pct)) and the MnS AF is shown in Figure 4.13 (b). When S content was lower than 0.002 wt pct, MnS AF increased from 0 ppm to approximately 20 ppm. At the current stage, the cause of MnS AF decrease from 21 ppm to 13 ppm when the predicted S content in MnS increased from 0.002 wt pct to 0.0028 wt pct remained unclear and will be studied further. Figure 4.13 shows that Equation (4.9) can successfully predict the MnS AF in most of the Series 2 heats. The same procedure can be repeated for Series 1 to generate an equation similar to Equation (4.9) as the same strong correlation between  $T.Ca/T.S$  and MnS AF as in Series 2 had been revealed in Figure 4.11. However, the fractions of estimated S in MnS inclusions varied only from 0.03 to 0.11 in Series 1, which was significantly narrower than the 0.02 to 0.70 range seen in Series 2 (Figure 4.13 (a)). Due to this limited range in Series 1, the equation of SPC for 0.6 wt pct Mn will not be reported here.

$$\text{Fraction of S in MnS} = \frac{\frac{T.AF_{MnS}}{MW_{MnS}}}{\frac{T.AF_{MnS}}{MW_{MnS}} + \frac{T.AF_{CaS}}{MW_{CaS}}} \quad (4.10)$$

The aforementioned findings cannot directly explain the difference in MnS inclusion distribution between Series 2 and Series 3 seen in Figure 4.10. To investigate this

difference, the authors studied the influence of carbon content in steel on MnS inclusion formation. For this purpose, an analytical model proposed by Won and Thomas [51] was used to calculate the microsegregation during solidification. This model and its variations have been widely used in many solidification-related studies [52–55]. The segregation model uses steel chemistries, kinetics, and thermodynamic data, and cooling conditions as inputs to calculate the liquidus,  $T_{\text{liq}}$ , and solidus temperatures,  $T_{\text{sol}}$ , and the solute  $i$  concentration in liquid steel,  $C_{[i]}$ , at any solid fraction,  $f_s$ , using Equation (4.11).  $C_{[i],0}$  and  $k_i^j$  are the initial concentration and the equilibrium partition coefficient of component  $i$ , respectively. Parameter  $\beta_i$  is a function of the diffusion coefficient in the appropriate solid phase,  $D_i^j$ , solidification time,  $t_f$ , and secondary dendrite arm spacing,  $\lambda_{SDAS}$ . The data used for the calculation are summarized in Table 4.2.  $k_i^\delta$  and  $k_i^\gamma$  are the  $\delta$ -Fe/liquid and  $\gamma$ -Fe/liquid equilibrium partition coefficients of component  $i$ , respectively.  $D_i^\delta$  and  $D_i^\gamma$  are the diffusion coefficients in  $\delta$ -Fe and  $\gamma$ -Fe, respectively. To calculate the  $T_{\text{liq}}$  temperature and the start temperature of  $\delta$ -Fe to  $\gamma$ -Fe transformation during cooling ( $T_{\text{Ar4}}$ ), the slopes of phase boundaries on the phase diagrams,  $m_i$  and  $n_i$  for  $T_{\text{liq}}$  and  $T_{\text{Ar4}}$  were used, respectively. All other parameters can be calculated using the procedure documented in a previous study [199]; hence, will not be repeated here. The principle is to first calculate the equilibrium  $T_{\text{sol}}$ , and the solid-liquid interfacial concentration as the initial guesses. Then uses substituting the diffusion parameter,  $\beta_i$ , equilibrium partition coefficient,  $k_i$  of component  $I$  at the equilibrium  $T_{\text{sol}}$  into Equation (4.11) to calculate the new solid-liquid interfacial concentration when solid fraction equals to 1. The new interfacial concentrations give a new  $T_{\text{sol}}$  based on the value of phase boundary slopes  $m_i$  and  $n_i$ . Usually after two iterations,  $T_{\text{sol}}$  will converge, which is true  $T_{\text{sol}}$  due to segregation. Then the concentration of any solute in steel at any temperature,  $T$ , between the  $T_{\text{liq}}$  and  $T_{\text{sol}}$  can be calculated using Equation (4.11). The solid fraction,  $f_s$ , at  $T$  was determined through trial and error by increasing  $f_s$  from 0 to 1 with step size of 0.001.  $C_{[i]}$  calculated using any  $f_s$  value has a corresponding  $T_{\text{sol}}$ . The  $f_s$  that gives the closest  $T_{\text{sol}}$  to the  $T$  is the correct value. Now, the temperature, solid fraction and interfacial temperature are all known.

$$C_{[i]} = C_{[i],0} \left[ 1 + f_s (\beta_i k_i - 1) \right]^{\frac{1-k_i}{\beta_i k_i - 1}} \quad (4.11)$$

Table 4.2 Physical properties used for calculation of concentration change due to segregation <sup>[199,200]</sup>

	$k_i^{\delta/L}$	$k_i^{\gamma/L}$	$D_i^{\delta} \times 10^4$ (m <sup>2</sup> /s)	$D_i^{\gamma} \times 10^4$ (m <sup>2</sup> /s)	$m_i$ (K/pct)	$e_i$ (K/pct)
C	0.19	0.34	0.0127Exp(-81379/RT)	0.15Exp(-143511/RT)	78	-1122
Mn	0.77	0.79	0.76Exp(-224430/RT)	0.055Exp(-249366/RT)	4.9	-12
S	0.05	0.035	4.56Exp(-214639/RT)	2.4Exp(-223426/RT)	38	160
Si	0.7	0.52	8Exp(-248948/RT)	0.3Exp(-251458/RT)	7.6	60
Al	0.6	0.6	5.9Exp(-241417/RT)	5.9Exp(-241417/RT)	3.6	0*

\*: Data not available in the literature

One composition representing each series was used to demonstrate the effects of composition on phase transformation during segregation. C, Mn, Si, and Al concentrations were the average values from the corresponding series, and S levels were kept the same. For calculation of Series 1, Series 2 and Series 3, 0.06C-0.54Mn, 0.19C-0.96Mn and 0.06C-1.12Mn were used respectively together with a constant 0.0021S-0.022Si-0.044Al.

An assumed constant 10 K/min cooling rate was used here when calculating the concentration profiles. Based on the concentration change of C, Mn, S, Si, and Al, the evolution of each phase during solidification was calculated. The calculated solid fraction with respect to the temperature is presented in Figure 4.14. Figure 4.14 compares the decrease in steel temperature estimated based on a fixed cooling rate (solid line) and increase in the local transformation temperature calculated using segregated concentration (dashed line) for three series of heats. At  $f_s \approx 0.7$ ,  $\delta$  to  $\gamma$  transformation would start in a Series 2 heat because the estimated steel temperature at that moment became lower than the  $\delta$  to  $\gamma$  transformation temperature. The  $\delta$  to  $\gamma$  transformation temperature ( $T_{Ar4}$ ) was calculated using Equation (4.12). After the transformation had started, the fraction of  $\delta$ -Fe was assumed to decrease parabolically to 0 when  $[C] = 0.53$  wt pct <sup>[51]</sup>. An identical approach had been used in previous studies <sup>[51,56-58]</sup>. In the present study, the peritectic transformation was assumed to be controlled solely by C content in liquid steel at the liquid-solid interface. Close to the end of solidification, segregation increased  $[C]$  to around 0.58 wt pct in the chosen Series 2 heat. Therefore, the fraction of  $\delta$ -Fe was zero when the total solid fraction was close to 1.

$$T_{Ar4} = 1392 - \sum_i n_i k_i^{\delta} C_{[i]} \quad (4.12)$$

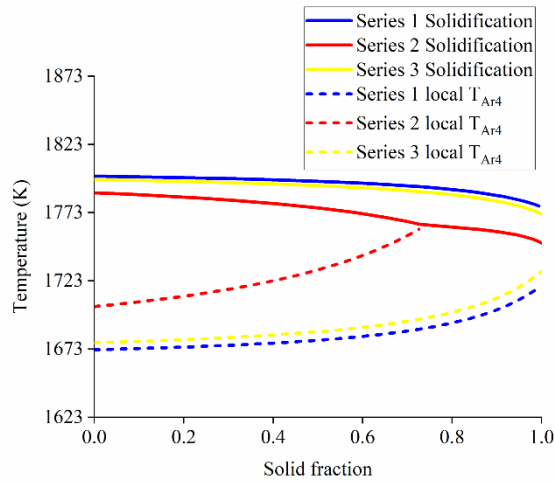


Figure 4.14 Comparison of estimated steel temperature and calculated local transformation temperature change during solidification in industrial heats.

Based on the difference in Fe phases between the series, the authors propose that MnS inclusions in Series 2 heats were mainly formed through Reaction (4.14). The solubility product of MnS ( $K_{sp}$ ) in the  $\delta$  and  $\gamma$  phases was calculated using Equation (4.15) and (4.16), respectively [52]. For any given temperature, the value for  $K_{sp}$  to form MnS in  $\gamma$ -Fe will be slightly lower than that in  $\delta$ -Fe. In other words, lower Mn and S concentrations are needed to form MnS. Further, relatively high concentrations of C and Si in Series 2 heats increase the activity coefficient of S [59], making Reaction (4.14) thermodynamically more favorable to proceed for Series 2 heats. Secondly, if Reaction (4.13) was the MnS formation route, some intermediates of the CaS to MnS transformation must exist. Inclusions with such composition were defined as CaS-MnS type in ASPEX analysis. However, CaS-MnS type inclusions were not observed in any sample from Series 2 (Figure 4.2 (b)). A similar phenomenon should also occur in other CaS containing inclusions such as CaS-other type. But again, such inclusions were not found in the ASPEX analysis. In conclusion, the authors believe that Reaction (4.14) is thermodynamically more favorable to proceed, and Reaction (4.13) hardly occurred to form MnS inclusions for Series 2 heats.

In the case of  $\delta$ -Fe rich (Series 3 heats) samples, the authors propose that both Reaction (4.13) and Reaction (4.14) likely occurred and led to the formation of MnS as complexes and as nearly pure inclusions, respectively. Hence, MnS could be observed in various inclusion types in Series 3. However, Figure 4.11 (a) shows no correlation between MnS AF and SPC for Series 3 heats. The reason could be Reaction (4.14) and Reaction (4.17) were the only reactions considered when establishing the concept of SPC being dependent only on the  $T.Ca/T.S$  ratio. With the additional CaS to MnS transformation in Reaction (4.13), the amount of MnS is possible to be higher than the prediction based on SPC.



$$\log(K_{\text{sp},\delta}) = 4.092 - \frac{10590}{T} \quad (4.15)$$

$$\log(K_{\text{sp},\gamma}) = 4.76 - \frac{12000}{T} \quad (4.16)$$



Overall, based on the discussed industrial data, the distribution of S between CaS and MnS can be correlated with SPC. This suggests for a given S content, increasing the  $T.\text{Ca}/T.\text{S}$  ratio to make  $\text{SPC} > 0.6$  would effectively prevent MnS inclusions from forming if steel compositions are similar to those of Series 1 and 2. However, the distribution of S in Series 3 heats cannot yet be estimated and requires further studies in the future.

It had been shown in number of studies that forming spherical or spindle CaS-MnS largely suppress the detrimental effects of angular MnS inclusions<sup>[60-62]</sup>. Therefore, the precipitation of MnS with other inclusions as in Series 3 heats (Figure 4.10 (c)) likely shows less detrimental effects than the MnS precipitates seen in Series 2 (Figure 4.10 (b)). With some analysis, it has been assumed that such difference likely depends on the phase of steel. MnS complexes were more common when  $\gamma$ -Fe did not form. In the present study, the transformation of  $\delta$ -Fe or  $\gamma$ -Fe was controlled mainly by carbon. Deploying alternative countermeasures of avoiding the formation of a large fraction of  $\gamma$ -Fe may still promote MnS complex formation, but that was not the focus of the present work.

#### 4.3.4 Evaluation of calcium treatment in industrial heats

The effectiveness of Ca treatment on the modification of oxides inclusions and control of sulfide inclusions was evaluated by applying the correlations discussed in the above sections. These correlations are modified CTI for oxide modification, dimensionless Ca for CaS stability, and SPC for controlling MnS formation.  $\text{CA}_x$ , CaS, and MnS inclusions control was quantified through the difference between the measured Ca content in steel and the desired Ca content. The method can be best explained with an example.

The first step is to establish targets for control of CaS, MnS and  $\text{CA}_x$  inclusions. The inclusion control targets are assumed to be CaS AF lower than 20 ppm, no presence of

MnS type inclusions and more than 90 pct of the  $CA_x$  inclusions having at least 50 wt pct liquid phase. Then based on the trend observed in the industrial heats, the value of dimensionless Ca needs to be lower than 1 (Figure 4.8),  $T.Ca/T.S$  ratio needs to be 1.65 times of the  $T.Mn$  content (Figure 4.12), and the value of modified CTI needs to be larger than 0.5 (Figure 4.5). Here, an heat from Series 2, Heat A, was used as an example. Heat A had composition of 0.87Mn-0.0016S-0.048Al-0.0023Ca, all compositions are in wt pct. Substituting the values for  $T.S$ ,  $T.Al$  and dimensionless Ca into Equation (4.5) suggests that the value for  $T.Ca$  needed to achieve the dimensionless Ca equals to 1 is 23.7 ppm. Substituting the values for  $T.S$  and  $T.Mn$  into Equation (4.8) suggests that the  $T.ca$  needed to eliminate MnS type inclusions in tundish is 23.4 ppm. Equation (4.4) suggests that  $T.Ca$  equal to 16.2 ppm is required to achieve modified CTI larger than 0.5. These three Ca content values can be considered as the  $x$ ,  $y$  and  $z$  coordinates and plotted on a cartesian plane. Figure 4.15 presents such plot where the red datapoint ( $x = 23.7$ ,  $y = 23.4$ ,  $z = 16.2$ ) represents the  $T.Ca$  content required for control of different type of inclusions in Heat A. The measured  $T.Ca$  content in the corresponding heat was 23 ppm, which is plotted on Figure 4.15 as the black datapoint ( $x = 23$ ,  $y = 23$ ,  $z = 23$ ). The distance between the two coordinates,  $d$ , indicated by the dashed line is 6.8. The smaller the  $d$  value the closer the measured  $T.Ca$  is to the  $T.Ca$  required to achieve the preset CaS, MnS and  $CA_x$  inclusions controlling targets. These steps can be repeated for any heat studied in the present work as a method of quantifying the overall level of success for CaS, MnS and  $CA_x$  inclusions control. The expression to calculate the value of  $d$  is shown as Equation (4.18). Weighing coefficients  $a$ ,  $b$  and  $c$  are introduced to describe the priority of CaS, MnS, and  $CA_x$  inclusions control, respectively. When a control of all three types of inclusions is considered equally important, the values of  $a$ ,  $b$  and  $c$  are set as 1. On the other hand, if one wishes to prioritize  $CA_x$  control over CaS and MnS control,  $c$  can be assigned a larger value than that of  $a$  and  $b$ .

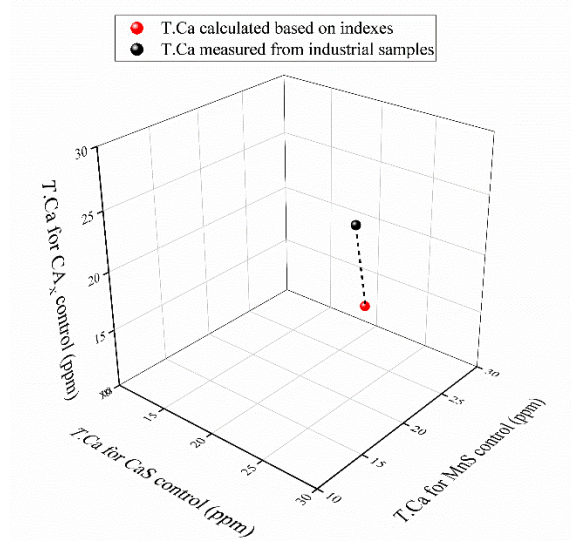


Figure 4.15 Schematic diagram for evaluation the overall effectiveness of CaS, MnS and CA<sub>x</sub> inclusion control.

$$d = \sqrt{a(T. Ca - x)^2 + b(T. Ca - y)^2 + c(T. Ca - z)^2} \quad (4.18)$$

Equation (4.18) may also be used to estimate the optimum *T.Ca* content, because for any combination of *a*, *b*, *c*, *x*, *y* and *z*, there must exist a *T.Ca* that gives the lowest *d* value. Let's take Heat A as an example again. By setting *x* = 23.7, *y* = 23.4, and *z* = 16.2, and all weighing coefficients equal to 1, the dependency of *d* on *T.Ca* can be plotted in Figure 4.16 (a) as the black solid curve 1. The *T.Ca* equals 21 ppm is considered as the optimum Ca content because it gives the minimum *d* value. The measured *T.Ca* of Heat A is only 2 ppm higher than the 21 ppm optimum *T.Ca*. This suggests a good inclusion control would have been observed for this heat. Figure 4.16 (b) presents the AF of all inclusion types observed in Heat A. The AF of CaS and CaS-other were 5.5 ppm and 7.1 ppm, respectively, which were well below the preset target value (CaS AF < 20 ppm). The AF of MnS was also virtually not visible in Figure 4.16 (b), suggesting it was well controlled in this heat. The average C/A ratio in this heat was 0.95±0.44, which means more than 90 pct of the CA<sub>x</sub> had higher than 50 wt pct liquid phase. This cannot be directly shown in Figure 4.16 (b), but one should notice that the AF of solid CA<sub>x</sub> inclusions was hardly visible.

The finding discussed above are all based on setting all three weighing coefficient to 1. Adjusting the weighing coefficients alters the results. In the case of Heat A, prioritize CaS AF reaching 20 ppm by changing the weighing coefficients to *a* = 3, *b* = 1, *c* = 1 produces curve 2 in Figure 4.16 (a). The minimum of curve 2 can be found at *T.Ca* equals to 22 ppm, which is slightly higher than that of curve 1. This suggests the *T.Ca* content would increase CaS AF to 20 ppm, which is the hypothetical target for CaS control set earlier. Increasing the importance of eliminating MnS inclusions by change the weighing

coefficients to  $a = 1, b = 3, c = 1$  produced curve 3. The optimum  $T.Ca$  in this case again slightly increases to 22 ppm. Such result suggests using 22 ppm  $T.Ca$  can reduce more MnS in Heat A. Changing weighing coefficients to  $a = 1, b = 1, c = 3$  gives curve 4, which suggests only 19 ppm  $T.Ca$  content is needed to ensure over 90 pct of the  $CA_x$  contain at least 50 wt pct liquid phase. The values of weighing coefficients used here are an example. The exact values of  $a, b$  and  $c$  may vary depending on operation parameters and steel grade and most likely needed to gain through experiences.

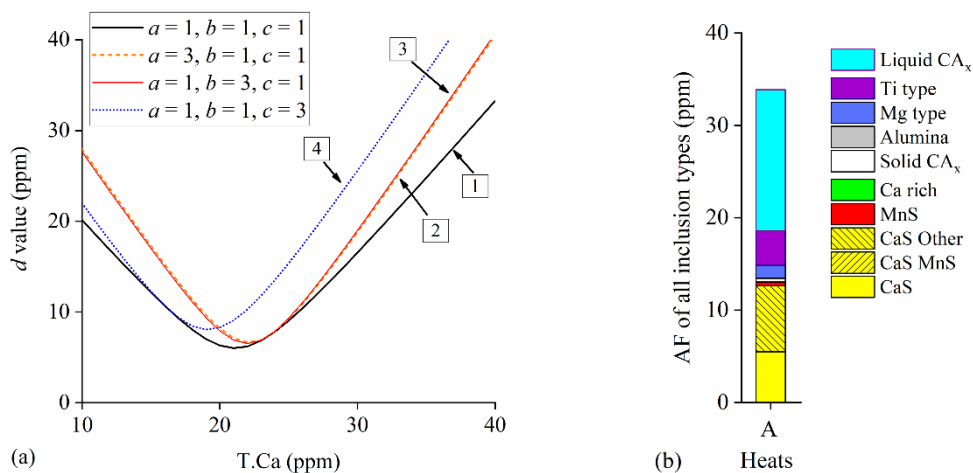


Figure 4.16 (a) Dependency of  $d$  value on  $T.Ca$  content for Heat A with  $x = 23.7$ ,  $y = 23.4$ , and  $z = 16.2$  and varying weighing coefficients and (b) AF of all inclusion types in Heat A tundish sample.

The comparison of  $d$  values and AF of all inclusion types for three more heats is shown in Figure 4.17. As shown in Figure 4.17 (a), the measured  $T.Ca$  content is 7 ppm lower than the optimum  $T.Ca$  predicted using Equation (4.18) for Heat B when all weighing coefficients are set to 1. The difference is larger than that for Heat A, shown in Figure 4.16. In the case of Heat B, lower than optimum  $T.Ca$  content led to insufficient CaS; hence, a high MnS AF was observed, shown in Figure 4.17 (b). In Heat C, the measured  $T.Ca$  is 8 ppm lower than the predicted optimum  $T.Ca$  content. For this heat, not only some MnS type inclusions, but also high AF of solid  $CA_x$  can be observed in Figure 4.17 (b). This indicates that the  $T.Ca$  content was not sufficient to reach a desirable extent of  $CA_x$  modification. For Heat D on contrary, the measured  $T.Ca$  is 10 ppm higher than optimum  $T.Ca$  content. As a result, while solid  $CA_x$  and MnS can not be seen in Figure 4.17 (b), the AF of CaS inclusions was high as approximately 25 ppm. Based on Figure 4.16 and Figure 4.17, it can be inferred that Equation (4.18) has a potential of evaluating and predicting overall level of success in inclusion control and predicting the optimum Ca content.

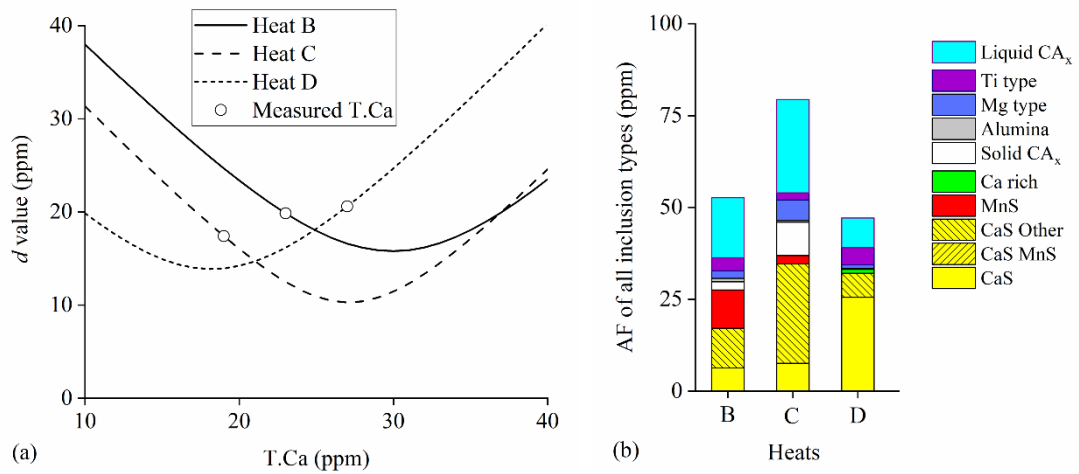


Figure 4.17 Comparison of (a) the measured  $T.Ca$  content and the estimated optimum  $T.Ca$  and (b) AF of all inclusion types in tundish sample in Heat B, Heat C and Heat D.

#### 4.4 Summary

The effects of steel chemistry on the modification of oxide inclusions and formation of sulfide inclusions by calcium treatment were studied using 37 industrial samples obtained from tundish. The findings are summarized as follows:

1. A parameter based on the Al, Ca and S contents of liquid steel, modified CTI (modified Ca treatment index) has been proposed to help improve the control of  $CA_x$  inclusion modification. It has been found that the  $CaO/Al_2O_3$  ratio of liquid calcium aluminate inclusions gradually increases with modified CTI. When modified CTI is higher than 0.5, more than 90 pct of the  $CA_x$  inclusions are expected to be at least 50 wt pct liquid phase.
2. Dimensionless Ca can be an indicator of over-modification of oxide inclusions. When dimensionless Ca is greater than 1, CaS inclusions become stable and the area fraction (AF) of CaS inclusions increases. Hence, the chemistry-dependent dimensionless Ca can be used to quantify the level of success of CaS control.
3. A linear correlation between the  $T.Ca/T.S$  ratio and Mn content of the steel to achieve low MnS AF has been proposed, as  $T.Ca/T.S = 1.65T.Mn$ . Also, the sulfur partition coefficient (SPC) as a function of the  $T.Ca/T.S$  ratio has been proposed to estimate the distribution of S between CaS and MnS.
4. The formation mechanism of MnS inclusions may vary depending on the steel phases during solidification. Therefore, distinct MnS distribution between inclusion types can be observed in steel with different C contents. As a result, no strict relation can be found between  $T.Ca/T.S$  and SPC in low C high Mn heats at the current stage of the study.
5. The success level of Ca treatment on  $CA_x$ , CaS, and MnS inclusions control may be quantified and evaluated based on the difference between the optimum and actual

Ca content. Reversing the process allows one to determine the optimum Ca content for a known steel chemistry, but the results may differ depending on the different priority of controlling the amount of CA<sub>x</sub>, CaS, and MnS inclusions. Overall, this method suggests a more comprehensive analysis of the Ca addition strategy.

#### 4.5 Acknowledgement

The authors would like to thank the Natural Sciences and Engineering Research Council of Canada (grant number CRDPJ = 505545-16) for funding this research. The authors would also like to thank Dr. Stanley Sun and Dr. Li Sun from ArcelorMittal Dofasco for help with inclusion analysis.

#### 4.6 Reference

- 1 R.J.F. K. Larsen, K. Larsen, and R.J. Fruehan: *Iron Steelmak.*, 1990, vol. 17, pp. 45–52.
- 2 D. Zhao, H. Li, C. Bao, and J. Yang: *ISIJ Int.*, 2015, vol. 55, pp. 2115–24.
- 3 N. Verma, P.C. Pistorius, R.J. Fruehan, M. Potter, M. Lind, and S.R. Story: *Metall. Mater. Trans. B Process Metall. Mater. Process. Sci.*, 2011, vol. 42, pp. 720–9.
- 4 L.F. Zhang and B.G. Thomas: *ISIJ Int.*, 2003, vol. 43, pp. 271–91.
- 5 J. Guo, S. Cheng, Z. Cheng, and L. Xin: *Steel Res. Int.*, 2013, vol. 84, pp. 545–53.
- 6 S.K. Choudhary and A. Ghosh: *ISIJ Int.*, 2008, vol. 48, pp. 1552–9.
- 7 N. Verma, P.C. Pistorius, R.J. Fruehan, M. Potter, M. Lind, and S. Story: *Metall. Mater. Trans. B Process Metall. Mater. Process. Sci.*, 2011, vol. 42, pp. 711–9.
- 8 M.K. Sardar, S. Mukhopadhyay, U.K. Bandopadhyay, and S.K. Dhua: *Steel Res. Int.*, 2007, vol. 78, pp. 136–40.
- 9 B. Harcsik and G. Karoly: *Steel Res. Int.*, 2013, vol. 84, pp. 129–35.
- 10 L. Jiang, K. Cui, and H. Hänninen: *J. Mater. Process. Technol.*, 1996, vol. 58, pp. 160–5.
- 11 H. Yaguchi: *J. Appl. Metalwork.*, 1986, vol. 4, pp. 214–25.
- 12 C. Wang, X. Liu, J. Gui, Z. Du, Z. Xu, and B. Guo: *Vacuum*, 2020, vol. 174, p. 109209.
- 13 M.A. Baker and J.E. Castle: *Corros. Sci.*, 1993, vol. 34, pp. 667–82.
- 14 M.N. Inés and G.A. Mansilla: *Acta Microsc.*, 2013, vol. 22, pp. 20–5.
- 15 Q. Meng, G.S. Frankel, H.O. Colijn, and S.H. Goss: *Nature*, 2003, vol. 424, pp. 389–90.
- 16 J. Xu, F. Huang, and X. Wang: *Metall. Mater. Trans. B Process Metall. Mater. Process. Sci.*, 2016, vol. 47, pp. 1217–27.
- 17 G. Yang and X. Wang: *ISIJ Int.*, 2015, vol. 55, pp. 126–33.
- 18 Y. Liu, L. Zhang, Y. Zhang, H. Duan, Y. Ren, and W. Yang: *Metall. Mater. Trans. B Process Metall. Mater. Process. Sci.*, 2018, vol. 49, pp. 610–26.

- 19 K. Miao, A. Haas, M. Sharma, W. Mu, and N. Dogan: *Metall. Mater. Trans. B Process Metall. Mater. Process. Sci.*, 2018, vol. 49, pp. 1612–23.
- 20 Y. Higuchi, M. Numata, S. Fukagawa, and K. Shinme: *ISIJ Int.*, 1996, vol. 36, pp. S151–4.
- 21 Y. Ren, L.F. Zhang, and S. Li: *ISIJ Int.*, 2014, vol. 54, pp. 2772–9.
- 22 S. Abdelaziz, G. Megahed, I. El-Mahallawi, and H. Ahmed: *Ironmak. Steelmak.*, 2009, vol. 36, pp. 432–41.
- 23 T. Yoshioka, Y. Shimamura, A. Karasev, Y. Ohba, and P.G. Jönsson: *Steel Res. Int.*, 2017, vol. 88, pp. 1–9.
- 24 W. Yang, L.F. Zhang, X. Wang, Y. Ren, X. Liu, and Q. Shan: *ISIJ Int.*, 2013, vol. 53, pp. 1401–10.
- 25 N. Verma, P.C. Pistorius, R.J. Fruehan, M.S. Potter, H.G. Oltmann, and E.B. Pretorius: *Metall. Mater. Trans. B Process Metall. Mater. Process. Sci.*, 2012, vol. 43, pp. 830–40.
- 26 Y. Wang, X. Sun, L. Zhang, and Y. Ren: *J. Mater. Res. Technol.*, 2020, vol. 9, pp. 11351–60.
- 27 S. Devi, R.K. Singh, N. Sen, and N. Pradhan: *Mater. Sci. Forum*, 2020, vol. 978 MSF, pp. 12–20.
- 28 J. Li, G. Cheng, Q. Ruan, J. Li, J. Pan, and X. Chen: *ISIJ Int.*, 2018, vol. 58, pp. 1042–51.
- 29 X. Deng, C. Ji, S. Guan, L. Wang, J. Xu, Z. Tian, and Y. Cui: *Ironmak. Steelmak.*, 2019, vol. 46, pp. 522–8.
- 30 W. Yang, C. Guo, C. Li, and L. Zhang: *Metall. Mater. Trans. B Process Metall. Mater. Process. Sci.*, 2017, vol. 48, pp. 2267–73.
- 31 Z.W. Hou, M. Jiang, E.J. Yang, S.Y. Gao, and X.H. Wang: *Metall. Mater. Trans. B Process Metall. Mater. Process. Sci.*, 2018, vol. 49, pp. 3056–66.
- 32 S. Sun, L. Sun, S. Waterfall and D. Liao, ArcelorMittal Global R&D – Hamilton: in *Proceedings of 2018 China Symposium on Sustainable Steelmaking Technology*, vol. 2, Tianjing, 2018
- 33 M. Imagumbai and T. Takeda: *ISIJ Int.*, 1994, vol. 34, pp. 574–83.
- 34 K. Miao, M. Nabeel, N. Dogan, and S. Sun: *Metall. Mater. Trans. B Process Metall. Mater. Process. Sci.*, 2021, vol. 52, pp. 3151–66.
- 35 S. Sun, S. Waterfall, N. Strobl, D. Liao, and D. Holdridge: *Miner. Met. Mater. Ser.*, 2017, vol. Part F5, pp. 347–57.
- 36 S.R. Story, T.J. Piccone, R.J. Fruehan, and M. Potter: *Iron Steel Technol.*, 2004, vol. 1, pp. 163–9.
- 37 B. Kumar, S. Mishra, M.B.V. Rao, and G.G. Roy: *Ironmak. Steelmak.*, 2019, vol. 46, pp. 454–62.
- 38 V. Gollapalli, M.B.V. Rao, P.S. Karamched, C.R. Borra, G.G. Roy, and P. Srirangam: *Ironmak. Steelmak.*, 2018, pp. 1–8.
- 39 P. Shen and J. Fu: *Materials (Basel)*, 2019, vol. 12, p. 197.

- 40 S.T. Kim, S.H. Jeon, I.S. Lee, and Y.S. Park: *Corros. Sci.*, 2010, vol. 52, pp. 1897–904.
- 41 F. Wang, H. Guo, W. Liu, S. Yang, S. Zhang, and J. Li: *Materials (Basel)*., 2019, vol. 12, p. 1034.
- 42 C. Blais, G. L'Espérance, H. LeHuy, and C. Forget: *Mater. Charact.*, 1997, vol. 38, pp. 25–37.
- 43 Y. Tomita: *J. Mater. Sci.*, 1994, vol. 29, pp. 2873–8.
- 44 L. Shi, J. Chen, and D.O. Northwood: *J. Mater. Eng.*, 1991, vol. 13, pp. 273–9.
- 45 F. Schamber: ASPEX Corp., 2011, pp. 1–7.
- 46 D. Kruger and A. Garbers-Craig: *Metall. Mater. Trans. B Process Metall. Mater. Process. Sci.*, 2017, vol. 48, pp. 1514–32.
- 47 Y. Wang, H. Tang, T. Wu, G. Wu, and J. Li: *Metall. Mater. Trans. B Process Metall. Mater. Process. Sci.*, 2017, vol. 48, pp. 943–55.
- 48 R. V. Väinölä, L.E.K. Holappa, and P.H.J. Karvonen: *J. Mater. Process. Tech.*, 1995, vol. 53, pp. 453–65.
- 49 E.T. Turkdogan: *Fundamentals of Steelmaking*, The Institute of Materials, London, 1996.
- 50 R. Maiti and E.B. Hawbolt: *J. Mater. Energy Syst.*, 1985, vol. 6, pp. 251–62.
- 51 Y.M. Won and B.G. Thomas: *Metall. Mater. Trans. A Phys. Metall. Mater. Sci.*, 2001, vol. 32, pp. 1755–67.
- 52 R. Diederichs and W. Bleck: *Steel Res. Int.*, 2006, vol. 77, pp. 202–9.
- 53 S.K. Choudhary and A. Ghosh: *ISIJ Int.*, 2009, vol. 49, pp. 1819–27.
- 54 Y. Shen, S. Yang, J. Liu, H. Liu, R. Zhang, H. Xu, and Y. He: *Steel Res. Int.*, 2019, vol. 90, p. 1800546.
- 55 R. Guan, C. Ji, M. Zhu, and S. Deng: *Metall. Mater. Trans. B Process Metall. Mater. Process. Sci.*, 2018, vol. 49, pp. 2571–83.
- 56 I.M.M. Das, N. Kumar, and M. Paliwal: *JOM*, 2019, vol. 71, pp. 2780–90.
- 57 J.J.R. Mondragón, M.H. Trejo, M.J.C. De Román, and H. Solís T: *ISIJ Int.*, 2008, vol. 48, pp. 454–60.
- 58 H. Liu, D. Hu, and J. Fu: *Materials (Basel)*., 2019, vol. 12, p. 2028.
- 59 B. Deo and R. Boom: *Fundamentals of Steelmaking Metallurgy*, Pearson Education Limited, Harlow, United Kingdom, 1993.
- 60 Y. Tomita: *Metall. Mater. Trans. A Phys. Metall. Mater. Sci.*, 1990, vol. 21, pp. 2739–46.
- 61 G. Li, F. Wang, R. Hui, and W. Cao: *Int. J. Miner. Metall. Mater.*, 2009, vol. 16, pp. 650–3.
- 62 J. Moon, S.J. Kim, and C. Lee: *Met. Mater. Int.*, 2013, vol. 19, pp. 45–8.

## **Chapter 5 Coarsening Mechanisms of CaS Inclusions in Ca-treated**

### **Steels**

This chapter is a pre-publication version of the article published in *Metals*, 2022, Volume 12, DOI: 10.3390/met12050707. This chapter explores the growth and coarsening of CaS inclusions under experimental and industrial conditions. The theoretical coarsening due to Ostwald ripening, mass transport, Brownian collision, and Stokes collision were compared with the observed average diameter change of CaS inclusions in three experiments. All details of the calculation were reported in this chapter to ensure reproducibility. The experiments were conducted with 20 ppm and 30 ppm S but similar high 35 ppm Ca. It was found that the average diameter of CaS inclusions increased with time in all experiments. The coarsening of CaS inclusions cannot be explained by one coarsening mechanism and must experience the transition of coarsening mechanism. The initial growth was found to be controlled by mass transport and the later coarsening was dependent on collision-related Brownian motion. This change in coarsening mechanism is supported by a decrease in Ca concentration and an increase in collision volume. A similar trend of changing coarsening mechanism was observed in industrial conditions, except turbulent flow instead of Brownian collision is the governing collision-related coarsening mechanism. This finding is supported by the calculation of particle size distribution change using the population balance equation.

The three experiments and associated analyses were completed by the primary author. Dr. Muhammad Nabeel assisted with the experiments. The industrial samples and associated inclusion analysis were completed by ArcelorMittal Dofasco and share with the author by Dr. Stanley Sun. Dr. Li Sun from ArcelorMittal Dofasco provided training for using automated SEM and ASPEX for inclusion analysis. The manuscript was drafted by the primary author. The contributions of all co-authors, Dr. Muhammad Nabeel, and Dr. Neslihan Dogan include providing suggestions and revising the manuscript.

## Coarsening Mechanisms of CaS Inclusion in Ca-Treated Steels

Keyan Miao\*, Muhammad Nabeel, Neslihan Dogan

Keyan Miao, Ph.D Student, [miaok@mcmaster.ca](mailto:miaok@mcmaster.ca)

Department of Materials Science and Engineering, McMaster University, 1280 Main Steet West, Hamilton, Ontario, L8S4L8, Canada

Muhammad Nabeel, Postdoctoral Fellow,

Department of Materials Science and Engineering, McMaster University, 1280 Main Steet West, Hamilton, Ontario, L8S4L8, Canada

Neslihan Dogan, Associate Professor

Department of Materials Science and Engineering, McMaster University, 1280 Main Steet West, Hamilton, Ontario, L8S4L8, Canada

### Abstract

In this work, the coarsening mechanisms of CaS inclusions in liquid steel were investigated by analyzing inclusions in experimental and industrial samples. A detailed particle size distribution evolution was reported. The observed CaS coarsening rate was compared with the theoretical coarsening rate calculated by using the models proposed in the literature. For both experimental and industrial data, it was observed that the coarsening mechanisms varied during different stages of Ca treatment. It was found that in the early stage (after Ca addition) of experiments and during Ca addition under industrial conditions, the coarsening of CaS was governed by diffusion-controlled growth. As the Ca dissolved in steel diminished, the coarsening was governed by collision-dependent mechanisms. For experimental conditions, the growth of CaS was controlled by the Brownian collisions, while the coarsening by turbulent collisions was the dominant mechanism under industrial conditions.

### 5.1 Introduction

A few decades ago, calcium treatment was introduced to improve steel castability by modifying solid  $\text{Al}_2\text{O}_3$  inclusions to liquid or semi-liquid calcium aluminates inclusions ( $\text{CA}_x$ , C and A denote CaO and  $\text{Al}_2\text{O}_3$ , respectively). Inclusions with compositions similar to  $\text{C}_3\text{A}$ ,  $\text{C}_{12}\text{A}_7$ , and CA are usually considered to be liquid or semi-liquid at steelmaking temperature, as opposed to solid  $\text{CA}_x$ , that are  $\text{CA}_2$  and  $\text{CA}_6$ . This is achieved by calcium reacting with oxygen in  $\text{Al}_2\text{O}_3$  inclusions. It is important to note that calcium has a high affinity to sulfur, so CaS inclusions are a common product of the calcium treatment. The formation of CaS inclusions does have some advantages. For example, the presence of CaS as transient CaS can act as a source of Ca supply for the

modification of oxide inclusions [1,2]. Moreover, precipitating S in the form of CaS suppresses the formation of MnS inclusions. However, an excess amount of stable CaS inclusions is usually considered detrimental, as they behave similarly to other solid inclusions [3–5], such as Al<sub>2</sub>O<sub>3</sub>. The impact of CaS inclusions on both the castability and the product quality is related to their size. The presence of larger CaS inclusions accelerates the clogging and deteriorates the product's physical properties. To the best of the authors' knowledge, despite being a well-known inclusion type, there is no research on the growth of CaS inclusions in steelmaking conditions.

The common coarsening mechanisms are diffusion-controlled growth, coarsening due to Ostwald ripening, Brownian motion, ascending velocity difference, and laminar and turbulent flows [6–9]. The diffusion-controlled growth mechanism is applicable to conditions where the rate of inclusion coarsening is limited by the mass transport of species in liquid steel. Ostwald ripening is a unique diffusion-related scenario driven by the concentration gradient at the interface associated with different inclusion sizes. As a result, some inclusions grow at the expense of smaller ones. Continuous irregular motion causes inclusions to move randomly in the liquid steel. Such motion independent of fluid flow is characterized as Brownian motion, leading to the collision and coalescence of inclusions. The coarsening of inclusions due to the ascending velocity of small inclusions is suggested to be proportional to the square of their radii [10], so the larger inclusions may encounter smaller ones during floatation, which then increases the inclusion size. Inclusions can also collide and coalesce when driven by laminar and turbulent flows. Two approaches in the literature are applied to determine the growth mechanisms of inclusions. The first compares the change in the average diameter of inclusions detected using SEM with those predicted by various theoretical coarsening mechanisms. The one that gives the closest agreement is considered to be the predominant mechanism. This approach was used in the work of Suzuki et al. [7] to determine the coarsening mechanism of SiO<sub>2</sub> inclusions in continuous casting slabs and test ingots. The mechanism was reported to be Ostwald ripening, as the theoretical prediction of Ostwald ripening had the best agreement with the observations. The same approach was also used by Ohta and Suito [6] for MgO, ZrO<sub>2</sub>, Al<sub>2</sub>O<sub>3</sub>, CaO-Al<sub>2</sub>O<sub>3</sub>, and MnO-SiO<sub>2</sub> inclusions in laboratory studies. The observed size change slightly deviated from the theoretical prediction; hence, they concluded Ostwald ripening to be the predominant mechanism but suggested that the effect of Stokes motion cannot be neglected. Wang et al. [8] also studied the impact of steel and inclusion compositions on the growth of oxide inclusions in experimental conditions using a similar method. Again, the reported mechanism was Ostwald ripening, but only during the first 10 min after aluminum (Al) addition. The mechanisms for the latter part were not reported. Overall, the previous studies emphasized the importance of Ostwald ripening on the growth of many oxide inclusions. It was unclear why the primary diffusion-controlled growth was never discussed in those studies and only included the unique diffusion-related mechanism of Ostwald ripening. Further, the first approach is accessible, and relationships between the inputs and the

predicted inclusion size are clearly defined. However, it is essential to note that the particle size distribution (PSD), which provides more detail about the coarsening process, cannot be obtained through this method.

The second method to predict the change in inclusion diameter is to utilize the population balance equations (PBE). It calculates how a fixed number of monomers are distributed between clusters; hence, they become inclusions of different sizes. This approach was first suggested in the study of Smoluchowski [11] and allows one to calculate the PSD. Later, this approach was used by Zhang and Pluschkell [9] and Zhang and Lee [12] to study the coarsening rate of  $\text{Al}_2\text{O}_3$  inclusions. Based solely on the PBE calculation, Zhang and Pluschkell [9] suggested that after the initial nucleation,  $\text{Al}_2\text{O}_3$  grew by Ostwald ripening and then by Brownian motion and turbulent collision for inclusions with diameters smaller than  $2\ \mu\text{m}$  and larger than  $4\ \mu\text{m}$ , respectively. However, the calculated PSD was not validated against any experimental or industrial data. Such shortness was improved later in the work of Zhang and Lee [12], whose calculation of the PBE reached the same 103 inclusions in terms of the coarsening mechanism of  $\text{Al}_2\text{O}_3$ , except Stokes motion was proposed to be also effective starting about 1 min after the initial nucleation. Moreover, the PSD predicted based on PBE was compared with the experimentally observed PSD. The predicted and the observed values for the PSD of  $\text{Al}_2\text{O}_3$  inclusions were in agreement for the initial stage of the defined experimental conditions. Some studies [13,14] used only quantification of collision frequency in PBE to determine the controlling coarsening mechanism, and they did not predict the evolution of PSD. An example is the work of Yin et al. [13], who studied the formation and growth of TiN clusters. By comparing the collision volume of Brownian collision, turbulent collision, and Stokes collision, they showed that the effect of Brownian collision on TiN growth was less significant than the other two collision mechanisms. Another example is the modeling work by Rimbert et al. [14] on precipitation and agglomeration of aluminum titanates. Again, by calculating the collision volume, Brownian motion was found to govern the growth of small micron size inclusions, and the increase in inclusion size caused the dominant mechanism to shift to collision in the turbulent flow, then Stokes motion. Overall, the PBE-based studies usually found diffusion to be significant in the early stages and later aggregation, but depending on the inclusion type and size, the significance of different collision-related mechanisms may differ. Compared to the first approach, all coarsening mechanisms can be considered simultaneously when applying the PBE, and their overall effects on the PSD can be studied. As the PBE is a more fundamental way of calculating the size change, it takes more calculation power and is less accessible [15]. Because diffusion-related growth mechanisms (Ostwald ripening and diffusion-controlled growth) depend primarily on the correct estimation of the number of monomers, applying the complete form of PBE, including both diffusion- and collision-related coarsening mechanisms to calculate the evolution of PSD of inclusions can be challenging.

The authors conducted laboratory-scale inclusion modification experiments at 1873 K using synthetic steel with compositions similar to a typical LCAK commercial product. Moreover, industrial samples were retrieved from the ladle after Ca addition and from tundish. The characteristics of inclusions were analyzed mainly using an automated SEM-EDS system called ASPEX. The present study focused on understanding the growth mechanism of the CaS inclusions in experimental and industrial conditions. This was done by comparing the observed and the predicted size change of CaS inclusions by different controlling mechanisms. The effect of coagulation on the evolution of CaS PSD was also calculated using PBE. The results were compared with the observed change in inclusion number density to reveal the critical coarsening mechanisms in industrial conditions.

## 5.2 Experimental Methodology

The high-temperature experimental setup is shown in Figure 5.1. In total, 0.3 g graphite rod, 6.5 g Mn, electrolytic Fe, and an appropriate amount of FeS depending on the targeted S content were placed inside an Al<sub>2</sub>O<sub>3</sub> crucible at room temperature and then heated in the vertical tube furnace to 1873 K and held for 10 min to homogenize the melt. Throughout the experiment, 99.999% Ar gas was fed into the furnace at a rate of 0.5 L/min to maintain a protective atmosphere. After that, Al and Si were added to deoxidize the steel melt. The melt was homogenized for an additional 15 min after deoxidation. Thereafter, Ca was added. The Ca addition technique was adopted from Verma et al. [3]. A mixture of electrolytic Fe and Ca enclosed in a capsule of steel shim was guided to the crucible. It helped Ca to immerse into the melt and increased the recovery rate. The total mass of raw materials was approximately 500 g.

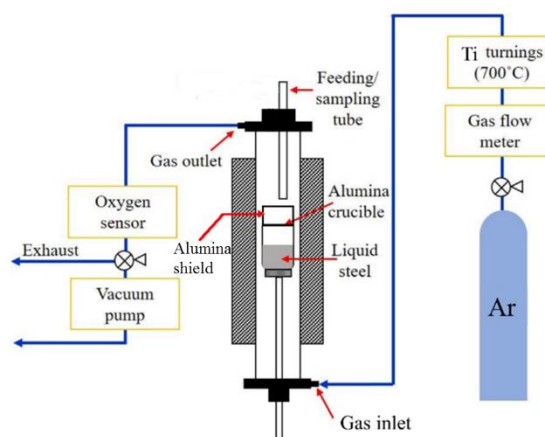


Figure 5.1 Schematic diagram of the experimental setup.

The present study used data from three laboratory experiments and four industrial heats. The compositions are summarized in Table 1. This study did not involve Heat 2 [2], which was studied in the authors' previous work due to a low number of CaS inclusions.

The laboratory experiments are denoted in the form of “[S content (ppm)][final Ca content (ppm)]”.

Pin-shaped samples with 0.005 m diameter and about 0.1 m length were taken at 1, 3, 5, 10, and 20 min after Ca addition and were cooled in air. Additional samples were taken at 30 and 40 min in Exp. 2025. The sample taken during the experiment are referred to as “pin samples”. The rest of the experimental steel was cooled inside the furnace at a rate of 10 K/min. Samples taken from the remaining steel are “bulk samples”. Lollipop samples were taken from ladle and tundish in 4 industrial heats. The lollipop samples are approximately 10 mm × 32 mm × 35 mm. A schematic diagram and the dimensions are shown in Figure 5.2.

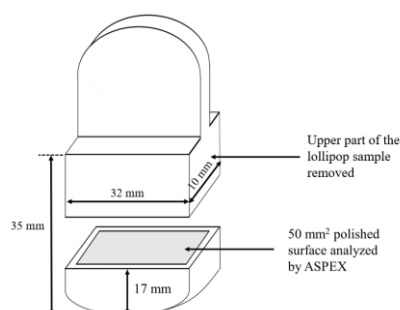


Figure 5.2 Schematic diagram of the lollipop sample.

The surface of collected pin samples was cleaned, then the pin samples were sectioned for chemical analysis and inclusions analysis. Al, Si, Mn, and Ca contents of steel samples were measured using inductively coupled plasma optical emission spectrometry (ICP-OES). In Exp. 2035 and Exp. 3035 (see Table 1), an initial 0.03 wt. pct. Al content was achieved. All concentrations have the unit of wt. pct. in this study unless specified. In Exp. 2025, no Al was added. The Mn, Si, and S contents were constant in an experiment, but Al increased from the initial concentration due to Ca-crucible reaction. The change was more significant in Exp. 2035 and Exp. 3035 because the initial Ca contents were higher. In Exp. 2035 and Exp. 3035, the initial Ca contents were 56 and 41 ppm, respectively, then decreased to 35 ppm in both experiments. In Exp. 2025, the Ca content reduced from 40 to 25 ppm. LECO™ CS744 carbon/sulfur analyzer was used to measure the S and C contents of steel samples. Total oxygen (T.O.) in Exp. 2035 were analyzed using a LECO™ ON736 oxygen/nitrogen analyzer. The measured concentrations were confirmed using pulse-height distribution analysis (spark OES-PDA).

A cross-section of every pin sample and a bulk sample was analyzed using an automated SEM-EDS system (ASPEX) to study the characteristics of inclusions. The automated SEM detects inclusion based on the contrast between the inclusions and the steel matrix. The SEM determines the geometric center of an inclusion, then 16 chords (diameters)

are drawn, passing through the center. The average of all 16 chords is the average diameter of the inclusion. This should not be confused with the average diameter of multiple inclusions (average diameter for short), denoted as  $d_{avg}$ . Connecting the ends of all chords determines the shape, perimeter and area. The details are discussed in elsewhere [16]. The inclusions with the longest diameter ( $d_{max}$ ) larger than 2  $\mu\text{m}$  were detected. A detailed discussion on steel chemistry change and the methodology of inclusion analysis can be found in the authors' previous publication [2] and will not be repeated here.

The detailed composition of the industrial samples can be found in Table 1. Sampling time slightly varies from heat to heat. Ladle samples L1 to L5 of Heat 1 were taken at 1848 K, and after 1, 2, 3, 4, and 5 min of the start of Ca addition. For the other three heats, only one sample (L5) was taken after Ca addition close to the end of ladle refining. Samples T1 and T2 were from tundish when about 30 and 80 t steel was cast from a 165-ton tundish at 1833 K. Lollipop samples were taken to conduct inclusion analysis. The samples were cut at 12 cm from the bottom. The intersecting surface of the lower part was cleaned and polished, then analyzed using the same automated SEM-EDS system, so the experimental and industrial inclusion data are comparable.

Based on inclusion compositions, the observed inclusions were classified into Ca-rich, liquid  $CA_x$ , solid  $CA_x$ ,  $Al_2O_3$ , CaS, CaS-other, CaS-MnS, and MnS. Liquid  $CA_x$  includes  $C_3A$ ,  $C_{12}A_7$ , and CA inclusions, whereas solid  $CA_x$  includes  $CA_2$  and  $CA_6$  inclusions. Ca-rich inclusions have higher CaO content than that in the liquid  $CA_x$ . CaS-other inclusions are those with compositions between CaS and  $CA_x$ . CaS-MnS inclusions have a significant fraction of both CaS and MnS phases; however, their fractions are not high enough to be considered as single-phase CaS or MnS. The CaS type inclusions still contain both CaS and MnS phases, but the CaS phase is more dominant. The term "CaS" refers to CaS type inclusions for simplicity unless otherwise specified.

Table 5.1 Chemical composition of experimental and industrial samples (wt. pct.).

Laboratory Experiments							
Exp. #	C	Si	Al	Mn	S (ppm)	Ca (ppm)	O (ppm)
2035	0.06	0.27	0.09	1.09	21	56–35	21–35
3035	0.06	0.23	0.06	0.98	31	41–36	n/a
2025	0.05	0.26	0.03	0.91	22	40–25	n/a
Industrial Samples							
1	0.05	0.23	0.03	1.14	28	44–32	20
3	0.06	0.22	0.03	1.07	29	47–34	20
4	0.05	0.22	0.03	1.13	18	40–30	20
5	0.06	0.21	0.04	1.12	18	69–35	20

### 5.3 Methods of Calculating Coarsening of CaS Inclusions

This study applied two methods described in the introduction section to determine the coarsening mechanism of CaS inclusions under laboratory and industrial conditions. Both calculation methods are explained in detail in this section.

The first method was to compare the evolution of the average diameter of CaS inclusions against the theoretical growth rate predicted by individual mechanisms. Mechanisms 1 to 5 listed below were considered in the present study.

1. Diffusion-controlled growth due to concentration gradient created by the Gibbs-Thomson effect (Ostwald ripening);
2. Diffusion-controlled growth;
3. Collision and coalescence due to the effect of Brownian motion;
4. Collision and coalescence due to ascending velocity difference (Stokes motion);
5. Collision and coalescence due to flow of the melt.

The second method, which was mainly used to study the coarsening of CaS inclusions under industrial conditions, was the population balance equation (PBE). Collision-related mechanisms 3 to 5 were considered. Mechanisms 1 and 2 were not used to calculate PBE because of the difficulty in estimating the number of CaS monomers that participate in the growth of CaS inclusions. The change in the volumetric number density of CaS inclusions calculated by PBE considering mechanisms 3 to 5 was compared with the observed number density change. The similarities between the two indicated the contribution of collision-related coarsening mechanisms.

#### 5.3.1 Determination of the Rate-Controlling Component

To calculate the coarsening rate of inclusion due to Ostwald ripening, the first step is to determine the rate-controlling component. Equation (5.1) [6–8] is the expression of change in average radius,  $r$ , from initial radius,  $r_0$ , during the time,  $t$ , at temperature,  $T$ . In Equation (5.1), the second term is the coarsening rate.  $\gamma$  is the interfacial tension between steel and CaS type inclusion,  $MV_i$  is the molar volume per mole of component  $I$  in a compound,  $D_i$  is the diffusion coefficient of component  $I$ , and  $C_{[i],b}$  and  $C_{(i)}$  are the concentrations of component  $I$  in the bulk melt and in inclusion, respectively. CaS type inclusions studied are considered as non-stoichiometric CaS-CA<sub>x</sub>-MnS complexes, so among Ca, Al, O, and S, the one that gives the lowest coarsening rate is the controlling component.

$$r^3 = r_0^3 + \frac{4}{9} \frac{2\gamma MV_i D_i C_{[i],b}}{RT(C_{(i)} - C_{[i],b})} t \quad (5.1)$$

The diffusion coefficients of Ca, Al, O, and S in steel at 1873 K used in calculations were obtained from the literature [17,18]. The diffusion coefficient of Ca at 1873 K was  $3.0 \times 10^{-9} \text{ m}^2/\text{s}$ , and those for S and O were  $4.3 \times 10^{-9}$  and  $3.1 \times 10^{-9} \text{ m}^2/\text{s}$ , respectively. The diffusion coefficient of Al in liquid iron equaled  $3.5 \times 10^{-9} \text{ m}^2/\text{s}$ . The steel-CaS interfacial tension was assumed to be 0.6 N/m, which is similar to MnS and other sulfides such as FeS and  $\text{Cu}_2\text{S}$  [19], as the exact value was never reported in the literature. The interfacial tension of liquid  $\text{CA}_x$  with a weight percentage of CaO between 35 and 55 pct. can be found in the literature [20]. For  $\text{CA}_x$  with CaO lower than 35 wt. pct., the interfacial tension was assumed to increase linearly to 2 N/m, which was the reported interfacial tension of  $\text{Al}_2\text{O}_3$  [21–25]. The values used for density,  $\rho$ , of  $\text{C}_{12}\text{A}_7$ , CA,  $\text{CA}_2$  and  $\text{CA}_6$  were 2690, 2560, 2920 and  $3790 \text{ kg/m}^3$ , respectively [8,26]. A value of  $2602 \text{ kg/m}^3$  was used for CaS. The ratio between inclusion density and the molar mass can be used to calculate  $MV_i$ . Moreover, the inclusion densities were used to calculate  $C_{(i)}$ , the concentration of component  $I$  in inclusions.

The mass fractions of dissolved Ca, Al, O, and S in steel were assumed to be 0.2 ppm, 0.04 wt. pct., 3 ppm, and 20 ppm, respectively. The conversion from mass fractions to mass concentration of component  $I$ ,  $C_{[i],b}$ , used the temperature–density correlation proposed by A.F. Crawley [27].

One can notice that in Table 2 the calculated coarsening rates of  $\text{C}_{12}\text{A}_7$ , CA, and CaS inclusions are consistently the lowest when Ca was considered as the rate-controlling element. This indicates that Ca is most likely the rate-controlling component. The calculated coarsening rates of  $\text{CA}_2$  and  $\text{CA}_6$ , assuming that Ca is the rate-controlling element, are comparable and higher than those calculated for O, respectively. This suggests that the latter is the rate-controlling component. However, by noticing that CaS type inclusions only contained less than 10 wt. pct. of  $\text{CA}_x$  phase with a composition close to  $\text{CA}_2$  and  $\text{CA}_6$  during solidification (CaS composition evolution is included in a later section), Ca being the rate-controlling component as suggested in Table 2 is a more appropriate assumption. When the fraction of  $\text{CA}_x$  phase was higher, which only occurred in Exp. 2035, the modification extent of the  $\text{CA}_x$  phases was equal to or higher than CA phase. In that case, the rate-controlling component was Ca. Therefore, Ca was used as the rate-controlling component in the present work when calculating the CaS diameter change controlled by Ostwald ripening.

Table 5.2 The comparison of calculated coarsening rate (m<sup>3</sup>/s) of different CA<sub>x</sub> and CaS to determine the rate-controlling component, namely, Ca, Al, O, and S.

	Ca	Al	O	S
C <sub>12</sub> A <sub>7</sub>	3.52 × 10 <sup>-19</sup>	1.79 × 10 <sup>-15</sup>	4.99 × 10 <sup>-18</sup>	
CA	6.93 × 10 <sup>-18</sup>	1.20 × 10 <sup>-14</sup>	4.65 × 10 <sup>-17</sup>	
CA <sub>2</sub>	1.02 × 10 <sup>-17</sup>	9.97 × 10 <sup>-15</sup>	2.25 × 10 <sup>-17</sup>	
CA <sub>6</sub>	4.15 × 10 <sup>-17</sup>	1.24 × 10 <sup>-15</sup>	1.24 × 10 <sup>-17</sup>	
CaS	1.38 × 10 <sup>-18</sup>			4.95 × 10 <sup>-16</sup>

### 5.3.2 Coarsening Due to Ostwald Ripening

As Ca was determined to be the rate-controlling component, Equation (5.2) was used to calculate the change in the average radius of CaS inclusions due to Ostwald ripening. The theories of Ostwald ripening had already been discussed in numerous studies [28–30]; hence, they will not be discussed here.

$$r^3 = r_0^3 + \frac{4}{9} \frac{2\gamma MV_{Ca} D_{Ca} C_{[Ca],b}}{RT(C_{(Ca)} - C_{[Ca],b})} t \quad (5.2)$$

When calculating the coarsening rate of CaS type inclusions, their average composition from each sample were used to estimate  $\gamma$ ,  $MV_{Ca}$  and  $C_{(Ca)}$ . In the work of Wang et al. [8], the interfacial tension of CA<sub>x</sub> was calculated using Equation (5.3), where  $x_i$  represents the molar fraction. The similar approach was used to calculate the interfacial tension of non-stoichiometric CaS-CA<sub>x</sub>-MnS complexes, i.e., CaS type inclusions, through Equation (5.4). The approach of predicting the molar volume of slag was used to estimate the molar volume of inclusions. In Equation (5.5),  $x_{Ca}$  is the molar fraction of Ca and  $MV$  denotes molar volume. The molar volumes of CaO, Al<sub>2</sub>O<sub>3</sub>, CaS and MnS can be found in the literature [20,26]. Similarly, the method of estimating the density of slag [20] was applied to calculate the density of inclusion  $\rho_P$  in Equation (5.6). Calculating  $\rho_P$  allows one to obtain  $C_{(Ca)}$  based on the mass fraction of CaO and CaS of the average composition of CaS type inclusions.

$$\gamma_{CA_x} = x_{CaO} \cdot \gamma_{CaO} + x_{Al_2O_3} \cdot \gamma_{Al_2O_3} \quad (5.3)$$

$$\gamma_{CaS-CA_x-MnS} = x_{CaS} \cdot \gamma_{CaS} + x_{CA_x} \cdot \gamma_{CA_x} + x_{MnS} \cdot \gamma_{MnS} \quad (5.4)$$

$$MV_{Ca} = \frac{x_{CaO} \cdot MV_{CaO} + x_{Al_2O_3} \cdot MV_{Al_2O_3} + x_{CaS} \cdot MV_{CaS} + x_{MnS} \cdot MV_{MnS}}{x_{Ca}} \quad (5.5)$$

$$\rho_P = \frac{x_{CaO} \cdot MW_{CaO} + x_{Al_2O_3} \cdot MW_{Al_2O_3} + x_{CaS} \cdot MW_{CaS} + x_{MnS} \cdot MW_{MnS}}{x_{CaO} \cdot MV_{CaO} + x_{Al_2O_3} \cdot MV_{Al_2O_3} + x_{CaS} \cdot MV_{CaS} + x_{MnS} \cdot MV_{MnS}} \quad (5.6)$$

The concentration of dissolved Ca in the bulk melt was proposed to be 0.2 ppm during the industrial Ca injection process in the literature [31]. In the present study, Ca addition was conducted once in each experiment. Because of the volatile nature of Ca, the  $C_{[Ca],b}$  was assumed to decrease from 0.2 ppm to equilibrium  $C_{[Ca],eq}$  following Equation (5.7) [32] starting at 1 min after Ca addition. The values of  $C_{[Ca],eq}$  were calculated using FactSage 7.2 based on the steel chemistries.  $k_{Ca}$  is the mass transfer coefficient of Ca in steel, which was suggested to be in the range of  $2.35 \times 10^{-4}$  to  $3.53 \times 10^{-4}$  m/s in a previous study with a similar experimental approach as the present study [32]. An average value of  $2.94 \times 10^{-4}$  m/s was used here. The term  $\frac{A}{V}$  in Equation (5.7) is the steel-Ar interfacial area per unit volume of steel calculated based on the geometry of the crucibles.

$$\ln \left( \frac{C_{[Ca],b} - C_{[Ca],eq}}{C_{[Ca],0} - C_{[Ca],eq}} \right) = -k_{Ca} \frac{A}{V} t \quad (5.7)$$

The diameter change of CaS inclusions was assumed to be neglectable after the solidification was completed. The solidus temperature was estimated to be 1773 K for all experiments using Equation (5.8) [33], and the estimated value was confirmed with FactSage calculation. So, with a 10 K/min cooling rate, the temperature decrease from 1873 to 1773 K was considered to be 10 min.

$$T_{sol}(K) = 1809 - 344[\%C] - 183.5[\%S] - 124.5[\%P] - 6.8[\%Mn] - 12.3[\%Si] - 4.1[\%Al] - 1.4[\%Cr] - 4.3[\%Ni] \quad (5.8)$$

### 5.3.3 Coarsening Due to Ca Diffusion

It was suggested in the literature that when the coarsening of inclusion is controlled by diffusion, the movement of the steel-inclusion interface can be expressed using Equation (5.9) [34].  $C_{[Ca],i}$  is the concentration of Ca at the steel-inclusion interface. Its values were calculated using a simplification of the method adapted by Tabatabaei et al. [35]. Assuming the  $CA_x$  at the surface of CaS type inclusions was insignificant, the calculation started with the mass balance at the interface, as given by Equation (5.10), where  $n_i$  denotes the transfer of component  $i$  through the boundary layer.

$$r^2 = r_0^2 + 2D_{Ca} \frac{C_{[Ca],b} - C_{[Ca],i}}{C_{(Ca)} - C_{[Ca],i}} t \quad (5.9)$$

$$n_{Ca} = n_S \quad (5.10)$$

Then, at any  $r$  exists

$$4\pi r^2 k_{m,ca}(X_{[Ca],i} - X_{[Ca],b}) = 4\pi r^2 k_{m,s}(X_{[S],i} - X_{[S],b}) \quad (5.11)$$

$X_{[i],i}$  is the molar concentration of component  $i$  in steel. The mass transfer coefficient,  $k_{m,i}$ , was suggested to follow the expression as Equation (5.12) [35]

$$Sh = \frac{k_{m,i}d}{D_i} \quad (5.12)$$

where  $d$  is the diameter of inclusion. Sherwood number,  $Sh$ , can be assumed to have a constant value of 2 for small inclusions in liquid steel with low viscosity [36]. Substituting Equation (5.12) into Equation (5.11) gives

$$D_{Ca}(X_{[Ca],i} - X_{[Ca],b}) = D_S(X_{[S],i} - X_{[S],b}) \quad (5.13)$$

When modeling the modification of  $CA_x$  inclusions, the concentration of O dissolved in steel was assumed to be at the level after Al deoxidation and before Ca addition. In other words, calcium would only affect the local steel chemistry at the early stage [35]. Using a similar assumption, the dissolved S content was considered to decrease linearly with time from a measured T.S concentration to the calculated equilibrium dissolved S concentration. Combining all the aforementioned assumptions with the concentration of other steel constituents allow one to determine  $X_{[Ca],b}$  and  $X_{[S],b}$ . It is common to consider that equilibrium is maintained at the steel-inclusion interface [37–40]. With the assumption that  $CA_x$  phases were insignificant at the surface of CaS type inclusions, the only equilibrium established on the CaS surface was Reaction (5.14).



and must satisfy

$$K_{eq} = \frac{a_{CaS}}{(h_{Ca}w_{[Ca],i})(h_S w_{[S],i})} = \frac{1}{\left(h_{Ca} \frac{X_{[Ca],i} MW_{Ca}}{\rho_{steel}}\right) \left(h_S \frac{X_{[S],i} MW_S}{\rho_{steel}}\right)} \quad (5.15)$$

where  $h_i$  is the activity coefficient and  $\rho_{steel}$  is the density of steel. Equilibrium constant,  $K_{eq}$ , was calculated based on the standard Gibbs Energy through Equation (5.16), which is the summation of  $\Delta G^\circ$  of related reactions from the literature [41,42].  $K_{eq}$  at 1873 K calculated using Equation (5.16) was confirmed to be similar to  $K_{eq}$  proposed in the literature [43–45].

$$\Delta G^\circ = -692158 + 205.33T \text{ J/mol} \quad (5.16)$$

Equation (5.13) was solved in conjunction with Equation (5.15) to obtain  $C_{[S],i}$  and  $C_{[Ca],i}$ . The latter was substituted into Equation (5.9) to calculate the average diameter of CaS type inclusions with time.

### 5.3.4 Coarsening Due to Brownian Motion

The inclusions collide and coalesce due to their random motion. In that case, the change of volumetric inclusion number,  $N_V$ , can be calculated as suggested in Equation (5.17) [6,11,46].  $N_{V,0}$ ,  $k_B$  and  $\eta$  are the initial volumetric inclusion number density, Boltzmann constant and steel viscosity, respectively. Equation (5.18) expresses the conversion from inclusion volume fraction,  $f$ , to  $N_V$ . Equation (5.18) can be rearranged to write  $N_V$  as a function of  $f$  and  $r$ , and  $N_{V,0}$  as a function of  $f_0$  and  $r_0$ . Substituting  $N_{V,0}$  and  $N_V$  in Equation (5.17) gives Equation (5.19). The volume fraction was calculated by first converting the planar size distribution given by ASPEX to volumetric size distribution through the Schwartz–Saltykov method. The detailed procedure is available elsewhere [47]. Then, the total volume of CaS inclusions per unit volume of steel was estimated. The effect of temperature on steel viscosity,  $\mu$ , was reported in the literature [48]. It covers the temperature from 1783 to 1853 K; therefore, the relation with temperature was extrapolated to 1773 and 1873 K.

$$N_V = \frac{N_{V,0}}{1 + \frac{8k_B T N_{V,0}}{3\mu} t} \quad (5.17)$$

$$f = \frac{4}{3} \pi r^3 N_V \quad (5.18)$$

$$r^3 = \frac{f}{f_0} r_0^3 + \frac{2k_B T f}{\pi \mu} t \quad (5.19)$$

### 5.3.5 Coarsening Due to Ascending Velocity Difference

Stoke's law predicts that larger inclusions ascend faster than the small ones. This causes relative motion between inclusions of different sizes, leading to collision and coalescence. The inclusion radius change due to ascending velocity difference can be expressed using Equation (5.20) [7]. Term  $g$  is the gravitational acceleration taken as 9.8 m/s<sup>2</sup>.

$$r = r_0 \left[ 1 - \frac{gf(\rho_{Fe} - \rho_P)r_0 t}{18\mu} \right]^{-1} \quad (5.20)$$

### 5.3.6 Coarsening Due to Melt Flow

Inclusions can also be brought to collide and coalesce due to melt flow. In the laboratory experiments, the melt had no controlled stirring. Ca was added during the early stage of an experiment and was rapidly consumed. During the dissolution of Ca, the Ca gas bubbles formed continuously but only for a limited time. Therefore, its contribution to stirring the melt was not taken into account for the coarsening of CaS inclusions in the analysis.

### 5.3.7 Coarsening Due to the Multiple Mechanisms Predicted by Population Balance Equation (PBE)

Smoluchowski [11] formulated the particle coagulation kinetics through PBE. A general form, Equation (5.21), expresses the rate of change of the volumetric number density of CaS inclusions in group  $k$ ,  $\frac{dN_{V,k}}{dt}$ . The volumetric population density of inclusions with size  $k$ ,  $N_{V,k}$ , can increase due to the coalescence of a pair of inclusions from group  $i$  and group  $j$ , which is the first term of Equation (5.21). The second term is the expression of inclusions becoming too large to remain in group  $k$  after coalescing with another inclusion of sufficiently large size. The number densities of CaS inclusions in group  $i$  and  $j$  are represented by  $N_{V,i}$  and  $N_{V,j}$ , respectively.  $\beta^C$  is the collision frequency function that quantifies the collective effects of Brownian motion,  $\beta^B$ , Stokes motion,  $\beta^S$ , as well as the turbulent flow,  $\beta^T$ , and laminar flow,  $\beta^G$ , on the growth of CaS inclusions. The detailed expressions are shown as Equations (5.22)–(5.26) [12].  $\varepsilon$  is the energy dissipation rate that quantifies the stirring power, and was also suggested to be correlated to  $\alpha$ , the coagulation coefficient [49].  $\frac{du}{dy}$  is the velocity gradient in the laminar shear zones, which are usually near the walls [12].

$$\frac{dN_{V,k}}{dt} = \frac{1}{2} \sum_{i=1, i+j=k}^k \beta_{ij}^C N_{V,i} N_{V,j} - \sum_{i=1}^k \beta_{ik}^C N_{V,i} N_{V,k} \quad (5.21)$$

$$\beta^B = \frac{2 k_B T}{3 \mu} (r_i + r_j) \left( \frac{1}{r_i} + \frac{1}{r_j} \right) \quad (5.22)$$

$$\beta^S = \frac{2 \pi g (\rho_{steel} - \rho_{CaS})}{9 \mu} |r_i - r_j| (r_i + r_j)^3 \quad (5.23)$$

$$\beta^T = 1.3 \pi^{0.5} \alpha \sqrt{\frac{\varepsilon \rho_{steel}}{\mu}} (r_i + r_j)^3 \quad (5.24)$$

$$\beta^G = \frac{4}{3}(r_i + r_j)^3 \left| \frac{du}{dy} \right| \quad (5.25)$$

$$\beta^C = \beta^B + \beta^S + \beta^T + \beta^G \quad (5.26)$$

In a later section, the combined contribution of relevant collision-related coarsening mechanisms on the evolution of PSD of CaS inclusions calculated using the PBE will be discussed. The particle-size-grouping (PSG) method introduced in the work of Nakaoka et al. [50] was used to simplify the calculation of PBE. This method was confirmed to give approximation close to the exact solution and had been used extensively in previous studies [51–53].

## 5.4 Results

### 5.4.1 CaS Growth in Experimental Conditions

Figure 5.3 shows the evolution of the area fraction (AF) of all inclusion types from the three laboratory experiments. The details of the evolution of inclusion types were discussed in the authors' previous publication [2]. The value for the AF of CaS inclusions increased continuously over time in Exp. 2035 and 3035. By the end of the 20-min experiment, the values for AF of CaS were 44 and 22 ppm in Exp. 2035 and 3035, respectively. The authors suggested that CaS inclusions were stable at 1873 K [2], so these inclusions were reaction products. In Exp. 2025, in comparison, CaS was thermodynamically stable in the first 10 min after Ca addition, but the AF values were low at around 2 ppm. The AF of CaS increased to 6 ppm in the 20-min sample, followed by a slight decrease in the 40-min sample, but high CaS AF was again observed in the bulk sample to be 12 ppm. Some CaS-CA<sub>x</sub> complexes, classified as CaS-other inclusions, were also found in these experiments. SEM images and EDS mappings of typical CaS inclusions are shown in Figure 5.4 to provide some insight about their shape and structures. One can easily notice that the CaS inclusions were close to spherical. Therefore, in both methods of determining the coarsening mechanisms, CaS inclusions were assumed to be spherical for simplicity.

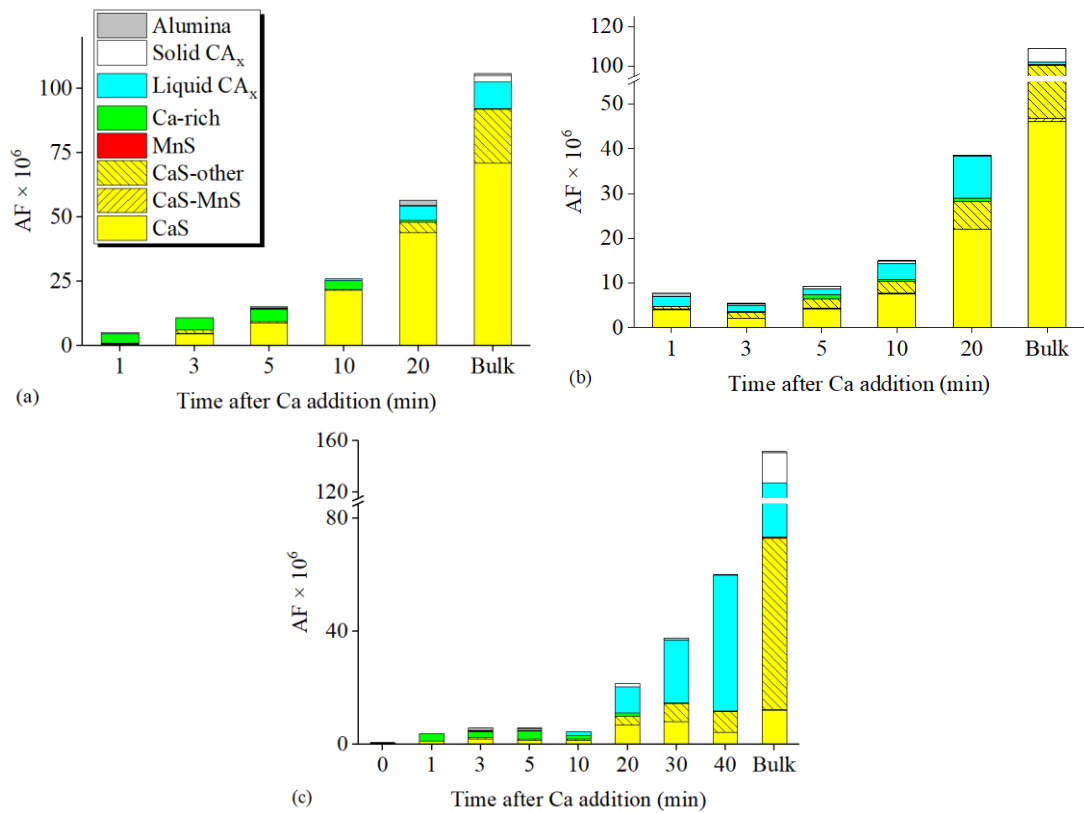


Figure 5.3 Evolution of area fraction (AF) of inclusions in (a) Exp. 2035, (b) Exp. 3035, and (c) Exp. 2025.

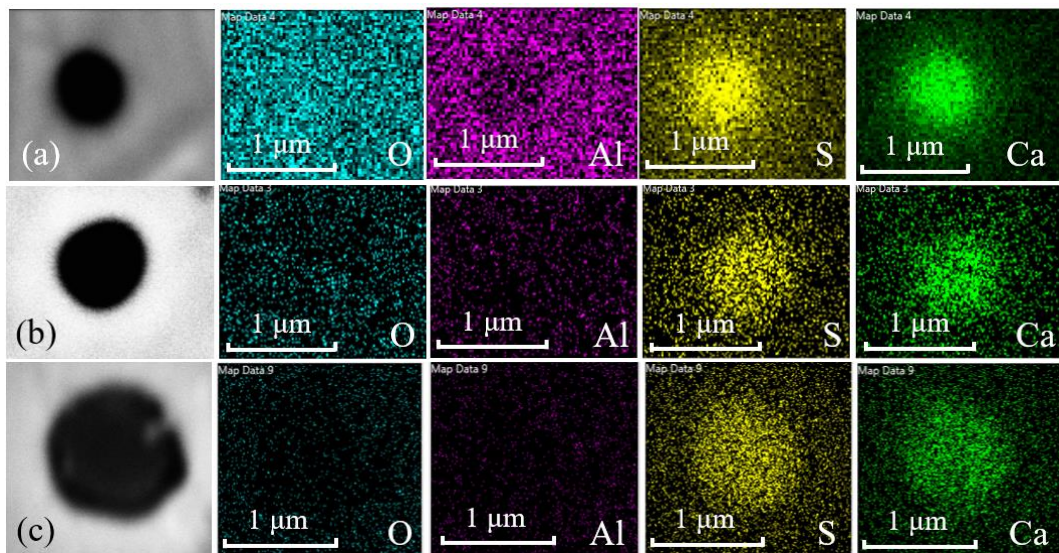


Figure 5.4 SEM-EDS elemental maps of CaS inclusion in (a) 1-min sample of Exp. 2035, (b) 3-min sample of Exp. 2035 and (c) 20-min sample of Exp. 3035.

The evolutions of the average diameter and the composition of CaS type inclusions are shown in Figure 5.5. The CaS type inclusions in samples taken in Exp. 2035 were composed of initially 27 wt. pct. CaO. The fraction of CaO phase decreased to 3 wt. pct

when the experiment was close to the end. Because Ca mainly reacted with O in the early stage (Figure 5.3 (a)), CaS type inclusions (whose number was small) contained approximately 10 wt. pct. MnS. As more CaS formed as Exp. 2035 proceeded, less S was available to react with Mn, so MnS content in CaS decreased. Some concentration of  $\text{Al}_2\text{O}_3$  phase was also found in the CaS type inclusions. CaS fraction increased from 58 wt. pct. to 88 wt. pct. during the 20 min experiment. In Exp. 3035, on the contrary, the fraction of CaO phase never exceeded 4 wt. pct. and the maximum MnS phase fraction was at 8 wt. pct. because CaS inclusions were formed directly through Ca and S reaction. [2] As a result, the fractions of CaS were constantly above 82 wt. pct. The distribution of phases within CaS inclusions from Exp. 2025 were similar to that of Exp. 2035 in the early stages. The fraction of CaO phase can be higher than 25 wt. pct. during the first 10 min after Ca addition. That was because Al was not added before Ca addition; hence, a significant portion of Ca added reduced  $\text{Al}_2\text{O}_3$  from the crucible and became a vital oxygen bearer. However, starting at 10 min, the fraction of the CaS phase was constantly higher than 75 wt. pct.

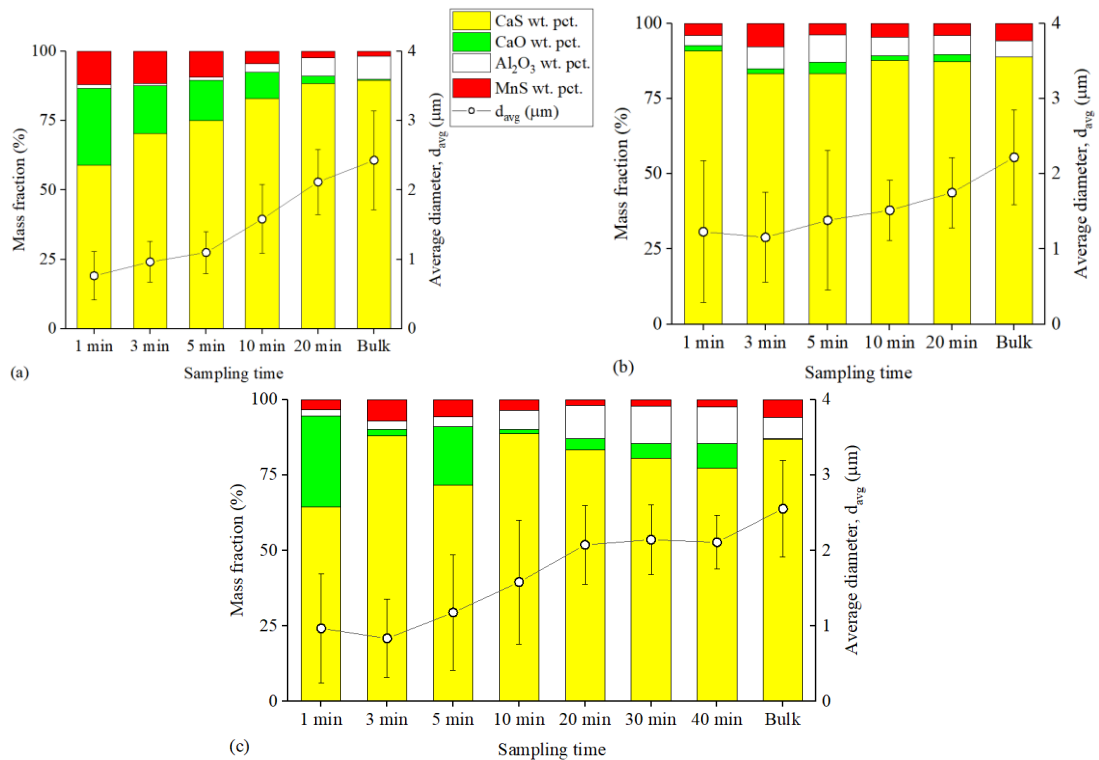


Figure 5.5 Average diameters and compositions of CaS type inclusions in (a) Exp. 2035, (b) Exp. 3035, and (c) Exp. 2025.

Both the average diameters and the standard deviations of the CaS inclusions are included in Figure 5.5. In Exp. 2035, at least 150 CaS inclusions were analyzed in each sample by ASPEX, except for the first sample, in which the number of inclusions was 41. The average diameter of CaS inclusions was initially  $0.8 \mu\text{m}$ , then gradually increased to about  $2.1 \mu\text{m}$  within 20 min after Ca addition at 1873 K, then slightly

increased further to 2.4  $\mu\text{m}$  in the bulk sample. The standard deviation for the average diameter values increased marginally from about 0.3 to 0.4  $\mu\text{m}$ . In Exp. 3035, 26 CaS inclusions were detected in the first sample. The number of CaS in later samples varied from 60 to 628. CaS average diameter increased from 1.2 to 1.7  $\mu\text{m}$ , and increased by another 0.5  $\mu\text{m}$  during solidification to end with 2.2  $\mu\text{m}$  average diameter in the final bulk sample. Because of the relatively smaller number of CaS inclusions analyzed, especially in the first sample, the standard deviation fluctuated in Exp. 3035. The number of CaS inclusions detected in Exp. 2025 was lower than in Exp. 2035 and Exp. 3035 because of the relatively lower Ca content and S content. In most samples of Exp. 2025, the number of detected CaS can be as low as 10, such as in the 1-min sample. The number gradually increased to about 50 in the 20, 30, and 40-min samples. In bulk, a total of 104 CaS inclusions were analyzed by ASPEX. During the first 20 min of Exp. 2025, the average diameter of CaS increased from 1 to 2.1  $\mu\text{m}$ . Thereafter, generally it did not change until the last bulk sample, which was found to be 2.6  $\mu\text{m}$ . Notice that a decrease in standard deviation from 0.8 to 0.5  $\mu\text{m}$  occurred at 20 min.

The detailed evolution of CaS particle size distributions (PSD) of the three experiments is shown in Figure 5.6. The  $x$ -axis and the  $y$ -axis are shown in logarithmic form for better visualization. The increase in the average diameter and the planer number density ( $N_A$ ) of CaS inclusions from Exp. 2035 were apparent during the first 5 min after Ca addition. The CaS showed a log-normal distribution starting at 3 min, indicated by the iconic parabolic shape [54–56]. One can notice that the left side of the 1, 3, and 5-min PSD curves overlapped. This trend means a consistent “supply” of newly formed small inclusions. High-temperature phenomena including inclusion formation were rarely reported to be limited by the chemical reaction rate [7,12,35,57,58], so the formation of new, small inclusions would largely depend on the rate of mass transport in the early stage of the experiment. As the experiment proceeded, the PSD curve shifted rightward while keeping a similar shape from 5 min to 20 min after Ca addition, indicating the disappearance of smaller inclusions. This was considered the result of collision and coalescence.

During the first 5 min of the Exp. 3035, the PSD curve barely changed. That was potentially related to lower Ca supply in Exp. 3035 than that of Exp. 2035. In Exp. 3035, the total Ca content was initially 42 ppm and remained stable. Then, the dissolved Ca concentrations were likely lower in Exp. 3035. This would affect the growth rate of CaS inclusions when mass transport was the controlling mechanism. However, as the CaS inclusions grew over time, they became detectable. And with the collision occurring at the same time, inclusions coalesced, and the rightward shift of the PSD curve became apparent, as seen from the 10-min PSD curve in Figure 5.6 (d). The following steps of the Exp. 3035 at 1873 K were similar to the later stages of Exp. 2035.

Similarly, CaS inclusions in Exp. 2025 started with a relatively high number of

submicron inclusions. The PSD remained almost unchanged in the first 3 min after Ca addition. Then, until 10 min, the PSD curve shifted rightward, with the peak moved from  $d_{avg}$  equals 0.8 to 1.3  $\mu\text{m}$ . Because of the presence of submicron size inclusions, the growth of CaS inclusions was still mainly relevant to mass transport. A sudden change in the shape of PSD was observed at 20 min after Ca addition, where small CaS inclusions disappeared, and  $N_A$  of inclusions larger than 2  $\mu\text{m}$  drastically increased compared to the previous sample. This can be considered to signify the coarsening through collision and coalescence.

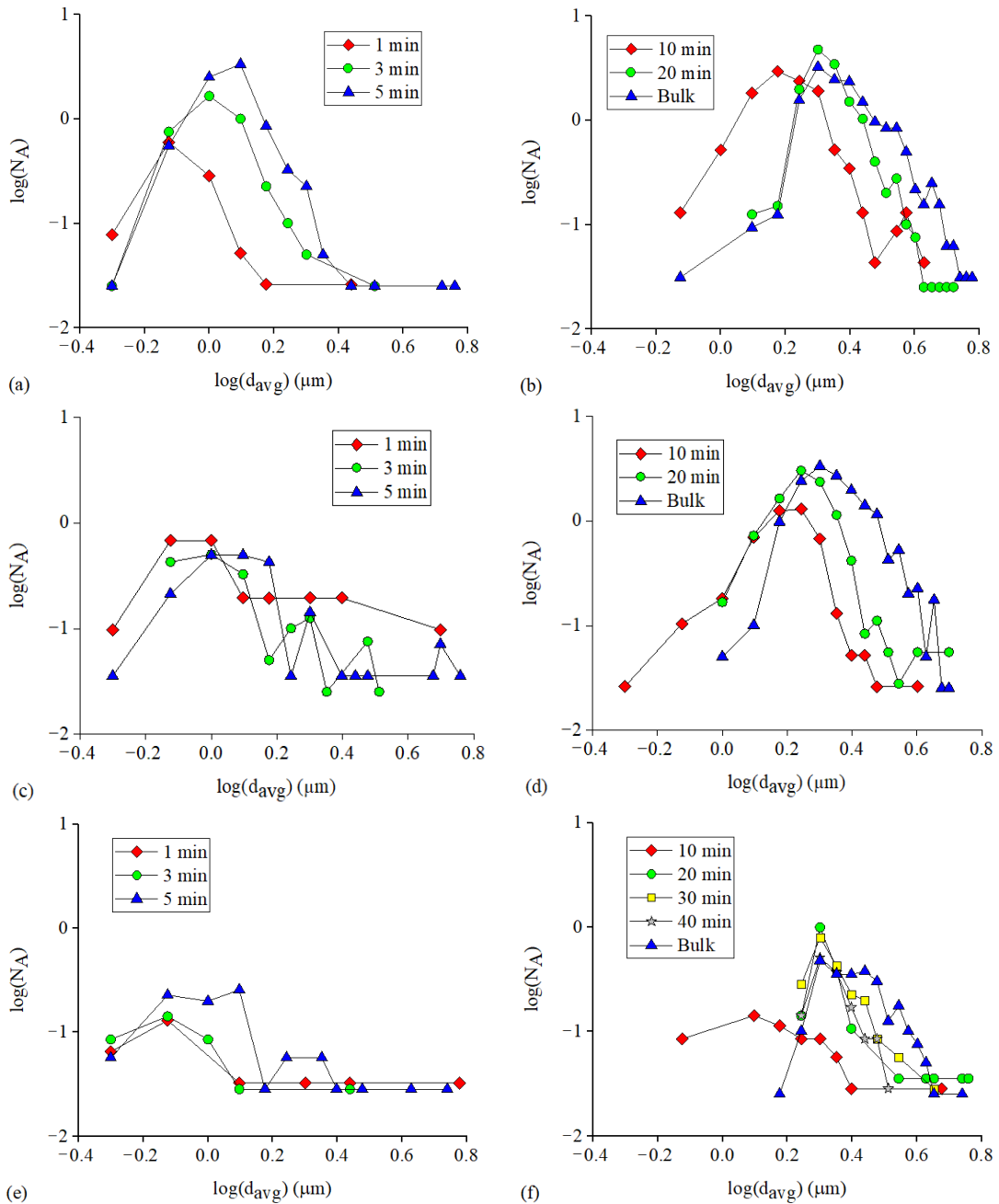


Figure 5.6 The particle size distribution of CaS type inclusions in (a,b) Exp. 2035, (c,d) Exp. 3035, and (e,f) Exp. 2025.

During solidification, the PSD curve evidently broadened and deviated from the symmetrical shape seen in the last pin sample in all experiments. In Exp. 2035, the  $N_A$  of CaS inclusions with a diameter larger than  $3.25 \mu\text{m}$  ( $\log(d_{\text{avg}}) > 0.51$ ) shown as the right side of the PSD evidently increased, while the left side of the PSD peak remained practically unchanged. A similar trend can also be observed in Exp. 2025 in Figure 5.6 (f). In Exp. 3035, the entire PSD shifted further to the right during solidification, and the width of the curve increased. These observations were correctly reflected by the change

of average diameter and standard deviation shown in Figure 5.5, which were potentially due to the precipitation of CaS phase and MnS phase on CaS type inclusions.

#### 5.4.2 CaS Growth in Industrial Conditions

The coarsening behaviors of CaS inclusions in samples taken from ladle and tundish during steel-refining processes are evaluated in this section. For this purpose, lollipop samples from four industrial heats were studied. The evolution of the average diameter of CaS type inclusions with respect to sample number is shown in Figure 5.7. In Figure 5.7, small offsets are introduced on the  $x$ -axis to improve readability.

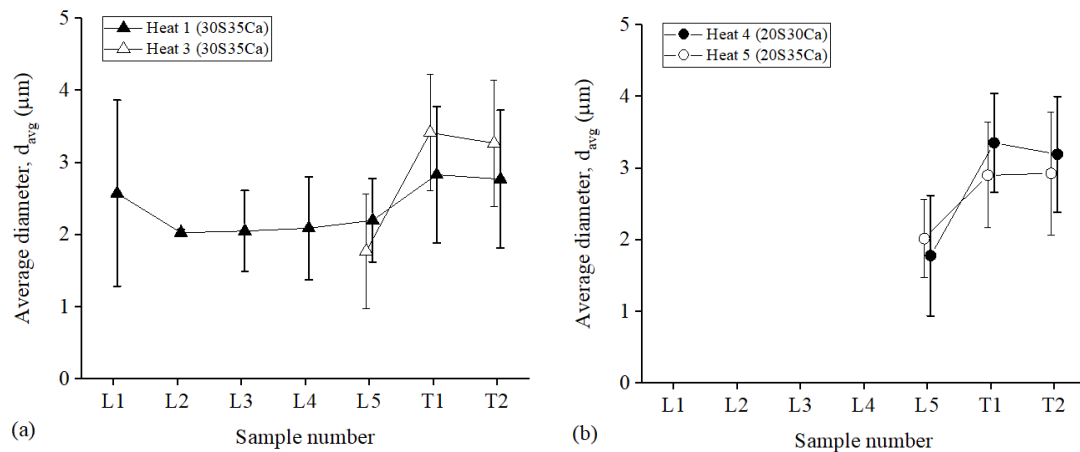


Figure 5.7 Evolution of the average diameters of CaS type inclusions in samples taken from (a) Heats 1 and 3–30 ppm S and 35 ppm T.Ca and (b) Heats 4 and 5–20 ppm S and 35 ppm T.Ca.

Figure 5.7 suggests that once the CaS type inclusions were observed, their average diameters were already at around 2  $\mu\text{m}$  regardless of heat chemistries. In Exp. 2035 and Exp. 3035, it took about 20 min for the average diameter of CaS to increase to slightly above 2  $\mu\text{m}$ . This was longer than the roughly 5-min Ca addition in industrial conditions, meaning that some differences exist between the coarsening of CaS in the two conditions. Comparing the first tundish sample (T1) with the ladle sample after Ca addition (L5), the increase in CaS average diameter is apparent. In Heat 1 and Heat 5, the difference between T1 and L5 was 0.6 and 0.9  $\mu\text{m}$ , respectively. For Heat 3 and Heat 4, the difference was higher at 1.6  $\mu\text{m}$ .

The evolution of the PSD of CaS inclusions in Heat 1 is shown in Figure 5.8 for a more detailed discussion. It is worth mentioning that Figure 5.8 is based on the ASPEX analysis, including inclusions with  $d_{\text{max}}$  (longest diameter of a non-spherical inclusion) larger than 0.5  $\mu\text{m}$ . This will be referred to as 0.5  $\mu\text{m}$  analysis for simplicity. All other plots and related discussions are based on the ASPEX analysis, including inclusions with  $d_{\text{max}} > 2 \mu\text{m}$ . The ASPEX processing time drastically increased when decreasing the  $d_{\text{max}}$

threshold from 2 to 0.5  $\mu\text{m}$ , so the 0.5  $\mu\text{m}$  analysis was only performed on samples of Heat 1.

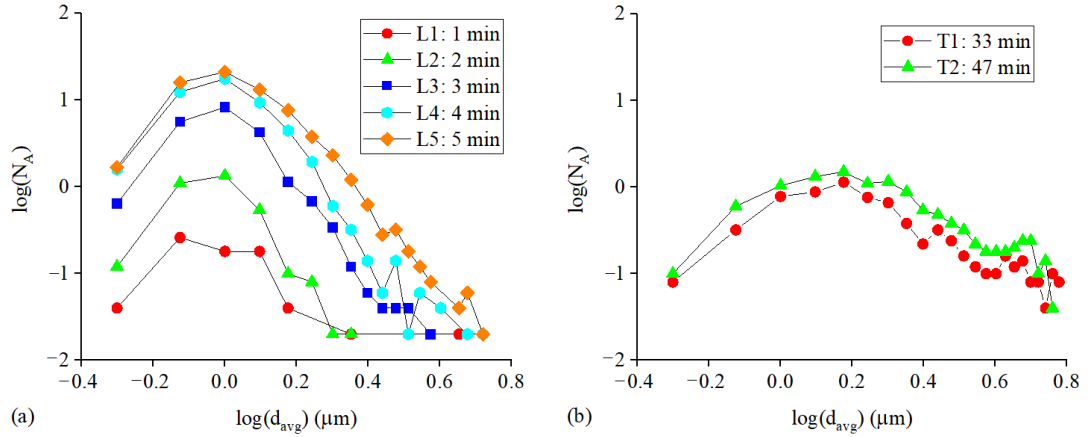


Figure 5.8 The evolution of particle size distribution for CaS type inclusions in Heat 1 including inclusions with  $d_{max} > 0.5 \mu\text{m}$  (a) ladle samples and (b) tundish samples.

Figure 5.8 (a) includes the PSD of CaS inclusions from all the ladle samples in Heat 1. One can see that the PSD shares a very similar pattern in all five ladle samples. Small CaS inclusions formed immediately after Ca addition, showing the parabolic shape associated with the typical log-normal distribution. During the Ca addition from L1 to L5, the number density ( $N_A$ ) of all sizes increased. This caused the PSD curves to remain similar in all ladle samples, with the peak at around  $\log(d_{avg})$  equal to 0. This is reflected in Figure 5.7 by a stable average CaS inclusion diameter. The change in the PSD of CaS inclusions from ladle to tundish was very apparent in Figure 5.8 (b). The PSD of tundish samples compared to the PSD of ladle samples appeared much broadened and shifted rightward. This is reflected in Figure 5.7 (a) by the increased average diameter and standard deviation in T1 compared to L5. At 33 min after Ca addition, the  $N_A$  of inclusions with  $\log(d_{avg}) < 0.24$  decreased by at least one order of magnitude, while the  $N_A$  of inclusions with  $\log(d_{avg}) > 0.24$  slightly increased.

## 5.5 Discussion

The evolution of PSD in all three experiments suggests that the diameter change of CaS inclusions was related to mass transport in the early stage and later depended on coagulation. To better understand the inclusion coarsening kinetics, the present work compares the change of average diameter of CaS inclusions observed through the experiments with models explained in the previous section.

### 5.5.1 Coarsening Mechanisms of CaS Inclusions under Experimental Conditions

The diameter change calculated using the methods explained in the previous sections was plotted and compared with the observed average diameters of CaS inclusions in Exp. 2035, Exp. 3035 and Exp. 2025 in Figure 5.9. For modeling calculations, the initial diameter of CaS inclusions was set to be  $0.01 \mu\text{m}$  in all conditions. The final diameter predicted from lowest to highest are through the mechanisms of Stokes motion, Ostwald ripening, diffusion-controlled growth, and Brownian motion for all three experiments. The diameter changes due to Ostwald ripening and Stokes motion are insignificant, with less than  $0.2 \mu\text{m}$  regardless of experimental conditions, which clearly underpredict the CaS inclusions diameter change. The diffusion-controlled growth shows a rapid increase in the first 5 min but then decreases. The predicted diameter decrease is less apparent in Exp. 3035 than the other two experiments. The Brownian motion predicts the most significant change among the four mechanisms included in Figure 5.9. The CaS inclusion diameters are expected to increase by 2.0, 1.9, and  $1.3 \mu\text{m}$  in Exp. 2035, Exp. 3035 and Exp. 2025, respectively.

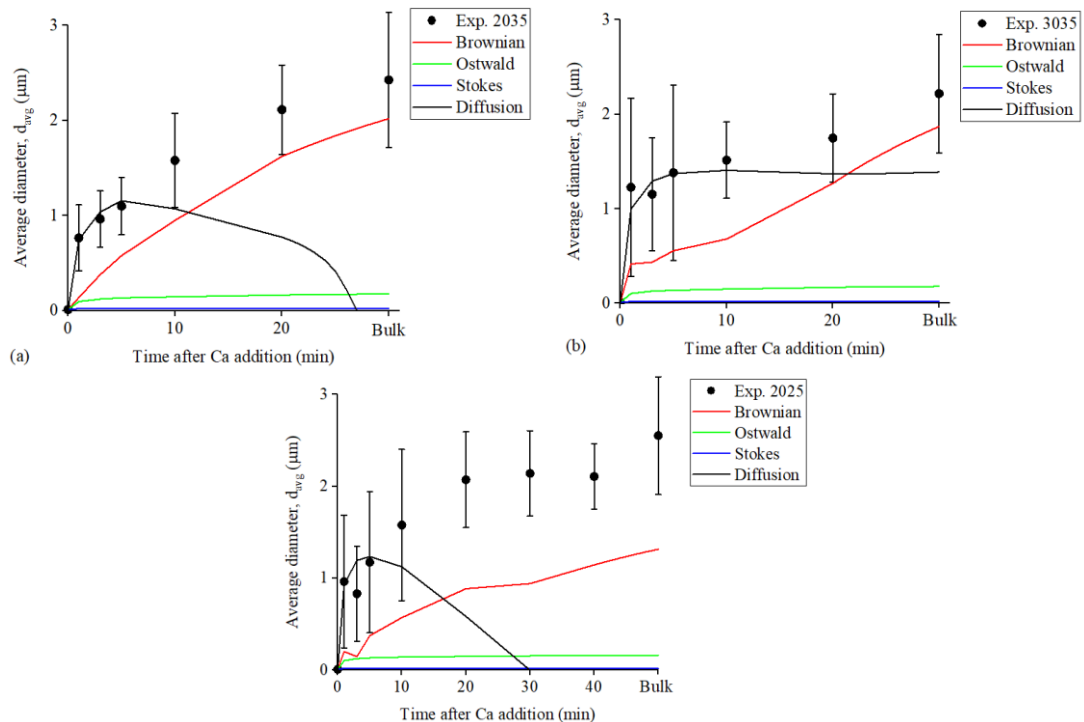


Figure 5.9 Comparison of the average diameters of CaS type inclusions in samples taken in (a) Exp. 2035, (b) Exp. 3035, and (c) Exp. 2025, and predicted using different coarsening mechanisms.

The authors noticed that the diffusion-controlled growth agrees with the experimental results in the first 5 min after Ca addition when assuming the initial dissolved Ca

concentration being 0.1 ppm for Exp. 2035 and 0.15 ppm for Exp. 3035 and Exp. 2025. After that, the rate of growth controlled by Brownian motion is very similar to the experimentally observed growth rate. In fact, if considering the dominant CaS coarsening mechanism changed from Ca diffusion to Brownian motion at 5 min after Ca addition, one can obtain Figure 5.10. The solid lines in Figure 5.10 are the theoretical change due to diffusion already shown in Figure 5.9. The dashed lines were calculated by simply taking the average diameter calculated for diffusion-controlled growth at 5 min as the initial diameter and calculating the diameter change considering Brownian motion thereafter. A reasonable agreement between the experimental results and the models can be achieved by considering the transition between coarsening mechanisms. The diameter change in Exp. 3035 was over-predicted by the model for Brownian motion. Equation (5.19) shows that the radius change is related to the ratio of the new-to-old volume fraction  $\frac{f}{f_0}$ . If not, all  $f_0$  participated in the formation of new CaS inclusions, for example, when some formed CaS-other inclusions,  $\frac{f}{f_0}$  would be over-predicted; hence, so would  $r$ . Diffusion-controlled CaS formation/dissolution predicts a major decrease in the average diameter of CaS inclusions in Exp. 2035 and Exp. 2025 and some decrease in Exp. 3035 (Figure 5.9 black lines). In reality, diffusion-controlled growth and coarsening through Brownian collision must have occurred simultaneously. Overprediction was observed in Figure 5.10 because the diameter decrease due to diffusion was not incorporated in the calculation of dashed lines shown in Figure 5.10.

The authors are aware that the theoretical growth shown in Figure 5.10 cannot accurately predict the diameter of CaS inclusions in the course of experiments. However, the focus of the present study is not to establish a model that calculates the CaS diameter change but to determine the coarsening mechanisms. Figures Figure 5.9 and Figure Figure 5.10 do show that none of the four coarsening mechanisms considered can independently explain the growth of CaS observed in Exp. 2035, Exp. 3035 and Exp. 2025. A transition of the controlling coarsening mechanism is clear in the experiments. The diameter change of CaS inclusions was initially governed by the diffusion and later related to Brownian-motion-driven collisions.

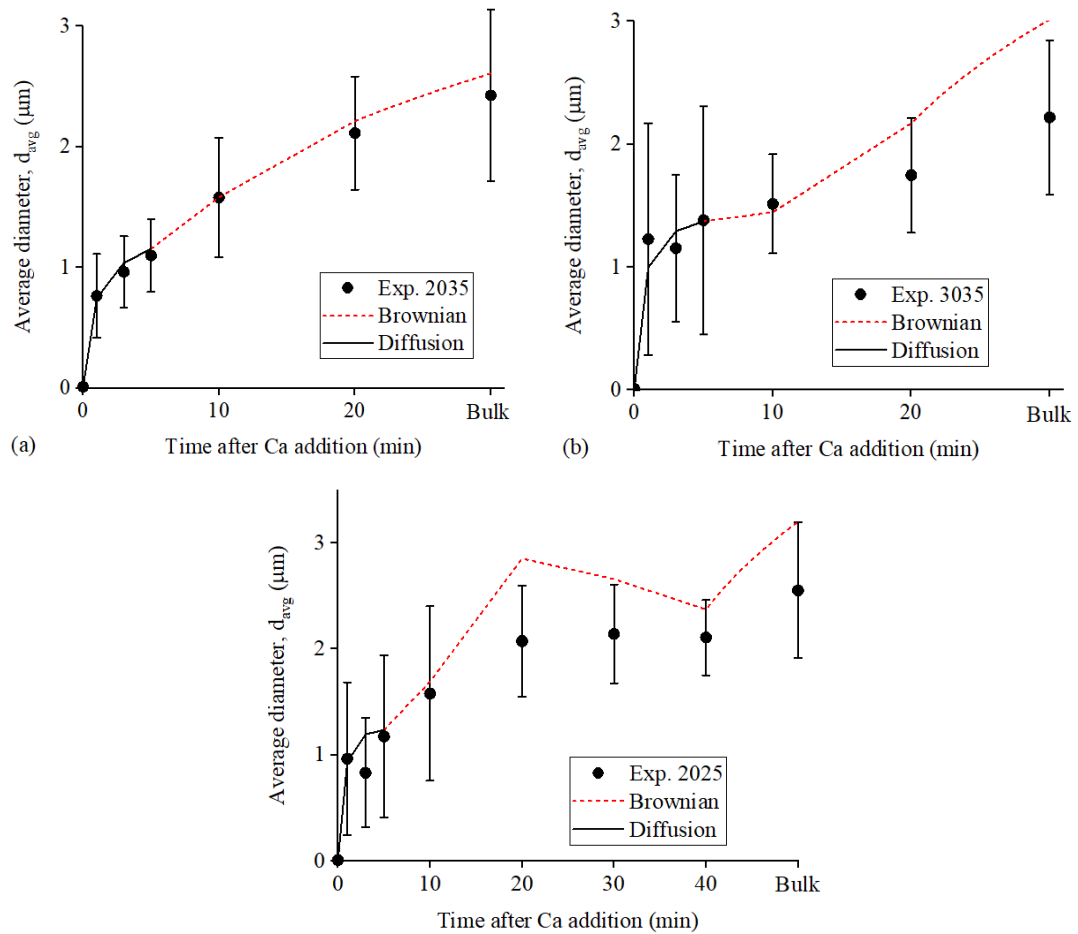


Figure 5.10 Comparison of the average diameters of CaS type inclusions in samples taken from (a) Exp. 2035, (b) Exp. 3035, and (c) Exp. 2025, and predicted based on diffusion-controlled growth followed by Brownian motion.

## 5.5.2 Cause of Change in Coarsening Mechanisms

The authors further analyzed the cause of the change in the dominating coarsening mechanism. The change in the driving force over experimental time was calculated for the diffusion-controlled growth mechanism, as shown in Figure 5.11. According to Equation (5.7), the Ca concentration in metal bulk,  $C_{[Ca],b}$ , decreased over time; therefore, the driving force rapidly reduced. In other words, the influence of Ca diffusion on the size change of CaS inclusions became insignificant. The coarsening of CaS inclusions stopped after 5 min from Ca addition (Figure 5.9). Later, the driving force in Exp. 2035 and Exp. 2025 was negative while that of Exp. 3035 remained much closer to 0. The variation in driving force is related to the difference in sulfur content. With a higher  $C_{[S],i}$  given by the lower S levels,  $C_{[Ca],i}$  to maintain Equilibrium (5.14) in Exp. 2035 and Exp. 2025 were higher than that of Exp. 3035. So, the concentration differences,  $C_{[Ca],b} - C_{[Ca],i}$ , from Equation (5.9) were slightly negative starting from 10 min after Ca addition; hence, negative slopes were seen in Figure 5.9 (a), (c). The lower  $C_{[Ca],i}$  in

Exp. 3035 was able to maintain  $C_{[Ca],b} - C_{[Ca],i}$  much closer to 0 before Exp. 3035 ended, so the theoretical diameter change due to diffusion is less apparent in Figure 5.9 (b). Further, for all experimental conditions, the importance of Brownian motion on the coarsening of CaS inclusions increased over time. This is due to the fact that Brownian motion largely depends on the volume fraction of inclusions of interest. The volume fraction of CaS inclusions increased with time as shown in Figure 5.12 for all three experiments. The Brownian motion eventually became the dominant coarsening mechanism at 5 min after Ca addition.

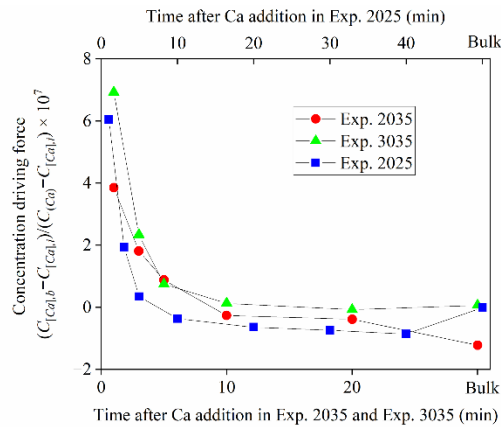


Figure 5.11 Change of driving force for Ca diffusion in Exp. 2035, Exp. 3035, and Exp. 2025.

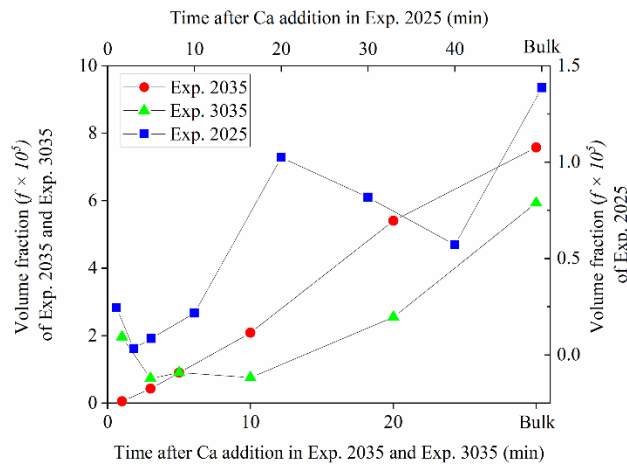


Figure 5.12 Variation in the volume fraction of CaS inclusions over time in Exp. 2035, Exp. 3035, and Exp. 2025.

The significance of Brownian motion over the Stokes motion can be explained by the difference in frequency of collision. The change in collision frequency function,  $\beta$ , of inclusion pairs with a diameter  $d_i$  and  $d_j$  is shown in Figure 5.13. Figure 5.13 (a)–(d) correspond to  $d_i$  equal to 0.5, 1, 2, and 3  $\mu\text{m}$ , respectively. These values cover the

diameter range of CaS type inclusions shown in Figure 5.5 (a). The range of  $d_j$  was set from 0 to 4  $\mu\text{m}$  in all four plots. The temperature was set to 1873 K and the viscosity was equal to  $2.3 \times 10^{-3} \text{ kg}/(\text{m}\cdot\text{s})$ . The values for steel density and CaS density were 6975 and 2650  $\text{kg}/\text{m}^3$ , respectively. Even though the densities were estimated, the authors confirmed that slight density change opposes minor change on the orders of magnitudes of  $\beta$  values; hence, it has no impact on the findings.

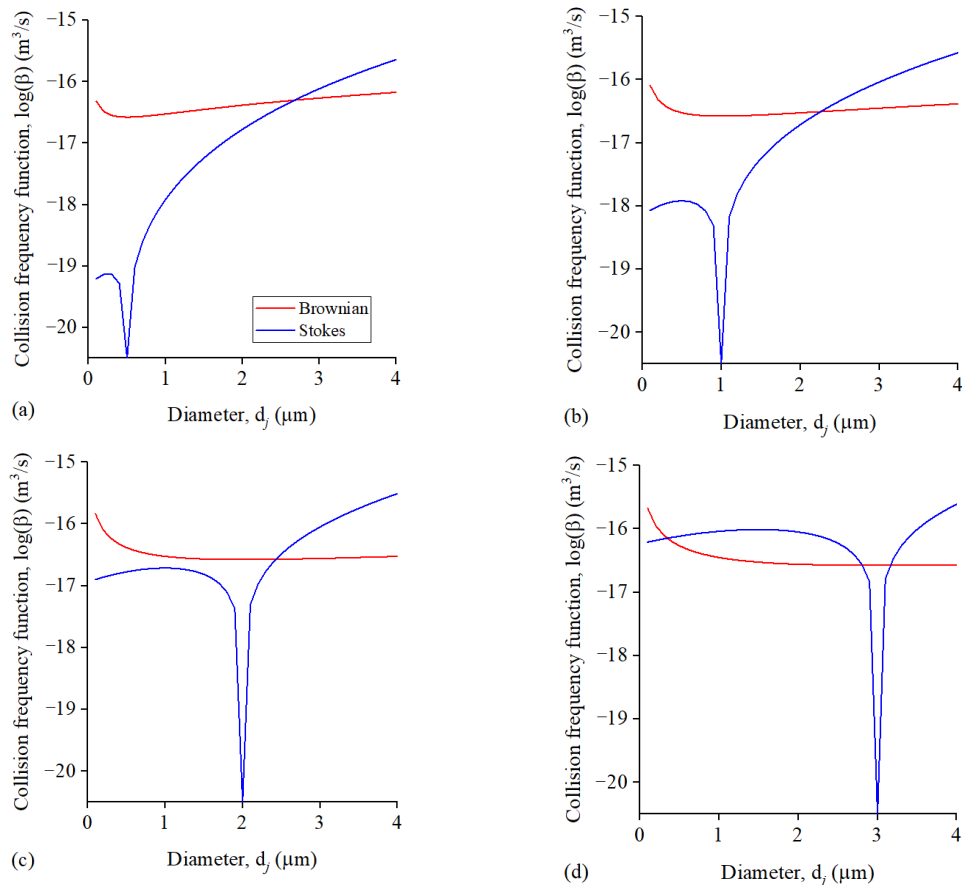


Figure 5.13 Comparison of collision frequency function of Brownian motion and Stokes motion for an inclusion of diameter  $d_i$  (a) 0.5  $\mu\text{m}$ , (b) 1  $\mu\text{m}$ , (c) 2  $\mu\text{m}$ , (d) 3  $\mu\text{m}$  and varied  $d_j$ .

In Figure 5.13, the frequency function of Brownian motion,  $\beta^B$ , remains stable at the same order of magnitude, i.e., around  $-17$  to  $-16 \text{ m}^3/\text{s}$ , for all four  $d_i$ . The values are slightly higher at lower  $d_j$ , but decrease to a stable level as  $d_j$  increases. In comparison, when  $d_i < 2 \mu\text{m}$ ,  $\beta^S$  values are generally lower than that of  $\beta^B$  until  $d_j$  increases to higher than approximately  $2.5 \mu\text{m}$ . That is partially due to the presence of the dip at  $d_j$  equals to  $d_i$ . The reason being inclusions of similar sizes show no relative motion while ascending; hence, they cannot coalesce during flotation. The  $\beta^S$  are higher than  $\beta^B$  in Figure 5.13 (d) across almost the entire  $d_j$  range. Based on Figure 5.5 and Figure 5.13, it can be inferred that the frequency of inclusions to collide is higher due to Brownian

motion than due to Stokes motion in almost the entire size range of CaS type inclusions observed in the experimental conditions. As a result, the prediction given by the Brownian motion model is relatively more in agreement with the experimental data, as seen in Figure 5.9. The collision frequency due to Stokes motions is higher when an inclusion in an inclusion pair is close to 3  $\mu\text{m}$ . Still, according to Figure 5.5 and Figure 5.6, inclusions of such diameters are a small portion of the entire CaS population in the experiments, and they are mainly found close to the end of experiments. With the limited available time for further collision, the effect of Stokes motion is understandably low.

The analysis of three experimental results strongly suggests that the coarsening of CaS inclusions would be governed by the diffusion-controlled growth mechanism in laboratory conditions when Ca supply is sufficient for a limited time. After Ca evaporates, CaS inclusions may either stop growing or start to dissociate. Because of that, the growth will depend more on the Brownian collision. These findings are in line with the general trend, i.e., diffusion to collision transition reported in the previous studies [12,59], and should also be applicable to industrial conditions where the growth of CaS inclusions is not interfered by the steel flow. At the current stage, a mathematical model incorporating all coarsening mechanisms has not been established yet to predict the evolution of PSD of CaS inclusions. It will be the focus of a later study.

### 5.5.3 Coarsening Mechanisms of CaS Inclusions under Industrial Conditions

To determine the coarsening mechanism of CaS inclusions under industrial conditions, the effects of collision-related mechanisms on the rate of CaS volumetric population density were calculated using Equations (5.21)–(5.26).

The collision-related coarsening mechanisms in industrial conditions include Brownian motion, Stokes motion, and laminar and turbulent flows. For Equations (5.22) and (5.23), a constant viscosity of  $2.55 \times 10^{-3} \text{ kg}/(\text{m}\cdot\text{s})$  was used. The energy dissipation rate,  $\varepsilon$ , varies with operation conditions and locations in ladle and tundish. The exact values were not measured during the sampling of industrial heats available for this study. However, it was reported that when gas was injected at a rate of  $8.4 \text{ m}^3/\text{hr}$ , the velocity gradient varied from  $0.7$  to  $3.5 \text{ s}^{-1}$ , and the energy dissipation rate was from  $0.001$  to  $0.007 \text{ m}^2/\text{s}^3$  close to the top of the ladle, where samples were taken [60]. Similar values were also reported in other studies [61,62]. With a similarly low Ar flow rate used in Heat 1, the velocity gradient,  $\frac{du}{dy}$ , of  $2 \text{ s}^{-1}$  was used to calculate  $\beta^G$ , and  $\beta^T$  was calculated using  $\varepsilon$  equals  $1 \times 10^{-3} \text{ m}^2/\text{s}^3$ . The values of coagulation coefficient,  $\alpha$ , were estimated using the data reported for the steel- $\text{Al}_2\text{O}_3$  system by Taniguchi et al. [49], as data of the steel-CaS system were not available in the literature. The calculation was conducted for both the ladle and tundish samples of Heat 1. The data of  $0.5 \mu\text{m}$  analysis was used as

the input to calculate the rate of change  $\frac{dN_V}{dt}$  due to collisions using PBE and compared with the apparent rate of change  $\frac{\Delta N_V}{\Delta t}$ . The values for  $\frac{\Delta N_V}{\Delta t}$  were calculated through dividing the  $N_V$  difference between the two samples by elapsed time between them. The comparisons are shown in Figure 5.14.

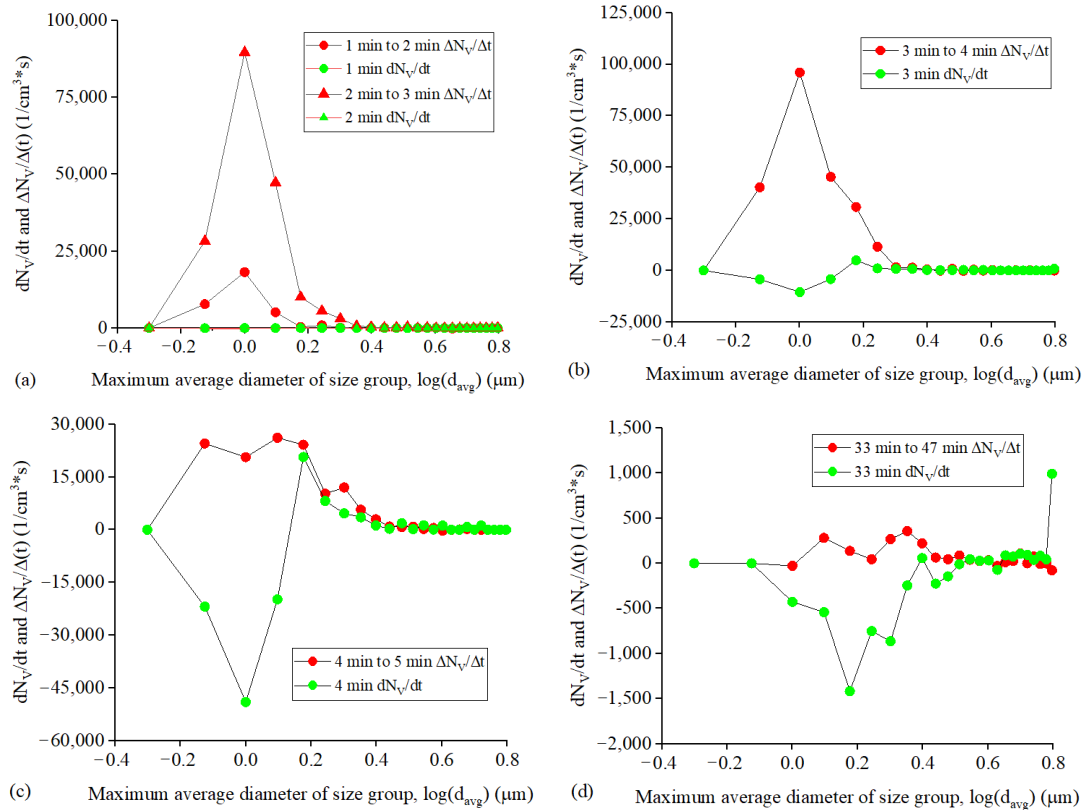


Figure 5.14 Comparison of the observed rate of change of CaS population density and the calculated rate of change of population density due to collision in the ladle at (a) 1 min and 2 min, (b) 3 min, and (c) 4 min after Ca addition, and (d) in tundish at 33 min after Ca addition.

Figure 5.14 (a) shows that in the first three minutes after Ca injection started, the  $\frac{\Delta N_V}{\Delta t}$  are evidently positive for inclusions lower than  $2 \mu\text{m}$ . This is already shown in Figure 5.8. However, the calculated  $\frac{dN_V}{dt}$  appears to be effectively a straight line, suggesting at the time that the combined effects of Brownian motion, Stokes motion, and laminar and turbulent flow cannot explain the growth of CaS inclusions. Considering that the actual PSD changes (red marks in Figure 5.14) are the results of growth by diffusion and coalescence, the authors suggest that during the first three minutes of Heat 1, the diffusion control would be the dominant mechanism for CaS inclusions growth. A similar explanation could be offered for the inclusion growth from 3 min to 4 min after Ca

injection started, as shown in Figure 5.14 (b). The only exception is that the PBE predicted the PSD change due to collision to become slightly more noticeable compared to the earlier stages but is still lower than  $\frac{\Delta N_V}{\Delta t}$ . However, at the very end of Ca addition, similarities between  $\frac{\Delta N_V}{\Delta t}$  and  $\frac{dN_V}{dt}$  can be spotted. Starting from  $d_{avg}$  equals 1.5  $\mu\text{m}$  or higher ( $\log(d_{avg}) > 0.18$ ), the observed and PBE predicted number density change are generally the same in Figure 5.14 (c). The effect of diffusion was still significant, as disagreement can be found for the rate of change of inclusions smaller than 1.5  $\mu\text{m}$  ( $\log(d_{avg}) < 0.18$ ). The peak of  $\frac{\Delta N_V}{\Delta t}$  in Figure 5.14 (c) is not as apparent as that is in Figure 5.14 (a), (b) because of the negative  $\frac{dN_V}{dt}$ . The phenomenon in Figure 5.14 (c) suggests that the effect of coalescence became comparable with diffusion only at the very end of the Ca injection process. No sample was taken from the ladle later than 5 min after Ca injection started, but based on the trend shown from Figure 5.14 (a)–(c), the similarity between curves of  $\frac{\Delta N_V}{\Delta t}$  and  $\frac{dN_V}{dt}$  is highly likely to further increase.

In the tundish, the values of  $\frac{\Delta N_V}{\Delta t}$  drastically decreased compared to those for samples from the ladle. The change was less than  $500 \text{ cm}^{-3}\text{s}^{-1}$  in all size groups, with the maximum value seen for inclusions with  $d_{avg}$  between 2 and 2.5  $\mu\text{m}$ . This is again very different from the calculated  $\frac{dN_V}{dt}$  due to collision and coalescence. This finding suggests that diffusion was still an important mechanism for CaS inclusions' growth in the tundish.

Overall, Figure 5.14 suggests that the growth of CaS inclusions in Heat 1 depended dominantly on diffusion-controlled growth at the early stage because the size of inclusions was small during this time. As the volume fraction of inclusions increased, the effect of collision and coalescence became comparable. There was a constant supply of Ca during injection [31], so CaS grew by Ca diffusion throughout the ladle-refining process. During the tundish treatment, even though the Ca injection stopped, the decreased temperature must reduce the extent of modification of  $\text{CA}_x$  and the solubility of Ca. Both prevented the dissolved Ca concentration from dropping; hence, CaS inclusions could continue growing through diffusion. The authors suggest that a similar route also occurred for Heats 3 to Heat 5. However, analyses provided in Figure 5.14 cannot be generated for those heats because only one sample was taken from the ladle, and the 0.5  $\mu\text{m}$  analysis was not conducted.

The contribution of different collision-related coarsening mechanisms, i.e., Brownian motion, Stokes motion, and laminar and turbulent flow, can be quantified using the  $\beta$

values. The comparisons are shown in Figure 5.15.  $d_i$  and  $d_j$  in Figure 5.15 include the range of CaS inclusions seen in the industrial samples.

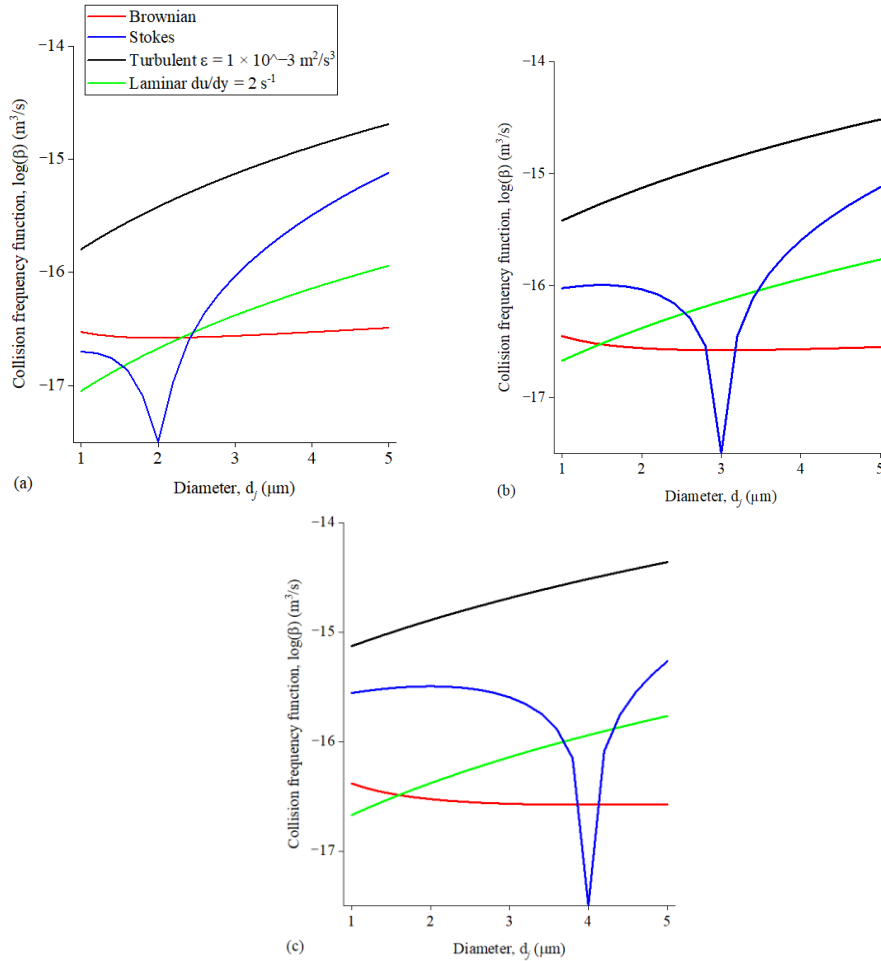


Figure 5.15 Comparison of collision frequency function for Brownian motion, Stokes motion, and laminar and turbulent flow for an inclusion with a diameter  $d_i$  of (a) 2  $\mu\text{m}$ , (b) 3  $\mu\text{m}$ , (c) 4  $\mu\text{m}$  and varied  $d_j$ .

Figure 5.15 shows that the values for  $\beta^T$  can reach up to  $-14$  order of magnitude when one assumes the energy dissipation rate of  $1 \times 10^{-3} \text{ m}^2/\text{s}^3$ . The values for  $\beta^T$  are always higher than those of  $\beta^B$ ,  $\beta^S$  and  $\beta^G$ . The values of  $\beta^B$  and  $\beta^G$  are about one order of magnitude less regardless of the inclusion sizes. The values for  $\beta^S$  can reach close to those for  $\beta^T$  for some combinations of  $d_i$  and  $d_j$ . For example, when  $d_i$  and  $d_j$  are equal to 2  $\mu\text{m}$  and 5  $\mu\text{m}$ , the values for  $\beta^T$  and  $\beta^S$  are  $2.04 \times 10^{-15}$  and  $7.6 \times 10^{-16} \text{ m}^3/\text{s}$ , respectively (Figure 5.15 (a)). In such a scenario, both mechanisms are responsible for the coarsening of CaS inclusions, while in other cases, the contribution of turbulent flow was dominant over the other three mechanisms. The significance of turbulent flow had also been reported in previous theoretical studies [60,63].

Overall, this study suggests that the coarsening mechanisms of CaS type inclusions followed the same route in experimental and industrial conditions. When there is sufficient Ca available at the early stage, diffusion-controlled growth is particularly critical. After more CaS inclusions formed, the increased collision volume and in some cases decreased dissolved Ca concentration made the coarsening process depend on collision-related coarsening mechanisms. As in the laboratory conditions, the dominant mechanism later becomes Brownian motion with the absence of flow. When the system is stirred like the industrial conditions, the turbulent flow will influence the coarsening process.

## 5.6 Conclusions

The coarsening mechanisms of CaS inclusions under experimental and industrial conditions were studied in this work. The findings are summarized as follows:

1. Under the experimental conditions, the coarsening rate of CaS inclusions is initially controlled by the Ca diffusion. As experiments proceed, the rate of diffusion-controlled growth decreases with the rate of Ca transport due to the decrease in Ca concentration in steel. During the same time, the volume fraction of CaS inclusions increases, and the Brownian motion becomes a controlling coarsening mechanism.
2. Determining the coarsening mechanisms based on the similarities between the observed and the calculated diameters of inclusions has the limitation of not incorporating the effect of each mechanism when the growth of inclusions depends on multiple mechanisms for an extended time. Hence, such a method may be only appropriate if there is limited or no mechanism change or the transition time is short, as seen in some experiments.
3. The increasing importance of the collision-dependent coarsening mechanism also occurs in industrial conditions. Because of the stirring effects in ladle and tundish, the turbulent flow becomes responsible for the CaS size change sometime after Ca injection starts. Because of the stable Ca supply during Ca injection and the decrease in the modification extent of  $CA_x$ , the diffusion-controlled growth remains important during both ladle and tundish treatments.

## 5.6 Acknowledgement

The authors want to thank Dr. Stanley Sun and Dr. Li Sun at ArcelorMittal Dofasco for their valuable time and fruitful discussions. The authors also acknowledge Canadian Centre for Electron Microscopy (CCEM) at McMaster University for assistance with SEM analysis.

## 5.7 References

1. Verma, N.; Pistorius, P.C.; Fruehan, R.J.; Potter, M.; Lind, M.; Story, S.R. Transient Inclusion Evolution during Modification of Alumina Inclusions by Calcium in Liquid Steel: Part II Results and Discussion. *Metall. Mater. Trans. B* **2011**, *42*, 720–729. <https://doi.org/10.1007/s11663-011-9517-2>.
2. Miao, K.; Nabeel, M.; Dogan, N.; Sun, S. Experimental Study of Inclusion Modification by Ca in AHSS. *Metall. Mater. Trans. B Process Metall. Mater. Process. Sci.* **2021**, *52*, 3151–3166. <https://doi.org/10.1007/s11663-021-02243-1>.
3. Verma, N.; Pistorius, P.C.; Fruehan, R.J.; Potter, M.; Lind, M.; Story, S. Transient Inclusion Evolution during Modification of Alumina Inclusions by Calcium in Liquid Steel: Part I Background Experimental Techniques and Analysis Methods. *Metall. Mater. Trans. B* **2011**, *42*, 711–719. <https://doi.org/10.1007/s11663-011-9516-3>.
4. Liu, Y.; Zhang, L.; Zhang, Y.; Duan, H.; Ren, Y.; Yang, W. Effect of Sulfur in Steel on Transient Evolution of Inclusions during Calcium Treatment. *Metall. Mater. Trans. B* **2018**, *49*, 610–626. <https://doi.org/10.1007/s11663-018-1179-x>.
5. Geldenhuis, J.M.A.; Pistorius, P.C. Minimisation of Calcium Additions to Low Carbon Steel Grades. *Ironmak. Steelmak.* **2000**, *27*, 442–449. <https://doi.org/10.1179/030192300677769>.
6. Ohta, H.; Suito, H. Effects of Dissolved Oxygen and Size Distribution on Particle Coarsening of Deoxidation Product. *ISIJ Int.* **2006**, *46*, 42–49. <https://doi.org/10.2355/isijinternational.46.42>.
7. Suzuki, M.; Yamaguchi, R.; Murakami, K.; Nakada, M. Inclusion Particle Growth during Solidification of Stainless Steel. *ISIJ Int.* **2001**, *41*, 247–256. <https://doi.org/10.2355/isijinternational.41.247>.
8. Wang, L.; Li, J.; Yang, S.; Chen, C.; Jin, H.; Li, X. Nucleation and Ostwald Growth of Particles in Fe-O-Al-Ca Melt. *Sci. Rep.* **2018**, *8*, 1135. <https://doi.org/10.1038/s41598-018-19639-w>.
9. Zhang, L.; Pluschkell, W. Nucleation and Growth Kinetics of Inclusions during Liquid Steel Deoxidation. *Ironmak. Steelmak.* **2003**, *30*, 106–110. <https://doi.org/10.1179/030192303225001766>.
10. Sahai, Y.; Sinha, A.K. Mathematical Modeling of Inclusion Transport and Removal in Continuous Casting Tundishes. *ISIJ Int.* **1994**, *33*, 556–566. <https://doi.org/10.2355/isijinternational.33.556>.
11. Smoluchowski, M. V. An Experiment on Mathematical Theorization of Coagulation Kinetics of the Colloidal Solutions. *Z. Phys. Chem.* **1917**, *92*, 129–168.
12. Zhang, J.; Lee, H.G. Numerical Modeling of Nucleation and Growth of Inclusions in Molten Steel Based on Mean Processing Parameters. *ISIJ Int.* **2004**, *44*, 1629–1638. <https://doi.org/10.2355/isijinternational.44.1629>.
13. Yin, X.; Sun, Y.; Yang, Y.; Deng, X.; Barati, M.; McLean, A. Effect of Alloy Addition on Inclusion Evolution in Stainless Steels. *Ironmak. Steelmak.* **2017**, *44*,

- 152–158. <https://doi.org/10.1080/03019233.2016.1185285>.
14. Rimbart, N.; Claudotte, L.; Gardin, P.; Lehmann, J. Modeling the Dynamics of Precipitation and Agglomeration of Oxide Inclusions in Liquid Steel. *Ind. Eng. Chem. Res.* **2014**, *53*, 8630–8639. <https://doi.org/10.1021/ie403991e>.
  15. Li, C.; Cai, R. Tutorial: The Discrete-Sectional Method to Simulate an Evolving Aerosol. *J. Aerosol Sci.* **2020**, *150*, 105615. <https://doi.org/10.1016/j.jaerosci.2020.105615>.
  16. Schamber, F. *Introduction to Automated Particle Analysis by Focused Electron Beam*; ASPEX Corp, Delmont, PA, USA: 2011; pp. 1–7.
  17. Lu, D. Kinetics, Mechanisms and Modelling of Calcium Treatment of Steel. Ph.D. Thesis, McMaster University, Hamilton, ON, Canada, 1992.
  18. Beskow, K.; Viswanathan, N.N.; Jonsson, L.; Sichen, D. Study of the Deoxidation of Steel with Aluminum Wire Injection in a Gas-Stirred Ladle. *Metall. Mater. Trans. B* **2001**, *32*, 319–328. <https://doi.org/10.1007/s11663-001-0055-1>.
  19. Oikawa, K.; Ohtani, H.; Ishida, K.; Nishizawa, T. The Control of the Morphology of MnS Inclusions in Steel during Solidification. *ISIJ Int.* **1995**, *35*, 402–408. <https://doi.org/10.2355/isijinternational.35.402>.
  20. Allibert, M.; Gaye, H.; Geisler, J.; Janke, D.; Keene, B.J.; Kirner, D.; Kowalski, M.; Lehmann, J.; Mills, K.C.; Neuschütz, D.; et al. *Slag Atlas*, 2<sup>nd</sup> ed.; Eisenhuttenleute, V.D., Ed.; Verlag Stahleisen GmbH: Dusseldorf, Germany, 1995; ISBN 3-514-00457-9.
  21. Yang, W.; Duan, H.; Zhang, L.; Ren, Y. Nucleation, Growth, and Aggregation of Alumina Inclusions in Steel. *JOM* **2013**, *65*, 1173–1180. <https://doi.org/10.1007/s11837-013-0687-z>.
  22. Li, Z.; Zeze, M.; Mukai, K. Surface Tension and Wettability of Liquid Fe-16mass%Cr-S Alloy with Alumina. *Mater. Trans.* **2003**, *44*, 2108–2113. <https://doi.org/10.2320/matertrans.44.2108>.
  23. Ogino, K. The Wettability of Solid Oxides by Liquid Iron. *Tetsu-to-Hagane* **1973**, *59*, 1237.
  24. Pradhan, D.; Mantha, D.; Reddy, R.G. Thermodynamics of Interfacial Properties between Liquid Iron, Liquid Silicon and Solid Oxide Substrates. *High Temp. Mater. Process.* **2009**, *28*, 203–210. <https://doi.org/10.1515/HTMP.2009.28.4.203>.
  25. Poirier, D.R.; Yin, H.; Suzuki, M.; Emi, T. Interfacial Properties of Dilute Fe-O-S Melts on Alumina Substrates. *ISIJ Int.* **1998**, *38*, 229–238. <https://doi.org/10.2355/isijinternational.38.229>.
  26. Robie, R.A.; Bethke, P. *Molar Volumes and Densities of Minerals*; United States Department of the Interior Geological Survey: Washington, DC, USA, 1962.
  27. Crawley, A.F. Densities of Liquid Metals and Alloys. *Int. Metall. Rev.* **1974**, *19*, 32–48. <https://doi.org/10.1179/imt.1974.19.1.32>.
  28. Baldan, A. Progress in Ostwald Ripening Theories and Their Applications to Nickel-Base Superalloys. Part I: Ostwald Ripening Theories. *J. Mater. Sci.* **2002**, *37*, 2171–2202. <https://doi.org/10.1023/A:1015388912729>.

29. Voorhees, P.W. The Theory of Ostwald Ripening. *J. Stat. Phys.* **1985**, *38*, 231–252. <https://doi.org/10.1007/BF01017860>.
30. Yao, J.H.; Elder, K.R.; Guo, H.; Grant, M. Theory and Simulation of Ostwald Ripening. *Phys. Rev. B* **1993**, *47*, 14110–14125. <https://doi.org/10.1103/PhysRevB.47.14110>.
31. Tabatabaei, Y.; Coley, K.S.; Irons, G.A.; Sun, S. Model of Inclusion Evolution During Calcium Treatment in the Ladle Furnace. *Metall. Mater. Trans. B* **2018**, *49*, 2022–2037. <https://doi.org/10.1007/s11663-018-1266-z>.
32. Zhang, L.; Liu, Y.; Zhang, Y.; Yang, W.; Chen, W. Transient Evolution of Nonmetallic Inclusions During Calcium Treatment of Molten Steel. *Metall. Mater. Trans. B* **2018**, *49*, 1841–1859. <https://doi.org/10.1007/s11663-018-1289-5>.
33. Diederichs, R.; Bleck, W. Modelling of Manganese Sulphide Formation during Solidification, Part I: Description of MnS Formation Parameters. *Steel Res. Int.* **2006**, *77*, 202–209. <https://doi.org/10.1002/srin.200606375>.
34. Wilkinson, D.S. *Mass Transport in Solids and Fluids*; Cambridge University Press: Cambridge, UK, 2000.
35. Tabatabaei, Y.; Coley, K.S.; Irons, G.A.; Sun, S. A Multilayer Model for Alumina Inclusion Transformation by Calcium in the Ladle Furnace. *Metall. Mater. Trans. B* **2018**, *49*, 375–387. <https://doi.org/10.1007/s11663-017-1120-8>.
36. Szekely, J.; Themelis, N.J. *Rate Phenomena in Process Metallurgy*; John Wiley & Sons Inc., New York, NY, USA, 1971; pp. 609–617.
37. Bouris, D.; Bergeles, G. Investigation of Inclusion Re-Entrainment from the Steel-Slag Interface. *Metall. Mater. Trans. B* **1998**, *29*, 641–649. <https://doi.org/10.1007/s11663-998-0099-6>.
38. Okuyama, G.; Yamaguchi, K.; Takeuchi, S.; Sorimachi, K. Effect of Slag Composition on the Kinetics of Formation of Al<sub>2</sub>O<sub>3</sub> MgO Inclusions in Aluminum Killed Ferritic Stainless Steel. *ISIJ Int.* **2008**, *40*, 121–128. <https://doi.org/10.2355/isijinternational.40.121>.
39. Park, J.H.; Kim, D.S. Effect of CaO-Al<sub>2</sub>O<sub>3</sub>-MgO Slags on the Formation of MgO-Al<sub>2</sub>O<sub>3</sub> Inclusions in Ferritic Stainless Steel. *Metall. Mater. Trans. B* **2005**, *36*, 495–502. <https://doi.org/10.1007/s11663-005-0041-0>.
40. Ren, Y.; Zhang, L.; Pistorius, P.C. Transformation of Oxide Inclusions in Type 304 Stainless Steels during Heat Treatment. *Metall. Mater. Trans. B* **2017**, *48*, 2281–2292. <https://doi.org/10.1007/s11663-017-1007-8>.
41. Han, Q.; Zhang, X.; Chen, D.; Wang, P. The Calcium-Phosphorus and the Simultaneous Calcium-Oxygen and Calcium-Sulfur Equilibria in Liquid Iron. *Metall. Trans. B* **1988**, *19*, 617–622. <https://doi.org/10.1007/BF02659153>.
42. Song, B.; Han, Q. Equilibrium of Calcium Vapor with Liquid Iron and the Interaction of Third Elements. *Metall. Mater. Trans. B* **1998**, *29*, 415–420. <https://doi.org/10.1007/s11663-998-0119-6>.
43. Deo, B.; Boom, R. *Fundamentals of Steelmaking Metallurgy*; Pearson Education Limited: Harlow, UK, 1993.

44. Inoue, R.; Suito, H. Calcium Desulfurization Equilibrium in Liquid Iron. *Steel Res.* **1994**, *65*, 403–409. <https://doi.org/10.1002/srin.199401184>.
45. Japan Society for the Advancement of Science and the 19<sup>th</sup> Committee on Steelmaking. *Steelmaking Data Sourcebook*; Japan Society for the Promotion of Science Edition; Gordon and Breach Science Publishers: New York, NY, USA, 1988.
46. Saffman, P.G.; Turner, J.S. Corrigendum: On the Collision of Drops in Turbulent Clouds. *J. Fluid Mech.* **1970**, *196*, 599. <https://doi.org/10.1017/S002211208800285X>.
47. Takahashi, J.; Suito, H. Evaluation of the Accuracy of the Three-Dimensional Size Distribution Estimated from the Schwartz-Saltykov Method. *Metall. Mater. Trans. A* **2003**, *34*, 171–181. <https://doi.org/10.1007/s11661-003-0218-6>.
48. Malczewski, J.; Piekarski, M. *Modele Procesów Transportu Masy, Pędu I Energii*; Wydaw. Nauk. PWN: Warszawa, Mazowsze, Poland, 1992.
49. Taniguchi, S.; Kikuchi, A.; Ise, T.; Shoji, N. Model Experiment on the Coagulation of Inclusion Particles in Liquid Steel. *ISIJ Int.* **1996**, *36*, S117–S120. [https://doi.org/10.2355/isijinternational.36.suppl\\_s117](https://doi.org/10.2355/isijinternational.36.suppl_s117).
50. Nakaoka, T.; Taniguchi, S.; Matsumoto, K.; Johansen, S.T. Particle-Size-Grouping Method of Inclusion Agglomeration and Its Application to Water Model Experiments. *ISIJ Int.* **2001**, *41*, 1103–1111. <https://doi.org/10.2355/isijinternational.41.1103>.
51. Xu, K.; Thomas, B.G. Particle-Size-Grouping Model of Precipitation Kinetics in Microalloyed Steels. *Metall. Mater. Trans. A* **2012**, *43*, 1079–1096. <https://doi.org/10.1007/s11661-011-0938-y>.
52. Nakaoka, T.; Matsumoto, K.; Taniguchi, S. Turbulent Coagulation Model Considering Effects of London-van Der Waals Force and Wettability. *Prog. Comput. Fluid Dyn.* **2008**, *8*, 270–275. <https://doi.org/10.1504/PCFD.2008.019480>.
53. Ling, H.; Zhang, L.; Li, H. Mathematical Modeling on the Growth and Removal of Non-Metallic Inclusions in the Molten Steel in a Two-Strand Continuous Casting Tundish. *Metall. Mater. Trans. B* **2016**, *47*, 2991–3012. <https://doi.org/10.1007/s11663-016-0743-5>.
54. Seo, M.D.; Cho, J.W.; Kim, K.C.; Kim, S.H. Evolution of Non-Metallic Inclusions in Ultra Low Carbon Steel after Aluminum Deoxidization. *ISIJ Int.* **2014**, *54*, 475–481. <https://doi.org/10.2355/isijinternational.54.475>.
55. Van Ende, M.A.; Guo, M.; Zinngrebe, E.; Blanpain, B.; Jung, I.H. Evolution of Non-Metallic Inclusions in Secondary Steelmaking: Learning from Inclusion Size Distributions. *ISIJ Int.* **2013**, *53*, 1974–1982. <https://doi.org/10.2355/isijinternational.53.1974>.
56. Zinngrebe, E.; Van Hoek, C.; Visser, H.; Westendorp, A.; Jung, I.H. Inclusion Population Evolution in Ti-Alloyed Al-Killed Steel during Secondary Steelmaking Process. *ISIJ Int.* **2012**, *52*, 52–61. <https://doi.org/10.2355/isijinternational.52.52>.
57. Han, Z.J.; Liu, L.; Lind, M.; Holappa, L. Mechanism and Kinetics of Transformation of Alumina Inclusions by Calcium Treatment. *Acta Metall. Sin. (Engl. Lett.)* **2006**,

- 19, 1–8. [https://doi.org/10.1016/S1006-7191\(06\)60017-3](https://doi.org/10.1016/S1006-7191(06)60017-3).
58. Miao, K.; Haas, A.; Sharma, M.; Mu, W.; Dogan, N. In Situ Observation of Calcium Aluminate Inclusions Dissolution into Steelmaking Slag. *Metall. Mater. Trans. B* **2018**, *49*, 1612–1623. <https://doi.org/10.1007/s11663-018-1303-y>.
59. Zhang, L.; Thomas, B.G.G. *Inclusion Nucleation, Growth, and Mixing during Steel Deoxidation*; Report No. CCC200206; University of Illinois at Urbana-Champaign: Urbana-Champaign, IL, USA, 2003; pp. 1–19.
60. Söder, M.; Jönsson, P.; Jonsson, L. Inclusion Growth and Removal in Gas-Stirred Ladles. *Steel Res. Int.* **2004**, *75*, 128–138. <https://doi.org/10.1002/srin.200405938>.
61. Kwon, Y.J.; Zhang, J.; Lee, H.G. A CFD-Based Nucleation-Growth-Removal Model for Inclusion Behavior in a Gas-Agitated Ladle during Molten Steel Deoxidation. *ISIJ Int.* **2008**, *48*, 891–900. <https://doi.org/10.2355/isijinternational.48.891>.
62. Zhang, L.; Taniguchi, S.; Cai, K. Fluid Flow and Inclusion Removal in Continuous Casting Tundish. *Metall. Mater. Trans. B* **2000**, *31*, 253–266. <https://doi.org/10.1007/s11663-000-0044-9>.
63. Ferreira, M.E.; Pistorius, P.C.; Fruehan, R.J. Liquid Inclusion Collision and Agglomeration in Calcium-Treated Aluminum-Killed Steel. *Front. Mater.* **2021**, *8*, 736807. <https://doi.org/10.3389/fmats.2021.736807>.

## Chapter 6 Coarsening Mechanisms of Calcium Aluminates in Ca-treated Steels

### 6.1 Introduction

The calcium aluminate inclusions ( $CA_x$ , C, and A denote CaO and  $Al_2O_3$ , respectively) are not considered to have detrimental effects on the production process as long as they are properly modified to liquid or semi-liquid. However, any large inclusion including  $CA_x$  remained in the final product is a defect such as micro-notches<sup>[201]</sup>, so harm may be directly related to size. For example, it was reported that the fatigue lives of high strength steels were inversely dependent on the size of inclusions<sup>[202]</sup>, but only if they were above a critical size.<sup>[203]</sup> Further, it was suggested that steel endurance depends on the morphology more than on the quantity of inclusions.<sup>[201]</sup> As the large  $CA_x$  inclusions may exert negative effects on steel properties, it is important to understand the coarsening mechanisms that govern the size change of  $CA_x$  type inclusions.

To the best of the author's knowledge, no researchers discussed the mechanisms of  $CA_x$  inclusions coarsening in detail until more recently. Wang et al.<sup>[24]</sup> studied the nucleation and growth of  $CA_x$  inclusions by Ostwald ripening at 1873 K. They compared the observed coarsening rate of  $CA_x$  inclusions with the theoretical rate predicted by the Lifshitz-Slyozov-Wagner theory. The results suggested the observed and the calculated coarsening rates agree at 360 seconds and 600 seconds after Al addition but were different in the later samples. A subsequent study by the same group<sup>[195]</sup> suggested the coarsening rate depends on collision and floatation based on the inclusion size distribution trend evolved in the experiments. They also reported that the population balance model overpredicted the number density change, and proposed it was because not all inclusion coagulates after the collision. It was shown in the previous studies<sup>[22,72]</sup> that liquid  $CA_x$  inclusions in contact with each other can be separated by the flow of the melt due to the lack of attraction force between them. The studies were based on the observation of inclusions on the steel/Ar surface. However, it is likely the same scenario when liquid inclusions were fully submerged. Nevertheless, Wang et al.<sup>[195]</sup> concluded that the coarsening of  $CA_x$  inclusions was initially dependent on Ostwald ripening and later controlled by the collision between inclusions.

In this chapter, the coarsening behaviors of  $CA_x$  inclusions observed in the experimental studies are discussed and compared with the data obtained from industrial practice to provide insight into their coarsening mechanism.

## 6.2 Experimental Methodology

The calcium treatment laboratory experiments started with heating an Al<sub>2</sub>O<sub>3</sub> crucible containing electrolytic iron and the appropriate amount of graphite, Mn, and FeS (for S content control) to 1873 K to homogenize the melt. Then Si and Al were added for deoxidation. Depending on the targeted Ca content, 0.4 g, 0.8 g, or 1.2 g Ca was then added to modify the inclusions. Pin samples were taken at 1 min, 3 min, 5 min, 10 min, and 20 min after Ca addition. In some experiments, additional pin samples were taken at 15 min, 30 min, and 40 min after adding Ca. The remaining melt was left in the crucible to cool with the furnace. A bulk sample was taken from the solidified melt in every experiment. Before the start of the experiments, the furnace was evacuated and backfilled with high-purity Ar gas, which was constantly fed during the experiments to create a protective atmosphere to avoid unexpected oxidation. Synthetic steels of 500 g with an initial composition of 0.06C-1Mn-0.03Al-0.25Si were used in the laboratory study. The detailed experimental procedures and the evolution of steel chemistries were reported in Chapter 3. <sup>[17]</sup>

The Ca, Al, Si, and Mn contents of laboratory samples were analyzed using Induction Coupled Plasma Optical Emission Spectrometry (ICP-OES). And the C and S contents were determined by a LECO C/S (CS744) analyzer. The chemical composition of the laboratory samples is summarized in Table 6.1. All concentrations have the unit of wt pct unless specified. The experiment numbers were denoted in the form of “[S content (ppm)][final Ca content (ppm)]”. The inclusion analysis was completed using an automated SEM-EDS system named ASPEX. Based on the EDS results, inclusions were classified into different types. At the same time, the morphological information of all inclusions was also measured by ASPEX. A brief description of the working principle of ASPEX is available in Chapter 3 and a more detailed description can be found elsewhere. <sup>[186]</sup>

Industrial samples were also used to study the size change of CA<sub>x</sub> inclusions. Lollipop samples were taken from the ladle after Ca addition and from the tundish. The schematic diagram and the dimensions of the lollipop sample are shown in Figure 6.1. A total of five industrial heats were studied and their compositions were summarized in Table 6.1. The ladle samples were numbered as L1, L2, L3, etc. and the tundish samples were numbered as T1 and T2. In Heat 1, ladle samples L1 to L5 were taken at 1 min, 2 min, 3 min, 4 min, and 5 min after Ca addition started, respectively. In Heat 2, ladle samples were taken at 0 min, 2 min, 4 min and 6 min after Ca addition was finished. In Heats 3 – 5, only one ladle sample was taken from the ladle after Ca addition. Samples T1 and T2 were from tundish when about 30 and 80 t steel was cast from a 165-ton tundish. The same inclusion analysis on experimental samples was conducted on all the industrial samples.

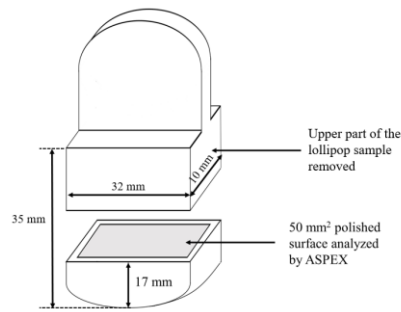


Figure 6.1 Schematic diagram of the lollipop sample.

Table 6.1 Chemical composition of laboratory and industrial tundish samples (wt pct)

Laboratory samples						
Exp. #	C	Si	Al	Mn	S (ppm)	Ca (ppm)
2035	0.06	0.27	0.09	1.09	21	56 – 35
3035	0.06	0.23	0.06	0.98	31	42 – 36
2025	0.06	0.26	0.03	0.91	22	39 – 26
2020	0.06	0.2	0.05	0.76	23	29 – 21
3020	0.06	0.24	0.06	1	17	37 – 17
2010	0.06	0.27	0.036	0.91	19	10 – 9
3010	0.05	0.26	0.03	0.91	22	15 – 8
Industrial samples						
Heat #	C	Si	Al	Mn	S (ppm)	Ca (ppm)
1	0.05	0.23	0.03	1.14	28	44 – 32
2	0.05	0.21	0.03	1.2	10	45 – 22
3	0.06	0.22	0.03	1.07	29	47 – 34
4	0.05	0.22	0.03	1.13	18	40 – 30
5	0.06	0.21	0.04	1.12	18	69 – 35

## 6.3 Results

### 6.3.1 CA<sub>x</sub> Growth in Experimental Conditions

The area fraction (AF) changes of CA<sub>x</sub> inclusions in experiments included in Table 6.1 are shown with respect to time in Figure 6.2. CA<sub>x</sub> inclusions here are classified into five classes namely; C<sub>3</sub>A, C<sub>12</sub>A<sub>7</sub>, CA, CA<sub>2</sub>, and CA<sub>6</sub>, by ASPEX. The values for AF of CA<sub>x</sub> inclusions were negligible in the early samples when only including inclusions larger than 2 μm, which was the standard ASPEX analysis approach. The selection criteria of inclusions were explained in Chapter 3. [17] The size of CA<sub>x</sub> inclusions evolved over time and eventually was detected in the ASPEX analysis. As a result, CA<sub>x</sub> AF increased as

experiments proceed. This hypothesis was confirmed in the work of Ferreira et al. [23], who reported the profusion of small inclusions in a sample taken 1 minute after Ca addition. The type of  $CA_x$  inclusions formed depends on the Ca content. One could see  $C_{12}A_7$  and  $C_3A$  inclusions can be observed in Exp. 2035, Exp. 3035 and Exp. 2025 because of the high Ca content of the steel. While in the other experiments treated with 20 ppm and 10 ppm Ca, the  $CA_x$  types were  $C_{12}A_7$  and CA inclusions.

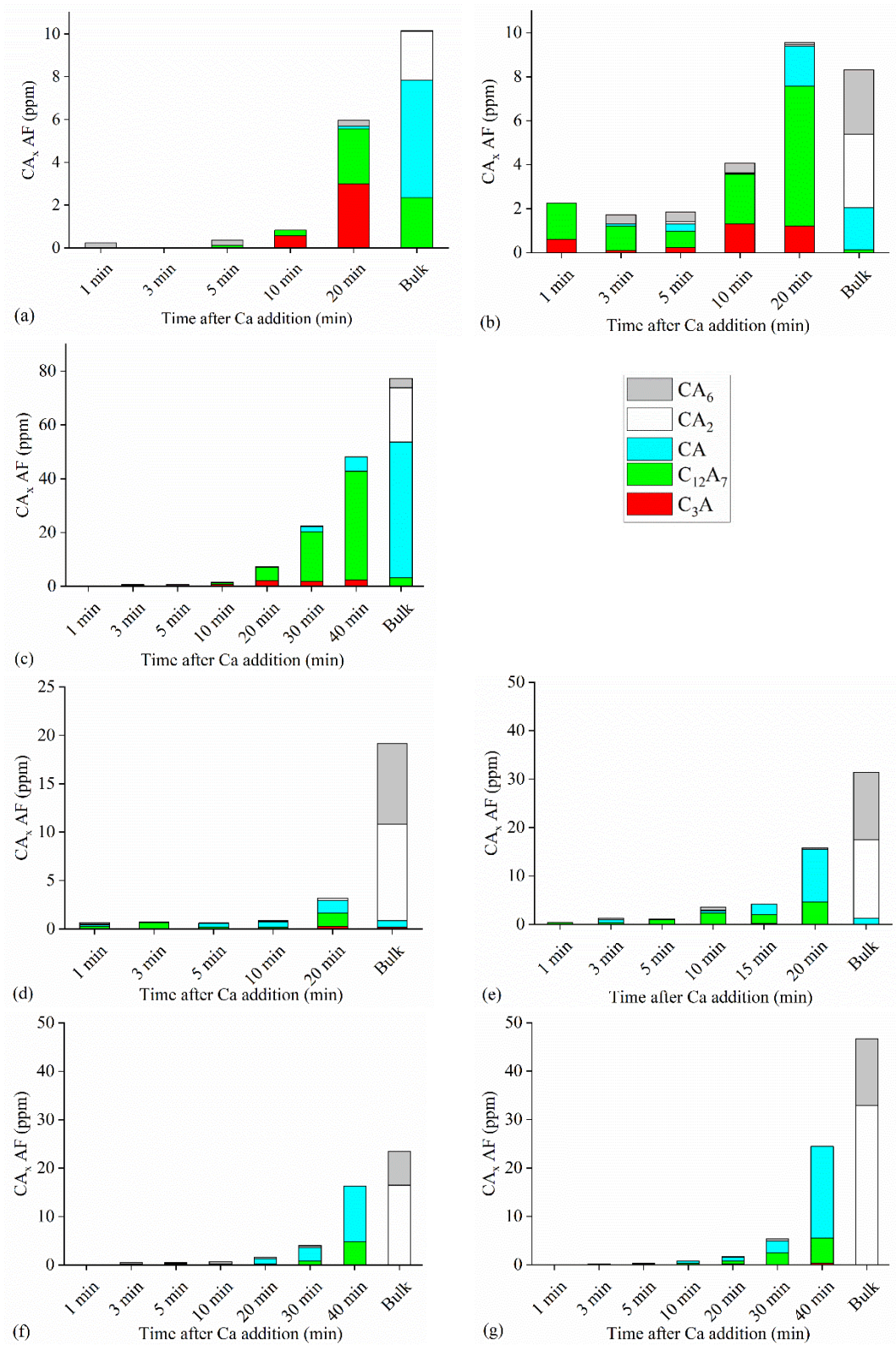


Figure 6.2 Area fraction of  $CA_x$  type inclusions in (a) Exp. 2035, (b) Exp. 3035, (c) Exp. 2025 (d) Exp. 2020, (e) Exp. 3020, (f) Exp. 2010, (g) Exp. 3010

The evolutions of the average diameter of different  $CA_x$  type inclusions in laboratory

experiments are shown in Figure 6.3. The average  $d_{\text{avg}}$  of  $\text{CA}_x$  type inclusions in a sample is reported in Figure 6.3 only if more than five of that  $\text{CA}_x$  inclusions were found in a sample.

In Exp. 2035,  $\text{C}_3\text{A}$ , and  $\text{C}_{12}\text{A}_7$  inclusions were detected, each having an average diameter of 2.2  $\mu\text{m}$  and 2.1  $\mu\text{m}$ , respectively. As predicted by thermodynamics, after solidification, the CaO content in  $\text{CA}_x$  inclusions decreased. CA and  $\text{CA}_2$  inclusions were detected, and their average diameters were 2.3  $\mu\text{m}$  and 2.2  $\mu\text{m}$ , respectively, which were similar to that of  $\text{C}_3\text{A}$  and  $\text{C}_{12}\text{A}_7$  inclusions from the previous 20-minute sample. In Exp. 3035, the difference between  $\text{C}_3\text{A}$  and  $\text{C}_{12}\text{A}_7$  inclusions diameter was observed in the 10-minute sample, but their average diameters “converged” again to 2  $\mu\text{m}$  at 20 minutes after Ca addition. The average diameters of CA,  $\text{CA}_2$ , and  $\text{CA}_6$  inclusions were at a similar level as  $\text{C}_3\text{A}$  and  $\text{C}_{12}\text{A}_7$  inclusions when observed in the same sample. Also, one could notice, that even though there were some fluctuations, generally the average  $d_{\text{avg}}$  of all  $\text{CA}_x$  inclusions were around 2  $\mu\text{m}$  in all samples of Exp. 3035. This trend of stable  $\text{CA}_x$  inclusion  $d_{\text{avg}}$  was also observed in Exp. 2020, Exp. 3020 and Exp. 3010. In Exp. 2020 and Exp. 3010, the maximum difference between the average diameters of  $\text{C}_{12}\text{A}_7$  and CA inclusions from the same sample was merely 0.1  $\mu\text{m}$ . While in Exp. 3020, the differences were slightly noticeable, especially in the 10-minute sample, in which the difference between the average diameters of  $\text{C}_{12}\text{A}_7$  and CA inclusions was about 0.5  $\mu\text{m}$ . The similarities between different  $\text{CA}_x$  inclusion types can also be observed in the bulk sample from these experiments, especially in Exp. 2020 and Exp. 3020. In the Exp. 3010, the difference between the average diameter of  $\text{CA}_2$  and  $\text{CA}_6$  inclusions was 0.4  $\mu\text{m}$ .

In Exp. 2025 and Exp. 2010, the  $d_{\text{avg}}$  change over time was more noticeable than in the other experiments. In both experiments, the average  $d_{\text{avg}}$  was around 1  $\mu\text{m}$  at 5 minutes after Ca addition. Then the average size gradually approached 2  $\mu\text{m}$ . In Exp. 2025, such an increase in inclusion diameter was achieved within 20 minutes after Ca addition, while in Exp. 2010, the average  $d_{\text{avg}}$  did not reach 2  $\mu\text{m}$  until much later, i.e., at 40 minutes after Ca addition. The reason for a different trend from other experiments remains unclear and requires further investigation. However, overall, Figure 6.3 (a) to (g) suggest that in all steel compositions, the size differences between different  $\text{CA}_x$  inclusions, regardless of their compositions, were very insignificant. Also, the coarsening of  $\text{CA}_x$  inclusions at 1873 K seems to stop after average  $d_{\text{avg}}$  reached around 2  $\mu\text{m}$  and only increased again during solidification.

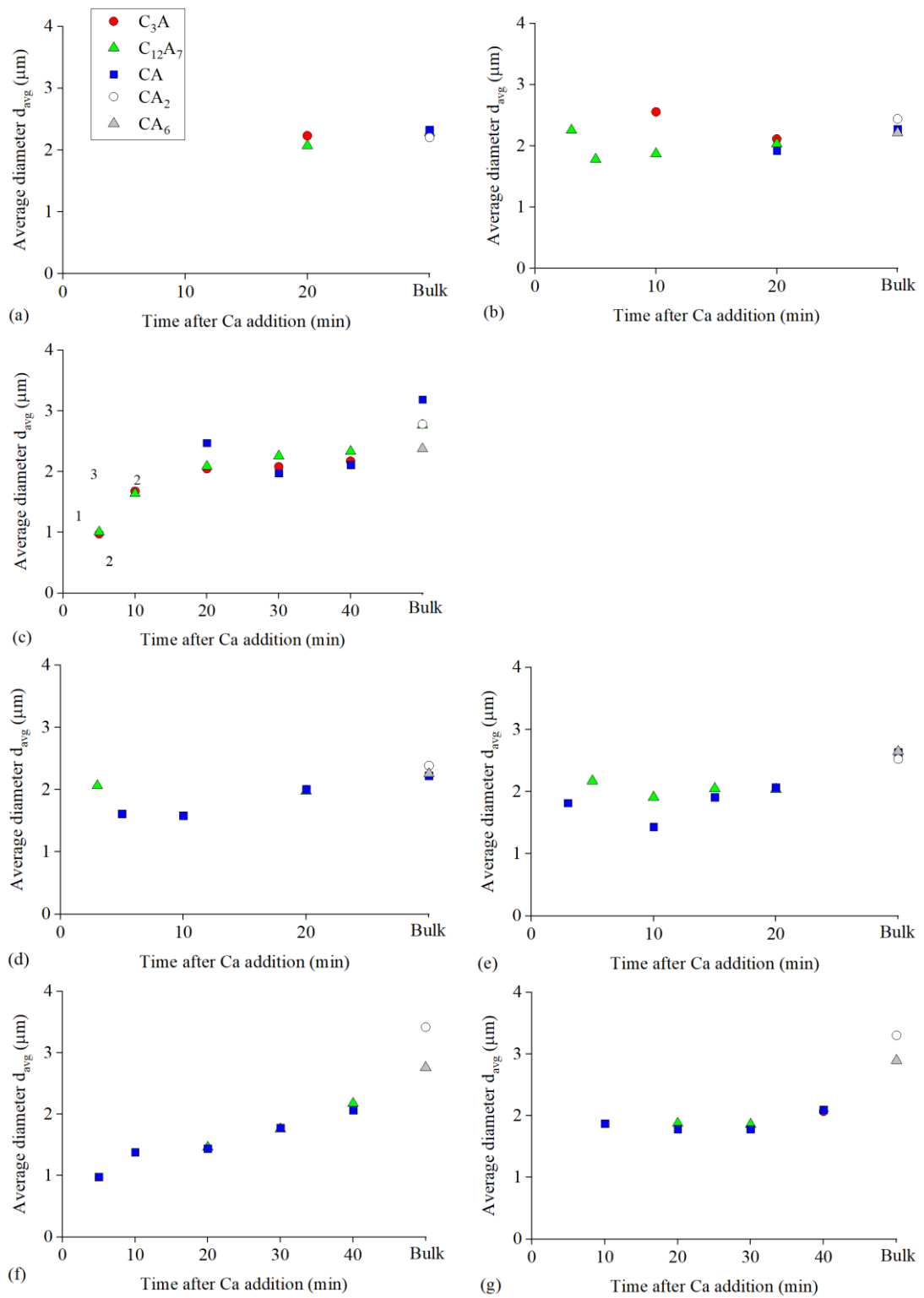


Figure 6.3 Average diameters of  $CA_x$  type inclusions in (a) Exp. 2035, (b) Exp. 3035, (c) Exp. 2025 (d) Exp. 2020, (e) Exp. 3020, (f) Exp. 2010, (g) Exp. 3010

### 6.3.2 CA<sub>x</sub> Growth in Industrial Conditions

Figure 6.4 shows the evolution of CA<sub>x</sub> AF in five industrial heats. One could easily notice that the CA<sub>x</sub> AF tends to increase significantly in the T1 sample compared to the last ladle sample. The total CA<sub>x</sub> AF doubled in Heat 1 and Heat 2, increased by 25 ppm and 22 ppm, respectively. The changes were even more significant in Heat 3 to Heat 5, with a minimum of 30 ppm increase in Heat 4.

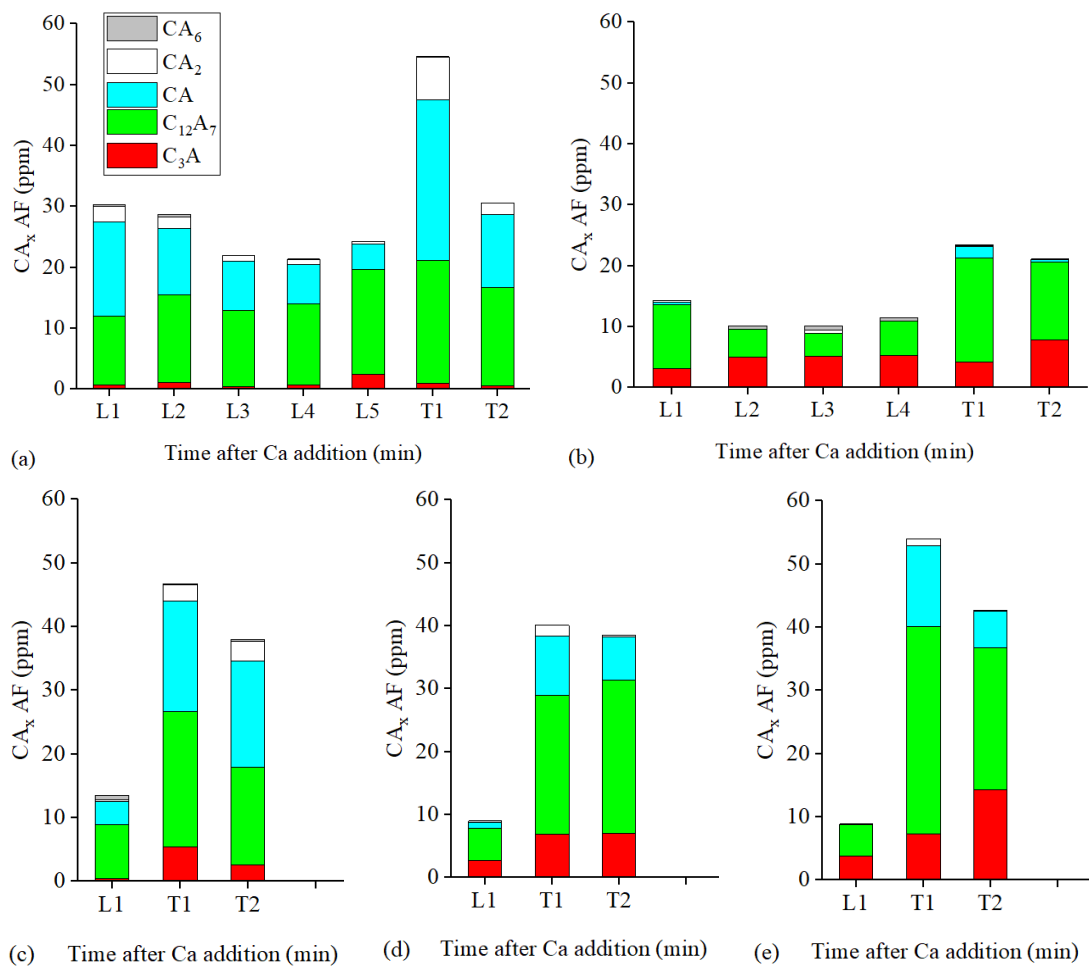


Figure 6.4 Area fraction of CA<sub>x</sub> type inclusions in (a) Heat 1, (b) Heat 2, (c) Heat 3, (d) Heat 4 and (e) Heat 5

The evolution of the average diameters of the CA<sub>x</sub> inclusions is shown in Figure 6.5. The evolution trend in industrial conditions was similar to that in the experimental conditions. In Heat 1, the average diameter values of C<sub>12</sub>A<sub>7</sub> and CA inclusions were approximately 2.8 μm from L1 to L4 samples. The difference between  $d_{avg}$  values of these inclusions was 0.8 μm and became less than 0.3 μm except in sample L5. The  $d_{avg}$  of C<sub>3</sub>A inclusions tends to be approximately 0.5 μm to 1 μm lower than the  $d_{avg}$  of C<sub>12</sub>A<sub>7</sub> and CA inclusions. Similarly, the differences between  $d_{avg}$  values for the two dominant CA<sub>x</sub> inclusion types:

$C_3A$  and  $C_{12}A_7$ , were low with a maximum value of  $0.2 \mu\text{m}$ .

In Heat 2, the  $d_{\text{avg}}$  of all  $CA_x$  inclusion types were approximately  $2.5 \mu\text{m}$  through the entire industrial process. Some  $d_{\text{avg}}$  increase can be observed in Heat 3 to Heat 5 from L1 through T2, but generally, the values for  $d_{\text{avg}}$  were between  $2 \mu\text{m}$  and  $3 \mu\text{m}$  in all samples. The similarities between  $d_{\text{avg}}$  of different  $CA_x$  inclusion types were also observed in Heat 2 to Heat 5.,

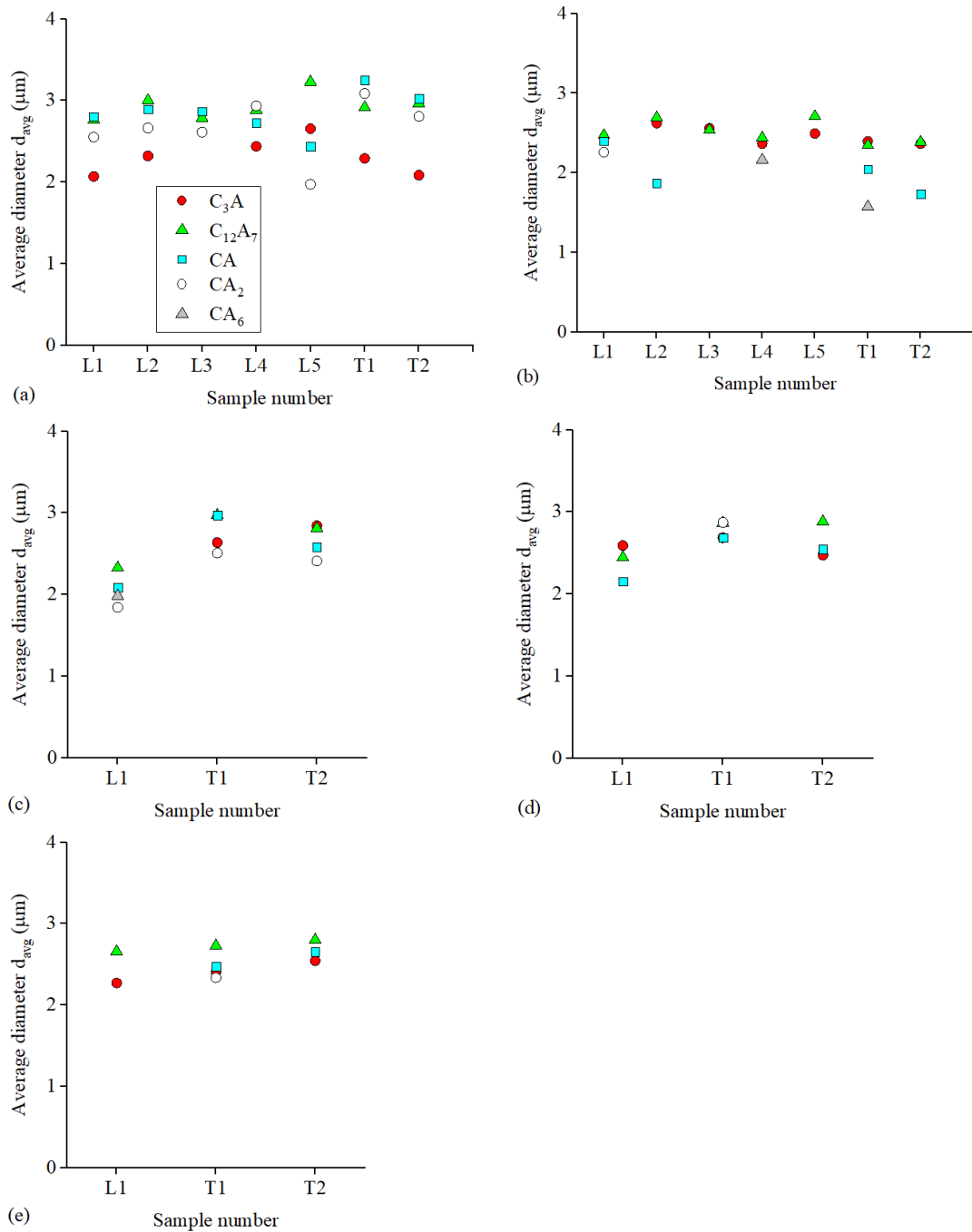


Figure 6.5 Evolution of the average diameter of  $\text{CA}_x$  type inclusions from industrial heats (a) Heat 1, (b) Heat 2, (c) Heat 3, (d) Heat 4, and (e) Heat 5

## 6.4 Discussion

### 6.4.1 Coarsening Mechanisms of $\text{CA}_x$ under Experimental Conditions

In both experimental and industrial samples, the value for average  $d_{avg}$  of  $\text{CA}_x$  inclusions remained stable. In experiments, the average  $d_{avg}$  were similar starting 10 minutes after

Ca addition. In industrial conditions, similar average  $d_{avg}$  were observed in the same heat. This finding indicates that the coarsening process slowed down drastically after Ca addition. Previous studies [24,195] suggested that the coarsening mechanism of  $CA_x$  inclusions is initially Ostwald ripening then changes to collision-related mechanisms. The effect of Ostwald ripening cannot be verified with the experimental results in the present study due to the lack of detectable  $CA_x$  inclusions in samples taken before 10 minutes after Ca addition. But comparing the observed  $d_{avg}$  change with the theoretical change due to Ostwald ripening can still provide some insight into the coarsening mechanisms. Equation (6.1) expresses the effects of steel and inclusion properties on the rate of Ostwald ripening. In experimental conditions, with the decreasing dissolved Ca concentration in the bulk steel,  $C_{[Ca],b}$ , the growth rate of  $CA_x$  inclusions by Ostwald ripening also decreases. The method and the parameters needed for calculating Equation (6.1) are provided in the Chapter 5.

$$r^3 = r_0^3 + \frac{4}{9} \frac{2\gamma MV_{Ca} D_{Ca} C_{[Ca],b}}{RT(C_{(Ca)} - C_{[Ca],b})} t \quad (6.1)$$

Figure 6.6 compares the values for  $CA_x$   $d_{avg}$  in Exp. 3035 with the theoretical  $d_{avg}$  of  $C_3A$ ,  $CA$ , and  $CA_6$  inclusions predicted by Equation (6.1). The theoretical predictions support that growth can only be attributed to Ostwald ripening in the very early stage. Regardless of the types of  $CA_x$  inclusions, the growth rate by Ostwald ripening is only significant in the approximately 3 minutes after Ca addition, then quickly reaches a plateau as  $C_{[Ca],b}$  decreased.

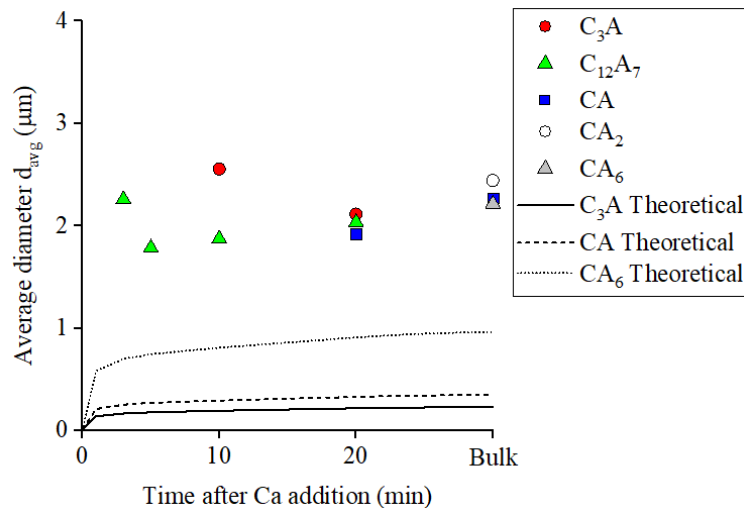


Figure 6.6 Comparison of the average diameters of  $CA_x$  inclusions in samples taken in Exp. 3035 and the theoretical coarsening rate

The theoretical coarsening rate predicted by the collision-related mechanisms is not included in Figure 6.6 because the existing models discussed in the previous chapter

assume coagulation always occurs upon collision, which may not be the case for liquid  $CA_x$  inclusions as suggested in a previous study.<sup>[195]</sup> If fully submerged liquid  $CA_x$  inclusions behave the same as they do on the steel surface, then, two liquid inclusions can easily be separated from each other after the collision; hence coagulation and size increase do not occur. However, a fraction of the collision between liquid  $CA_x$  inclusions must still result in coagulation otherwise the difference between theoretical and observed  $CA_x$   $d_{avg}$  in Figure 6.6 cannot be explained. The collision frequency depends on the number density of inclusions, which is expected to be higher in the early than the later stage of experiments. Therefore, successful coagulation mainly occurred in the early stage when the inclusions were under the preset detection limit of the automated SEM, and it rarely occurred after the number density of  $CA_x$  inclusions decreased and they became detectable in ASPEX. Another potential reason for the lack of further size increase is the flotation of inclusions. Larger inclusions have higher ascending velocity,<sup>[195]</sup> which means they may be removed more rapidly. Therefore, they were rarely observed in the ASPEX analysis. Either way, as a result, the  $CA_x$  AF changes in Figure 6.2 were mainly affected by the increase in the number densities of detectable  $CA_x$  inclusions instead of their size.

More noticeable size changes of  $CA_x$  inclusions were observed from the last pin sample (taken at 1873 K) to the bulk sample, especially for Exp. 2010 and Exp. 3010. In these two experiments, the diameter change was approximately 1  $\mu\text{m}$ , while in the other five experiments, the difference was lower than 0.5  $\mu\text{m}$ . The general increasing trend may be explained as solid  $CA_x$  inclusions started to form during solidification, coagulation may be more common because of the increased attraction forces between solid inclusions compare to a pair of liquid inclusions.<sup>[39,63,72]</sup> The modification extents of  $CA_x$  inclusions were lower in Exp. 2010 and Exp. 3010, so more  $CA_x$  inclusions were able to transform to solid  $CA_x$  inclusions that allow coagulation to happen; hence, more increase in average diameter during solidification. The attraction force between calcium aluminate inclusions on the liquid steel surface was calculated based on their acceleration when agglomeration<sup>[63]</sup> and had been modeled in previous studies.<sup>[38,161]</sup> However, liquid inclusions may behave differently when fully submerged compared to on the surface of the steel. Without the means to observe the behavior of inclusions inside the liquid steel, validating the hypothesis of low attraction force will be difficult.

The hypotheses proposed above may be justified with the more complete data on the size distribution of inclusions including those with  $d_{max} < 2 \mu\text{m}$ , which is not available at the current stage. It can be a point worth discussing in future studies.

#### **6.4.2 Coarsening Mechanisms of $CA_x$ under industrial conditions**

Figure 6.7 shows the evolution of the combined particle size distribution (PSD) of all three liquid  $CA_x$  inclusions in Heat 1. The PSD were constructed based on the 0.5  $\mu\text{m}$

ASPEX analysis to show the detailed evolution trend of the smaller inclusions.

One can notice that even though L1 had less number density,  $N_A$ , L1, L2, and L3 had a similar PSD of inclusions shown in Figure 6.7 (a). While the PSD peak was at  $d_{avg} = 1 \mu\text{m}$  ( $\log(d_{avg}) = 0$ ) for L2 and L3 samples, a plateau can be found in the L1 sample probably due to limited time to form sufficient  $CA_x$  inclusions. From L3 to L5 samples, the PSD showed no significant change and were almost over-lapping in Figure 6.7 (b). Figure 6.7 (c) exhibits a very apparent change in PSD from the L5 sample to the T1 sample as the PSD shifted rightward, indicating the disappearance of smaller inclusions and the formation of bigger ones. No further major PSD change can be observed from the T1 sample to the T2 sample. The cause of the significant change in PSD from L5 to T1 was not clear. The potential reason could be related to the long-elapsed time, as the possibility of two liquid  $CA_x$  inclusions coagulating after the collision is low but not zero, and the tapping process could also introduce extra turbulence that served as an external force for coagulation. As for the bigger inclusions, there are two potential reasons for the lack of PSD change. The first is due to the difficulty of agglomeration between liquid inclusions, large liquid  $CA_x$  inclusions simply did not grow by agglomeration. The second potential reason is that larger inclusions are generally easier to remove through floatation either by their buoyancy of force or by the ascending gas bubbles.<sup>[42]</sup> However, without the mean of observing the behavior of micron-sized inclusions inside the melt, validating the first hypothesis may be difficult.

A drastic change in PSD from L5 to T1 would normally lead to a change in  $d_{avg}$ ; however, it was not found in Figure 6.5 (a). Figure 6.5 (a) was constructed based on ASPEX analysis for inclusions  $d_{max} > 2 \mu\text{m}$  and the changes of small inclusions were not recognized. The PSD evolutions with only  $CA_x$  inclusions with  $d_{max} > 2 \mu\text{m}$  are shown in Figure 6.7 (d) to (f) for comparison. The PSD are hardly distinguishable; hence, the average diameters appear unchanged in Figure 6.5 (a). Overall, the PSD of Heat 1 shown in Figure 6.7 supports liquid  $CA_x$  inclusions growing very slowly so apparent size change should not be expected without long-elapsed time or the help of external flow.

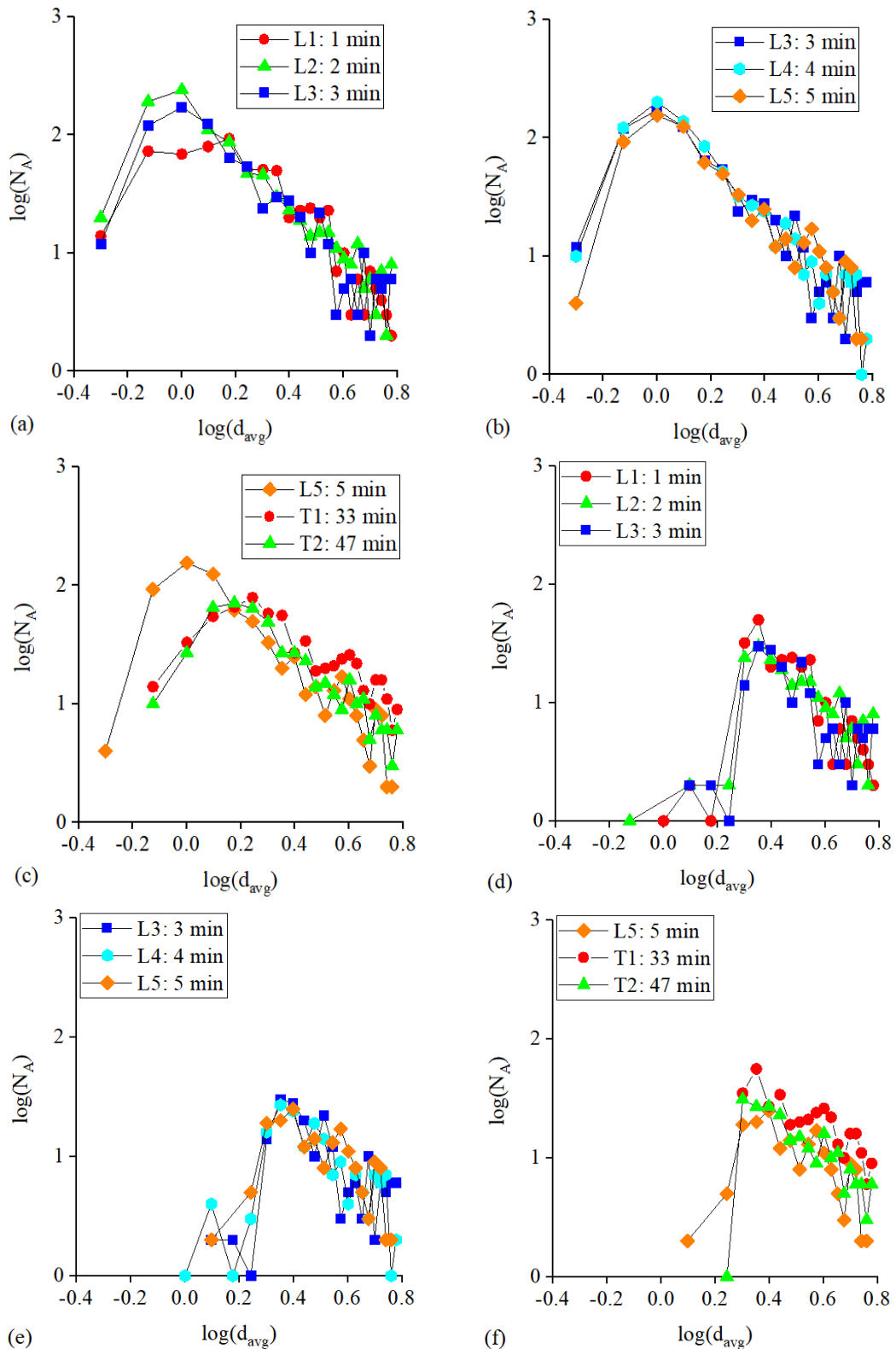


Figure 6.7 The evolution of particle size distribution for liquid  $CA_x$  type inclusions in Heat 1 including inclusions with  $d_{max} > 0.5 \mu m$  (a) (b) ladle samples (c) tundish samples. (d) (e) (f) Size distribution including inclusions with  $d_{max} > 2 \mu m$

Unfortunately, 0.5  $\mu\text{m}$  ASPEX was not conducted on the samples for Heats 2 to Heat 5. However, the author does believe evolution trends similar to Heat 1 should occur in these heats. The PSD of Heat 2 shown in Figure 6.8 mainly had  $N_A$  increase from L4 to T1, while the pattern of the PSD curves remained similar in all samples. As a result, the average diameters do not change significantly in Figure 6.5 (b). The fact that PSD curves of inclusions with  $d_{\text{max}} > 2 \mu\text{m}$  remained essentially unchanged does support the hypothesis that the coarsening process of liquid  $\text{CA}_x$  inclusions is generally slow. Just like the experiments,  $N_A$  instead of  $d_{\text{avg}}$  change was the cause of AF increase in Figure 6.4.

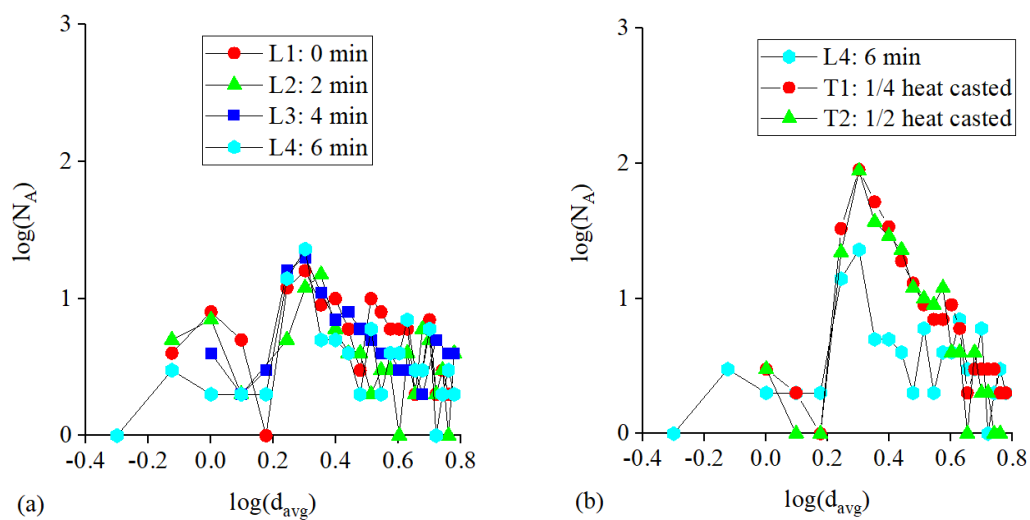


Figure 6.8 The evolution of liquid  $\text{CA}_x$  type inclusion particle size distribution in Heat 2 including inclusions with  $d_{\text{max}} > 2 \mu\text{m}$  (a) ladle samples (b) tundish samples

The evolutions of PSD of  $\text{CA}_x$  inclusions in Heat 3, Heat 4, and Heat 5 are shown in Figure 6.9. Figure 6.9 (a), (b) and (c) all indicate a major change in PSD occurred from the ladle sample after Ca addition to the first tundish sample but no further significant change in  $N_A$  or pattern of the PSD can be observed. The difference between L1 and T1 PSD is naturally reflected in the average diameter change in Figure 6.5. The peak of L1 PSD in Figure 6.9 (a) is very apparent at  $d_{\text{avg}} = 2 \mu\text{m}$  ( $\log(d_{\text{avg}}) = 0.3$ ) which caused the average diameters to be close to  $2 \mu\text{m}$  in Figure 6.5 (c) in L1. The coarsening of  $\text{CA}_x$  inclusions during the time between L1 and T1 of Heat 3 allowed the increase in  $N_A$  and the peak broadening of the PSD in Figure 6.9 (a); hence, the average diameters of  $\text{CA}_x$  inclusions appear slightly increased in Figure 6.5 (c) to approximately  $2.8 \mu\text{m}$ . On the other hand, the PSD of the L1 sample in Heat 4 and Heat 5 were both in similar shape as the PSD of the L1 sample, so the change in average diameter was less significant in Figure 6.5 (d) and (e). No conclusion can be drawn on the behavior of liquid  $\text{CA}_x$  inclusions in Heat 3, Heat 4, and Heat 5 in ladle as only one sample was taken in each heat, but it was very clear that coarsening of  $\text{CA}_x$  inclusions was negligible in tundish. Overall, the findings based on the industrial data are in agreement with that of the

experimental results discussed in the previous section, that the coarsening of  $CA_x$  inclusions is very slow after their average  $d_{avg}$  reaches approximately  $2\ \mu\text{m}$  to  $3\ \mu\text{m}$ . A similar understanding was reached in the previous studies on the coarsening process of  $CA_x$  inclusions. [23,195] Ostwald ripening is responsible for the growth of  $CA_x$  inclusions only in the early stage. The sizes of  $CA_x$  inclusions do change due to coagulation, but the rate will be slow starting a short time after Ca addition.

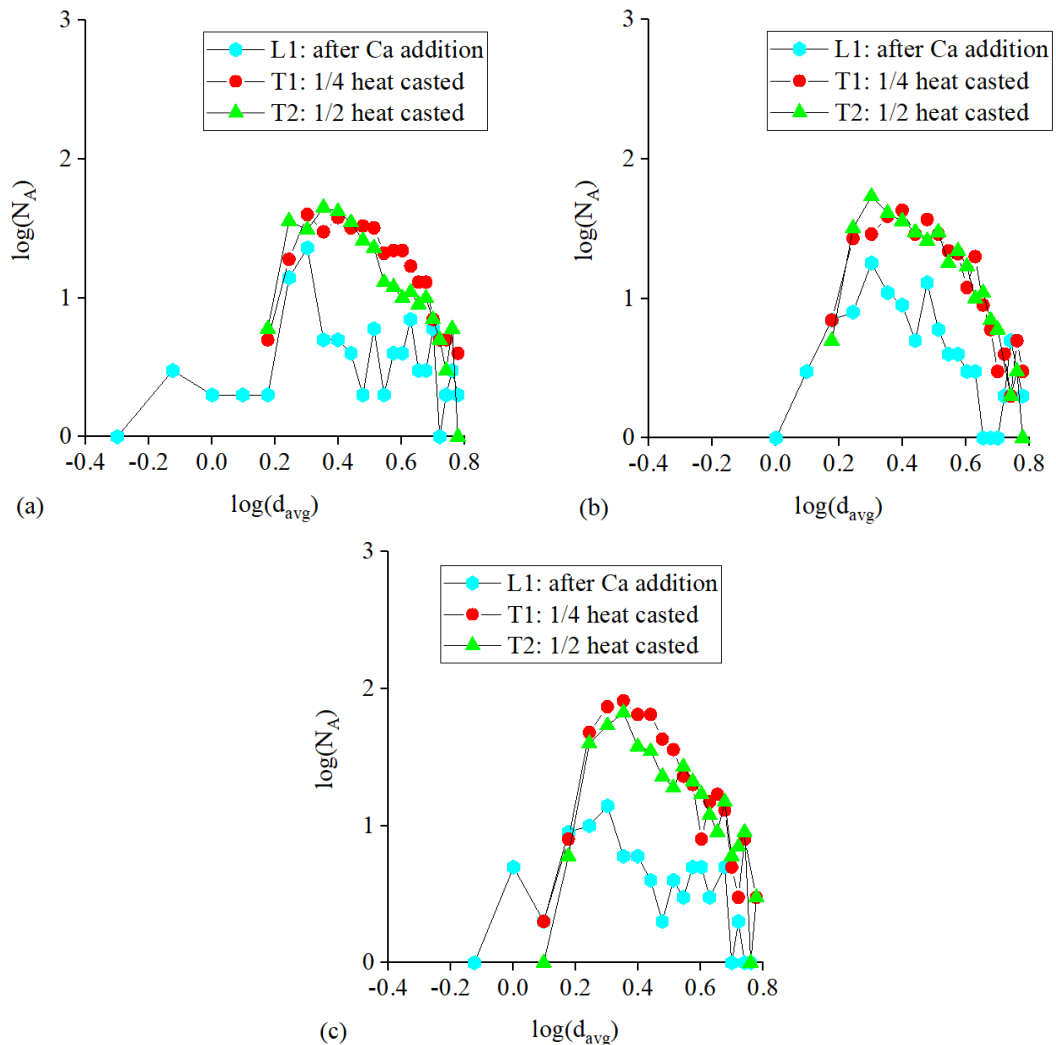


Figure 6.9 The evolution of liquid  $CA_x$  type inclusion particle size distribution in (a) Heat 3, (b) Heat 4, and (c) Heat 5 including inclusions with  $d_{max} > 2\ \mu\text{m}$

## 6.4 Conclusion

The coarsening processes of  $CA_x$  inclusions in experimental and industrial conditions were studied using the ASPEX analysis results. The findings are summarized as follows:

1. The sizes of different types of liquid  $CA_x$  inclusions in the same sample are similar,

which suggests the modification process has an insignificant effect on the size of  $CA_x$  inclusions.

2. An increase in the apparent diameter can happen during solidification, especially when Ca content is low. The potential reason is that more solid  $CA_x$  inclusions are formed, and they are known to have a stronger tendency to coagulate upon collision than liquid  $CA_x$  inclusions.
  
3. The coarsening of  $CA_x$  inclusions is also limited in the ladle and in the tundish, which is in agreement with the findings based on the experimental data, but the size of  $CA_x$  inclusions will increase during the transfer of melt from ladle to tundish. Both the experimental and industrial data suggest the coarsening of liquid  $CA_x$  inclusions is generally slow after the initial stages, which can be attributed to Ostwald ripening. Further size change of  $CA_x$  inclusions depends on coagulation but the rate will be slow. The two potential reasons are coagulation upon collision may not guarantee a pair of liquid inclusions and the more rapid removal of larger inclusions. Improvements in the analysis techniques may be needed in future work to draw a solid conclusion on the coarsening mechanisms of  $CA_x$  inclusions.

## **Chapter 7 Concluding Remarks**

This thesis focuses on understanding the evolution of inclusions during the calcium treatment process. A number of laboratory experiments were conducted to investigate the effects of S and Ca contents on the composition, population, and size of inclusions commonly seen after Ca addition. The findings are based on mainly the two-dimensional analysis performed by automated SEM-EDS. Based on the analysis, the modification mechanisms, and coarsening mechanisms of inclusions were revealed. Also, indexes were proposed to evaluate and predict the effectiveness of Ca treatment for industrial operations.

### **7.1 Key Findings and Contributions**

#### **7.1.1 General Overview**

Chapter 1 provides the background and explains the objectives of the present study. Chapter 2 focuses on reviewing the fundamentals of the calcium treatment, including its effects on the composition and morphology of inclusions. The relevant experimental techniques were reviewed as well. Based on this information, a knowledge gap is identified, and the motivation of this study is explained explicitly.

Chapter 3 is a systematic study that fulfills the first sub-object stated in Section 1.2. This chapter contributed to explaining the role of CaO inclusions during the modification mechanism of alumina inclusions by Ca treatment. Moreover, the author established a modification index to determine the conditions that cause over-modification, and the findings were successfully validated against experimental and industrial heats.

Chapter 4 fulfills the second sub-objective declared in Section 1.2 by establishing more modification indexes related to different purposes of calcium treatment. The control of  $CA_x$ , CaS, and MnS inclusions was correlated with an independent modification index that can be calculated using the Mn, Al, S, and Ca contents of steel. This chapter, to the author's knowledge, is the first to present a method to evaluate the modification extent of all three inclusion types. The proposed method has the potential of predicting optimum Ca content based on the steel chemistries and inclusion control, thereby providing useful guidelines to improve the calcium treatment process in practice.

Chapter 5 is the first study that reports the size change of CaS inclusions under experimental and industrial conditions. Chapter 5 explains the coarsening of CaS inclusions by comparing the observed values for the average diameter of CaS inclusions with the theoretical values based on four different coarsening mechanisms.

Chapter 6 applies the same methodology to explain the coarsening of  $CA_x$  inclusions. The size change of  $CA_x$  inclusions was found to be insignificant starting a few minutes after Ca addition under experimental and industrial conditions. This distinct behavior, in comparison to the coarsening of CaS inclusions reported in Chapter 5, was proposed due to the lack of coagulation after the collisions that involve modified liquid or semi-liquid  $CA_x$  inclusions. This chapter is considered a preliminary study on this topic but does have the novelty of being the first study that reported the size evolution of  $CA_x$  inclusions in industrial conditions.

### 7.1.2 Specific Findings

Inclusion analysis and calculations were conducted to improve understanding of inclusion evolutions and relations with steel chemistries after Ca addition. The objectives of the project specified in Chapter 1 have been fulfilled, the key findings are as follows:

1. There exist two modification mechanisms for  $Al_2O_3$  inclusions. When steel chemistry allows the formation of CaO inclusions, they are the major oxygen bearer by reducing  $Al_2O_3$  inclusions. Then transformation from CaO to CaS occurs and the free oxygen reacts with dissolved Al to form other oxides, most likely  $Al_2O_3$ . Then the newly formed  $Al_2O_3$  inclusions are modified by CaS inclusions. Whereas in the absence of CaO formation, the modification mechanism involves the direct reaction between  $Al_2O_3$  inclusions and dissolved Ca to form  $CA_x$  inclusions. Depending on the Ca content, CaS inclusions can form at this stage. Subsequently,  $Al_2O_3$  and  $CA_x$  inclusions are modified by CaS inclusions as the main source of Ca.
2. In steel containing 20 ppm to 30 ppm S, when the Ca content is as high as 35 ppm, the area fraction and the number of CaS inclusions increase due to the thermodynamic stability of CaS. When Ca content is 20 ppm or below, the area fraction and the number of liquid  $CA_x$  inclusions increase instead of that of CaS inclusions.
3. An index called dimensionless Ca was established based on the stability of CaS for known Ca, Al, and S contents of liquid steel. This index allows for predicting the over-modification of alumina inclusions by Ca. Dimensionless Ca > 1 means the steel chemistry allows the formation of thermodynamically stable CaS inclusions. This was validated against the industrial data. The dimensionless Ca is linearly correlated to the AF of CaS inclusions in tundish samples. This allows one to estimate the AF of CaS inclusions if the Ca, S and Al contents are known.

4. The modified calcium treatment index (CTI) determines the percentage of  $CA_x$  inclusions with more than 50 pct liquid phase based on Ca, S, and Al contents of the liquid steel. Industrial data signifies the modified  $CTI > 0.5$  in a sample means at least 90 pct of  $CA_x$  inclusions contain more than 50 pct liquid phase.
5. The findings in the present study suggest a ratio of T.Ca/T.S to eliminate MnS inclusions can be estimated as  $T.Ca/T.S = 1.65T.Mn$  if the S content of liquid steel is lower than 40 ppm. This was confirmed with the data reported in the literature focusing on industrial heats containing 1.5 wt pct Mn.
6. A method is proposed to quantify and evaluate the effectiveness of Ca treatment based on the deviation of actual Ca content from the ideal contents calculated using the three modification indexes. For a higher deviation value,  $d$ , more CaS, solid  $CA_x$ , or MnS inclusions form. This is validated against the industrial data. Moreover, T.Ca corresponds to the minimum  $d$  value and can be considered as the optimum Ca content. This allows one to design the process considering all important inclusions relevant to calcium treatment simultaneously.
7. The coarsening mechanism of CaS inclusions varies over the modification process. In experimental conditions, due to initial high concentrations of Ca in steel, the growth of CaS inclusions is controlled mainly by mass transfer in steel. As the Ca concentration decreases, the size change becomes dependent on the Brownian collision. Under the industrial conditions, the early stage is the same but because of the agitation, collision due to turbulent flow is the governing mechanism for CaS inclusions size change.
8. The size change of liquid  $CA_x$  inclusions is significant only during a short time after Ca addition in all experimental conditions studied. In industrial conditions,  $CA_x$  inclusions also do not show meaningful size change except when transferring from ladle to tundish.

## 7.2 Future Works

In Chapter 4, the MnS inclusions in 0.06C-1Mn Series 3 heats were distributed between different inclusions types and did not show an apparent correlation with the T.Ca/T.S ratio. This was explained as MnS inclusions were formed through different mechanisms in different steel phases. This argument was based on a segregation model. It is preferential to examine the samples from heats similar to compositions of Series 1 to Series 3 steel and reveal whether steel phases were indeed different. Also, additional data from heats belonging to Series 3 may allow one to determine the T.Ca/T.S needed to eliminate MnS inclusions in those conditions.

Agreements between good modification results and low deviation from ideal Ca content were found and vice versa. However, no modification has been conducted using the optimum Ca content calculated using the method proposed in Chapter 4. Therefore, the effectiveness of this method needs to be further validated by conducting calcium treatment experiments and industrial trials under the proposed guidelines.

Chapter 6 presented a drastic increase in the size of  $CA_x$  inclusions in liquid steel after the melt was transferred from ladle to tundish. Due to a lack of  $CA_x$  inclusion population in samples taken at a short time after Ca addition, their coarsening mechanism in the early stage remains unclear and requires further investigation.

More importantly, Chapter 5 and Chapter 6 proposed the coarsening mechanisms of CaS and  $CA_x$  inclusions in experimental and industrial conditions based on similarities between observed and calculated size change. However, this is different from accurately predicting the size change. The effects of mass transport, as well as the effects of flotation on inclusion size distribution, were not included in the calculations. Since it is well known that the size of inclusions can be correlated with various properties of the final product, it will be useful to develop a model that calculates the CaS and  $CA_x$  particle size distribution during the modification process. The population balance equation is likely going to be used for this purpose.

Additional work should be done on the morphology of inclusions formed during modification. The structure, how multiple phase inclusions are constructed, and the shape and roughness of the inclusions were not discussed in this study. Therefore, it would be worth studying these subjects in the future.

## Reference

- 1 B. Deo and R. Boom: *Fundamentals of Steelmaking Metallurgy*, Pearson Education Limited, Harlow, United Kingdom, 1993.
- 2 L. Holappa and O. Wijk: in *Treatise on Process Metallurgy*, vol. 3, Elsevier, 2014, pp. 347–72.
- 3 E.T. Turkdogan: *Fundamentals of Steelmaking*, The Institute of Materials, London, 1996.
- 4 Z.J. Han, L. Liu, M. Lind, and L. Holappa: *Acta Metall. Sin. (English Letter)*, 2006, vol. 19, pp. 1–8.
- 5 Y. Ito, M. Suda, Y. Kato, H. Nakato, and K. Sorimachi: *ISIJ Int.*, 1996, vol. 36, pp. S148–50.
- 6 M.K. Sardar, S. Mukhopadhyay, U.K. Bandopadhyay, and S.K. Dhua: *Steel Res. Int.*, 2007, vol. 78, pp. 136–40.
- 7 J.M.A. Geldenhuis and P.C. Pistorius: *Ironmak. Steelmak.*, 2000, vol. 27, pp. 442–9.
- 8 Y. Liu, L. Zhang, Y. Zhang, H. Duan, Y. Ren, and W. Yang: *Metall. Mater. Trans. B Process Metall. Mater. Process. Sci.*, 2018, vol. 49, pp. 610–26.
- 9 Y. Ren, L.F. Zhang, and S. Li: *ISIJ Int.*, 2014, vol. 54, pp. 2772–9.
- 10 V. Gollapalli, M.B.V. Rao, P.S. Karamched, C.R. Borra, G.G. Roy, and P. Srirangam: *Ironmak. Steelmak.*, 2019, vol. 46, pp. 663–70.
- 11 J. Xu, F. Huang, and X. Wang: *Metall. Mater. Trans. B*, 2016, vol. 47, pp. 1217–27.
- 12 X. Wang, X. Li, Q. Li, F. Huang, H. Li, and J. Yang: *Steel Res. Int.*, 2014, vol. 85, pp. 155–63.
- 13 Y. Tabatabaei, K.S. Coley, G.A. Irons, and S. Sun: *Metall. Mater. Trans. B Process Metall. Mater. Process. Sci.*, 2018, vol. 49, pp. 375–87.
- 14 M. Lind and L. Holappa: *Metall. Mater. Trans. B Process Metall. Mater. Process. Sci.*, 2010, vol. 41, pp. 359–66.
- 15 Y. Higuchi, M. Numata, S. Fukagawa, and K. Shinme: *ISIJ Int.*, 1996, vol. 36, pp. S151–4.
- 16 M. Imagumbai and T. Takeda: *ISIJ Int.*, 1994, vol. 34, pp. 574–83.
- 17 K. Miao, M. Nabeel, N. Dogan, and S. Sun: *Metall. Mater. Trans. B Process Metall. Mater. Process. Sci.*, 2021, vol. 52, pp. 3151–66.
- 18 S. Sun, S. Waterfall, N. Strobl, D. Liao, and D. Holdridge: *Miner. Met. Mater. Ser.*, 2017, vol. Part F5, pp. 347–57.
- 19 S.R. Story, T.J. Piccone, R.J. Fruehan, and M. Potter: *Iron Steel Technol.*, 2004, vol. 1, pp. 163–9.
- 20 G. Yang and X. Wang: *ISIJ Int.*, 2015, vol. 55, pp. 126–33.
- 21 B. Kumar, S. Mishra, M.B.V. Rao, and G.G. Roy: *Ironmak. Steelmak.*, 2019, vol. 46, pp. 454–62.
- 22 Y. Kang, B. Sahebkar, P.R. Scheller, K. Morita, and D. Sichen: *Metall. Mater.*

- Trans. B Process Metall. Mater. Process. Sci.*, 2011, vol. 42, pp. 522–34.
- 23 M.E. Ferreira, P.C. Pistorius, and R.J. Fruehan: *Front. Mater.*, 2021, vol. 8, pp. 1–10.
- 24 L. Wang, J. Li, S. Yang, C. Chen, H. Jin, and X. Li: *Sci. Rep.*, 2018, vol. 8, pp. 1–11.
- 25 J. Rieger, V. Colla, I. Matino, T.A. Branca, G. Stubbe, A. Panizza, C. Brondi, M. Falsafi, J. Hage, X. Wang, B. Voraberger, T. Fenzl, V. Masaguer, E.L. Faraci, L. di Sante, F. Cirilli, F. Loose, C. Thaler, A. Soto, P. Frittella, G. Foglio, C. di Cecca, M. Tellaroli, M. Corbella, M. Guzzon, E. Malfa, A. Morillon, D. Algermissen, K. Peters, and D. Snaet: *Metals (Basel)*, 2021, vol. 11, p. 1202.
- 26 J. Feng and Y. Bao, eds.: *College Planning Materials: Iron and Steel Metallurgy Tutorial*, Metallurgical Industry Press, 1991.
- 27 F. Oeters: *Metallurgy of Steelmaking*, 1994.
- 28 L. Ya, Z. Yang, Z. Ren, Y. Sun, and S. Zhou: *College Planning Materials: Steel School*, 1st edn., Metallurgical Industry Press, Beijing, 2010.
- 29 C. Barr, S. Da Sun, M. Easton, N. Orchowski, N. Matthews, and M. Brandt: *Surf. Coatings Technol.*, 2018, vol. 340, pp. 126–36.
- 30 L. Holappa: in *Treatise on Process Metallurgy*, vol. 3, Elsevier Ltd, 2014, pp. 301–45.
- 31 The Ellingham Diagram, University of Cambridge Website, [https://www.doitpoms.ac.uk/tlplib/ellingham\\_diagrams/ellingham.php](https://www.doitpoms.ac.uk/tlplib/ellingham_diagrams/ellingham.php).
- 32 W. Choi, H. Matsuura, and F. Tsukihashi: *ISIJ Int.*, 2011, vol. 51, pp. 1951–6.
- 33 H. Ohta and H. Suito: *ISIJ Int.*, 2003, vol. 43, pp. 1293–300.
- 34 A. Ghosh: *Secondary Steelmaking: Principles and Applications*, 2000.
- 35 M. Allibert, H. Gaye, J. Geisler, D. Janke, B.J. Keene, D. Kirner, M. Kowalski, J. Lehmann, K.C. Mills, D. Neuschütz, R. Parra, C. Saint Jours, P.J. Spencer, M. Susa, M. Tmar, and E. Woermann: *Slag Atlas*, 2nd edn., Verlag Stahleisen GmbH, Dusseldorf, 1995.
- 36 J. Lehmann and M. Nadif: *Rev. Mineral. Geochemistry*, 2011, vol. 73, pp. 493–511.
- 37 P.K. Iwamasa and R.J. Fruehan: *Metall. Mater. Trans. B*, 1997, vol. 28, pp. 47–57.
- 38 W. Mu, N. Dogan, and K.S. Coley: *Metall. Mater. Trans. B Process Metall. Mater. Process. Sci.*, 2017, vol. 48, pp. 2379–88.
- 39 H. Yin, H. Shibata, T. Emi, and M. Suzuki: *ISIJ Int.*, 1997, vol. 37, pp. 936–45.
- 40 H. Tozawa, Y. Kato, K. Sorimachi, and T. Nakanishi: *ISIJ Int.*, 2008, vol. 39, pp. 426–34.
- 41 L.F. Zhang and S. Taniguchi: *Int. Mater. Rev.*, 2000, vol. 45, pp. 59–82.
- 42 W. Lou and M. Zhu: *Metall. Mater. Trans. B Process Metall. Mater. Process. Sci.*, 2013, vol. 44, pp. 762–82.
- 43 X. Guo, J. Godinez, N.J. Walla, A.K. Silaen, H. Oltmann, V. Thapliyal, A.

- Bhansali, E. Pretorius, and C.Q. Zhou: *AISTech - Iron Steel Technol. Conf. Proc.*, 2021, vol. 2021-June, pp. 874–89.
- 44 H. Arai, K. Matsumoto, S.I. Shimasaki, and S. Taniguchi: *ISIJ Int.*, 2009, vol. 49, pp. 965–74.
- 45 Q. Wang, Y. Liu, A. Huang, W. Yan, H. Gu, and G. Li: *Metall. Mater. Trans. B Process Metall. Mater. Process. Sci.*, 2020, vol. 51, pp. 276–92.
- 46 T. Wetzig, A. Baaske, S. Karrasch, N. Brachhold, M. Rudolph, and C.G. Aneziris: *Ceram. Int.*, 2018, vol. 44, pp. 23024–34.
- 47 Widyantoro, D. Dhaneswara, J. Fajar Fatriansyah, M. Reza Firmansyah, and Y. Prasetyo: *MATEC Web Conf.*, 2019, vol. 269, p. 07002.
- 48 S. jian Li, G. guang Cheng, Z. qi Miao, L. Chen, and X. yan Jiang: *Int. J. Miner. Metall. Mater.*, 2019, vol. 26, pp. 291–300.
- 49 Y. Ji, C. Liu, Y. Lu, H. Yu, F. Huang, and X. Wang: *Metall. Mater. Trans. B Process Metall. Mater. Process. Sci.*, 2018, vol. 49, pp. 3127–36.
- 50 J.Y. Choi and H.G. Lee: *ISIJ Int.*, 2003, vol. 43, pp. 1348–55.
- 51 H. Abdeyazdan, N. Dogan, M.A. Rhamdhani, M.W. Chapman, and B.J. Monaghan: *Metall. Mater. Trans. B Process Metall. Mater. Process. Sci.*, 2014, vol. 46, pp. 208–19.
- 52 B.J. Monaghan, H. Abdeyazdan, N. Dogan, M.A. Rhamdhani, R.J. Longbottom, and M.W. Chapman: *ISIJ Int.*, 2015, vol. 55, pp. 1834–40.
- 53 H. Abdeyazdan, B.J. Monaghan, R.J. Longbottom, M.A. Rhamdhani, N. Dogan, and M.W. Chapman: *Metall. Mater. Trans. B Process Metall. Mater. Process. Sci.*, 2017, vol. 48, pp. 1970–80.
- 54 B.J. Monaghan, S.A. Nightingale, L. Chen, and G.A. Brooks: in *International Conference on Molten Slags Fluxes and Salts*, 2004, pp. 585–94.
- 55 J. Liu, F. Verhaeghe, M. Guo, B. Blanpain, and P. Wollants: *J. Am. Ceram. Soc.*, 2007, vol. 90, pp. 3818–24.
- 56 B.J. Monaghan, L. Chen, and J. Sorbe: *Ironmak. Steelmak.*, 2005, vol. 32, pp. 258–64.
- 57 J.-Y. Choi, H.-G. Lee, and J.-S. Kim: *ISIJ Int.*, 2002, vol. 42, pp. 852–60.
- 58 M. Valdez, K. Prapakorn, A.W. Cramb, and S. Sridhar: *Ironmak. Steelmak.*, 2002, vol. 29, pp. 47–52.
- 59 Z.H.I. Sun, X. Guo, J. Van Dyck, M. Guo, and B. Blanpain: *AIChE J.*, 2013, vol. 59, pp. 2907–16.
- 60 X. Guo, Z.H.I. Sun, J. Van Dyck, M. Guo, and B. Blanpain: *Ind. Eng. Chem. Res.*, 2014, vol. 53, pp. 6325–33.
- 61 S.H. Amini, M.P. Brungs, S. Jahanshahi, and O. Ostrovski: *Metall. Mater. Trans. B Process Metall. Mater. Process. Sci.*, 2006, vol. 37, pp. 773–80.
- 62 S. Amini, M. Brungs, and O. Ostrovski: *ISIJ Int.*, 2007, vol. 47, pp. 32–7.
- 63 B. Coletti, B. Blanpain, S. Vantilt, and S. Sridhar: *Metall. Mater. Trans. B*, 2003, vol. 34, pp. 533–8.
- 64 K. Miao, A. Haas, M. Sharma, W. Mu, and N. Dogan: *Metall. Mater. Trans. B*

- Process Metall. Mater. Process. Sci.*, 2018, vol. 49, pp. 1612–23.
- 65 Y. Ueshima, H. Kato, K. Kondo, and T. Mizoguchi: *High Temp. Mater. Process.*, 2012, vol. 31, pp. 431–8.
- 66 S. Abdelaziz, G. Megahed, I. El-Mahallawi, and H. Ahmed: *Ironmak. Steelmak.*, 2009, vol. 36, pp. 432–41.
- 67 S. Basak, R. Kumar Dhal, and G.G. Roy: *Ironmak. Steelmak.*, 2010, vol. 37, pp. 161–8.
- 68 D. Lu: Ph.D thesis, McMaster University, 1992.
- 69 T. Kawawa and R. Imai: *Tetsu-to-Hagane*, 1977, vol. 63, pp. 1965–74.
- 70 M. Jiang, X. Wang, B. Chen, and W. Wang: *ISIJ Int.*, 2010, vol. 50, pp. 95–104.
- 71 B. Khurana, S. Spooner, M.B.V. Rao, G.G. Roy, and P. Srirangam: *Metall. Mater. Trans. B Process Metall. Mater. Process. Sci.*, 2017, vol. 48, pp. 1409–15.
- 72 H. Yin, H. Shibata, T. Emi, and M. Suzuki: *ISIJ Int.*, 1997, vol. 37, pp. 946–55.
- 73 Y. Gao and K. Sorimachi: *ISIJ Int.*, 1993, vol. 33, pp. 291–7.
- 74 G.M. Faulring, J.W. Farrell, and D.C. Hilty: *Ironmak. Steelmak.*, 1980, vol. 7, pp. 14–20.
- 75 Y. Wu, S. Song, Z. Xue, and M. Nath: *ISIJ Int.*, 2019, vol. 59, pp. 1178–83.
- 76 K. Kawakami, T. Taniguchi, and K. Nakashima: *Tetsu-to-Hagane*, 2007, vol. 93, pp. 743–52.
- 77 S. Yang, L. Zhang, L. Sun, J. Li, and K.D. Peaslee: *Iron Steel Technol.*, 2012, vol. 9, pp. 245–58.
- 78 S.K. Choudhary and A. Ghosh: *ISIJ Int.*, 2008, vol. 48, pp. 1552–9.
- 79 C. Liu, X. Gao, S. Ueda, and S. Kitamura: *ISIJ Int.*, 2019, vol. 59, pp. 268–76.
- 80 J.H. Shin, Y. Chung, and J.H. Park: *Metall. Mater. Trans. B Process Metall. Mater. Process. Sci.*, 2017, vol. 48, pp. 46–59.
- 81 L. Holappa and H. Ylonen: *Steelmak. Proc.*, 1986, pp. 277–83.
- 82 G. Ye, P. Jonsson, and T. Lund: *ISIJ Int.*, 1996, vol. 36, p. Supplement, S105–S108.
- 83 N. Verma, P.C. Pistorius, R.J. Fruehan, M. Potter, M. Lind, and S.R. Story: *Metall. Mater. Trans. B Process Metall. Mater. Process. Sci.*, 2011, vol. 42, pp. 720–9.
- 84 Y. Ren, Y. Zhang, and L. Zhang: *Ironmak. Steelmak.*, 2017, vol. 44, pp. 497–504.
- 85 W. Yang, L.F. Zhang, X. Wang, Y. Ren, X. Liu, and Q. Shan: *ISIJ Int.*, 2013, vol. 53, pp. 1401–10.
- 86 S. Yang, Q. Wang, L. Zhang, J. Li, and K. Peaslee: *Metall. Mater. Trans. B*, 2012, vol. 43, pp. 731–50.
- 87 J.H. Park, D.S. Kim, and S.B. Lee: *Metall. Mater. Trans. B Process Metall. Mater. Process. Sci.*, 2005, vol. 36, pp. 67–73.
- 88 W. Yang, X. Wang, L. Zhang, and W. Wang: *Steel Res. Int.*, 2013, vol. 84, pp. 878–91.

- 89 L. Holappa, M. Hämäläinen, M. Liukkonen, and M. Lind: *Ironmak. Steelmak.*, 2003, vol. 30, pp. 111–5.
- 90 D. Yang, X. Wang, G. Yang, P. Wei, and J. He: *Steel Res. Int.*, 2014, vol. 85, pp. 1517–24.
- 91 L. Luyckx, J.R. Bell, A. McLean, and M. Korchynsky: *Metall. Trans.*, 1970, vol. 1, pp. 3341–50.
- 92 S. Abraham, R. Bodnar, J. Raines, and Y. Wang: *J. Iron Steel Res. Int.*, 2018, vol. 25, pp. 133–45.
- 93 Y. Murakami and H. Usuki: *Int. J. Fatigue*, 1989, vol. 11, pp. 299–307.
- 94 C. Temmel, B. Karlsson, and N.G. Ingesten: *Metall. Mater. Trans. A Phys. Metall. Mater. Sci.*, 2006, vol. 37, pp. 2995–3007.
- 95 Y. Tomita: *J. Mater. Sci.*, 1994, vol. 29, pp. 2873–8.
- 96 L. Shi, J. Chen, and D.O. Northwood: *J. Mater. Eng.*, 1991, vol. 13, pp. 273–9.
- 97 K. Taguchi, H. Ono-Nakazato, D. Nakai, T. Usui, and K. Marukawa: *ISIJ Int.*, 2003, vol. 43, pp. 1705–9.
- 98 Y. Guo, S. He, G. Chen, and Q. Wang: *Metall. Mater. Trans. B Process Metall. Mater. Process. Sci.*, 2016, vol. 47, pp. 2549–57.
- 99 R. Piao, H.G. Lee, and Y.B. Kang: *ISIJ Int.*, 2014, vol. 53, pp. 2132–41.
- 100 C. Gatellier, H. Gaye, J. Lehmann, J.N. Pontoire, and F. Castro: *Steelmak. Conf.*, 1991, pp. 827–34.
- 101 D.Z. Lu, G.A. Irons, and W.K. Lu: *Ironmak. Steelmak.*, 1991, vol. 18, pp. 342–6.
- 102 Q. Wang, L. Zhang, S. Seetharaman, S. Yang, W. Yang, and Y. Wang: *Metall. Mater. Trans. B Process Metall. Mater. Process. Sci.*, 2016, vol. 47, pp. 1594–612.
- 103 H. Suito and R. Inoue: *ISIJ Int.*, 1996, vol. 36, pp. 528–36.
- 104 J. Yang, X. Wang, M. Jiang, and W. Wang: *J. Iron Steel Res. Int.*, 2011, vol. 18, pp. 8–14.
- 105 G. Okuyama, K. Yamaguchi, S. Takeuchi, and K. Sorimachi: *ISIJ Int.*, 2008, vol. 40, pp. 121–8.
- 106 H. Mu, T. Zhang, R.J. Fruehan, and B.A. Webler: *Metall. Mater. Trans. B Process Metall. Mater. Process. Sci.*, 2018, vol. 49, pp. 1665–74.
- 107 J.H. Shin and J.H. Park: *ISIJ Int.*, 2018, vol. 58, pp. 88–97.
- 108 S. Chen, M. Jiang, X. He, and X. Wang: *Int. J. Miner. Metall. Mater.*, 2012, vol. 19, pp. 490–8.
- 109 J.H. Voncken: *The Rare Earth Elements: An Introduction*, vol. 53, 2016.
- 110 L. Wang, Y. Liu, Q. Wang, and K. Chou: *ISIJ Int.*, 2015, vol. 55, pp. 970–5.
- 111 H. Li, Y. Yu, X. Ren, S. Zhang, and S. Wang: *J. Iron Steel Res. Int.*, 2017, vol. 24, pp. 925–34.
- 112 H. Wang, Y. Bao, J. Zhi, C. Duan, S. Gao, and M. Wang: *ISIJ Int.*, 2021, vol. 61, pp. 657–66.
- 113 L. Shi and D.O. Northwood: *J. Mater. Sci.*, 1992, vol. 27, pp. 5343–7.

- 114 L. Shi, J. Chen, and D.O. Northwood: *J. Mater. Eng. Perform.*, 1992, vol. 1, pp. 21–7.
- 115 M. Opiela and A. Grajcar: *Arch. Foundry Eng.*, 2012, vol. 12, pp. 129–34.
- 116 B. Li, H. Zhu, J. Zhao, M. Song, J. Li, and Z. Xue: *Steel Res. Int.*, 2022, vol. 93, pp. 1–9.
- 117 J. Maciejewski: *Handb. Case Hist. Fail. Anal.*, 2020, pp. 199–207.
- 118 J. Guan, L. Wang, C. Zhang, and X. Ma: *Tribol. Int.*, 2017, vol. 106, pp. 123–31.
- 119 K.I. Yamamoto, H. Yamamura, and Y. Suwa: *ISIJ Int.*, 2011, vol. 51, pp. 1987–94.
- 120 R. Wang, Y. Bao, Z. Yan, D. Li, and Y. Kang: *Int. J. Miner. Metall. Mater.*, 2019, vol. 26, pp. 178–85.
- 121 H. Yu, X. Liu, H. Bi, and L. Chen: *J. Mater. Process. Technol.*, 2009, vol. 209, pp. 455–61.
- 122 C. Liu, R.I. Revilla, D. Zhang, Z. Liu, A. Lutz, F. Zhang, T. Zhao, H. Ma, X. Li, and H. Terryn: *Corros. Sci.*, 2018, vol. 138, pp. 96–104.
- 123 Y. Hu, W. Chen, H. Han, and R. Bai: *Ironmak. Steelmak.*, 2017, vol. 44, pp. 28–35.
- 124 H. Tervo, A. Kaijalainen, T. Pikkarainen, S. Mehtonen, and D. Porter: *Mater. Sci. Eng. A*, 2017, vol. 697, pp. 184–93.
- 125 Y. Tomita: *Metall. Trans. A*, 1990, vol. 21, pp. 2739–46.
- 126 J. Moon, S.J. Kim, and C. Lee: *Met. Mater. Int.*, 2013, vol. 19, pp. 45–8.
- 127 G. Li, F. Wang, R. Hui, and W. Cao: *Int. J. Miner. Metall. Mater.*, 2009, vol. 16, pp. 650–3.
- 128 G. Ghosh, P. Rostron, R. Garg, and A. Panday: *Eng. Fract. Mech.*, 2018, vol. 199, pp. 609–18.
- 129 A.A. Benzerga and J.B. Leblond: *Adv. Appl. Mech.*, 2010, vol. 44, pp. 169–305.
- 130 K.M.M. Rahman, W. Qin, J.A. Szpunar, J. Kozinski, M. Song, and N. Zhu: *Philos. Mag.*, 2021, vol. 101, pp. 976–96.
- 131 R. V. Väinölä, L.E.K. Holappa, and P.H.J. Karvonen: *J. Mater. Process. Tech.*, 1995, vol. 53, pp. 453–65.
- 132 R. Maiti and E.B. Hawbolt: *J. Mater. Energy Syst.*, 1985, vol. 6, pp. 251–62.
- 133 P. Juvonen: Ph.D. thesis, Helsinki University of Technology, 2004.
- 134 P. Jonsson, N. Anmark, and A. Karasev: *Materials (Basel)*, 2015, vol. 8, pp. 751–82.
- 135 L. Zhang, W. Pluschkell, and B.G. Thomas: in *85th steelmaking Conference*, Nashville, 2002, pp. 463–76.
- 136 M. Suzuki, R. Yamaguchi, K. Murakami, and M. Nakada: *ISIJ Int.*, 2001, vol. 41, pp. 247–56.
- 137 J. Zhang and H.G. Lee: *ISIJ Int.*, 2004, vol. 44, pp. 1629–38.
- 138 H. Ohta and H. Suito: *ISIJ Int.*, 2006, vol. 46, pp. 14–21.
- 139 H. Ohta and H. Suito: *ISIJ Int.*, 2006, vol. 46, pp. 42–9.

- 140 H. Ohta and H. Suito: *Metall. Mater. Trans. B*, 1998, vol. 29, pp. 119–29.
- 141 J. Alemán, A. V. Chadwick, J. He, M. Hess, K. Horie, R.G. Jones, P. Kratochvíl, I. Meisel, I. Mita, G. Moad, S. Penczek, and R.F.T. Stepto: *Pure Appl. Chem.*, 2007, vol. 79, pp. 1801–29.
- 142 A. Baldan: *J. Mater. Sci.*, 2002, vol. 37, pp. 2171–202.
- 143 L. Zhang and W. Pluschkell: *Ironmak. Steelmak.*, 2003, vol. 30, pp. 106–10.
- 144 X. Yin, Y. Sun, Y. Yang, X. Deng, M. Barati, and A. McLean: *Ironmak. Steelmak.*, 2017, vol. 44, pp. 152–8.
- 145 X. Zhang and R.H. Davis: *J. Fluid Mech.*, 1991, vol. 230, pp. 479–504.
- 146 M. Smoluchowski: *Z Phys. Chem*, 1917, vol. 92, pp. 129–68.
- 147 P.G. Saffman and J.S. Turner: *J. Fluid Mech.*, 1970, vol. 196, p. 599.
- 148 S. Taniguchi, A. Kikuchi, T. Ise, and N. Shoji: *ISIJ Int.*, 1996, vol. 36, pp. S117–20.
- 149 L. Wang, Q. Zhang, S. Peng, and Z. Li: *ISIJ Int.*, 2005, vol. 45, pp. 331–7.
- 150 M. Söder, P. Jönsson, and L. Jonsson: *Steel Res. Int.*, 2004, vol. 75, pp. 128–38.
- 151 K. Higashitani, R. Ogawa, G. Hosokawa, and Y. Matsuno: *J. Chem. Eng. Japan*, 1982, vol. 15, pp. 299–304.
- 152 X. Guo, J. Godinez, N.J. Walla, A.K. Silaen, H. Oltmann, V. Thapliyal, A. Bhansali, E. Pretorius, and C. Zhou: *Processes*, 2021, vol. 9, p. 1048.
- 153 K. Nakajima, H. Ohta, H. Suito, and P. Jönsson: *ISIJ Int.*, 2006, vol. 46, pp. 807–13.
- 154 M.D. Seo, J.W. Cho, K.C. Kim, and S.H. Kim: *ISIJ Int.*, 2014, vol. 54, pp. 475–81.
- 155 E. Zinngrebe, C. Van Hoek, H. Visser, A. Westendorp, and I.H. Jung: *ISIJ Int.*, 2012, vol. 52, pp. 52–61.
- 156 D. Ramkrishna and M.R. Singh: *Annu. Rev. Chem. Biomol. Eng.*, 2014, vol. 5, pp. 123–46.
- 157 S. Friedlander: *Smoke, Dust, and Haze Fundamentals of Aerosol Dynamics*, 2nd edn., Oxford university Press, Inc., New York, 2000.
- 158 C.J. Meyer and D.A. Deglon: *Miner. Eng.*, 2011, vol. 24, pp. 719–30.
- 159 H. Lei, K. Nakajima, and J. He: *ISIJ Int.*, 2010, vol. 50, pp. 1735–45.
- 160 H. Lei and J. He: *J. Mater. Sci. Technol.*, 2012, vol. 28, pp. 642–6.
- 161 W. Mu, N. Dogan, and K.S. Coley: *Metall. Mater. Trans. B Process Metall. Mater. Process. Sci.*, 2017, vol. 48, pp. 2092–103.
- 162 H. Ling, L. Zhang, and H. Li: *Metall. Mater. Trans. B Process Metall. Mater. Process. Sci.*, 2016, vol. 47, pp. 2991–3012.
- 163 D.L. Swift and S.K. Friedlander: *J. Colloid Sci.*, 1964, vol. 19, pp. 621–47.
- 164 Y. Ueshima, S. Mizoguchi, T. Matsumiya, and H. Kajioka: *Metall. Trans. B*, 1986, vol. 17, pp. 845–59.
- 165 P. Kaushik, J. Lehmann, and M. Nadif: *Metall. Mater. Trans. B Process Metall. Mater. Process. Sci.*, 2012, vol. 43, pp. 710–25.
- 166 K. Mizukami, K. Kawakami, M. Sugiyama, and M. Tsuji: *Tetsu-To-*

- Hagane/Journal Iron Steel Inst. Japan*, 2009, vol. 95, pp. 51–8.
- 167 G. Nastasi, R. Wester, V. Colla, and R. Noll: *Metall. Anal.*, 2013, vol. 33, pp. 9–13.
- 168 L. Zhang and B.G. Thomas: *ISIJ Int.*, 2003, vol. 43, pp. 271–91.
- 169 H.F. Jacobi: *Steel Res. Int.*, 2005, vol. 76, pp. 595–602.
- 170 J.C. Pandey, M. Raj, T.K. Roy, and T. Venugopalan: *Metall. Mater. Trans. B*, 2008, vol. 39, pp. 439–46.
- 171 D.E. Heard: *Analytical Techniques for Atmospheric Measurement*, Blackwell Publishing, Oxford, UK, 2006.
- 172 844 Series Combustion Analyzer, <https://www.leco.com/product/844-series>.
- 173 P. Kaushik, H. Pielet, and H. Yin: *Ironmak. Steelmak.*, 2009, vol. 36, pp. 561–71.
- 174 L. Zhang, Y. Liu, Y. Zhang, W. Yang, and W. Chen: *Metall. Mater. Trans. B Process Metall. Mater. Process. Sci.*, 2018, vol. 49, pp. 1841–59.
- 175 Q. Ren and L. Zhang: *Metall. Mater. Trans. B Process Metall. Mater. Process. Sci.*, 2020, vol. 51, pp. 589–600.
- 176 C. Lyons and P. Kaushik: *Steel Res. Int.*, 2011, vol. 82, pp. 1394–403.
- 177 R. Inoue, S. Ueda, T. Ariyama, and H. Suito: *ISIJ Int.*, 2011, vol. 51, pp. 2050–5.
- 178 C. Xuan, W. Mu, Z.I. Olano, P.G. Jönsson, and K. Nakajima: *Steel Res. Int.*, 2016, vol. 87, pp. 911–20.
- 179 H. Doostmohammadi, A. Karasev, and P.G. Jönsson: *Steel Res. Int.*, 2010, vol. 81, pp. 398–406.
- 180 O.T. Ericsson, M. Lionet, A. V. Karasev, R. Inoue, and P.G. Jönsson: *Ironmak. Steelmak.*, 2012, vol. 39, pp. 67–75.
- 181 A. Chino, Y. Kawai, H. Kutsumi, and M. Kawakami: *ISIJ Int.*, 1996, vol. 36, pp. S144–7.
- 182 D. Janis, A. Karasev, and P.G. Jönsson: *ISIJ Int.*, 2015, vol. 55, pp. 2173–81.
- 183 A. Khursheed: *Scanning Electron Microscope Optics and Spectrometers*, World Scientific, 2010.
- 184 M. Harris, O. Adaba, S. Lekakh, R. O’Malley, and L. Von Richards: *AISTech - Iron Steel Technol. Conf. Proc.*, 2015, vol. 3, pp. 3315–25.
- 185 S. Abraham, J. Raines, and R. Bodnar: in *AISTech - Iron and Steel Technology Conference Proceedings*, vol. 1, 2013, pp. 1069–84.
- 186 F. Schamber: *ASPEX Corp.*, 2011, pp. 1–7.
- 187 J.P. Raines, S. Abraham, R.L. Bodnar, and Y. Wang: *Int. Symp. Recent Dev. Plate Steels*, 2011, pp. 329–42.
- 188 G. Casuccio, M. Potter, F. Schwerer, R.J. Fruehan, and S. Story: *Development of the Automated Steel Cleanliness Analysis Tool (ASCAT)*, Pittsburgh, 2005.
- 189 M. Abdulsalam, N. Gao, B.A. Webler, and E.A. Holm: *Front. Mater.*, 2021, vol. 8, pp. 1–10.
- 190 M. Abdulsalam, M. Jacobs, and B.A. Webler: in *Metallurgical and Materials*

- Transactions B: Process Metallurgy and Materials Processing Science*, vol. 52, 2021, pp. 3970–85.
- 191 N. Gao, M. Abdulsalam, M. Potter, G. Casuccio, E. Holm, and B. Webler: in *2019 AISTech Conference Proceedings*, vol. 1, AIST, 2019, pp. 2155–60.
- 192 W. Zhao, F. Chen, H. Huang, D. Li, and W. Cheng: *Comput. Intell. Neurosci.*, 2021, vol. 2021, pp. 1–13.
- 193 Y. Liu, Y. Zhang, L. Zhang, Y. Ren, P. Shen, and Y. Luo: *Steel Res. Int.*, 2018, vol. 89, pp. 1–11.
- 194 S. Sun, L. Sun, S. Waterfall, and D. Liao: in *Proceedings of 2018 China Symposium on Sustainable Steelmaking Technology*, Tianjing, 2018, pp. 1–18.
- 195 L. Wang, J. Li, S. Yang, C. Chen, H. Jin, and X. Li: *Sci. Rep.*, 2019, vol. 9, p. 3670.
- 196 S. Wang, J. Zhang, R. Cheng, and H. Ma: *Trans. Indian Inst. Met.*, 2018, vol. 71, pp. 2231–42.
- 197 W.V. Bielefeldt and A.C.F. Vilela: *Steel Res. Int.*, 2015, vol. 86, pp. 375–85.
- 198 Japan Society for the Advancement of Science and the 19th Committee on Steelmaking: *Steelmaking Data Sourcebook*, Gordon and Breach Science Publishers, New York, 1988.
- 199 S.K. Choudhary and A. Ghosh: *ISIJ Int.*, 2009, vol. 49, pp. 1819–27.
- 200 Y.M. Won and B.G. Thomas: *Metall. Mater. Trans. A Phys. Metall. Mater. Sci.*, 2001, vol. 32, pp. 1755–67.
- 201 J. Bellot and M. Gantois: *Trans Iron Steel Inst Jpn*, 1978, vol. 18, pp. 546–53.
- 202 P.A. Thornton: *J. Mater. Sci.*, 1971, vol. 6, pp. 347–56.
- 203 J. Zhang, S. Li, Z. Yang, G. Li, W. Hui, and Y. Weng: *Int. J. Fatigue*, 2007, vol. 29, pp. 765–71.